

**Longitudinal Structural and Functional Brain Network Changes during  
Epileptogenesis in a Rat Model of Temporal Lobe Epilepsy**

**Emma Christiaen**

Doctoral dissertation submitted to obtain the academic degree of  
Doctor of Biomedical Engineering

**Supervisors**

Prof. Christian Vanhove, PhD\* - Prof. Robrecht Raedt, PhD\*\*

\* Department of Electronics and Information Systems  
Faculty of Engineering and Architecture, Ghent University

\*\* Department of Head and Skin  
Faculty of Medicine and Health Sciences, Ghent University

October 2021



ISBN 978-94-6355-532-6

NUR 954

Wettelijk depot: D/2021/10.500/80

## **Members of the Examination Board**

### **Chair**

Prof. Hennie De Schepper, PhD, Ghent University

### **Other members entitled to vote**

Benedicte Descamps, PhD, Ghent University

Prof. Joanes Grandjean, PhD, Radboud Universiteit, the Netherlands

Elisabeth Jonckers, PhD, Universiteit Antwerpen

Prof. Daniele Marinazzo, PhD, Ghent University

Prof. Alfred Meurs, PhD, Ghent University

### **Supervisors**

Prof. Christian Vanhove, PhD, Ghent University

Prof. Robrecht Raedt, PhD, Ghent University



# Acknowledgements

Een doctoraat doe je niet alleen. Daarom zou ik graag iedereen bedanken die me tijdens de laatste vijf jaar gesteund heeft met goede raad, constructieve feedback, etentjes en feestjes, berichtjes, kaartjes en kaarsjes.

Als eerste zou ik graag mijn promotoren, prof. Chris Vanhove en prof. Robrecht Raedt, bedanken. Bedankt om in me te geloven en om me de kans te bieden een doctoraat te starten.

Chris, bedankt om altijd voor me klaar te staan. Je deur stond letterlijk en figuurlijk altijd open. Dankzij je positiviteit en praktische hulp ging ik na iedere wekelijkse meeting vol goeie moed verder, ook al zag ik het een uurtje voordien soms niet meer zitten. Je rust en vertrouwen straalden op mij af en deden me geloven in een goede afloop. Ik had me geen betere promotor kunnen voorstellen.

Robrecht, je enthousiasme en passie voor onderzoek zorgden voor heel veel nieuwe ideeën tijdens onze maandelijkse meetings. Als bioloog zorgde je er ook voor dat we de biologische betekenis en medische relevantie van ons onderzoek en onze resultaten niet uit het oog verloren. Samen met Chris vormde je voor mij het ideale promotorenduo. Bedankt!

I would like to thank the members of the examination board, prof. Joanes Grandjean, dr. Elisabeth Jonckers, prof. Daniele Marinazzo, prof. Alfred Meurs and dr. Benedicte Descamps, for their time, their valuable and constructive feedback, and the interesting discussion during

the internal defense. I would also like to thank prof. Hennie De Schepper for taking on the role of Chair of the examination board.

Bene, je was niet alleen jurylid, maar je hebt me geholpen tijdens het hele doctoraatstraject, van de allereerste scan tot de allerlaatste scan, tijdens onze wekelijkse meetings, bij het omgaan met de ratten. Bedankt! Ik had het niet kunnen doen zonder jou.

Dan wil ik ook Marie bedanken, mijn PhD partner. We zijn samen gestart, hebben alles samen geleerd, en ook al zijn we dan elk onze eigen richting uitgegaan, toch kon ik altijd bij je terecht voor je mening en advies. Doctoreren was zo veel leuker en ging veel vlotter met twee. Ik vond het ontzettend leuk om met jou samen te werken. Bedankt!

Bedankt ook aan alle proffen van Medisip en 4Brain voor de constructieve feedback tijdens research meetings, presentaties en peer reviews, en om mijn publicaties met een kritische blik na te lezen.

Ik heb mijn doctoraat enorm graag gedaan en dat is voor een heel groot deel te danken aan de beste collega's die ik me kan voorstellen, zowel bij Medisip en bioMMeda, als bij 4Brain. Een doctoraat kan heel competitief zijn, maar dat is bij ons niet het geval. Iedereen steunt elkaar, is blij voor elkaars successen en vrolijkt elkaar op als het minder gaat. Jullie zijn niet alleen collega's, maar echte vrienden, voor het leven.

Als eerste wil ik mijn collega's van Medisip bedanken. Milan, je bent iemand op wie iedereen kan rekenen. Ik kon altijd bij je terecht, of het nu over ICT-gerelateerde zaken ging, of over de lay-out van onze thesis. Maar je bent ook gewoon een lieve, grappige en fantastische collega. Veel succes met de laatste loodjes, de huizenjacht en je nieuwe job bij Molecubes. Jolan, ik bewonder je oprechte interesse in andere mensen. Dat zal zeker van pas komen als dokter. Geen idee hoe iemand tegelijk kan doctoreren en geneeskunde studeren, maar jij doet het toch maar. Veel succes! Charlotte, je brengt leven in de brouwerij zodra je onze bureau binnenstapt. Bedankt om ons mee te nemen voor lunch in Ikea, om een barbecue voor Paulo te organiseren bij je thuis, om een kerstboom

te zetten in de keuken. Het zijn die dingen die van collega's vrienden maken. Mariele, I feel like you are the heart of Medisip, bringing the Belgian and international PhD students together. I had so much fun at the parties at your apartment, with homemade glühwein, cookies, and singing along with the Backstreet Boys. I wish you the best of luck in the future, with your public defense and at your new home in Aalst. Jens (Maebe), nu Milan, Mariele en ik vertrekken wordt het nogal leeg bij Medisip. Hopelijk komen er snel een paar nieuwe PhD studenten bij om je gezelschap te houden in jullie bureau. En anders mag je altijd mijn plaatsje in onze bureau innemen. Gert, ik ben er zeker van dat je door je gedrevenheid en kritische ingesteldheid een bijdrage zult kunnen leveren aan de diagnose en behandeling van psychische stoornissen. Maar ocharme je proefpersonen! Emma, proficiat met je FWO beurs! Ik ken je nog niet zo goed, maar ik weet zeker dat je dat super zal doen. Kate, you started your PhD just before COVID, so I haven't seen you that much, but I wish you the best of luck with your PhD.

I also want to thank the former PhD students at Medisip: Kim, Jens, Willeke, Stijn, Paulo, Ester, Thibault, Prakash, Gwenaëlle, Amir, Tim and Marek. In het bijzonder wil ik Kim bedanken. Je was mijn meter en hebt me meteen wegwijs gemaakt op Infinity en in Blok B. Bedankt om me in te leiden in de wereld van diffusie MRI. Ik vond het ook heel leuk om samen op conferentie te gaan naar San Sebastian en Parijs, en ik ben blij dat ik je ook nu nog tegenkom, in Goettingen of gewoon op Infinity. Jens (Mincke), we moesten je delen met de bio-ingenieurs, maar wanneer je bij ons op de bureau zat, zat de sfeer er meteen in. Ik heb dankzij jou geleerd dat een blauw scherm op een Windows computer niet per se betekent dat hij gecrasht is. Bedankt ook voor je feedback op mijn interne verdediging. Ik denk dat we allemaal een beetje geschrokken waren toen je stem plots uit het niets klonk!

Natuurlijk mag ik ook Saskia en Inge niet vergeten te bedanken voor alle administratieve hulp tijdens mijn doctoraat. Ook bedankt aan Jurgen voor alle computer-gerelateerde hulp, vooral toen mijn computer crashte.

I would like to thank the colleagues at bioMMeda as well. Lunches at IBiTech were always a lot of fun, thanks to your interesting and funny stories.

Thank you to my colleagues at 4Brain: Marie, Latoya, Charlotte G., Wouter, Jana, Anirudh, Charlotte B., Silke, Erine, Jeroen, Simona, Helen, Lars, Sielke and Lien. Even though I'm not a 'full' member of 4Brain, you have always made me feel like I was. We had a lot of fun together, during birthday parties with homemade pizza, burgers and fries at De Frietketel, a comedy show by Brigitte Kaandorp, selling cake at the open garden, karaoke in Vienna, and many dinners and after-work events. We also went on some work-related trips together, although something always seemed to go wrong, like when our flight was cancelled in Vienna or when we didn't make it to the SWO Midwinter meeting. Thank you to the 4Brain colleagues at K12 as well: Sofie, Elien, Ann and Mathieu.

Ook wil ik mijn thesisstudenten Yi, Pieter-Jan en Marjoleen bedanken. Jullie hebben alle drie bijgedragen aan mijn doctoraat en ik vond het heel interessant om jullie te mogen begeleiden.

Daarnaast zou ik graag mijn vrienden willen bedanken. Bedankt voor jullie interesse in mijn onderzoek en om voor de nodige afleiding te zorgen. Vooral ook bedankt aan Saar om mijn thesis na te lezen!

Als laatste zou ik nog mijn familie willen bedanken. Bedankt voor alle berichtjes en succeswensen, bedankt om kaarsjes te branden en bedankt om mijn papers te lezen. Dankjewel aan mijn oma's en opa's om altijd met veel interesse te luisteren als ik over mijn onderzoek vertel. En vooral dankjewel aan mijn mama en papa, en mijn zussen Marie en Klara, om me altijd en onvoorwaardelijk te steunen. Om er gewoon te zijn.

# Samenvatting

Epilepsie is een neurologische aandoening die gekenmerkt wordt door herhaaldelijke epileptische aanvallen. Het is één van de meest voorkomende neurologische aandoeningen en treft wereldwijd meer dan 50 miljoen mensen. De meest voorkomende soort epilepsie is temporaalkwabepilepsie (*temporal lobe epilepsy*, TLE). TLE wordt vaak veroorzaakt door een initieel precipiterend letsel, zoals status epilepticus, een beroerte, hersentrauma, een hersentumor, of een infectie van het centrale zenuwstelsel. Momenteel is het nog niet mogelijk om te voorspellen welke patiënten epilepsie zullen ontwikkelen na een dergelijk letsel en welke patiënten niet, voornamelijk omdat er weinig gekend is over hoe normale hersenen omgevormd worden tot epileptische hersenen, een proces dat epileptogenese genoemd wordt. Daarom is het belangrijk om meer inzicht te krijgen in de basismechanismes van epileptogenese, wat zou kunnen helpen om biomerkers te vinden voor de prognose van de ziekte. Hoewel TLE een focale soort epilepsie is, waarbij aanvallen ontstaan in structuren van de temporale kwab, is er meer en meer bewijs dat laat vermoeden dat afwijkende epileptogene netwerken een rol spelen in deze aandoening. Deze netwerken omvatten niet enkel hersenregio's die behoren tot de temporale kwab, maar ook extratemporale regio's, zoals subcorticale regio's en de neocortex. Hersennetwerken zijn een combinatie van structurele en functionele netwerken. Daarbij kunnen structurele netwerken gezien worden als de 'hardware' van de hersenen en functionele netwerken als de 'software' die de hardware gebruikt om specifieke taken uit te voeren. In TLE zijn afwijkingen in zowel structurele als functionele netwerkconnectiviteit vastgesteld.

De doelstelling van dit proefschrift was meer inzicht te krijgen in de mechanismes van epileptogenese, met als uiteindelijk doel het vinden van een biomarker om te voorspellen welke patiënten epilepsie zullen ontwikkelen na een initieel precipiterend letsel. Daartoe werden veranderingen in structurele en functionele netwerkconnectiviteit tijdens epileptogenese onderzocht in een rattenmodel van TLE met behulp van geavanceerde magnetische resonantie beeldvorming (*magnetic resonance imaging*, MRI).

Structurele netwerkconnectiviteit kan onderzocht worden met diffusie-gewogen MRI (*diffusion-weighted MRI*, dMRI). Deze beeldvormingstechniek detecteert de diffusie van water, op basis waarvan de microstructuur en structurele integriteit van de hersenen in kaart gebracht kunnen worden. Het meest eenvoudige en meest gebruikte model voor diffusie is het diffusie-tensor-model. Dat model is echter niet specifiek voor microstructuur en is niet nauwkeurig wanneer complexe wittestofconfiguraties voorkomen. Een meer geavanceerd model dat deze beperkingen kan overwinnen is multischil-multiweefsel-beperkte-sferische-deconvolutie (*multi-shell multi-tissue constrained spherical deconvolution*, MSMT-CSD). Op basis van dat model kan een nauwkeurigere schatting van de wittestofstructuren in de hersenen (tractografie) bekomen worden. Daarnaast kan met behulp van fixel-gebaseerde analyse (*fixel-based analysis*, FBA) informatie over specifieke populaties van wittestofstructuren verkregen worden uit dit model, en kan de structurele integriteit van deze populaties onderzocht worden. De topologie van hersennetwerken kan geëvalueerd worden aan de hand van de grafentheorie. In de grafentheorie worden de hersenen weergegeven als een netwerk dat bestaat uit knopen (*nodes*), meestal hersenregio's, en takken (*edges*) die de relatie tussen de knopen voorstellen. Verschillende grafentheoretische parameters kunnen berekend worden om het netwerk te beschrijven en te kwantificeren.

In **Hoofdstuk 5** werden de structurele netwerktopologie en integriteit van witte stof onderzocht met behulp van longitudinale dMRI, tractografie en FBA op basis van het MSMT-CSD model in het intraperitoneaal kainaat (*intraperitoneal kainic acid*, IPKA) rattenmodel van TLE. Deze studie had twee doelstellingen: 1) onderzoeken hoe het structurele her-

sennetwerk verandert tijdens epileptogenese in het IPKA rattenmodel en welke hersenregio's het meest aangetast zijn en 2) nagaan of de veranderingen in netwerktopologie gerelateerd zijn aan veranderingen in de integriteit van witte stofbanen, beoordeeld aan de hand van FBA. De resultaten toonden aan dat globale graad, een maat voor structurele connectiviteit, en lokale efficiëntie, een maat voor segregatie of lokale interconnectiviteit, daalden tijdens epileptogenese in de IPKA groep. Daarnaast was er een daling in globale efficiëntie en een stijging in karakteristieke padlengte, wat wees op een daling in integratie of globale communicatie-efficiëntie. De lokale graad daalde in verschillende hersenregio's die deel uitmaakten van het limbische systeem en het defaultnetwerk (*default-mode network*, DMN), vooral tijdens de vroege fase van epileptogenese. De analyse van de integriteit van witte stof aan de hand van FBA toonde aan dat de vezeldichtheid (*fiber density*, FD) en bundeldichtheid en -doorsnede (*fiber-density-and-cross-section*, FDC) daalden tijdens vroege en late epileptogenese in verschillende witte stofbanen, zoals de commissura anterior, het corpus callosum, het cingulum, de capsula interna en de fimbria, wat wijst op een daling in intra-axonale volumefractie. Dat sluit aan bij de neuropathologische veranderingen, zoals neurodegeneratie en gliose, die zich voordoen na status epilepticus in het IPKA model. Daarnaast constateerden we ook dat globale graad, globale efficiëntie en lokale efficiëntie in het structurele netwerk positief gecorreleerd waren met FDC en de bundeldoorsnede (*fiber-bundle cross-section*, FC) in IPKA dieren. Dat wijst erop dat de daling in graad, integratie en segregatie tijdens epileptogenese waarschijnlijk gelinkt is aan een daling in axonale dichtheid of een daling in de integriteit van de belangrijkste witte stofbanen in de hersenen van de rat.

Veranderingen in de integriteit van witte stof kunnen ook een invloed hebben op de functionele netwerkconnectiviteit in de hersenen. Functionele hersennetwerken kunnen geïdentificeerd en onderzocht worden met behulp van functionele MRI in rusttoestand (*resting state functional MRI*, rsfMRI), een beeldvormingstechniek die het mogelijk maakt om de activiteit in de volledige hersenen te visualiseren. In **Hoofdstuk 6** werden veranderingen in de functionele netwerktopologie in een

rattenmodel van TLE geëvalueerd met behulp van longitudinale rsfMRI en grafentheorie-analyse. Daarnaast werd het potentieel onderzocht van functionele netwerktopologie om het optreden van aanvallen na een letsel te voorspellen. Het doel van deze studie was driedig: 1) karakteriseren hoe de functionele organisatie van het rattenbrein verandert na status epilepticus (SE) en tijdens de ontwikkeling van TLE; 2) identificeren welke hersengebieden de hoogste mate van connectiviteitsveranderingen hebben; 3) evalueren of connectiviteitsveranderingen geassocieerd zijn met het optreden van spontane aanvallen. Een analyse van het functionele hersennetwerk toonde aan dat de clusteringscoëfficiënt en lokale efficiëntie afnamen tijdens epileptogenese, wat wijst op een afname in segregatie of lokale interconnectiviteit. De karakteristieke padlengte nam toe en de globale efficiëntie nam af, wat wijst op een afname in integratie of globale communicatie-efficiëntie. De nodale graad nam af in de meest verbonden hersengebieden in het baselinenetwerk, wat wijst op een verlies in connectiviteitssterkte. De meeste van deze regio's maakten deel uit van het DMN van de rat. De functionele connectiviteit, segregatie en integratie namen het meest significant af tussen 1 en 3 weken na SE. Na dit tijdstip bleef de netwerktopologie ongewijzigd. De hersenregio die het meest ingrijpend veranderde in zijn functionele connectiviteit tijdens epileptogenese was de retrospleniale cortex, één van de belangrijkste knopen van het DMN van de rat. Daarnaast zagen we dat de frequentie van aanvallen in de chronische epilepsiefase gecorreleerd was met de functionele connectiviteit, integratie en segregatie 1 week na SE en met de functionele integratie en segregatie 16 weken na SE. Bovendien was de frequentie van aanvallen positief gecorreleerd met de graad van verschillende hersenregio's, bepaald 1 week na SE. Tot deze regio's behoren de hippocampus en thalamus, twee regio's die zwaar getroffen zijn door neurodegeneratie en gliose na SE. Bijgevolg kunnen we stellen dat hoe meer functioneel gedeconnecteerd deze hersenregio's zijn na KA-geïnduceerde SE, hoe minder waarschijnlijk het is dat aanvallen optreden in de chronische epilepsiefase. Die associaties tussen aanvalsfrequentie en functionele connectiviteitsparameters wijzen allemaal op een nogal onverwachte bevinding, namelijk dat hoe meer het hersennetwerk aangetast wordt door KA-geïnduceerde SE, hoe kleiner de kans is dat

spontane epileptische aanvallen worden gegenereerd. Het blijkt dus dat het hersennetwerk een minimale mate van organisatie moet behouden om het ontstaan van aanvallen mogelijk te maken. Dat komt overeen met de krachtige therapeutische effecten van resectieve/deconnecterende chirurgie als behandeling voor epilepsie. De correlatie tussen de netwerkparameters en de aanvalsfrequentie 1 week na SE is erg interessant, omdat we op dat tijdstip nooit spontane epileptische aanvallen hebben geregistreerd in het IPKA-model voor TLE. Dat geeft aan dat netwerkreorganisatie bij een initieel precipiterend letsel een voorspellende waarde zou kunnen hebben en mogelijk een biomarker zou kunnen zijn voor de ontwikkeling en progressie van epilepsie.

In de meeste rsfMRI-studies wordt aangenomen dat functionele connectiviteit constant is tijdens de scansessie. In werkelijkheid varieert het echter op een veel kortere tijdschaal. Om deze snelle veranderingen in kaart te brengen, kan dynamische functionele connectiviteitsanalyse worden gebruikt. In **Hoofdstuk 7** werden dynamische veranderingen in functionele netwerktopologie tijdens de ontwikkeling van epilepsie onderzocht met behulp van rsfMRI data verkregen in het IPKA rattenmodel van TLE. Het doel van deze studie was tweeledig: 1) karakteriseren hoe de dynamische functionele connectiviteit en netwerktopologie van de hersenen van ratten veranderen na SE en tijdens de ontwikkeling van TLE, en 2) evalueren of deze veranderingen geassocieerd zijn met het optreden van spontane aanvallen. Met behulp van een dynamische functionele connectiviteitsanalyse konden zes terugkerende staten van functionele connectiviteit worden onderscheiden in IPKA- en controledieren. De verblijftijd (d.w.z. hoe vaak een staat voorkomt) in de staten met de hoogste gemiddelde functionele connectiviteit was lager in de IPKA-groep dan in de controlegroep, terwijl de verblijftijd hoger was in de staten met de laagste gemiddelde functionele connectiviteit. In staten met een hogere gemiddelde functionele connectiviteit waren de clusteringscoëfficiënt en lokale efficiëntie ook hoger, wat wijst op een hoge segregatie of lokale interconnectiviteit. In deze staten was de karakteristieke padlengte lager en de lokale efficiëntie hoger, wat wijst op een hoge integratie of globale communicatie-efficiëntie. Op dezelfde manier

waren segregatie en integratie lager in staten met een lagere gemiddelde functionele connectiviteit. Het opdelen van in de tijd variërende globale grafentheoretische netwerkparameters in staten van functionele netwerk-topologie leidde tot vergelijkbare resultaten. De verblijftijd was lager in staten met een hogere functionele connectiviteit, segregatie en integratie in de IPKA-dieren. Het is interessant dat de aanvalsfrequentie positief gecorreleerd was met de verblijftijd in staten met een hoge gemiddelde functionele connectiviteit en hoge segregatie en integratie, en negatief met de verblijftijd in staten met een lage gemiddelde functionele connectiviteit en lage segregatie en integratie, 1 en 16 weken na SE. Onze bevindingen geven dus aan dat dieren waarvan het functionele hersennetwerk zich vaker bevindt in een staat met een hoge functionele connectiviteit, segregatie en integratie, meer chronische aanvallen hebben. Aangezien functionele connectiviteit meer beperkt is tot de staten met de laagste functionele connectiviteit, integratie en segregatie bij dieren met minder aanvallen, is het denkbaar dat tijdelijke verhogingen in functionele connectiviteit nodig zijn om aanvallen te genereren.

Samengevat was het doel van dit proefschrift om meer inzicht te krijgen in de mechanismen van epileptogenese, met als uiteindelijk doel het vinden van een biomarker om te voorspellen welke patiënten epilepsie zullen ontwikkelen na een initieel precipiterend letsel. Daartoe werden veranderingen in structurele en functionele hersennetwerken tijdens epileptogenese onderzocht in een rattenmodel van TLE met behulp van geavanceerde MRI. Longitudinale diffusie-gewogen en functionele MRI in rusttoestand, in combinatie met grafentheorie, onthulden dynamische veranderingen in structurele en functionele netwerktopologie tijdens epileptogenese in een rattenmodel van TLE. Meer specifiek namen structurele en functionele connectiviteit, integratie en segregatie af tijdens epileptogenese. Die veranderingen waren niet beperkt tot de epileptogene focus, maar waren wijdverspreid en troffen voornamelijk regio's van het limbische systeem en het defaultnetwerk. Structurele en functionele netwerktopologie veranderden het meest tijdens de vroege fase van epileptogenese, en de veranderingen waren gerelateerd aan een verminderde intra-axonale waterfractie in wittestofbanen. Dat geeft aan dat die elementen mogelijk

verband houden met neurodegeneratie en gliose, die gekende histopathologische kenmerken van vroege epileptogenese zijn. Veranderde functionele connectiviteit, integratie en segregatie tijdens de latente fase van epileptogenese waren gerelateerd aan de frequentie van chronische aanvallen. Dat duidt op het potentieel van functionele netwerktopologie als biomarker voor ziekteprognose na een initieel precipiterend letsel. Verder onderzoek is nodig om deze veelbelovende bevindingen te valideren.



# Summary

Epilepsy is a neurological disorder characterized by recurrent epileptic seizures. It is one of the most common neurological disorders, affecting more than 50 million people worldwide. The most common type of epilepsy is temporal lobe epilepsy (TLE). TLE is often caused by an initial precipitating injury, such as status epilepticus, stroke, head trauma, a brain tumor, or a central nervous system infection. However, not all patients who suffer such an injury, develop epilepsy. As of yet, it is not possible to predict which patients will develop epilepsy after an injury and which patients will not, mainly because little is known about how a normal brain is transformed into an epileptic brain, a process called epileptogenesis. Therefore, it is important to gain more insight into the basic mechanisms of epileptogenesis, which could help to find biomarkers for disease prognosis. While TLE is a focal epilepsy type, with seizures originating in temporal structures, increasing evidence suggests that abnormal epileptogenic networks are involved in this disorder. These networks not only consist of brain regions in the temporal lobe, but also of extratemporal regions, such as subcortical areas and the neocortex. Brain networks are a combination of structural and functional networks. Structural networks can be considered the ‘hardware’ of the brain, and functional networks the ‘software’, that uses the hardware to execute specific tasks. Abnormalities in both structural and functional network connectivity have been reported in TLE.

This dissertation aimed to gain more insight into the mechanisms of epileptogenesis, with the ultimate goal of finding a biomarker to predict which patients will develop epilepsy after an initial precipitating injury. To this end, alterations in structural and functional brain net-

works during epileptogenesis were investigated in a rat model of TLE using advanced magnetic resonance imaging (MRI).

Structural network connectivity can be assessed using diffusion-weighted MRI (dMRI). This imaging technique detects the diffusion of water, based on which the microstructure and structural integrity of the brain can be mapped. The most basic and most commonly used model of diffusion is the diffusion tensor model. However, this model is not specific to microstructure and is not accurate in the presence of complex white matter configurations. A more advanced model that can overcome these limitations is multi-shell multi-tissue constrained spherical deconvolution (MSMT-CSD). Based on this model, a more accurate estimation of white matter structures in the brain (tractography) can be obtained. In addition, information about specific white matter fiber populations can be derived from this model using fixel-based analysis (FBA), and the structural integrity of these populations can be assessed. The topology of brain networks can be assessed using graph theory. In graph theory, the brain is represented as a network consisting of nodes, usually brain regions, and edges that show the relationship between the nodes. Several graph theoretical measures can be calculated to describe and quantify the network. In **Chapter 5**, structural network topology and white matter integrity were investigated using longitudinal multi-shell dMRI, tractography and FBA based on the MSMT-CSD model in the intraperitoneal kainic acid (IPKA) rat model of TLE. The objectives of the study were twofold: 1) to investigate how the structural brain network changes during epileptogenesis in the IPKA rat model, and which brain areas are most affected and 2) to determine whether the changes in network topology are related to changes in the integrity of white matter tracts assessed using fixel-based analysis. We found that global degree, a measure of structural connectivity, and local efficiency, a measure of segregation or local interconnectivity, decreased in the IPKA group during epileptogenesis. In addition, global efficiency decreased and characteristic path length increased, which pointed to a decrease in integration or overall communication efficiency. Nodal degree decreased in several regions of the limbic system and the default-mode network (DMN), mainly dur-

ing early epileptogenesis. The analysis of white matter integrity using FBA revealed that fiber density (FD) and fiber-density-and-cross-section (FDC) were decreased during early and late epileptogenesis in the IPKA group in several white matter tracts, including anterior commissure, corpus callosum, cingulum, internal capsule and fimbria, which indicates that there is a decrease in intra-axonal volume fraction. This is in line with the neuropathological changes, such as neurodegeneration and gliosis, which are known to occur after status epilepticus in the IPKA model. Moreover, we also found that global degree, as well as global and local efficiency in the structural brain network were positively correlated with FDC and fiber-bundle cross-section (FC) in IPKA animals. This further indicates that decreased degree, integration and segregation during epileptogenesis are likely related to decreased axonal density or decreased white matter integrity in the main white matter tracts in the rat brain.

Changes in white matter integrity can also affect functional brain connectivity. Functional brain networks can be identified and investigated using resting state functional MRI (rsfMRI), an imaging technique that allows a visualisation of whole-brain activity. In **Chapter 6**, changes in functional network topology in a rat model of TLE were evaluated using longitudinal rsfMRI and graph theory analysis. In addition, the potential of functional network topology to predict seizure occurrence after an injury was investigated. The aim of this study was threefold: 1) to characterize how the functional organization of the rat brain changes after status epilepticus (SE) and during the development of TLE; 2) to identify brain regions with the highest degree of connectivity changes; 3) to evaluate whether connectivity changes are associated with the occurrence of spontaneous seizures. Analysis of the functional brain network revealed that clustering coefficient and local efficiency decreased during epileptogenesis, indicating a decrease in segregation or local interconnectivity. Characteristic path length increased and global efficiency decreased, indicating a decrease in integration or overall communication efficiency. Nodal degree decreased in the most highly connected brain regions in the baseline network, indicating a loss in connection strength. Most of these regions were part of the rat DMN. Functional connectivity, segregation

and integration decreased most significantly between 1 and 3 weeks post-SE. Beyond this time point, the network topology remained unchanged. The brain region which changed most profoundly in functional connectivity during epileptogenesis was the retrosplenial cortex, one of the most important nodes of the rat DMN. We also found that seizure frequency in the chronic epilepsy phase was correlated with functional connectivity, integration and segregation 1 week post-SE and with functional integration and segregation 16 weeks post-SE. In addition, seizure frequency was positively correlated with the degree of several brain regions, determined 1 week after SE. These regions included the hippocampus and thalamus, two regions heavily affected by neurodegeneration and gliosis in response to SE. In other words, the more functionally disconnected these brain regions are upon KA-induced SE, the less likely it is for seizures to occur in the chronic phase. These associations between seizure frequency and functional connectivity measures all point out a quite unexpected finding, namely that the more profoundly the brain network is affected by the KA-induced SE, the less likely it is that spontaneous epileptic seizures are generated. Thus it appears that the brain network needs to keep a minimal degree of organization to enable the emergence of seizures. This is in line with the potent therapeutic effects of resective/disconnective surgery as a treatment for epilepsy. The correlation between network measures and seizure frequency 1 week after SE is very interesting, since no spontaneous epileptic seizures were recorded at that time point in the IPKA model for TLE. This indicates that network reorganisation upon an initial precipitating injury might have a predictive value and could potentially be used as a biomarker for the development and progression of epilepsy.

In most rsfMRI studies, functional connectivity is assumed to be stationary during the scanning session. However, in reality, it varies on a much shorter time scale. To capture these fast changes, dynamic functional connectivity analysis can be used. In **Chapter 7**, dynamic changes in functional network topology during the development of epilepsy were investigated using rsfMRI data acquired in the IPKA rat model of TLE. The aim of this study was twofold: 1) to characterize how dynamic func-

tional connectivity and network topology of the rat brain change after SE and during the development of TLE, and 2) to evaluate whether these changes are associated with the occurrence of spontaneous seizures. Using dynamic functional connectivity analysis, six recurring states of functional connectivity could be distinguished in IPKA and control animals. Dwell time (i.e., how often a state occurs) in the states with the highest mean functional connectivity was lower in the IPKA group compared to the control group, while dwell time was higher in the states with the lowest mean functional connectivity. In states with a higher mean functional connectivity, clustering coefficient and local efficiency were higher as well, indicating a high segregation or local interconnectivity. In these states, characteristic path length was lower and local efficiency higher, indicating a high integration or overall communication efficiency. Similarly, segregation and integration were lower in states with a lower mean functional connectivity. The decomposition of time-varying global graph theoretical network metrics into states of functional network topology led to similar results. Dwell time was lower in states with a higher functional connectivity, segregation and integration in the IPKA animals. Interestingly, seizure frequency was positively correlated with dwell time in states with a high mean functional connectivity and high segregation and integration, and negatively with dwell time in states with a low mean functional connectivity and low segregation and integration, 1 and 16 weeks post-SE. As such, our findings indicate that animals that dwell in states with high functional connectivity, segregation and integration have more chronic seizures. Since functional connectivity is more restricted to the states with the lowest functional connectivity, integration, and segregation in animals that have fewer seizures, it is conceivable that temporary increases in functional connectivity might be necessary for seizures to be generated.

To conclude, the aim of this dissertation was to gain more insight into the mechanisms of epileptogenesis, with the ultimate goal of finding a biomarker to predict which patients will develop epilepsy after an initial precipitating injury. To this end, alterations in structural and functional brain networks during epileptogenesis were investigated in a rat model

of TLE using advanced MRI. Longitudinal diffusion-weighted and resting state functional MRI, in combination with graph theory, revealed dynamic changes in structural and functional network topology during epileptogenesis in a rat model of TLE. More specifically, structural and functional connectivity, integration, and segregation decreased during epileptogenesis. These changes were not limited to the epileptogenic focus, but were widespread, and mainly affected regions of the limbic system and the default-mode network. Structural and functional network topology changed most during early epileptogenesis, and the changes were related to reduced intra-axonal water fraction in white matter tracts. This indicates that these changes may be related to neurodegeneration and gliosis, which are known histopathological features of early epileptogenesis. Altered functional connectivity, integration, and segregation during the latent phase of epileptogenesis were related to chronic seizure frequency. This hints at the potential of functional network topology as a biomarker for disease prognosis after an initial precipitating injury. Further research is required to validate these promising findings.

# List of abbreviations

AD	axial diffusivity
ADC	apparent diffusion coefficient
AED	anti-epileptic drug
ALFF	amplitude of low frequency fluctuations
ANT	anterior nucleus of the thalamus
ATL	anterior temporal lobectomy
Au	auditory cortex
AWF	axonal water fraction
BOLD	blood oxygenation level-dependent
CA	cornu ammonis
CBF	cerebral blood flow
CBV	cerebral blood volume
Cg	cingulate cortex
CMRglu	cerebral metabolic rate of glucose
CMRO <sub>2</sub>	cerebral metabolic rate of oxygen
CMS	chronic mild stress
Cp	clustering coefficient
CPu	caudate putamen
CSD	constrained spherical deconvolution
CSF	cerebrospinal fluid
CT	computed tomography
DBS	deep brain stimulation
dFC	dynamic functional connectivity
DKI	diffusion kurtosis imaging
DLO	dorsolateral orbitofrontal cortex
DMN	default-mode network

DMPC	dorsal medial prefrontal cortex
dMRI	diffusion-weighted magnetic resonance imaging
DTI	diffusion tensor imaging
DWI	diffusion-weighted imaging
DWIs	diffusion-weighted images
EAS	extra-axonal space
EEG	electroencephalography
Eg	global efficiency
Eloc	local efficiency
EPI	echo-planar imaging
FA	fractional anisotropy
fALFF	fractional ALFF
FBA	fixel-based analysis
FC	fiber-bundle cross-section
FD	fiber density
FDC	fiber-density-and-cross-section
FDR	false discovery rate
FID	free induction decay
FLAIR	fluid attenuated inversion recovery
fmRI	functional magnetic resonance imaging
FOD	fiber orientation distribution
FOV	field of view
FWE	family-wise error
GABA	gamma-aminobutyric acid
GP	globus pallidus
$G_{PE}$	phase encoding gradient
$G_{RO}$	readout gradient
$G_{SS}$	slice selection gradient
HARDI	high angular resolution diffusion-weighted imaging
Hip	hippocampus
HRF	hemodynamic response function
IAS	intra-axonal space
ICA	independent component analysis
ILAE	International League Against Epilepsy
Ins	insula

IPKA	intraperitoneal kainic acid
KA	kainic acid
LMEM	linear mixed-effects model
L <sub>p</sub>	characteristic path length
LSD	least significant difference
MC	motor cortex
MD	mean diffusivity
MEG	magnetoencephalography
MR	magnetic resonance
MRI	magnetic resonance imaging
MSMT-CSD	multi-shell multi-tissue constrained spherical deconvolution
NAc	nucleus accumbens
NMDA	N-methyl-D-aspartate
PD	proton density
PET	positron emission tomography
PGSE	pulsed gradient spin echo
Pir	piriform cortex
PP	perforant path
PrL	prelimbic cortex
PtA	parietal association cortex
PtP	posterior parietal cortex
RD	radial diffusivity
ReHo	regional homogeneity
rf	radiofrequency
RNS	responsive neurostimulation
ROI	region of interest
RSC	retrosplenial cortex
rsfMRI	resting state functional magnetic resonance imaging
SE	status epilepticus
Sep	septum
SIFT	spherical-deconvolution informed filtering of tractograms
SNR	signal-to-noise ratio
SPECT	single-photon emission computed tomography
SSC	somatosensory cortex
Sub	subiculum

TE	echo time
TeA	temporal association cortex
Thal	thalamus
TLE	temporal lobe epilepsy
TR	repetition time
Vis	visual cortex
VMPC	ventral medial prefrontal cortex
VNS	vagus nerve stimulation
WMTI	white matter tract integrity
WTC	wavelet transform coherence

# List of publications

## Journal Papers

- Christiaen, E. & Goossens, M. G., Raedt, R., Descamps, B., Larsen, L. E., Craey, E., Carrette, E., Vonck, K., Boon, P. & Vanhove, C. (2019). Alterations in the functional brain network in a rat model of epileptogenesis: A longitudinal resting state fMRI study. *Neuroimage*, 202, 116144.
- Christiaen, E., Goossens, M. G., Descamps, B., Larsen, L. E., Boon, P., Raedt, R. & Vanhove, C. (2020). Dynamic functional connectivity and graph theory metrics in a rat model of temporal lobe epilepsy reveal a preference for brain states with a lower functional connectivity, segregation and integration. *Neurobiology of disease*, 139, 104808.
- Christiaen, E., Goossens, M. G., Descamps, B., Delbeke, J., Wadman, W., Vonck, K., Boon, P., Raedt, R. & Vanhove, C. (2021). White matter integrity in a rat model of epileptogenesis: structural connectomics and fixel-based analysis. *Brain Connectivity*.
- Goossens M. G., Larsen L. E., Vergaelen M., Wadman W., Van den Haute C., Desloovere J., Brackx W., Christiaen E., Craey E., Vanhove C., Vonck K., Boon P. & Raedt R. (2021). Level of hM4D(Gi) DREADD expression determines inhibitory and neurotoxic effects in the hippocampus. *Eneuro*.
- Bouckaert, C., Christiaen, E., Verhoeven, J., Descamps, B., De Meulenaere, V., Boon, P., Carrette, E., Vonck, K., Vanhove, C. & Raedt, R. (2021) Comparison of In Vivo and Ex Vivo magnetic

resonance imaging in a Rat Model for Glioblastoma. *Diagnostics*, 11(8), 1311.

- Proesmans, S., Raedt, R., Germonpré, C., Christiaen, E., Descamps, B., Boon, P., De Herdt, V. & Vanhove, C. (2021). Voxel-based analysis of [18F]-FDG brain PET in rats using data-driven normalization. *Accepted for publication in Frontiers in medicine*.
- Xu, Y. & Christiaen, E., Chen, Q., De Witte, S., Peremans, K., Dockx, R., Saunders, J., Vanhove, C. & Baeken, C. (2021) Network analysis reveals abnormal functional brain circuitry in anxious dogs. *Resubmitted to Frontiers in behavioral neuroscience after revision*.

## Conference Contributions

- Christiaen, E., Goossens, M.-G., Descamps, B., Raedt, R. & Vanhove, C. (2020). Dynamic functional connectivity and graph theory metrics in a rat model of temporal lobe epilepsy. 15th European Molecular Imaging Meeting (EMIM 2020). Poster presentation.
- Christiaen, E., Goossens, M.-G., Descamps, B., Raedt, R. & Vanhove, C. (2020). Dynamic functional connectivity and graph theory metrics in a rat model of temporal lobe epilepsy reveal a preference for brain states with a lower functional connectivity, segregation and integration. ISMRM Benelux Chapter meeting 2020. Poster presentation.
- Christiaen, E., Goossens, M.-G., Descamps, B., Raedt, R. & Vanhove, C. (2020). Dynamic functional connectivity in a rat model of temporal lobe epilepsy reveals a preference for brain states with a lower functional connectivity. SWO Midwinter meeting. Poster presentation and pitch.
- Goossens, M.-G., Boon, P., Christiaen, E., Vonck, K., Carrette, E., Desloovere, J., Van den Haute, C., Baekelandt, V., Wadman, W., Vanhove, C. & Raedt, R. (2019). Chemogenetic therapy strongly

suppresses hippocampal excitability and spontaneous seizures in a rat model for temporal lobe epilepsy. 5th Congress of the European Academy of Neurology. In *European Journal of Neurology* (Vol. 26, pp. 416–416).

- Goossens, M.-G., Christiaen, E., Boon, P., Vonck, K., Carrette, E., Desloovere, J., Van Den Haute, C., Baekelandt, V., Wadman, W., Vanhove, C. & Raedt, R. (2019). Chemogenetic suppression of spontaneous seizures in a rat model for temporal lobe epilepsy. Update@Kempenhaghe, 21st Annual international clinical symposium.
- Goossens, M.-G., Christiaen, E., Boon, P., Vonck, K., Carrette, E., Desloovere, J., Van Den Haute, C., Baekelandt, V., Wadman, W., Vanhove, C. & Raedt, R. (2019). Chemogenetic suppression of spontaneous seizures in a rat model for temporal lobe epilepsy. f-Tales.
- Goossens, M.-G., Christiaen, E., Boon, P., Vonck, K., Carrette, E., Desloovere, J., Van Den Haute, C., Baekelandt, V., Wadman, W., Vanhove, C. & Raedt, R. (2019). Chemogenetic suppression of spontaneous seizures in a rat model for temporal lobe epilepsy. Belgian Society for Neuroscience, 13th National congress.
- Goossens, M.-G., Christiaen, E., Boon, P., Vonck, K., Van Den Haute, C., Baekelandt, V., Wadman, W., Vanhove, C. & Raedt, R. (2019). Chemogenetic suppression of excitatory hippocampal neurons in non-epileptic and epileptic rats. Research Day & Student Research Symposium 2019.
- Christiaen, E., Goossens, M.-G., Descamps, B., Boon, P., Raedt, R. & Vanhove, C. (2018). Functional connectivity changes during epileptogenesis: a longitudinal resting-state functional MRI study. Belgian Brain Congress 2018. In *Front. Neurosci. Conference Abstract*. Poster presentation.
- Christiaen, E., Goossens, M.-G., Descamps, B., Boon, P., Raedt, R. & Vanhove, C. (2018). Functional connectivity changes during

- epileptogenesis: a longitudinal resting-state functional MRI study. 13th European Congress on Epileptology. In *Epilepsia* (Vol. 59, pp. S253–S253). Poster presentation.
- Christiaen, E., Goossens, M.-G., Descamps, B., Boon, P., Raedt, R. & Vanhove, C. (2018). Functional connectivity changes during epileptogenesis: a longitudinal rs-fMRI study. Joint annual meeting ISMRM-ESMRMB 2018. Poster presentation.
  - Christiaen, E., Goossens, M.-G., Descamps, B., Boon, P., Raedt, R. & Vanhove, C. (2018). Functional connectivity changes during epileptogenesis: a longitudinal resting-state fMRI study. 13th European Molecular Imaging Meeting (EMIM 2018). Poster presentation.
  - Goossens, M.-G., Desloovere, J., Christiaen, E., Van Lysebettens, W., Craey, E., Acharya, A., Boon, P., Vonck, K., Van den Haute, C., Baekelandt, V., Wadman, W., Vanhove, C. & Raedt, R. (2018). The effect of chemogenetic inhibition of excitatory neurons on hippocampal excitability and seizure frequency in a rat model. 13th European Congress on Epileptology. In *Epilepsia* (Vol. 59, pp. S22–S22).
  - Goossens, M.-G., Desloovere, J., Christiaen, E., Van Lysebettens, W., Craey, E., Acharya, A., Boon, P., Vonck, K., Van den Haute, C., Baekelandt, V., Wadman, W., Vanhove, C. & Raedt, R. (2018). The effect of chemogenetic inhibition of excitatory neurons on hippocampal excitability and seizure frequency in a rat model. Update@Kempenhaghe.nl, 20th Annual international clinical symposium.
  - Goossens, M.-G., Desloovere, J., Christiaen, E., Van Lysebettens, W., Craey, E., Acharya, A., Boon, P., Vonck, K., Van den Haute, C., Baekelandt, V., Wadman, W., Vanhove, C. & Raedt, R. (2018). The effect of chemogenetic inhibition of excitatory neurons on hippocampal excitability and seizure frequency in a rat model. Research Day & Student Research Symposium.

- Christiaen, E., Goossens, M.-G., Descamps, B., Boon, P., Raedt, R. & Vanhove, C. (2018). Functional connectivity changes during epileptogenesis: a longitudinal rs-fMRI study. 10th annual meeting ISMRM Benelux Chapter. Poster presentation.
- Christiaen, E., Goossens, M.-G., Descamps, B., Boon, P., Raedt, R. & Vanhove, C. (2017). Changes in functional brain networks during epileptogenesis in a rodent model of temporal lobe epilepsy. 12th National Congress of the Belgian Society for Neuroscience. Oral presentation.
- Christiaen, E., Goossens, M.-G., Descamps, B., Boon, P., Raedt, R. & Vanhove, C. (2017). Changes in functional brain networks during epileptogenesis in a rodent model of temporal lobe epilepsy. ESMRMB Congress 2017 - 34th Annual Scientific Meeting. Poster presentation.
- Christiaen, E., Goossens, M.-G., Descamps, B., Boon, P., Raedt, R. & Vanhove, C. (2017). Functional connectivity changes during epileptogenesis: a longitudinal rs-fMRI study. 16th National Day on Biomedical Engineering. Poster presentation and pitch.
- Christiaen, E., Descamps, B., Raedt, R. & Vanhove, C. (2021). White matter integrity in a rat model of epileptogenesis: structural connectomics and fixel-based analysis. 16th European Molecular Imaging Meeting. Poster presentation.

## Oral Presentations

- Alterations in the functional brain network in a rat model of epileptogenesis. 1st 4BRAIN Neuroscience Day, Ghent, Belgium (February 2019)
- Functional connectivity changes during epileptogenesis: a longitudinal resting-state fMRI study. 10th Annual meeting of the ISMRM Benelux Chapter, Antwerp, Belgium (January 2018)

- Functional connectivity changes during epileptogenesis: a longitudinal rs-fMRI study. 1st AMIE symposium, Ghent, Belgium (January 2018)
- Chemogenetic modulation of the most active hub in the functional network. Neu3Ca Forum, Kempenhaeghe, Heeze, The Netherlands (March 2017)

# Contents

<b>Acknowledgements</b>	<b>i</b>
<b>Samenvatting</b>	<b>v</b>
<b>Summary</b>	<b>xiii</b>
<b>List of abbreviations</b>	<b>xix</b>
<b>List of publications</b>	<b>xxiii</b>
<b>1 Introduction</b>	<b>1</b>
1.1 Context . . . . .	1
1.2 Outline . . . . .	3
<b>2 Epilepsy</b>	<b>7</b>
2.1 Introduction . . . . .	7
2.2 The brain . . . . .	7
2.2.1 Neuroanatomy . . . . .	7
2.2.2 Neurophysiology . . . . .	10
2.3 Seizures . . . . .	14
2.3.1 Seizure generation and propagation . . . . .	14
2.3.2 Seizure classification . . . . .	15
2.4 Diagnosis . . . . .	18
2.5 Treatment . . . . .	22
2.5.1 Anti-epileptic drugs . . . . .	22
2.5.2 Epilepsy surgery . . . . .	23
2.5.3 Neurostimulation . . . . .	25
2.5.4 Ketogenic diet . . . . .	27

2.6	Temporal lobe epilepsy . . . . .	27
2.6.1	Clinical features . . . . .	27
2.6.2	Epileptogenesis . . . . .	28
2.6.3	Hippocampal sclerosis . . . . .	31
2.6.4	Amygdalohippocampal interconnections . . . . .	31
2.6.5	Animal models of temporal lobe epilepsy . . . . .	33
<b>3</b>	<b>Structural and functional MRI</b>	<b>45</b>
3.1	Magnetic resonance imaging . . . . .	45
3.1.1	Introduction . . . . .	45
3.1.2	MRI scanner . . . . .	45
3.1.3	Basic principles of MRI . . . . .	46
3.1.4	Relaxation . . . . .	47
3.1.5	Spatial localization . . . . .	48
3.1.6	Spin echo and gradient echo . . . . .	51
3.1.7	Image contrast . . . . .	52
3.1.8	Small animal MRI . . . . .	54
3.2	Diffusion-weighted MRI . . . . .	55
3.2.1	Basic principles of diffusion-weighted MRI . . . . .	55
3.2.2	Diffusion-weighted MRI analysis methods . . . . .	64
3.3	Functional magnetic resonance imaging . . . . .	100
3.3.1	Basic principles of functional MRI . . . . .	100
3.3.2	Resting state fMRI analysis methods . . . . .	107
3.4	Diffusion MRI and resting state fMRI in TLE . . . . .	121
3.4.1	White matter and microstructural integrity in TLE	121
3.4.2	Structural and functional networks in TLE . . . . .	122
3.4.3	Potential clinical and preclinical applications . . . . .	123
<b>4</b>	<b>Research aims</b>	<b>135</b>
<b>5</b>	<b>Structural brain network in epilepsy</b>	<b>137</b>
5.1	Introduction . . . . .	138
5.2	Materials and methods . . . . .	141
5.2.1	Animals . . . . .	141
5.2.2	Status epilepticus . . . . .	141
5.2.3	Image acquisition . . . . .	141

5.2.4	Electrode implantation and EEG recording . . . . .	142
5.2.5	Image preprocessing . . . . .	143
5.2.6	Structural connectome . . . . .	143
5.2.7	Tractometry-based DTI analysis . . . . .	145
5.2.8	Fixel-based analysis . . . . .	145
5.2.9	Volume of enlarged ventricles . . . . .	146
5.2.10	Statistical analysis . . . . .	146
5.3	Results . . . . .	147
5.3.1	Ventricular volume . . . . .	147
5.3.2	Global network metrics . . . . .	148
5.3.3	Nodal degree . . . . .	149
5.3.4	DTI metrics in white matter tracts . . . . .	150
5.3.5	Fixel metrics in white matter tracts . . . . .	152
5.3.6	Correlations between network metrics and fixel met- rics . . . . .	155
5.3.7	EEG recording . . . . .	156
5.4	Discussion . . . . .	157
5.4.1	Disruption of the structural brain network during epileptogenesis . . . . .	157
5.4.2	Increased diffusivity in white matter tracts during epileptogenesis . . . . .	160
5.4.3	Decrease in FD and FDC in white matter tracts during epileptogenesis . . . . .	160
5.4.4	Decreased FD in control group: related to social isolation? . . . . .	162
5.4.5	Limitation . . . . .	162
5.5	Conclusion . . . . .	163
<b>6</b>	<b>Functional brain network in epilepsy</b>	<b>173</b>
6.1	Introduction . . . . .	174
6.2	Materials and Methods . . . . .	176
6.2.1	Animals . . . . .	176
6.2.2	Status epilepticus . . . . .	177
6.2.3	Image acquisition . . . . .	177
6.2.4	Electrode implantation . . . . .	178

6.2.5	EEG recording . . . . .	179
6.2.6	Data analysis . . . . .	180
6.3	Results . . . . .	187
6.3.1	Hippocampal volume loss during epileptogenesis . .	187
6.3.2	Decrease in correlation coefficients during epileptogenesis . . . . .	189
6.3.3	Decrease in global functional segregation and integration . . . . .	191
6.3.4	Decrease in connectivity strength in highly connected nodes . . . . .	193
6.3.5	Decrease in connectivity in connections of the retrosplenial cortex . . . . .	193
6.3.6	Correlation between changes in network measures and seizure frequency . . . . .	195
6.4	Discussion . . . . .	200
6.4.1	Temporal progression of network topology and link with time-dependent changes in structural lesions and seizure frequency . . . . .	200
6.4.2	Comparison with previous animal studies . . . . .	202
6.4.3	Comparison with patient studies . . . . .	203
6.4.4	Decrease in connectivity of the retrosplenial cortex	203
6.4.5	Correlation between changes in network measures and seizure frequency . . . . .	204
6.4.6	Study limitations . . . . .	205
6.5	Conclusion . . . . .	206
<b>7</b>	<b>Dynamic functional brain network</b>	<b>221</b>
7.1	Introduction . . . . .	222
7.2	Materials and methods . . . . .	224
7.2.1	Data set . . . . .	224
7.2.2	Animals . . . . .	224
7.2.3	Status epilepticus . . . . .	225
7.2.4	Image acquisition . . . . .	225
7.2.5	Electrode implantation . . . . .	226
7.2.6	EEG recording . . . . .	227

7.2.7	Dynamic functional brain network . . . . .	227
7.2.8	States of functional connectivity and functional network topology . . . . .	229
7.2.9	Dwell time and number of transitions . . . . .	231
7.2.10	Correlation with seizure frequency . . . . .	232
7.2.11	Influence of window length . . . . .	232
7.2.12	Validation of epileptic dynamic functional connectivity . . . . .	232
7.3	Results . . . . .	233
7.3.1	States of functional connectivity and network topology . . . . .	233
7.3.2	Percentage dwell time in states of functional connectivity and network topology . . . . .	238
7.3.3	Number of transitions between states of functional connectivity and network topology . . . . .	242
7.3.4	Correlation of mean global network metrics, percentage dwell time and number of transitions with seizure frequency . . . . .	245
7.3.5	Influence of window length . . . . .	247
7.3.6	Validation of epileptic dynamic functional connectivity . . . . .	248
7.4	Discussion . . . . .	249
7.4.1	Dwelling in states with a lower mean functional connectivity, segregation and integration . . . . .	249
7.4.2	Changes in variability of functional connectivity, segregation and integration . . . . .	250
7.4.3	Correlation with seizure frequency . . . . .	251
7.4.4	Dynamic functional connectivity in patients with TLE . . . . .	252
7.4.5	Validation data set . . . . .	253
7.4.6	Limitations . . . . .	253
7.4.7	Future work . . . . .	254
7.5	Conclusion . . . . .	254

<b>8</b>	<b>General discussion and conclusions</b>	<b>265</b>
8.1	Structural brain network in epilepsy . . . . .	265
8.1.1	Decreased structural network connectivity and efficiency during epileptogenesis . . . . .	266
8.1.2	Structural network changes are related to decreased intra-axonal volume fraction in white matter . . .	267
8.2	Functional brain network in epilepsy . . . . .	268
8.2.1	Decreased functional connectivity and network efficiency during epileptogenesis . . . . .	268
8.2.2	Decrease in connectivity of the retrosplenial cortex	269
8.2.3	Chronic seizure frequency is related to altered network topology during early epileptogenesis . . . . .	270
8.3	Dynamic functional brain network in epilepsy . . . . .	271
8.3.1	Dwelling in states with a lower mean functional connectivity, segregation and integration . . . . .	271
8.3.2	Chronic seizure frequency is related to dwelling in states with high functional connectivity, segregation and integration . . . . .	272
8.4	Limitations . . . . .	273
8.4.1	Controlling resting state fMRI data for nuisance signals . . . . .	273
8.4.2	Histological analysis . . . . .	274
8.5	Functional brain network in anxiety disorder . . . . .	274
8.6	Future perspectives . . . . .	277
8.6.1	Multilayer networks . . . . .	277
8.6.2	Biomarkers for epileptogenesis . . . . .	278
8.7	Conclusion . . . . .	280

# 1 | Introduction

## 1.1 Context

Epilepsy is a neurological disorder characterized by recurrent epileptic seizures [1]. It is one of the most common neurological disorders, affecting more than 50 million people worldwide [2]. The most common type of epilepsy is temporal lobe epilepsy (TLE) [3]. TLE is often caused by an initial precipitating injury, such as status epilepticus, stroke, head trauma, a brain tumor, or a central nervous system infection [4]. However, not all patients who suffer such an injury, develop epilepsy. As of yet, it is not possible to predict which patients will develop epilepsy after an injury and which patients will not, mainly because little is known about how a normal brain is transformed into an epileptic brain, a process called epileptogenesis. Therefore, it is important to gain more insight into the basic mechanisms of epileptogenesis, which could help to find biomarkers for disease prognosis [5]. In addition, it could aid the development of anti-epileptogenic therapies, i.e., therapies that prevent or delay the development of epilepsy [6].

While seizures can be controlled adequately with anti-epileptic drugs (AEDs) in many epilepsy patients, about 30% of patients still experience seizures despite trying multiple AEDs. These patients suffer from drug-resistant epilepsy [3]. They often experience comorbid diseases, psychological problems, social stigmatization, reduced quality of life, a higher risk of mortality and a shorter life expectancy because of their long-term, uncontrolled seizures [7]. Patients with drug-resistant epilepsy could benefit from resective surgery, which leads to seizure freedom in about 60% of patients [8]. However, not all patients are suitable candidates for

surgery. Other treatment options are neurostimulation, such as vagus nerve stimulation (VNS). While VNS is able to reduce seizure frequency in most patients, only 8% of patients become completely seizure free [9]. Predictive biomarkers for treatment response would greatly improve the treatment plan of epilepsy patients. Biomarkers that predict which patients will respond to which type of AED might shorten the search to find the right drug and would allow patients with drug-resistant epilepsy to be diagnosed sooner. These patients could then proceed to other treatment options much faster. Finding biomarkers to predict whether a patient will respond to surgery or neurostimulation, would prevent non-responders from undergoing unnecessary surgery. Gaining more insight into the mechanisms underlying epilepsy and epileptogenesis is essential in the search of these biomarkers. In addition, it can help the rational development of new treatment options for patients who still experience seizures despite trying the treatment options that are currently available.

While TLE is a focal epilepsy type, with seizures originating in temporal structures, increasing evidence suggests that abnormal epileptogenic networks are involved in this disorder. These networks not only consist of brain regions in the temporal lobe, but also of extratemporal regions, such as subcortical areas and the neocortex [10]. Brain networks are a combination of structural and functional networks [11]. Structural networks can be considered the ‘hardware’ of the brain, and functional networks the ‘software’, that uses the hardware to execute specific tasks. Abnormalities in both structural and functional network connectivity have been reported in TLE [10].

This dissertation aims to gain more insight into the mechanisms of epileptogenesis, with the ultimate goal of finding a biomarker to predict which patients will develop epilepsy after an initial precipitating injury. To this end, alterations in structural and functional brain networks during epileptogenesis are investigated in a rat model of TLE using longitudinal advanced magnetic resonance imaging (MRI).

## 1.2 Outline

In the following chapters, we will introduce the main topics of this dissertation, describe the experimental studies that were performed and their results, and discuss the findings and their relevance in research and clinical applications. In **Chapter 2**, an overview of epilepsy, and in particular temporal lobe epilepsy (TLE), is given. In **Chapter 3**, magnetic resonance imaging (MRI), diffusion-weighted MRI (dMRI) and resting state functional MRI (rsfMRI), the neuroimaging techniques used in this dissertation, and their applications in epilepsy are discussed. In **Chapter 4**, the aim of the dissertation is stated and the research questions that need to be answered are listed. Diffusion-weighted MRI studies in patients with TLE have reported widespread changes in white matter integrity. In **Chapter 5**, these changes are investigated using more advanced analysis methods in a longitudinal multi-shell dMRI study in a rat model of TLE. In addition, the effect of these changes on structural network topology is assessed. Changes in white matter integrity can also affect functional brain connectivity. In **Chapter 6**, functional network topology in a rat model of TLE is evaluated in a longitudinal rsfMRI study. Furthermore, the potential of functional network topology to predict seizure occurrence after an injury is investigated. In most rsfMRI studies, functional connectivity is assumed to be stationary during the scanning session. However, in reality, it varies on a much shorter time scale. In **Chapter 7**, dynamic changes in functional network topology are investigated. Finally, the findings of these experimental studies are discussed in **Chapter 8**. An application in a broader context is introduced and future perspectives in epilepsy research are explored.

## Bibliography

- [1] R. S. Fisher, W. V. E. Boas, W. Blume, C. Elger, P. Genton, P. Lee, and J. Engel Jr, “Epileptic seizures and epilepsy: definitions proposed by the international league against epilepsy (ILAE) and the international bureau for epilepsy (IBE),” *Epilepsia*, vol. 46, no. 4, pp. 470–472, 2005.
- [2] P. N. Banerjee, D. Filippi, and W. A. Hauser, “The descriptive epidemiology of epilepsy—a review,” *Epilepsy research*, vol. 85, no. 1, pp. 31–45, 2009.
- [3] J. Engel Jr, “Approaches to refractory epilepsy,” *Annals of Indian Academy of Neurology*, vol. 17, no. Suppl 1, p. S12, 2014.
- [4] L. Forsgren, E. Beghi, A. Oun, and M. Sillanpaa, “The epidemiology of epilepsy in Europe - a systematic review,” *European Journal of Neurology*, vol. 12, no. 4, pp. 245–253, apr 2005. [Online]. Available: <http://doi.wiley.com/10.1111/j.1468-1331.2004.00992.x>
- [5] B. P. Lucke-Wold, L. Nguyen, R. C. Turner, A. F. Logsdon, Y.-W. Chen, K. E. Smith, J. D. Huber, R. Matsumoto, C. L. Rosen, E. S. Tucker *et al.*, “Traumatic brain injury and epilepsy: underlying mechanisms leading to seizure,” *Seizure*, vol. 33, pp. 13–23, 2015.
- [6] A. Pitkänen, A. Nehlig, A. R. Brooks-Kayal, F. E. Dudek, D. Friedman, A. S. Galanopoulou, F. E. Jensen, R. M. Kaminski, J. Kapur, H. Klitgaard, W. Löscher, I. Mody, and D. Schmidt, “Issues related to development of antiepileptogenic therapies,” *Epilepsia*, vol. 54, no. SUPPL.4, pp. 35–43, aug 2013. [Online]. Available: [/pmc/articles/PMC3740390//pmc/articles/PMC3740390/?report=abstracthttps://www.ncbi.nlm.nih.gov/pmc/articles/PMC3740390/](https://pubmed.ncbi.nlm.nih.gov/3740390/)
- [7] K. D. Laxer, E. Trinka, L. J. Hirsch, F. Cendes, J. Langfitt, N. Delanty, T. Resnick, and S. R. Benbadis, “The consequences of refractory epilepsy and its treatment,” *Epilepsy & Behavior*, vol. 37, pp. 59–70, aug 2014. [Online].

Available: <http://www.ncbi.nlm.nih.gov/pubmed/24980390>  
<http://linkinghub.elsevier.com/retrieve/pii/S1525505014002054>

- [8] P. Boon, K. Vonck, V. De Herdt, A. Van Dycke, M. Goethals, L. Goossens, M. Van Zandijcke, T. De Smedt, I. Dewaele, R. Achten, W. Wadman, F. Dewaele, J. Caemaert, and D. Van Roost, “Deep brain stimulation in patients with refractory temporal lobe epilepsy.” *Epilepsia*, vol. 48, no. 8, pp. 1551–60, aug 2007. [Online]. Available: <http://www.ncbi.nlm.nih.gov/pubmed/17726798>
- [9] H. F. González, A. Yengo-Kahn, and D. J. Englot, “Vagus nerve stimulation for the treatment of epilepsy,” *Neurosurgery Clinics*, vol. 30, no. 2, pp. 219–230, 2019.
- [10] S. Chiang and Z. Haneef, “Graph theory findings in the pathophysiology of temporal lobe epilepsy,” *Clinical Neurophysiology*, vol. 125, no. 7, pp. 1295–1305, jul 2014. [Online]. Available: <http://linkinghub.elsevier.com/retrieve/pii/S1388245714001928>
- [11] M. Straathof, M. R. Sinke, R. M. Dijkhuizen, and W. M. Otte, “A systematic review on the quantitative relationship between structural and functional network connectivity strength in mammalian brains,” *Journal of Cerebral Blood Flow & Metabolism*, vol. 39, no. 2, pp. 189–209, 2019.



## 2 | Epilepsy

### 2.1 Introduction

Epilepsy is a neurological disorder characterized by recurrent unprovoked epileptic seizures [1]. It is one of the most common neurological disorders, affecting more than 50 million people worldwide [2]. In children, epilepsy is most often caused by congenital, developmental or genetic conditions. Head trauma, central nervous system infections and tumors can lead to the development of epilepsy at any age, and the most common cause of epilepsy in elderly people is cerebrovascular disease. In about 70% of patients with epilepsy, seizures can be controlled with anti-epileptic drugs [3]. Patients who still experience seizures despite treatment with appropriate drugs, suffer from drug-resistant epilepsy. The most common type of drug-resistant epilepsy is temporal lobe epilepsy (TLE) [4].

### 2.2 The brain

#### 2.2.1 Neuroanatomy

The brain is part of the nervous system, which is the communication and control network of the body. The nervous system comprises three subdivisions. The central nervous system, which consists of the brain and spinal cord, is the coordinating system. The peripheral nervous system, a complex network of nerves in the entire body, transfers information between the body and the brain. The autonomic nervous system is responsible for controlling basic functions, such as body temperature, blood pressure and heart rate, without being consciously aware of it [5].

Neurons are the functional units of the brain and are responsible for information processing. It is estimated that the brain contains 50 to 500 billion neurons. The cell body, or soma, of a neuron contains the organelles, such as the nucleus, mitochondria and ribosomes, the dendrites receive nerve signals, and the axon sends the signals onward (Figure 2.1). Despite the large number of neurons, these cells only make up less than 10 percent of the cells in the brain. The other cells are glial cells, or support cells [5]. Astrocytes play a role in the release and uptake of neurotransmitters at synapses, and in gliosis after injury. They also provide metabolic support and help to maintain homeostasis. Oligodendrocytes form the myelin that lines the axons of neurons. Myelin consists of layered phospholipid membranes, and supports and insulates the axons to speed up signal transduction. Microglia are cells of the immune system. They remove foreign or damaged material and protect from infection. Ependymal cells line the ventricles and compartments that contain cerebrospinal fluid (CSF). They also play a role in the circulation and production of CSF (Figure 2.1) [6].

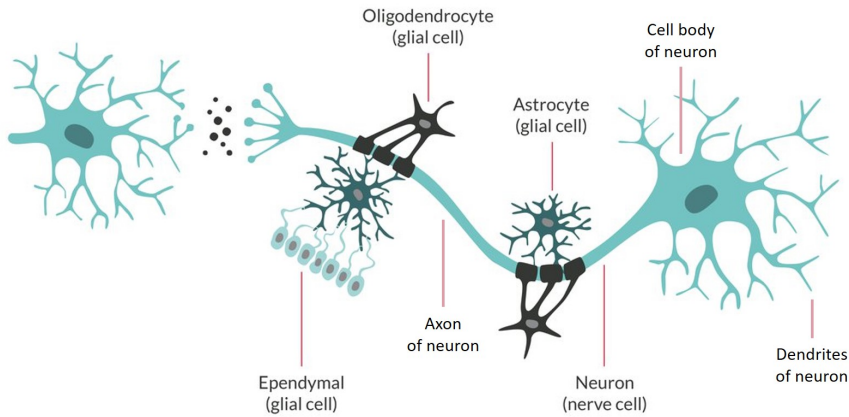


**Figure 2.1:** Cells of the brain: neurons, consisting of a cell body, dendrites to receive nerve signals and an axon to send the signals onward, astrocytes, oligodendrocytes and ependymal cells (Adapted from The Brain Tumour Charity).

On a macroscopic level, the brain is made up of grey matter and white matter. Grey matter is mainly located at the outer layer of the brain, called the cerebral cortex. It consists of neuronal cell bodies. The surface of the brain is convoluted, it consists of gyri (ridges) and sulci (grooves), which increases the surface area and is essential for effective functioning. In the inner part of the brain, clusters of grey matter, called nuclei, are present as well. Grey matter contains a lot of neurons, which enables information processing. White matter is made up of axons, which form connections and transfer information between neurons. Axons are lined with a myelin sheath, so they appear white on histology [7]. The brain is surrounded by CSF, a fluid produced in the ventricles, which are a series of connected cavities in the brain. CSF protects the brain from shocks, and contains proteins and glucose for neurons and white blood cells to counter infections [5].

The human brain can be subdivided into four parts: the telencephalon, diencephalon, brainstem and cerebellum (Figure 2.2A). The telencephalon or cerebrum makes up more than three quarters of the total brain volume. It can be split up into a left and right hemisphere, which are connected by white matter bundles, such as the corpus callosum, and anterior and posterior commissure [5].

The telencephalon consists of three parts: the cerebral cortex, limbic system and basal ganglia. The cerebral cortex is a layer of grey matter situated at the outermost part of the brain. It can be subdivided into four lobes: the frontal, temporal, parietal and occipital lobes (Figure 2.2B). The frontal lobe is the largest lobe. It plays a role in motor control, expressive language, regulating emotions, social interactions and personality, inhibition and motivation. The temporal lobe is involved in processing sensory input. It plays a role in visual memory, language comprehension, and the interpretation of sound. The parietal lobe receives somatosensory stimuli and is responsible for the integration of information of different senses. The occipital lobe contains the primary visual cortex and is involved in processing visual input [8]. The limbic system is a group of structures located underneath the cerebral cortex and above the brainstem, lateral to the thalamus. It is involved in emo-

tional, memory, and learning processing. The limbic system contains several regions of the telencephalon, including hippocampus, parahippocampal gyri, amygdala and cingulate gyrus, but also some regions of the diencephalon, such as the hypothalamus and anterior thalamic nuclei [5, 9]. The basal ganglia are subcortical grey matter structures. The most important nuclei are the striatum, which consists of the caudate nucleus and putamen, the pallidum, substantia nigra and subthalamic nucleus. The basal ganglia are responsible for the planning and execution of physical movements [5].

The diencephalon is located between the telencephalon and the brainstem. Its main component is the thalamus. This region is located at the center of the brain and acts as a sensory relay. It receives almost all sensory information, except for smell. The information is then sent to the cerebral cortex. The diencephalon also comprises the hypothalamus and pituitary gland. The hypothalamus plays an important role in conscious behavior, emotions and instincts, and is responsible for controlling the autonomic nervous system, such as blood pressure and heart rate. In addition, it releases hormones into the bloodstream. The pituitary gland controls the endocrine system. It releases hormones that regulate other endocrine glands in the body [5].

The brainstem is the part of the brain that is connected to the spinal cord. It comprises the midbrain, pons and medulla. It plays a role in mid- to low-order mental activities and autonomic control mechanisms, such as monitoring and controlling the respiratory rate, heart rate and blood pressure [5].

The cerebellum is located on the posterior side of the brainstem. It is responsible for coordinating body movement through muscle control, balance and posture, and equilibrium [5].

## 2.2.2 Neurophysiology

Information is transmitted throughout the brain via neurons. Neurons are electrically excitable cells that are able to receive and transmit information. They have a resting membrane potential of about -70 mV.

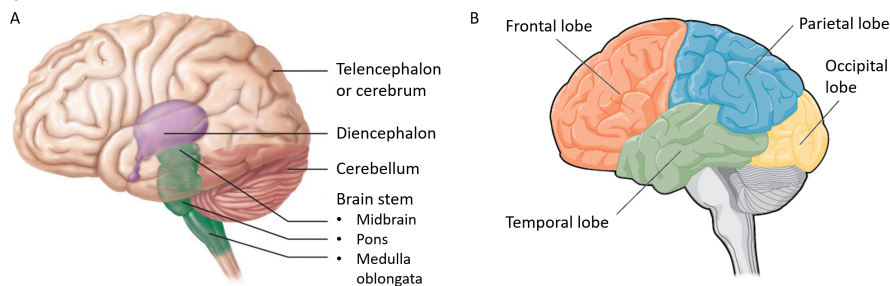


**Figure 2.2:** A) The human brain can be subdivided into four parts: the telencephalon, diencephalon, cerebellum and brainstem. B) The cerebral cortex can be subdivided into four lobes: the frontal, temporal, parietal and occipital lobes.

This membrane potential can be affected by charged ions such as potassium, sodium and chloride ions [10]. Information is transmitted along a neuron in the form of electrical impulses, or action potentials. Action potentials are generated when the membrane potential changes due to a difference in ion concentrations. First, the membrane potential depolarizes, i.e., it becomes less negative, mainly due to sodium influx. Then, the membrane potential repolarizes, returning to the resting potential, mostly due to potassium efflux. Finally, there is after-hyperpolarization, where the membrane potential recovers from an overshoot of repolarization (Figure 2.3). Since there is less extracellular sodium after the depolarization and the sodium channels are inactivated, neurons cannot generate a new action potential immediately after an action potential was generated [11].

The generated action potential travels along the axon until it reaches the synapse [11]. Synapses are the communication sites between neurons. The neurons are separated by a very thin space, called the synaptic cleft. Most synapses connect an axon with a dendrite of the postsynaptic neuron (axodendritic), but they can also connect an axon with a cell body (axosomatic) or with another axon (axoaxonic) [5, 12]. At the synapse, the action potential typically causes the release of neurotransmitters (chemical transmission), but it can also cause conduction of ionic currents (electrical transmission) [11]. The presynaptic terminal, i.e., the

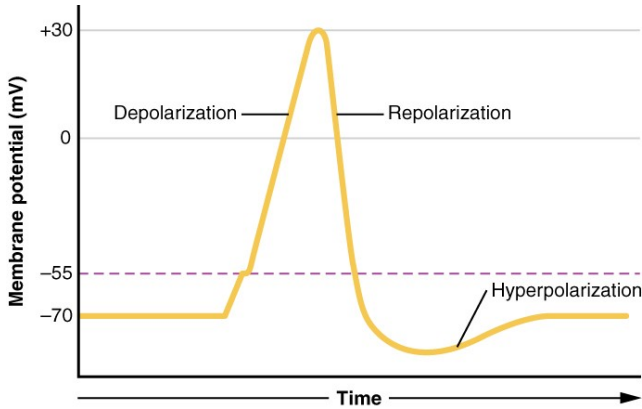


**Figure 2.3:** Neuronal action potential. First, the membrane potential becomes less negative, mainly due to sodium influx (depolarization). Then, it returns to the resting potential, mostly due to potassium efflux (repolarization). Finally, the membrane potential recovers from an overshoot of repolarization (after-hyperpolarization) [11].

end of the axon, contains vesicles with neurotransmitters. These neurotransmitters are released into the synaptic cleft when an action potential arrives at the axon terminal. The neurotransmitters diffuse across the synaptic cleft and bind to receptors on the postsynaptic neuron, causing either depolarization or an excitatory postsynaptic potential, or hyperpolarization or an inhibitory postsynaptic potential on the cell membrane of that neuron, depending on the type of neurotransmitter (Figure 2.4) [5]. The postsynaptic neuron integrates the input from all postsynaptic terminals to determine whether or not an action potential needs to be generated [12].

Several types of neurotransmitters are used in synaptic communication. They can be excitatory or inhibitory, and some are involved in specific brain functions. The main excitatory neurotransmitter in the central nervous system, and the most abundant one, is glutamate. It acts on ionotropic and metabotropic receptors. Excessive activation of glutamate receptors can lead to cell death, which is referred to as excitotoxicity. Glutamate plays a role in several neurological and psychiatric conditions, such as depression, addiction, schizophrenia and neurodegenerative diseases [13]. Gamma-aminobutyric acid (GABA) is the main

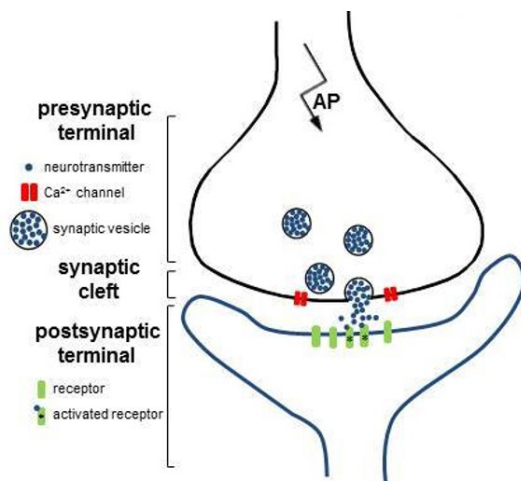


**Figure 2.4:** Synapse. An action potential arrives at the presynaptic terminal and causes release of neurotransmitter (blue dots) into the synaptic cleft. The neurotransmitter diffuses across the synaptic cleft and binds to receptors on the postsynaptic terminal (Adapted from [11]).

inhibitory neurotransmitter in the central nervous system. It binds to postsynaptic GABA receptors that modulate ion channels. This leads to hyperpolarization and stops action potentials. Abnormal GABA signaling is associated with many neurological and psychiatric diseases, and many pharmacological treatments act on GABA receptors [14]. Another common neurotransmitter is dopamine, which is mostly inhibitory. The degeneration of dopaminergic neurons in the substantia nigra is associated with Parkinson's disease. Serotonin is mainly a regulatory neurotransmitter and is involved in several mood states and diseases [12]. Norepinephrine plays a role in the body's response to stress and exercise, and is generally excitatory. Acetylcholine is an important neurotransmitter in several synapses in the body, such as the neuromuscular junction and autonomic ganglia, where it is usually excitatory [5, 12].

## 2.3 Seizures

An epileptic seizure is defined by the International League Against Epilepsy (ILAE) as “a transient occurrence of signs and/or symptoms due to abnormal excessive or synchronous neuronal activity in the brain” [1]. Seizures are usually transient or limited in time. An exception is status epilepticus, which is an extremely long or recurrent seizure. Sometimes, the end of a seizure is not very marked, because it is clouded by symptoms of the postictal state. Seizures can manifest in different ways, depending on where in the brain the seizure starts and how it propagates, but also depending on age, other diseases, medication and other factors. During a seizure, sensory, motor and autonomic function, consciousness, emotional state, memory, cognition and behavior can be affected. On an electroencephalogram (EEG), abnormal neuronal activity can be detected during a seizure. This activity can be inhibition or excitation, and the most common feature is abnormal enhanced synchrony of neuronal discharge [1].

### 2.3.1 Seizure generation and propagation

An epileptic seizure, characterized by hypersynchronous neuronal activity, usually starts in a specific region of the cortex and can propagate to other brain regions. Two phenomena occur when a seizure is generated: high-frequency bursts of action potentials and hypersynchronization of a neuronal population. At a neuronal level, an influx of extracellular  $\text{Ca}^{++}$  leads to the opening of voltage-dependent  $\text{Na}^+$  channels and an influx of  $\text{Na}^+$ . This causes sustained neuronal depolarization and results in a burst of action potentials. The depolarization reaches a plateau-like level when the burst of action potentials is completed. This is followed by rapid repolarization and hyperpolarization, mediated by GABA receptors and  $\text{Cl}^-$  influx, or  $\text{K}^+$  efflux, depending on the type of cell. This series of events is called a paroxysmal depolarizing shift (Figure 2.5) [15].

If there is enough neuronal activation to recruit neighboring neurons, the seizure can propagate. In a healthy brain, the spread of bursting activity is blocked by intact hyperpolarization and because inhibitory neurons

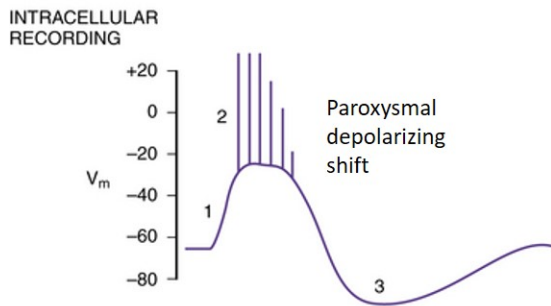


**Figure 2.5:** Paroxysmal depolarizing shift on intracellular recording. 1) Depolarization of the membrane potential ( $V_m$ ) leads to 2) a burst of action potentials, followed by 3) hyperpolarization (Adapted from [16]).

form a region of surrounding inhibition. If the bursting activity is high enough, it can recruit neighboring neurons using several mechanisms. It can lead to more extracellular  $K^+$ , which reduces the hyperpolarizing outward  $K^+$  currents, resulting in depolarization of surrounding neurons. It can also lead to an increase in  $Ca^{++}$  in presynaptic terminals, causing increased neurotransmitter release, and it can lead to the activation of N-methyl-D-aspartate (NMDA) receptors, a type of glutamate receptors, causing a higher influx of  $Ca^{++}$  and neuronal activation [15].

### 2.3.2 Seizure classification

Seizures can be classified into different types, which are listed in Table 2.1. First, a distinction is made between seizures with a focal onset, i.e., seizures that originate in one hemisphere, and seizures with a generalized onset, i.e., seizures that originate in both hemispheres. If it is not clear whether the onset is focal or generalized, a seizure is classified as 'of unknown onset'. Focal onset seizures can be subdivided into seizures with retained and impaired awareness [17]. It is important to differentiate between these two types, as it affects which activities an epilepsy patient can and cannot do, such as driving or operating dangerous machinery [15]. This distinction is not made for seizures with generalized onset, as awareness is almost always impaired during this type of seizures [17].

### **Focal onset seizures**

Focal onset seizures can also be subdivided into motor and non-motor seizures. A special type of focal seizures are focal to bilateral tonic-clonic seizures, formerly referred to as secondarily generalized tonic-clonic seizures. These are seizures that start in one hemisphere and then spread to both hemispheres [17].

Focal motor and non-motor seizures can be further categorized based on the first prominent manifestation. This can provide information about the seizure's brain region(s) of origin. For focal motor seizure, initial manifestations include automatisms, which are robotic repetitive semi-purposeful movements, such as lip-smacking or hand rubbing, focal loss of tone in a limb (atonic seizure), stiffening of a limb or the neck (tonic seizure), sustained rhythmical jerking or myoclonic brief irregular jerking (clonic seizure), thrashing or pedaling (hyperkinetic seizure) and flexion at the waist or flexion or extension of the arms (epileptic spasms) [17].

Focal non-motor seizures can be subdivided into autonomic seizures, behavioral arrest seizures, cognitive seizures, emotional seizures and sensory seizures. Autonomic seizures affect functions of the autonomic nervous system, including heart rate, blood pressure and gastrointestinal sensations. During a behavioral arrest seizure, the patient stops moving or 'freezes'. A focal cognitive seizure involves impaired cognition, such as problems with language, spatial perception or mathematical calculations. At the start of a focal emotional seizure, patients experience spontaneous fear, anxiety or joy, and may start laughing or crying involuntarily. A focal sensory seizure can manifest as tingling or numbness, visual symptoms, tastes, smells, sounds and other sensory impressions [17].

### **Generalized onset seizures**

Seizures with a generalized onset can be subdivided into motor and non-motor or absence seizures as well. Some of the types of generalized motor seizures share a name with a type of focal onset motor seizures. However, they can have a different pathophysiology or prognosis. A

**Table 2.1:** ILAE 2017 Classification of seizure types [17]

Focal Onset		Generalized Onset	Unknown Onset
Aware	Impaired Awareness	<b>Motor</b> tonic-clonic clonic tonic myoclonic myoclonic-tonic-clonic myoclonic-atonic atonic epileptic spasms <b>Non-motor (absence)</b> typical atypical myoclonic eyelid myoclonia	<b>Motor</b> tonic-clonic epileptic spasms <b>Non-motor</b> behavior arrest
<b>Motor Onset</b> automatisms atonic clonic epileptic spasms hyperkinetic myoclonic tonic <b>Non-motor Onset</b> autonomic behavior arrest cognitive emotional sensory			
Focal to bilateral tonic-clonic			

generalized tonic-clonic seizure starts with loss of awareness and a tonic phase, characterized by the stiffening of all limbs, followed by a clonic phase, during which there is sustained rhythmic jerking of limbs and face. A clonic seizure produces bilateral sustained rhythmical jerking of the limbs and/or head, without a tonic phase, and a tonic seizure is characterized by stiffening of all limbs, without a clonic phase. During a myoclonic seizure, a patient experiences unsustained irregular bilateral jerking of the limbs or face. A myoclonic-tonic-clonic seizure starts with a few bilateral myoclonic jerks, followed by a tonic-clonic seizure. A myoclonic-atonic seizure starts with myoclonic jerks as well, but is followed by a limp drop. During an atonic seizure or epileptic drop attack, a patient experiences sudden loss of muscle tone and strength, and they typically fall down. Generalized epileptic spasms are short seizures characterized by flexion at the trunk and flexion or extension of the limbs [17].

Generalized non-motor or absence seizures can be subdivided into typical, atypical and myoclonic seizures, and seizures with eyelid myoclonia. Typical absence seizures are characterized by a sudden halting of activity and can be accompanied by automatisms. Atypical absence seizures are very similar, but can begin and end more slowly, and more marked changes in tone can occur. If an absence seizure starts with a few myoclonic jerks, it is categorized as a myoclonic absence seizure. In some patients, eyelid myoclonia, i.e., jerks of the eyelids and an upward deviation of the eyeballs, can occur during absence seizures [17].

## 2.4 Diagnosis

Epilepsy is defined by the ILAE as “a disorder of the brain characterized by an enduring predisposition to generate epileptic seizures, and by the neurobiologic, cognitive, psychological, and social consequences of this condition. The definition of epilepsy requires the occurrence of at least one epileptic seizure” [18]. To diagnose epilepsy, a more practical definition is used, and epilepsy can be diagnosed if a patient has at least two unprovoked seizures more than 24 hours apart, if they have one unprovoked seizure and are as likely to have more seizures as they are after two unprovoked seizures, over a period of 10 years, or if they are diagnosed with an epilepsy syndrome [18].

When a patient has a paroxysmal event, i.e., a time-limited event with an abrupt onset and ending that usually recurs and tends to involve transient neurological symptoms, it is important to determine whether the patient had a seizure or a different paroxysmal event, whether the seizure was or was not provoked, and how likely it is that seizures will recur. Therefore, history and physical examination, as well as diagnostic tests are necessary. Epilepsy is a clinical diagnosis, made based on clinical judgment, since the tests are not always conclusive. Paroxysmal events that resemble, but are not epileptic seizures, include psychogenic nonepileptic seizures, syncope, migraine, transient ischemic attack and events caused by sleep or movement disorders [19].

First, a history of the paroxysmal event needs to be obtained. The event is often described by eyewitnesses, since patients cannot always give precise information. To obtain a detailed description, it is necessary to ask specific, direct questions, such as questions about altered consciousness, the characteristics of motor movements and the duration of the event. The medical and surgical history of the patient is important as well, since it can help to identify risk factors for epilepsy, such as childhood febrile seizures, encephalitis or meningitis, or head injury. Knowledge of medication use is relevant to determine whether or not the seizure was provoked. Certain types of medication can lower the threshold for seizure generation, while withdrawal from other types can induce seizures. Alcohol or substance abuse can also provoke seizures. Since some epilepsy syndromes are hereditary, information about a family history of epilepsy needs to be obtained as well. If the patient has had seizures before, specific information should be acquired about the age of onset, frequency of seizures, previous examinations and anti-epileptic medication [19].

Based on a physical examination of the patient, signs of systemic or focal brain diseases that may induce seizures can be detected. An elevated temperature may point to meningitis or encephalitis, rigidity of the neck suggests a central nervous system infection or subarachnoid hemorrhage, dysmorphic features may indicate chromosomal abnormalities and irregular heart rate can point to syncope [19].

For new-onset seizures, it is standard practice to perform blood tests to check whether the seizure could have been provoked. Sometimes, blood test are also performed in patients with established epilepsy, for example if the patient experiences unexplained worsening of seizures or to monitor the side effects of anti-epileptic drugs. Lumbar punctures are usually not performed in patients with new-onset seizures, unless the patient experiences symptoms that may point to a central nervous system infection or subarachnoid hemorrhage [19].

Electroencephalography (EEG) plays a very important role in the diagnosis of epilepsy. It measures electrical activity in the brain and can detect functional hyperexcitability in epilepsy. It can be used to deter-

mine whether a patient has a tendency for epileptic seizures, to indicate where, within the brain, a seizure originates, and to classify epilepsy syndromes. On EEG, epileptiform discharges can be detected. These are short transient increases in brain voltage in the form of spikes, sharp waves and spike-and-slow wave discharges. They can be focal, i.e., limited to one part of the scalp, or generalized, i.e., present in all areas of the scalp. Epileptiform discharges are typical for epilepsy, but also occur in 0.5 to 2% of people without epilepsy. The occurrence of a seizure can only be detected using EEG if it happens during the EEG recording. An example of an EEG of a seizure generated in the right temporal lobe is visualized in Figure 2.6. EEG has an epilepsy sensitivity of 50% and a specificity of 98 to 99%. Routine EEG should be the first evaluation of a suspected seizure. It usually takes 20 to 30 minutes, the patient should ideally be asleep and photic stimulation and hyperventilation are performed as activation procedures. Other types of EEG are sleep-deprived EEG, which is recorded after 24 hours of sleep deprivation to activate epileptiform discharges, ambulatory 24-hour EEG, if seizures occur daily, and video EEG monitoring, during which a patient is continuously monitored using video and EEG for days to weeks, often to determine whether an event is a seizure or to localize seizure onset for epilepsy surgery [19].



**Figure 2.6:** EEG of a seizure generated in the right temporal region, characterized by buildup of rhythmic activity [19].

Neuroimaging can be used to identify the cause of epilepsy or of an epilepsy syndrome. It can detect structural brain disease and exclude a growing mass lesion that needs immediate intervention. Neuroimaging is

performed in almost all patients with new-onset seizures. Magnetic resonance imaging (MRI) is the gold standard, because it has a better soft tissue contrast than computed tomography (CT). It can detect small and subtle brain regions that are not visible with CT. CT is only performed when MRI is not available or when seizures are thought to be caused by intracranial hemorrhage, an ischemic stroke or a tumor [19]. More details regarding neuroimaging will be discussed in the next chapter.

An optimal MRI protocol typically consists of T1-weighted, T2-weighted and fluid attenuated inversion recovery (FLAIR) sequences. A three dimensional T1-weighted image with an isotropic voxel size of maximum 1.5 mm provides information about anatomy and can differentiate grey and white matter. Such an image with isotropic voxels can also be reformatted in other orientations and can be used for post-acquisition processing, such as calculating hippocampal volumes. A T2-weighted image, acquired in at least two orthogonal planes with the smallest slice thickness possible, has a high sensitivity for detecting pathology. A FLAIR image suppresses any signal from the cerebrospinal fluid (CSF), so it is ideal for detecting lesions close to the CSF. A contrast-enhanced image with gadolinium is usually not necessary, but may be useful to visualize lesions associated with breakdown of the blood-brain barrier [20]. An example of hippocampal sclerosis on a T1-weighted and FLAIR image is visualized in Figure 2.7.

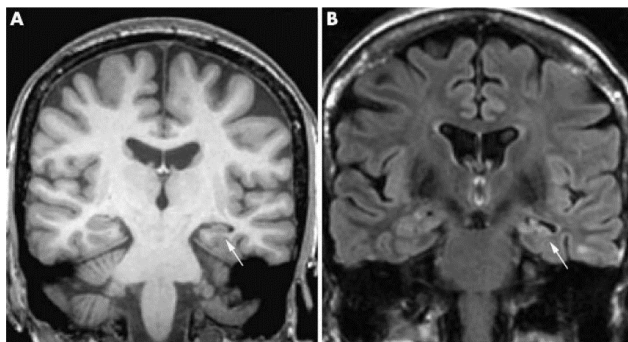


**Figure 2.7:** (A) T1-weighted MRI and (B) fluid attenuated inversion recovery (FLAIR) image of left hippocampal sclerosis, indicated with a white arrow (Adapted from [20]).

## 2.5 Treatment

### 2.5.1 Anti-epileptic drugs

Pharmacological treatment is the gold standard for treating epilepsy. Anti-epileptic drugs (AEDs) are used to reduce seizure frequency. They are a symptomatic treatment for seizures, but not a treatment for epilepsy itself [19].

Whether or not a patient should be treated with AEDs after a first seizure is a matter of debate. Anywhere between 16 to 62% of patients have a second seizure within 5 years after a first unprovoked seizure. The risk of recurrence is higher if the patient has an earlier neurologic injury that can cause seizures, if there is a structural abnormality on the MRI scan, if the EEG is highly epileptiform or if there is a family history of epilepsy. While treatment can reduce the risk of a second seizure, it does not eliminate it. Therefore, the decision of whether or not to treat with AEDs should be made individually for each patient, taking into account the possible negative effects of both a second seizure and AEDs on the patient [15, 19].

The goal of AED therapy is to obtain a seizure-free state. Therefore, the most appropriate AED needs to be selected, i.e., the AED that is most effective in preventing seizure and has the lowest likelihood of side effects. Most patients obtain seizure-freedom with one AED (monotherapy). If seizures persist, the dosage of the AED can be increased, until the maximum tolerated dose is reached. If the AED still fails, another drug can be added. If this drug is able to prevent seizures, the first AED can gradually be withdrawn. Sometimes, more than one AED is necessary to obtain seizure-freedom (polytherapy) [15]. To determine which drug is appropriate, it is important to know the seizure type of the patient, since AEDs have a different efficacy depending on the type of seizure. Some epilepsy syndromes also require a specific type of AED [19]. For more than 60% of patients who obtain seizure-freedom using AEDs, the drugs can eventually be withdrawn without recurrence of the seizures. Usually, the AEDs are withdrawn gradually over a period of 2 to 6 months, when the patient has been seizure-free for 2 to 4 years [15].

Not all patients obtain seizure-freedom using AEDs. If seizures still occur after adequate trials of at least two appropriate AEDs at the maximum tolerated dose, a patient suffers from drug-resistant epilepsy. While about 47% of patients respond to the first AED and 14% to a second one, it is very unlikely that they will respond to a third AED. About 30% of patients have drug-resistant epilepsy. These patients might benefit from alternative treatment options, such as epilepsy surgery, vagus nerve stimulation, deep brain stimulation or a ketogenic diet [19].

### 2.5.2 Epilepsy surgery

Patients with drug-resistant epilepsy should be referred to an epilepsy center for noninvasive presurgical evaluation. In these centers, a multidisciplinary team consisting of neurologists, neurosurgeons, neurophysiologists, neuroradiologists, neuropsychologists, and other specialists will decide whether or not epilepsy surgery is an option. The main goal of epilepsy surgery is to obtain seizure-freedom. Presurgical evaluation is required to determine whether a patient is a good candidate for surgery, which subtype of epilepsy they have and what the location of the focal epileptogenic zone, i.e., the region where seizures originate, is. Epilepsy surgery is typically most successful in a focal epilepsy syndrome with a well-localized epileptogenic zone [21].

Noninvasive presurgical evaluation starts with an extensive history and physical examination, to obtain information about seizure semiology and frequency, epilepsy duration and symptoms, and risk factors. Interictal EEG and long-term video-EEG are recorded to verify the diagnosis of epilepsy and to localize the epileptogenic zone, in combination with seizure semiology. A high-quality MRI is acquired to identify focal lesions consistent with the epileptogenic zone. An interictal positron emission tomography (PET) scan can be useful to detect a region with hypometabolic glucose metabolism that corresponds with the epileptogenic zone. In addition, an extensive neuropsychological evaluation is done to localize the symptomatogenic zone and to identify neurocognitive performance parameters that could be affected after surgery. If necessary, other modalities, such as ictal brain perfusion single-photon emission

computed tomography (SPECT) and interictal magnetoencephalography (MEG) can provide additional information. MEG and functional MRI can also be used to localize eloquent cortex, such as motor, sensory and language neocortices. Functional MRI can be a good noninvasive alternative to the Wada test, or intracarotid sodium amobarbital procedure, for lateralization of verbal and visuospatial memory. Noninvasive presurgical evaluation is often sufficient to localize the epileptogenic zone accurately enough to continue with surgical treatment. If this is not the case, intracranial EEG can be used to improve or confirm the localization [21].

For drug-resistant temporal lobe epilepsy (TLE), surgical resection is the gold standard. During anterior temporal lobectomy (ATL), the anterior hippocampus, amygdala, temporal pole and anterolateral temporal cortex are removed. Another common approach is selective amygdalo-hippocampectomy. Surgical treatment of TLE is typically quite successful, with up to 73% of patients obtaining seizure-freedom two years after ATL. Surgical resection can also be effective in focal neocortical epilepsy, with 40 to 60% of patients obtaining seizure-freedom. The outcome is typically better if the neocortical lesion can be detected using MRI and if it can be resected completely. If complete resection is not possible due to an overlap with eloquent cortex, multiple subpial transections could be a tissue-sparing alternative. A multilobar or multifocal epileptogenic zone, or a generalized epilepsy syndrome are very difficult to treat with epilepsy surgery. A palliative surgical option is corpus callosotomy, during which the corpus callosum is severed either completely, or just for the anterior two thirds. If a corpus callosotomy is not sufficient to reduce seizures, an anatomical or functional hemispherectomy may be an alternative [21].

### 2.5.3 Neurostimulation

#### Vagus nerve stimulation

Patients who are not candidates for epilepsy surgery, or who still have seizures after epilepsy surgery, could benefit from neuromodulation. The most common type of neuromodulation in epilepsy is vagus nerve stimulation (VNS). A VNS system consists of a lead that is wrapped around the left vagus nerve in the carotid sheath and a pulse generator implanted below the clavicle that sends electrical pulses to the nerve (Figure 2.8). About 60% of patients are responders to VNS treatment, i.e., their seizure frequency is reduced by at least 50%. The efficacy of VNS increases with the duration of the treatment. In addition, VNS has a positive effect on quality of life. However, only 8% of patients are completely seizure-free with VNS treatment. Next to the implantable VNS systems, noninvasive VNS systems are available as well. The main advantage of these systems is that adverse effects due to implantation, such as infection and vocal cord paresis, can be avoided. It also allows for increased customization of the stimulation paradigm [22].

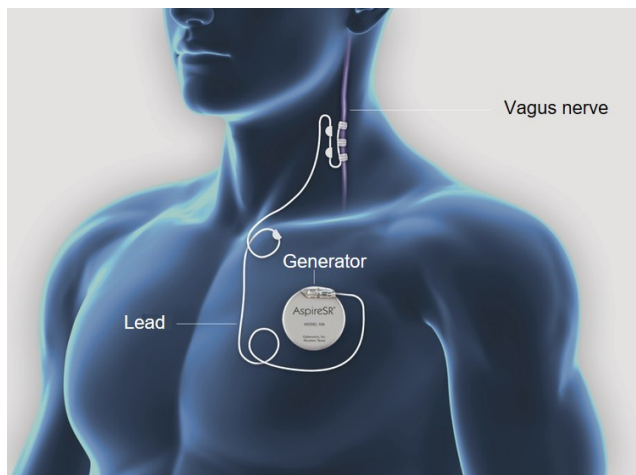


**Figure 2.8:** A vagus nerve stimulation (VNS) system, consisting of a lead wrapped around the left vagus nerve in the carotid sheath and a pulse generator implanted below the clavicle that sends electrical pulses to the nerve (Courtesy of LivaNova, Inc. Houston, TX) [22].

## Deep brain stimulation

Another type of neuromodulation is deep brain stimulation (DBS). In DBS, deep brain structures are stimulated electrically via implanted electrodes that are connected to a pulse generator. DBS of the anterior nucleus of the thalamus (ANT) is an approved treatment option for drug-resistant epilepsy in Europe, Canada and Australia. Other possible DBS targets include the thalamic nuclei, hippocampus and cerebellum. The mechanisms of action of DBS are not yet completely understood. DBS rarely leads to seizure freedom, but it reduces seizure frequency, which has a positive effect on quality of life, independence and cognition. ANT-DBS typically leads to a reduction in seizure frequency of 46% to 90% in half of all patients, and more than 70% of patients are responders, i.e., their seizure frequency is reduced by at least 50%. A similar efficacy was found for DBS in the hippocampus, with a reduction in seizure frequency of 48% to 95% in half of all patients, and a responder rate of more than 70% [23].

## Responsive neurostimulation

VNS and DBS are open-loop neurostimulation techniques, i.e., electrical impulses are delivered continuously or on a fixed schedule. Responsive neurostimulation (RNS), on the other hand, is a closed-loop approach. It continuously measures neural activity at the seizure focus and only stimulates if it detects epileptiform activity. RNS can be useful for patients with uncontrolled seizures in one or two epileptogenic foci. An RNS system consists of one or two depth and/or cortical strip leads, implanted at the epileptogenic foci, and a cranially seated neurostimulator. The settings for detection of abnormal activity and for the response can be tailored to the individual patient. RNS can successfully reduce seizure frequency, and its efficacy increases with treatment duration, leading to a reduction in seizure frequency of about 75%. In addition, responsive cortical stimulation leads to improved quality of life and cognitive function [24].

### 2.5.4 Ketogenic diet

An alternative treatment option for drug-resistant epilepsy is the ketogenic diet, which is high in fat, low in carbohydrates and low in proteins [25, 26]. In the classical ketogenic diet, the ratio in calories of fat to carbohydrate is 4:1. A less restricted variant is the Atkins diet, which is also used as a weight-reducing diet. In this diet, the ratio in calories of fat to carbohydrate is 2:1. The anti-seizure effect of the ketogenic diet might be attributed to the anticonvulsant effect of ketone bodies, although other theories have been suggested as well [26]. The ketogenic diet is mainly used in children with drug-resistant epilepsy [25]. Because the diet is unappetizing and hard to tolerate, it is difficult to adhere to it [26]. However, high success rates have been reported [25].

## 2.6 Temporal lobe epilepsy

The most common type of focal epilepsy is temporal lobe epilepsy (TLE). In TLE, seizures originate in temporal limbic structures [27]. Networks involving the amygdalohippocampal complex and entorhinal cortex play an important role in the generation and spread of seizures [28]. Temporal lobe epilepsy often starts with an initial precipitating injury, such as febrile seizures, head trauma, central nervous system infection or brain tumor [27, 28]. After a latent period of 5 to 10 years, during which the patient does not experience any seizures, spontaneous seizures start to occur. Usually, these seizures can be controlled with AEDs during the first few years, but over time, seizures start to recur and often become drug-resistant [29].

### 2.6.1 Clinical features

Temporal lobe epilepsy is characterized by spontaneous, progressive seizures [29]. The most common type of seizures in TLE are focal seizures with impaired awareness. At the beginning of a seizure, patients typically experience an aura, often with experiential or viscerosensory symptoms. The main seizure is characterized by motor arrest and staring, often accompanied by oral and manual automatisms with impaired awareness.

Autonomic symptoms may include pupillary dilatation, hyperventilation and tachycardia. During the postictal phase, amnesia and a period of confusion are common. Focal to bilateral tonic-clonic seizures are rare in TLE. On EEG, interictal anterior temporal spike-wave discharges are a common hallmark of TLE [27, 28].

### 2.6.2 Epileptogenesis

Epileptogenesis is the process during which a healthy brain is transformed into an epileptic brain [30]. It often starts following an initial injury, such as head trauma, status epilepticus, febrile seizures, or infection. Then, there is a latency period of 5 to 10 years before some patients start to experience spontaneous seizures. During this period, several structural and biochemical changes occur in the brain that allow spontaneous seizures to occur, and these changes continue to accumulate with each new seizure [29].

One of the main structural changes during epileptogenesis in TLE is neurodegeneration, which affects the pyramidal cells and interneurons in the cornu ammonis field CA1 and the hilus of the hippocampus, and to a lesser extent the pyramidal cells in CA2 and CA3 [31]. This causes a decreased size and a hardening of the hippocampus. Besides hippocampus, amygdala, entorhinal, perirhinal and parahippocampal cortices, and extratemporal regions, such as thalamus, piriform cortex and cerebellum, are affected as well [29, 31]. Gliosis is also often found in epileptic tissue, but it is not yet clear how it is related to epileptogenesis. Astroglial activation can increase inflammatory cytokine production, enhance excessive synaptic activity and cause activated astrocytes to migrate to the epileptic focus, leading to sclerosis [29]. Mossy fiber sprouting is another structural change that occurs during epileptogenesis. It is caused by recurrent seizures and is progressive. Mossy fiber sprouting is the formation of synapses between dentate granule cell axons and cells in the granule layer and inner molecular layer of the dentate gyrus (Figure 2.9). The effect of mossy fiber sprouting on epileptogenesis is not clear yet. On the one hand, dentate granule cells may become hyperexcitable due to the sprouting, when a sprouted axon of an excitatory cell forms a

synapse with another excitatory cell or even with itself, which could have a proepileptogenic effect. On the other hand, mossy fiber sprouting may help to reestablish inhibitory circuits that were lost during the initial injury, assuming that mossy fiber sprouts mainly innervate inhibitory neurons, which could counteract epileptogenesis [29]. Other structural changes during epileptogenesis include axonal injury, neurogenesis, dendritic plasticity and blood-brain barrier damage. Neurogenesis increases after SE and remains high for several weeks. Seizure activity can interfere with the normal migration of new neurons, which can lead to their ectopic location in the hilus, abnormal connectivity and enhanced excitability. Another hypothesis suggests that new neurons adapt to their epileptogenic environment and become less sensitive to glutamate and more to GABA [31]. Loss of dendritic spines, altered spine morphology and reduced dendritic branching during epileptogenesis may influence the availability and stoichiometry of several receptor types, which can affect the flow of information from afferent inputs. Disruption of the blood-brain barrier due to seizure activity, which causes angiogenesis, can evoke epileptiform activity, leading to a vicious cycle of seizure generation [31].

Besides these structural changes, biochemical changes have been reported during epileptogenesis as well. These include changes in ligand-gated and receptor-gated ion channels and are referred to as acquired channelopathies [31]. The glutamate receptor NMDA is upregulated in epileptic tissue and one of its subunits is assumed to contribute to neuronal hyperexcitability, synchronization, and seizure generation. The KA receptors, another type of glutamate receptors, play a role in epileptogenesis as well. One of its subunits, that is involved in presynaptic regulation of glutamate release, is upregulated in patients with TLE, indicating it plays a role in the generation and perseveration of spontaneous seizures. Another subunit is involved in postsynaptic response to glutamate release and GABA release modulation, and contributes to seizure propagation and cell death. Aberrant mossy fiber sprouts have a higher expression of KA receptors, indicating that upregulation of KA receptors enables the propagation of epileptic activity [29]. Initially, GABA signaling was

thought to be decreased during epileptogenesis, allowing for uncontrolled glutamate signaling. However, a complicated process takes place that involves qualitative and quantitative changes in GABA receptor subunits, and a change in GABA receptors from a hyperpolarization subtype to a depolarization subtype [29]. Several ion channels, such as chloride, potassium, sodium, and calcium channels, are involved in epileptogenesis and in changes in homeostasis. Chloride channels play a role in the differentiation of hyperpolarization and depolarization GABA receptors, and are involved in inhibitory signaling. Defects in  $\text{Ca}^{2+}$ -sensitive potassium channels, that control the firing frequency of action potentials and modulate neuronal excitability, play a role in epileptogenesis as well. Other potassium channels are involved in epileptogenesis because of potassium buffering of glial cells [29]. In a rat model of TLE, a shift in voltage-dependent inactivation of sodium channels in a depolarizing direction was observed in the hippocampus, which led to a persistently active  $\text{Na}^+$  influx [32].

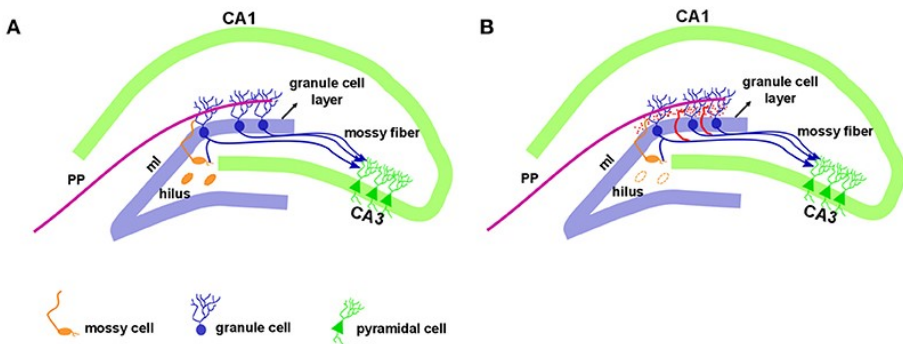


**Figure 2.9:** Hippocampal dentate gyrus in the healthy (A) and epileptic (B) brain. The dentate gyrus consists of three layers: the molecular layer (ml), granule cell layer and hilus. The granule cell layer contains many granule cells, the molecular layer contains their apical dendrites and the granule cell axons, also called mossy fibers, extend to the hilus. During epileptogenesis, mossy fiber targets in the hilus are lost, and as a result, mossy fibers sprout and form excessive synapses with cells in the inner molecular layer of the dentate gyrus (indicated in red). PP: perforant path [33].

### 2.6.3 Hippocampal sclerosis

A pathological finding that occurs in about 50% of patients with TLE is hippocampal sclerosis [27]. Hippocampal sclerosis refers to atrophy and astrogliosis in hippocampus, amygdala, parahippocampal gyrus and entorhinal cortex. It progresses over time due to recurrent seizures, but can also cause seizures [28]. Hippocampal sclerosis is typically associated with a worse prognosis, with only about 11% of patients obtaining seizure-freedom with AEDs. TLE is therefore the most common type of drug-resistant epilepsy. However, surgical resection is quite successful in these patients, with about 70 to 90% of patients obtaining seizure-freedom after surgery. In addition, early surgical intervention can prevent or improve comorbidities, such as psychiatric and social problems [27].

### 2.6.4 Amygdalohippocampal interconnections

The amygdalar nuclear complex and the hippocampal and parahippocampal region are often damaged in patients with TLE and are involved in about 70 to 80% of seizures originating in the temporal lobe [34]. These regions are important components of the limbic system, which are involved in emotion and memory. The amygdalar nuclear complex is composed of several nuclei, which can be subdivided into cortical amygdalar nuclei and basolateral amygdalar nuclei. Each of these nuclei has several interconnections with other amygdalar nuclei and other brain regions. The hippocampal and parahippocampal region refers to the hippocampal formation, which consists of the dentate gyrus, cornu ammonis fields CA1, CA2 and CA3 and the subiculum, and the parahippocampal cortices, such as the entorhinal and perirhinal cortex. Robust and complex interconnections exist between the amygdalar nuclei and the hippocampal and parahippocampal region (Figure 2.10) [35].

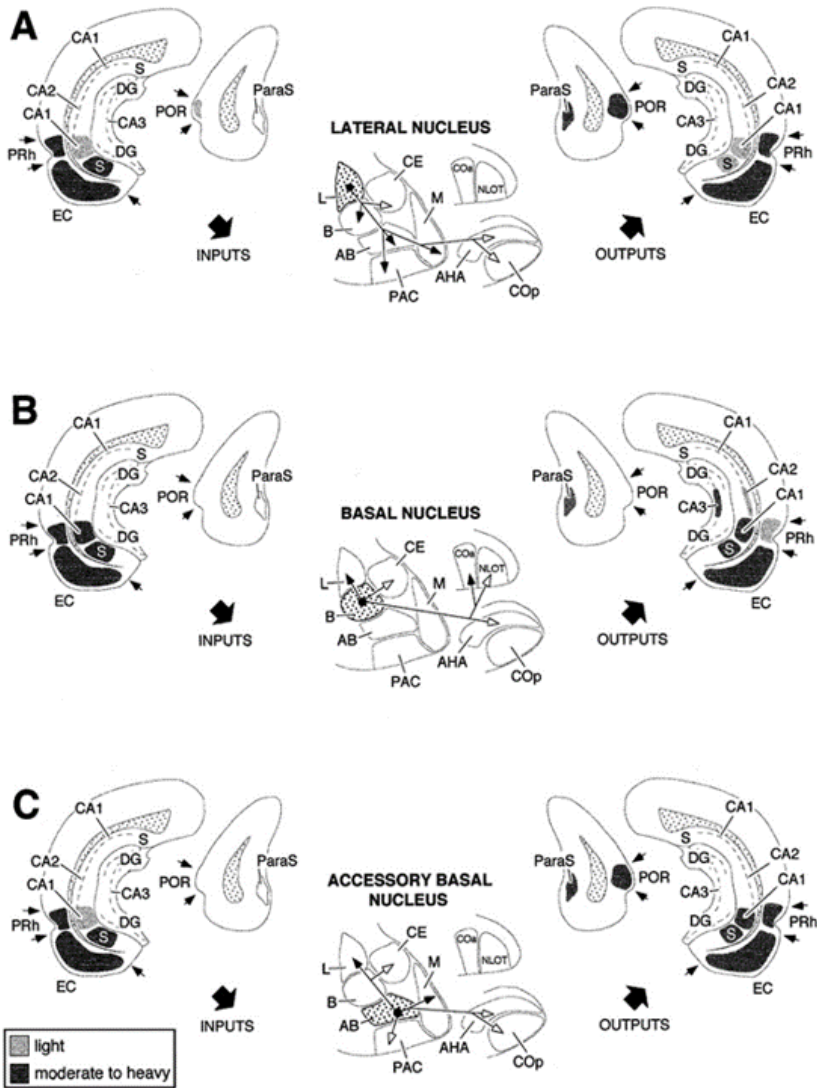


**Figure 2.10:** Summary of afferent and efferent connections between the amygdaloid complex (lateral, basal and accessory basal nucleus), hippocampal formation and perirhinal and postrhinal cortices in the rat brain. For detailed information about these connections, see [36]. Abbreviations: AB, accessory basal nucleus; AHA, amygdalohippocampal area; B, basal nucleus; CE, central nucleus; COa, anterior cortical nucleus; COP, posterior cortical nucleus; DG, dentate gyrus; EC, entorhinal cortex; L, lateral nucleus; M, medial nucleus; NLOT, nucleus of the lateral olfactory tract; paraS, parasubiculum; POR, postrhinal cortex; PRh, perirhinal cortex; S, subiculum [36].

The amygdala and hippocampal formation play an important role in TLE because they are highly interconnected. If a seizure is generated in either of these regions, it can easily spread to the other. Neuronal loss in these regions is often accompanied by damage to the projections originating in them [35]. One of the main projections from amygdala to hippocampus is a projection that ends in the temporal aspect of CA1 and subiculum. This projection is damaged in about 70% of resection samples in patients with drug-resistant TLE [34]. Kempainen and Pitkänen [34] investigated this projection in a rat model of TLE. They found severe neuronal loss in the lateral part of the basolateral amygdalar nuclear complex and several cortical amygdalar nuclei, and the projections originating in these regions had disappeared. However, the medial part of the posterior basolateral nucleus, and the projection originating from it, were largely preserved, and may be involved in the propagation of seizures and interictal bursting. Due to the loss of GABAergic neurons in the basolateral nucleus, there is loss of inhibition, increased excitability and a lowered seizure threshold in this region [35]. The increased excitability might promote the spread of seizures originating in the damaged amygdala to other regions, including the hippocampal formation [34, 35].

### **2.6.5 Animal models of temporal lobe epilepsy**

Animal models are an important tool to gain insight into the pathophysiology of TLE. They can be used to investigate injuries that can lead to epilepsy, the epileptogenic process and chronic epilepsy. In addition, animal models are essential for the rational development of new treatment options for epilepsy [37]. Several animal models can be used to study TLE, such as post-status epilepticus models induced by chemoconvulsants or electrical stimulation, kindling, tetanus toxin, hyperthermia, post-traumatic epilepsy and perinatal hypoxia/ischemia models (for review, see [38]). Post-status epilepticus models and the kindling model are explained in more detail below [39].

## Post-status epilepticus models

In post-status epilepticus models, an initial triggering process is induced with chemoconvulsants or electrical stimulation. This process is followed by a latent period, after which the animals start to develop spontaneous seizures. The initial triggering process is called status epilepticus, an acute episode of seizures. After 1 to 2 hours, this status epilepticus is usually interrupted using an anticonvulsant [39].

**Kainic acid models** Status epilepticus can be induced with the chemoconvulsant kainic acid (KA). KA is a cyclic analog of L-glutamate. It is an agonist of ionotropic, non-NMDA glutamate receptors. It can be administered intracerebrally or systemically and induces sustained neuronal depolarization, which causes seizure generation [39]. KA can be injected intracerebrally in the hippocampus, amygdala or lateral ventricle [39, 40]. Usually, KA doses of 0.4 to 2  $\mu\text{g}$  are administered, which leads to convulsive SE 5 to 60 minutes after the injection [41]. A disadvantage of intracerebral administration is that it requires surgery, and as such it is more labor-intensive and time-consuming. Additionally, animals tend to have a lower seizure frequency after intracerebral injection of KA, compared to systemic injection, which can be a disadvantage when the effect of an intervention on seizure frequency is investigated. KA can also be administered systemically. Initially, single doses of 12 to 18 mg/kg were administered intraperitoneally, subcutaneously or intravenously, but this was later optimized to multiple doses of 5 mg/kg to reduce mortality [39, 42]. After the injection(s), the animals start to display automatisms and a catatonic posture, myoclonic twitching of the head and limbs, and wet-dog shakes [41]. Epileptiform patterns can be seen on EEG, including interictal spikes in the entorhinal cortex, and ictal discharges starting in CA3 and amygdala, and propagating to thalamus, CA1 and frontal cortex. Epileptiform activity typically starts in the hippocampus, before clinical symptoms are observed. Not only interictal spike occur in the hippocampus, but also rhythmic patterns in the gamma frequency range (25-40 Hz) [41]. The neuropathological changes that occur after injection with KA include degeneration of

pyramidal cells in CA1 and CA3, and loss of parvalbumin-positive interneurons in CA1, entorhinal cortex and subiculum. Additionally, the density of GABAergic interneurons decreases in the basolateral part of the amygdala. Neurodegeneration after KA injections is bilateral and also affects extra-temporal regions, such as entorhinal cortex, proximal subiculum, claustrum, thalamus, caudate putamen and cerebral cortex [41]. Two days after SE, gliosis, brain edema, or neuronal shrinkage occur in piriform cortex, entorhinal cortex, olfactory bulb, substantia nigra, thalamus, and mesencephalon. In dentate gyrus, dispersion of the granule cell layer can be observed [41]. The disease progression after SE is characterized by a short latency phase of 7 to 9 days before any spontaneous seizures occur, followed by an exponential increase in seizure frequency, and eventually a plateau phase is reached around 17 weeks post-SE. While the progression of seizure frequency is similar in all animals, the final seizure frequency during the plateau phase varies between 14 and 49 seizures per day. Seizure consistently last around 56 seconds, which is similar to seizure duration in TLE patients, which is around 60 seconds [43]. Because of the similarities between the KA-induced rat model and patients with TLE in neuropathological changes, EEG patterns and disease progression, and because of the low mortality and the experience of the lab with this model, the intraperitoneal kainic acid rat model was deemed the most appropriate rat model for TLE to study changes in structural and functional network topology in this dissertation. However, there are also some differences between the model and TLE patients. While almost all rats become epileptic following SE, only 37% of patients develop epilepsy one year after SE, and 56% of patients three years post-SE. Additionally, the left and right hippocampus are very strongly connected in rats, which allows for seizures to spread more easily between the hemispheres. In patients with TLE, on the other hand, focal to bilateral clonic tonic seizures are rather rare, depending on the patient [43].

**Pilocarpine model** Another chemoconvulsant that can be used to induce status epilepticus in rodents is pilocarpine. Pilocarpine is a muscarinic acetylcholine receptor agonist [39]. It can be administered indi-

vidually in a dose of 340 to 380 mg/kg, or in combination with lithium. In the latter case, a subcutaneous injection of 3 mEq/kg lithium is followed by 30 mg/kg pilocarpine, which leads to more reliable epilepsy and a lower mortality rate [44]. Pilocarpine can also be injected intracerebrally in the piriform cortex or hippocampus. The neuropathological features of the pilocarpine model are similar to those of the KA-induced model and human TLE, although lesions occur more in the neocortex than the hippocampus. Neuronal loss can be found in hippocampus, cerebral cortex, olfactory cortices, amygdala, thalamus and substantia nigra. Other neuropathological features are the dispersion of the granule cell layer of the dentate gyrus and mossy fiber sprouting. EEG and behavioral changes are similar to those found in the KA-induced models and human TLE as well [39].

**Electrical stimulation models** Status epilepticus can also be induced using electrical stimulation, although this is used less often than chemoconvulsants [39]. Brain regions such as the perforant path, hippocampus and amygdala can be stimulated with electrical pulse trains to induce status epilepticus [45]. The neuropathological alterations caused by this type of stimulation correspond well with the pilocarpine and KA-induced models. Stimulation of the perforant path, amygdala and angular bundle all cause neuronal loss in the hippocampus. In addition, stimulation of the amygdala leads to neuronal loss in amygdala, piriform cortex, entorhinal cortex and thalamus, and causes aberrant mossy fiber sprouting in dentate gyrus. Stimulation of the angular bundle leads to extensive mossy fiber sprouting as well. While the histopathological findings of this model are in line with those in the pilocarpine and KA-induced models and human TLE, the need to implant electrodes makes this model less straightforward than the chemoconvulsant models [39].

### **Kindling models**

Unlike the previously described models, kindling models do not induce status epilepticus immediately. Instead, repeated subconvulsant levels of electrical stimulation or chemoconvulsants are used to trigger seizures.

Once a seizure is evoked, the animal is fully kindled. Electrical stimulation is used more often than chemoconvulsants [39]. Stimulation can be applied to several brain regions, including hippocampus, amygdala and olfactory regions [46]. The region most responsive to kindling is the amygdala. The most commonly used chemoconvulsants are pentylenetetrazole and bicuculline methiodide. For electrical stimulation, electrodes are implanted in the target brain region. Subconvulsant stimulation is applied repeatedly over several days to weeks. With each stimulation session, more seizure after-discharges are present on EEG. After a few weeks, seizures can be evoked by subconvulsant stimulation. Spontaneous seizures are rare in the kindling model [39].

The neuropathological features of kindling models are different from those found in post-status epilepticus models or human TLE [39]. Kindling of amygdala leads to neuronal loss and gliosis in the ipsilateral hemisphere, ranging from the olfactory bulb over the amygdala-piriform cortex to hippocampus and thalamus [47]. Aberrant mossy fiber sprouting in dentate gyrus was reported after both electrical stimulation and kindling with chemoconvulsants. Disadvantages of the kindling model are that it requires the implantation of electrodes and takes a long time to induce seizures. In addition, it resembles TLE less than post-status epilepticus models, since spontaneous seizures are rare and the pathological features are different. The advantage is that it allows for controlled stimulation of a specific area. The kindling model can be used to study TLE without hippocampal sclerosis [39].

## Bibliography

- [1] R. S. Fisher, W. V. E. Boas, W. Blume, C. Elger, P. Genton, P. Lee, and J. Engel Jr, “Epileptic seizures and epilepsy: definitions proposed by the international league against epilepsy (ILAE) and the international bureau for epilepsy (IBE),” *Epilepsia*, vol. 46, no. 4, pp. 470–472, 2005.
- [2] P. N. Banerjee, D. Filippi, and W. A. Hauser, “The descriptive epidemiology of epilepsy—a review,” *Epilepsy research*, vol. 85, no. 1, pp. 31–45, 2009.
- [3] J. W. Sander, “The epidemiology of epilepsy revisited,” *Current opinion in neurology*, vol. 16, no. 2, pp. 165–170, 2003.
- [4] J. Engel Jr, “Approaches to refractory epilepsy,” *Annals of Indian Academy of Neurology*, vol. 17, no. Suppl 1, p. S12, 2014.
- [5] R. Carter, S. Aldridge, M. Page, and S. Parker, *The human brain book*, P. Frances, Ed. New York, NY: DK Publishing, 2009.
- [6] P. E. Ludwig and J. M Das, *Histology, Glial Cells*. StatPearls Publishing, jun 2019. [Online]. Available: <http://www.ncbi.nlm.nih.gov/pubmed/28722974>
- [7] A. A. Mercadante and P. Tadi, *Neuroanatomy, Gray Matter*. StatPearls Publishing, jul 2020. [Online]. Available: <http://www.ncbi.nlm.nih.gov/pubmed/31990494>
- [8] K. Javed and F. Lui, *Neuroanatomy, Cerebral Cortex*. StatPearls Publishing, aug 2018. [Online]. Available: <http://www.ncbi.nlm.nih.gov/pubmed/30725932>
- [9] T. J. Torrico and S. Abdijadid, *Neuroanatomy, Limbic System*. StatPearls Publishing, jul 2019. [Online]. Available: <http://www.ncbi.nlm.nih.gov/pubmed/30860726>
- [10] P. E. Ludwig and M. Varacallo, *Neuroanatomy, Neurons*. StatPearls Publishing, jul 2019. [Online]. Available: <http://www.ncbi.nlm.nih.gov/pubmed/28723006>

- [11] I. Chen and F. Lui, *Neuroanatomy, Neuron Action Potential*. StatPearls Publishing, aug 2019. [Online]. Available: <http://www.ncbi.nlm.nih.gov/pubmed/31536246>
- [12] M. J. Caire and M. Varacallo, *Physiology, Synapse*. StatPearls Publishing, may 2019. [Online]. Available: <http://www.ncbi.nlm.nih.gov/pubmed/30252303>
- [13] Y. Zhou and N. C. Danbolt, “Glutamate as a neurotransmitter in the healthy brain,” pp. 799–817, 2014. [Online]. Available: [/pmc/articles/PMC4133642//pmc/articles/PMC4133642/?report=abstracthttps://www.ncbi.nlm.nih.gov/pmc/articles/PMC4133642/](https://www.ncbi.nlm.nih.gov/pmc/articles/PMC4133642/)
- [14] B. E. Jewett and S. Sharma, *Physiology, GABA*. StatPearls Publishing, aug 2018. [Online]. Available: <http://www.ncbi.nlm.nih.gov/pubmed/30020683>
- [15] E. B. Bromfield, J. E. Cavazos, and J. I. Sirven, “An introduction to epilepsy,” 2006.
- [16] C. E. Stafstrom and J. M. Rho, “Neurophysiology of Seizures and Epilepsy,” in *Swaiman’s Pediatric Neurology: Principles and Practice: Sixth Edition*. Elsevier Inc., may 2017, pp. 506–512. [Online]. Available: <https://jhu.pure.elsevier.com/en/publications/neurophysiology-of-seizures-and-epilepsy>
- [17] R. S. Fisher, “The new classification of seizures by the international league against epilepsy 2017,” *Current neurology and neuroscience reports*, vol. 17, no. 6, p. 48, 2017.
- [18] R. S. Fisher, C. Acevedo, A. Arzimanoglou, A. Bogacz, J. H. Cross, C. E. Elger, J. Engel, L. Forsgren, J. A. French, M. Glynn, D. C. Hesdorffer, B. I. Lee, G. W. Mathern, S. L. Moshé, E. Perucca, I. E. Scheffer, T. Tomson, M. Watanabe, and S. Wiebe, “ILAE Official Report: A practical clinical definition of epilepsy,” *Epilepsia*, vol. 55, no. 4, pp. 475–482, apr 2014.

- [19] B. F. Shneker, N. B. Fountain, and J. M. Orlowski, “Epilepsy,” *Disease-a-Month*, vol. 49, no. 7, pp. 426–478, jul 2003.
- [20] T. M. Salmenpera and J. S. Duncan, “Imaging in epilepsy,” *Journal of Neurology, Neurosurgery & Psychiatry*, vol. 76, no. suppl 3, pp. iii2–iii10, 2005.
- [21] D. J. Englot, “A modern epilepsy surgery treatment algorithm: incorporating traditional and emerging technologies,” *Epilepsy & Behavior*, vol. 80, pp. 68–74, 2018.
- [22] H. F. González, A. Yengo-Kahn, and D. J. Englot, “Vagus nerve stimulation for the treatment of epilepsy,” *Neurosurgery Clinics*, vol. 30, no. 2, pp. 219–230, 2019.
- [23] M. C. H. Li and M. J. Cook, “Deep brain stimulation for drug-resistant epilepsy,” *Epilepsia*, vol. 59, no. 2, pp. 273–290, feb 2018. [Online]. Available: <http://doi.wiley.com/10.1111/epi.13964>
- [24] T. L. Skarpaas, B. Jarosiewicz, and M. J. Morrell, “Brain-responsive neurostimulation for epilepsy (rns® system),” *Epilepsy research*, vol. 153, pp. 68–70, 2019.
- [25] C. B. Henderson, F. M. Filloux, S. C. Alder, J. L. Lyon, and D. A. Caplin, “Efficacy of the ketogenic diet as a treatment option for epilepsy: Meta-analysis,” *Journal of Child Neurology*, vol. 21, no. 3, pp. 193–198, mar 2006. [Online]. Available: <http://journals.sagepub.com/doi/10.2310/7010.2006.00044>
- [26] R. G. Levy, P. N. Cooper, P. Giri, and J. Weston, “Ketogenic diet and other dietary treatments for epilepsy,” *Cochrane Database of Systematic Reviews*, vol. 2012, no. 3, mar 2012. [Online]. Available: <https://www.cochranelibrary.com/cdsr/doi/10.1002/14651858.CD001903.pub2/full><https://www.cochranelibrary.com/cdsr/doi/10.1002/14651858.CD001903.pub2/abstract><https://www.cochranelibrary.com/cdsr/doi/10.1002/14651858.CD001903.pub2/full?cookiesEnabled>

- [27] J. Engel J., “Mesial temporal lobe epilepsy: What have we learned?” *Neuroscientist*, vol. 7, no. 4, pp. 340–352, aug 2001. [Online]. Available: <http://journals.sagepub.com/doi/10.1177/107385840100700410>
- [28] W. O. Tatum, “Mesial Temporal Lobe Epilepsy,” *Journal of Clinical Neurophysiology*, vol. 29, no. 5, pp. 356–365, oct 2012. [Online]. Available: <https://journals.lww.com/00004691-201210000-00002>
- [29] C. M. O’Dell, A. Das, G. Wallace, S. K. Ray, and N. L. Banik, “Understanding the basic mechanisms underlying seizures in mesial temporal lobe epilepsy and possible therapeutic targets: A review,” *Journal of Neuroscience Research*, vol. 90, no. 5, pp. 913–924, may 2012. [Online]. Available: <http://doi.wiley.com/10.1002/jnr.22829>
- [30] A. Pitkänen, K. Lukasiuk, F. Edward Dudek, and K. J. Staley, “Epileptogenesis,” *Cold Spring Harbor Perspectives in Medicine*, vol. 5, no. 10, oct 2015.
- [31] A. Pitkänen and K. Lukasiuk, “Molecular and cellular basis of epileptogenesis in symptomatic epilepsy,” *Epilepsy & behavior*, vol. 14, no. 1, pp. 16–25, 2009.
- [32] R. Ellerkmann, S. Remy, J. Chen, D. Sochivko, C. Elger, B. Urban, A. Becker, and H. Beck, “Molecular and functional changes in voltage-dependent na<sup>+</sup> channels following pilocarpine-induced status epilepticus in rat dentate granule cells,” *Neuroscience*, vol. 119, no. 2, pp. 323–333, 2003.
- [33] C. F. Cavarsan, J. Malheiros, C. Hamani, I. Najm, and L. Colvolan, “Is mossy fiber sprouting a potential therapeutic target for epilepsy?” *Frontiers in neurology*, vol. 9, p. 1023, 2018.
- [34] S. Kemppainen and A. Pitkänen, “Damage to the amygdalo-hippocampal projection in temporal lobe epilepsy: A tract-tracing study in chronic epileptic rats,” *Neuroscience*, vol. 126, no. 2, pp. 485–501, jan 2004.

- [35] A. J. McDonald and D. D. Mott, “Functional neuroanatomy of amygdalohippocampal interconnections and their role in learning and memory,” *Journal of neuroscience research*, vol. 95, no. 3, pp. 797–820, 2017.
- [36] A. Pitkänen, M. Pikkarainen, N. Nurminen, and A. Ylinen, “Reciprocal connections between the amygdala and the hippocampal formation, perirhinal cortex, and postrhinal cortex in rat: a review,” *Annals of the new York Academy of Sciences*, vol. 911, no. 1, pp. 369–391, 2000.
- [37] D. A. Coulter, D. C. McIntyre, and W. Löscher, “Animal Models of Limbic Epilepsies: What Can They Tell Us?” *Brain Pathology*, vol. 12, no. 2, pp. 240–256, apr 2006. [Online]. Available: [/pmc/articles/PMC2441870/https://www.ncbi.nlm.nih.gov/pmc/articles/PMC2441870/](https://www.ncbi.nlm.nih.gov/pmc/articles/PMC2441870/)
- [38] P. S. Buckmaster, “Laboratory animal models of temporal lobe epilepsy,” *Comparative medicine*, vol. 54, no. 5, pp. 473–485, 2004.
- [39] A. K. Sharma, R. Y. Reams, W. H. Jordan, M. A. Miller, H. L. Thacker, and P. W. Snyder, “Mesial temporal lobe epilepsy: pathogenesis, induced rodent models and lesions,” *Toxicologic pathology*, vol. 35, no. 7, pp. 984–999, 2007.
- [40] J. V. Nadler, B. W. Perry, and C. W. Cotmon, “Intraventricular kainic acid preferentially destroys hippocampal pyramidal cells,” *Nature*, vol. 271, no. 5646, pp. 676–677, 1978. [Online]. Available: <https://www.nature.com/articles/271676a0>
- [41] M. Lévesque and M. Avoli, “The kainic acid model of temporal lobe epilepsy,” *Neuroscience & Biobehavioral Reviews*, vol. 37, no. 10, pp. 2887–2899, 2013.
- [42] J. L. Hellier, P. R. Patrylo, P. S. Buckmaster, and F. E. Dudek, “Recurrent spontaneous motor seizures after repeated low-dose systemic treatment with kainate: assessment of a rat model of temporal lobe epilepsy,” *Epilepsy research*, vol. 31, no. 1, pp. 73–84, 1998.

- [43] B. Van Nieuwenhuyse, R. Raedt, M. Sprengers, I. Dauwe, S. Gadeyne, E. Carrette, J. Delbeke, W. Wadman, P. Boon, and K. Vonck, “The systemic kainic acid rat model of temporal lobe epilepsy: long-term eeg monitoring,” *Brain research*, vol. 1627, pp. 1–11, 2015.
- [44] D. B. Clifford, J. W. Olney, A. Maniotis, R. C. Collins, and C. F. Zorumski, “The functional anatomy and pathology of lithium-pilocarpine and high-dose pilocarpine seizures,” *Neuroscience*, vol. 23, no. 3, pp. 953–968, dec 1987.
- [45] J. P. Vicedomini and J. V. Nadler, “A model of status epilepticus based on electrical stimulation of hippocampal afferent pathways,” *Experimental Neurology*, vol. 96, no. 3, pp. 681–691, 1987. [Online]. Available: <https://pubmed.ncbi.nlm.nih.gov/3582552/>
- [46] D. C. McIntyre, D. Nathanson, and N. Edson, “A new model of partial status epilepticus based on kindling,” *Brain Research*, vol. 250, no. 1, pp. 53–63, oct 1982.
- [47] K. Inoue, K. Morimoto, K. Sato, N. Yamada, and S. Otsuki, “Mechanisms in the development of limbic status epilepticus and hippocampal neuron loss: an experimental study in a model of status epilepticus induced by kindling-like electrical stimulation of the deep prepyriform cortex in rats.” *Acta medica Okayama*, vol. 46, no. 2, pp. 129–139, apr 1992. [Online]. Available: <https://europepmc.org/article/med/1533485>



## 3 | Structural and functional magnetic resonance imaging

### 3.1 Magnetic resonance imaging

#### 3.1.1 Introduction

75 to 80% of the human consists of hydrogen, which is present in water and lipids. Magnetic resonance imaging (MRI) is an imaging technique that uses the presence and characteristics of hydrogen to create an image. Disease or injury are often associated with changes in the amount and characteristics of water in tissue, and MRI can detect these changes and be used as a diagnostic tool. In addition to visualizing anatomy and pathology, MRI can be used to explore organ function, in vivo chemistry and brain activity [1].

#### 3.1.2 MRI scanner

The main component needed for MRI is a magnet that creates a strong, static magnetic field. Most often a solenoidal superconducting electromagnet of niobium-titanium alloy wire is used. Liquid helium, sometimes in combination with liquid nitrogen, is used to keep the temperature of the magnet below 20° K. It is very important that the magnetic field is homogeneous, meaning it changes very little within the regions of interest. Because the magnetic field created by a superconducting magnet is always present, only non-magnetic metal can be present in the MRI room and special care has to be taken when imaging patients with surgical implants or metal fragments in their body. Patients with magnetic pacemakers or other crucial ferromagnetic implants should never be scanned.

To obtain spatial information in MR imaging, three additional orthogonal magnetic fields are needed. These fields, called gradient fields, are produced by gradient coils, loops of wire through which an electric current can flow. A radio frequency signal is necessary to obtain an actual MR image. This signal is generated by the radio frequency coils (Figure 3.1) [2].

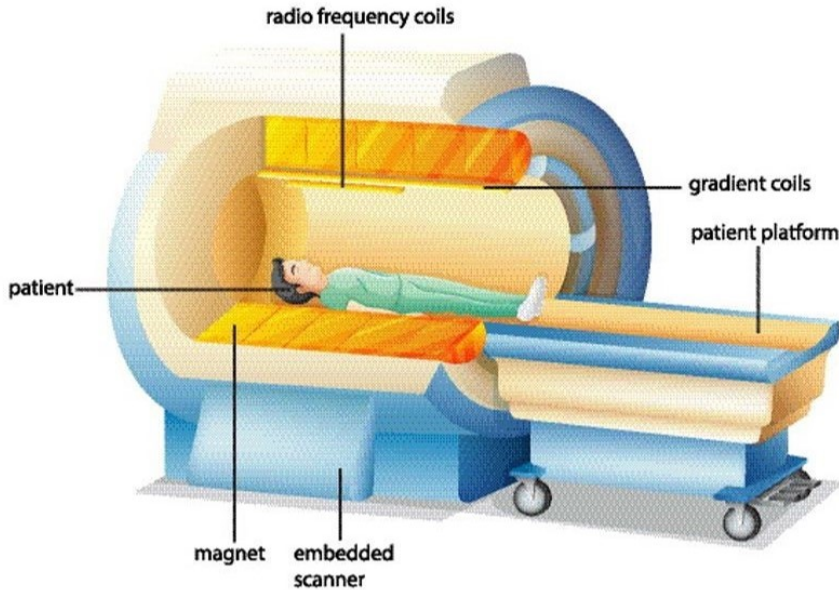


**Figure 3.1:** Schematic representation of an MRI scanner, showing the magnet, gradient coils and radio frequency coils. Adapted from BlueRingMedia/Shutterstock.com.

### 3.1.3 Basic principles of MRI

MR imaging is based on the principle that a nucleus that possesses spin interacts with a magnetic field. Almost every element possesses spin, i.e., it is constantly rotating around an axis at a fixed speed. This means almost every element can be examined using MR, but the  $^1\text{H}$  nucleus is by far used most often in MR imaging, mainly because it is so abundantly present in the human body. Other isotopes that are sometimes used in MRI are deuterium ( $^2\text{H}$ ), helium ( $^3\text{He}$ ), lithium ( $^7\text{Li}$ ), carbon ( $^{13}\text{C}$ ), phosphorus ( $^{31}\text{P}$ ), nitrogen ( $^{15}\text{N}$ ), oxygen ( $^{17}\text{O}$ ) and fluor ( $^{19}\text{F}$ ).

Hydrogen is a positively charged nucleus, so it does not only possess spin, but also has a magnetic moment. In the absence of an external magnetic field, all hydrogen atoms are oriented randomly, so their total magnetic moment is zero. However, when an external magnetic field ( $B_0$ ) is applied, the hydrogen atoms align with the field and start to precess about the magnetic field at the Larmor frequency, a frequency that depends on the type of nucleus and the strength of the applied magnetic field:  $\omega_L = \gamma B_0$ . This leads to a net magnetization  $M_0$  in the direction of the external magnetic field (Figure 3.2) [2].

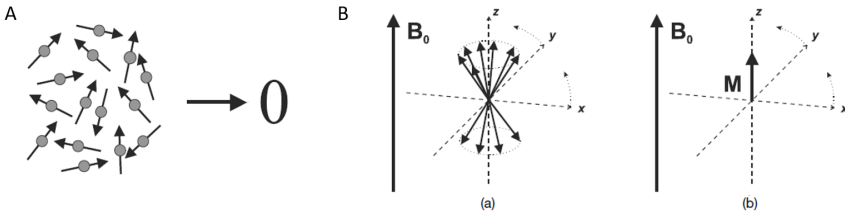


**Figure 3.2:** A) In the absence of a magnetic field, all hydrogen atoms are randomly oriented, so their total magnetic moment is zero. B) When an external magnetic field ( $B_0$ ) is applied, the hydrogen atoms align with the field and start to precess about the magnetic field at the Larmor frequency, which leads to a net magnetization  $M=M_0$  in the direction of the external magnetic field (Adapted from [2]).

### 3.1.4 Relaxation

The main concept of MRI is the transfer of energy. Energy is emitted in the form of a radiofrequency pulse (rf) and absorbed by the protons in the body. Then the protons reemit this energy and it is detected by the scanner. This process is called relaxation. The radiofrequency pulse is emitted at the Larmor frequency and with an orientation perpendicular to  $B_0$ , creating an effective field  $B_1$ . When the protons absorb the energy of the pulse, the direction of their rotation changes to an orientation that is perpendicular to both  $B_0$  and  $B_1$ . Usually, the radiofrequency pulse causes the rotation to shift to the transverse plane, in which case it is called a  $90^\circ$  pulse [2]. After the radiofrequency pulse has ended, the pro-

tons start to return to their equilibrium orientation. During this process, they emit energy at the Larmor frequency and start to precess around  $B_0$ . This creates a voltage in a receiver coil that is perpendicular to the transverse plane, called free induction decay (FID) [2]. Relaxation is the main contributor to image contrast in MRI. Two types of relaxation are used: T1 and T2 relaxation. During T1 relaxation, or spin-lattice relaxation, excited protons transfer their energy to their surroundings. The relaxation time T1 is the time it takes for the z component of the magnetization  $M$  to return to 63% of its initial value after the radiofrequency pulse has ended [2]. T2 relaxation, or spin-spin relaxation, is the process during which energy is transferred from one excited proton to another. This causes a loss of phase coherence and decreases the magnitude of the transverse component of  $M$ . The relaxation time T2 refers to the time it takes for the transverse component of  $M$  to decay to 37% of its original value. The main cause of loss of phase coherence is the movement of neighboring spins because of molecular vibrations or rotations. This causes the ‘real’ T2 relaxation. Another cause is nonuniformity of the magnetic field  $B_0$ . This contributes to  $T2^*$ , the total transverse relaxation time [2]. The principle of relaxation is visualized in Figure 3.3. In the presence of an external magnetic field, hydrogen atoms align with the magnetic field and precess at the Larmor frequency. Following a  $90^\circ$  rf pulse, the magnetization of the spins flips. Excited protons undergo T1 or spin-lattice relaxation and T2 or spin-spin relaxation [3].

### 3.1.5 Spatial localization

To be able to localize a signal’s point of origin within the body, gradients are applied to make the magnetic field spatially dependent. Gradients are magnetic fields that create a small linear variation in the total magnetic field. Because of this variation, the Larmor frequency of the protons in the body varies depending on their position in the magnet. When a radiofrequency pulse is emitted with a frequency that matches the Larmor frequency of protons in a specific volume of the body (pixel or voxel), only the protons in this volume will absorb and reemit the energy of the pulse and will contribute to the image. By varying the frequency

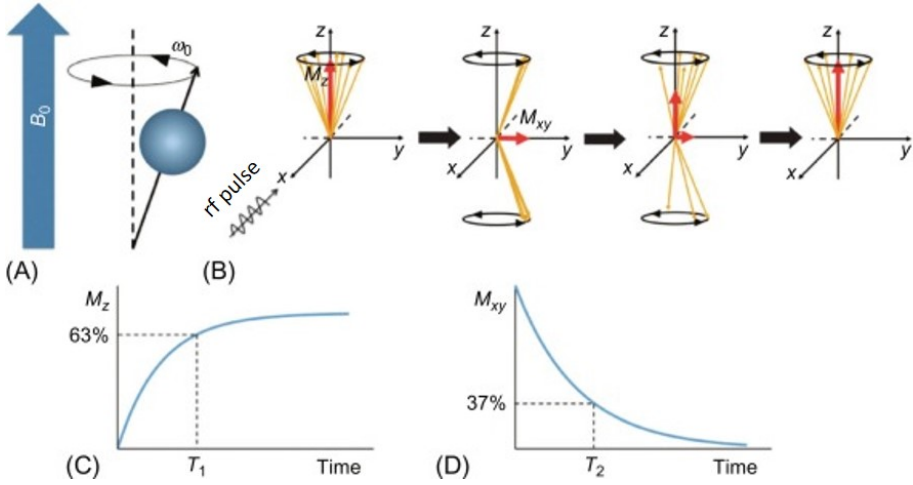


**Figure 3.3:** Principle of relaxation. (A) Hydrogen atoms align with the magnetic field and precess at the Larmor frequency. (B) Following a  $90^\circ$  radio frequency pulse, the magnetization of the spins flips. Excited protons undergo relaxation: (C)  $T_1$  or spin-lattice relaxation and (D)  $T_2$  or spin-spin relaxation [3].

and phase of the radiofrequency pulse, a complete image consisting of voxels can be constructed (Figure 3.4). In the  $x$ ,  $y$  and  $z$  directions, a physical gradient is applied. The three physical gradients are linked to three functional gradients used to construct an MR image: slice selection, readout or frequency encoding, and phase encoding.

The slice selection gradient  $G_{SS}$ , in combination with frequency-selective excitation, is used to restrict MR signals to a two-dimensional plane, or slice. The slice orientation, thickness and position depend on the direction and amplitude of the gradient. By varying the frequency of the rf pulse, different slices can be imaged. It is also possible to obtain signals from multiple slices at the same time (multislice imaging) by emitting multiple rf pulses with different frequencies [1, 2].

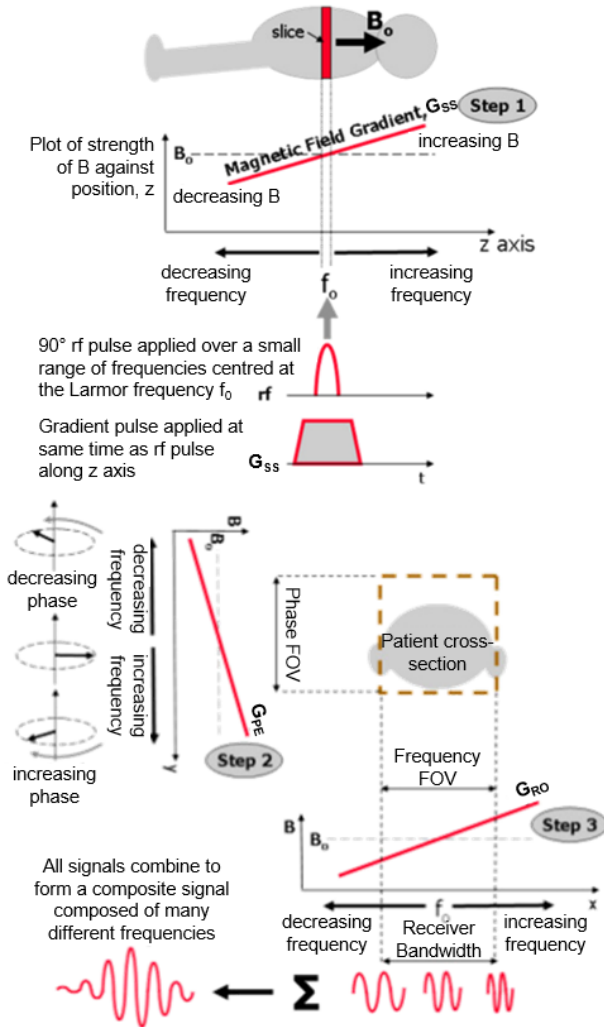


**Figure 3.4:** Spatial localization. Step 1) Slice selection: a magnetic field gradient  $G_{SS}$  is applied during the rf excitation pulse to select a slice of tissue. The Larmor frequency of the protons depends on the position along the gradient and resonance only occurs where it equals the frequency of the rf pulse,  $f_0$ . Step 2) Phase encoding: a phase encoding gradient,  $G_{PE}$ , is applied in a direction along the  $y$  direction, causing a phase shift that depends on the position of the proton along the axis. Step 3) Frequency encoding: a readout gradient,  $G_{RO}$ , is applied perpendicular to the phase encoding direction, while the MR signal echo is detected. The Larmor frequency depends on the position along the gradient. The detected MR signal from the slice contains many different frequencies. Adapted from [5].

The readout gradient  $G_{RO}$  is used to obtain one of the dimensions of the field of view (FOV) in the MR image. It is applied during the signal detection and causes the excited protons to precess at a different frequency depending on their location along the gradient direction. Based on this frequency and the amplitude of the readout gradient, the location of the protons can be calculated. The other dimension of the FOV is determined by the phase encoding gradient  $G_{PE}$ . The phase encoding gradient is applied perpendicularly to  $G_{SS}$  and  $G_{RO}$  and causes excited protons to precess slightly faster or more slowly. After the gradient is turned off, the precession frequency returns to its original value, but the phase is shifted. Depending on its location, a proton experiences a different amount of phase shift. The closer to the edge of the FOV, the greater the phase shift.  $G_{PE}$  is applied several times with different amplitudes and each time, the signal is detected. This way the entire FOV can be imaged [2].

The measured MR signals are collected in a matrix, called the k-space, which is the frequency-encoded representation of the MR signal. To obtain the actual MR image in a spatially encoded format, a 3D Fourier transformation has to be performed [4].

### 3.1.6 Spin echo and gradient echo

The FID is never measured directly, but echoes are created. Two types of echoes are used: spin echo and gradient echo [1]. A spin echo is created by emitting a second rf pulse of  $180^\circ$ , called a refocusing pulse. After the excitation pulse, protons start to dephase and after a while, part of the phase change depends on the applied magnetic field. When a  $180^\circ$  pulse is then applied, spins are rotated  $180^\circ$ , changing the sign of the phase change. If the phase change was smaller before the refocusing pulse, it will be larger afterwards, but the phase will still change a bit faster. Similarly, if the phase change was larger before the refocusing pulse, it will be smaller afterwards, and change more slowly. This will cause the spins to rephase, the FID will increase and reach a maximum. This is the spin echo. The time between the excitation pulse and the spin echo is called the echo time (TE). The refocusing pulse should be applied at

half the echo time. Gradient echoes are created by applying magnetic field gradients. This causes the field strength, and subsequently Larmor frequency, to vary along the direction of the gradient. Protons start to dephase and the FID quickly drops to zero. Then a second gradient is applied, with the same amplitude but opposite direction, which reverses the dephasing. The FID re-appears and its amplitude is highest when the spins have rephased. This signal is called a gradient echo. The time between the excitation pulse and the rephasing of the spins is the echo time (TE) [5].

An MR image is obtained using a pulse sequence, i.e., a combination of rf pulses, gradient pulses and timing that determines which type of image is acquired. A spin echo sequence is used most often. In this sequence, the rf pulse is followed by one or more  $180^\circ$  pulses. The time between two excitation pulses is called the repetition time (TR). In a gradient echo sequence, a gradient reversal is used to refocus the protons instead of a  $180^\circ$  pulse [2].

### 3.1.7 Image contrast

Different image contrasts can be obtained depending on the repetition time and echo time. The TR determines to what extent T1 relaxation contributes to the contrast. A longer TR means that more of the excitation pulse's energy can be dissipated through spin-lattice relaxation, so there will be less T1 weighting. The amount of T2 weighting in the image depends on the TE. If the TE is longer, there is more dephasing of protons, so lower signal amplitudes are obtained, and more signal is obtained from tissues with a longer T2 [2].

Different tissues have a different T1 and T2. For example, T1 is long in fluid, average in water-based tissues and short in fat-based tissues. T2 is also the longest in fluid, and longer in water-based tissues than in fat-based tissues (Figure 3.5). The image contrast also depends on the proton density (PD) or the amount of hydrogen in a volume. PD is higher in fluids, such as cerebrospinal fluid (CSF), than it is in tendon or bone. Signal intensity is generally higher in tissue with a high PD.

Overall, a short TE and short TR will lead to a T1-weighted image, a long TE and long TR will lead to a T2-weighted image and a short TE and long TR will lead to a PD-weighted image [1]. Examples of T1-, T2- and PD-weighted images are shown in Figure 3.6.

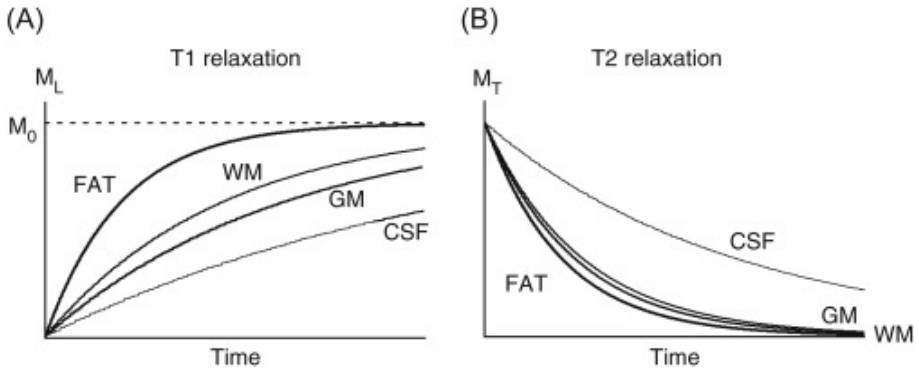


**Figure 3.5:** Different tissues have a different T1 and T2 relaxation times. A) T1 is long in fluid, such as cerebrospinal fluid (CSF), average in water-based tissues, such as grey matter (GM), and short in fat-based tissues, such as white matter (WM). B) T2 is longest in fluid (CSF), and longer in water-based tissues (GM) than fat-based tissues (WM) [6].

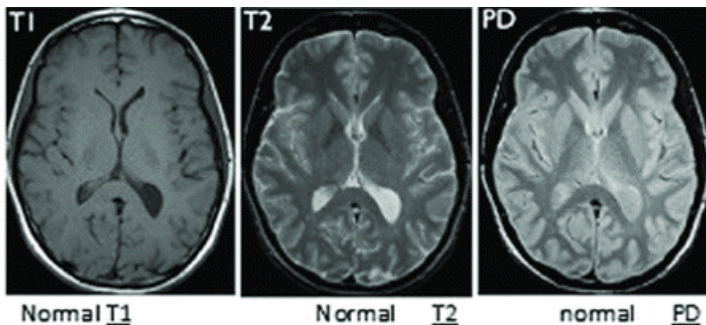


**Figure 3.6:** Example of a T1-weighted, T2-weighted and PD-weighted image [7].

### 3.1.8 Small animal MRI

When imaging small animals, such as rats or mice, it is important to have a high spatial resolution. For human brain imaging, a resolution of around 1 mm is used, while for rodent brain imaging, a resolution of about 0.1 mm is necessary. This means that voxel sizes in rodent brain imaging are about a 1000 times smaller than in human brain imaging. The signal-to-noise ratio (SNR) is directly related to the voxel size, so it is necessary to increase the SNR to obtain a high-quality image. One way to do this, is to use higher field strengths [8]. Preclinical MR systems usually use magnetic fields of 7 to 9.4 T, and sometimes even 11.7 T [9]. In addition, dedicated transmit-and-receive coils are used. These are placed very close to the body to obtain the best possible image quality. Because of the small voxel size, stronger gradients are needed as well. The SNR can also be increased using repeated signal acquisition, however, this leads to longer acquisition times [8].

One important difference between imaging humans and animals is the use of anesthesia to prevent motion [9]. Both injectable and inhalation anesthetics can be used in small animals, but it is recommended to use inhalation anesthesia. The advantages are the rapid onset and recovery, and better control over the dose and maintenance time. Furthermore, inhalation anesthesia is more quickly eliminated by the body via the lungs, when compared to injectable anesthetics, which have to be metabolized by the liver and passed by the kidneys, allowing for a faster recovery [9]. Isoflurane is the most commonly used inhalation anesthetic in small animal imaging. It is well tolerated, easy to control and there is no need for endotracheal intubation [8].

When using anesthesia during functional imaging, it is important to take into account its effects on the blood flow, blood oxygenation levels, and cardiac and respiratory function [9]. Isoflurane is known to affect functional connectivity, so for functional MRI, the injectable anesthetic medetomidine is a better choice. Using medetomidine, an alpha<sub>2</sub>-adrenoreceptor agonist, functional connectivity maps were found in rodents that were comparable to those in humans. Another option is to

use alpha-chloralose, however, this type of anesthesia requires intubation and mechanical ventilation. Medetomidine on the other hand is noninvasive, so it can be used for longitudinal experiments. Therefore, it is the preferred option [8].

Anesthesia typically causes autonomic nervous system depression, which leads to cardiovascular and respiratory depression and hypothermia. Therefore, physiological monitoring is crucial [9]. The respiratory rate can be assessed by placing a pressure sensor on the animal's chest to detect breathing motion. To monitor heart rate, an electrocardiograph (ECG) system with dedicated electrodes can be used. The recording of respiratory and heart rate can also be used to reduce motion artefacts, for example by using gating systems during image acquisition. Finally, it is important to monitor and maintain body temperature. Core temperature can be measured using a rectal thermometer. Hypothermia can be counteracted using external heating, such as circulating hot water blankets, blowing air, infrared light, electric pads or bubble wrap [9]. For MRI, it is important that the monitoring equipment does not contain any ferromagnetic material due to the high magnetic field. The equipment should not emit radio frequencies that might interfere with imaging and its power source should be filtered and isolated, or a battery should be used [9].

## 3.2 Diffusion-weighted magnetic resonance imaging

### 3.2.1 Basic principles of diffusion-weighted MRI

#### Introduction

In a glass of water, water molecules are constantly moving. Since they are not obstructed, they can move equally in all directions. This is called isotropic diffusion. If these molecules are hindered by a boundary, diffusion is no longer equal in all directions, which is called anisotropic diffusion. The displacement of water molecules can be measured using diffusion-weighted MRI (dMRI). Based on the amount and the direction

of diffusion, information about the local environment of the molecules can be obtained. For example, in cerebrospinal fluid, water molecules can move freely in all direction and diffusion is isotropic. In grey and white matter, diffusion is restricted by boundaries, such as cell membranes, which will lead to changes in the measured MRI signal. In white matter tracts, the boundaries are coherently oriented, so the change in MRI signal will depend on the measured direction. In the brain, diffusion is obstructed by different types of boundaries, such as macromolecules, organelles and cell membranes. Depending on the type of boundaries and diffusion, the measured MRI signal will be affected differently. Based on the changes in the MRI signal in different directions, information can be obtained about the underlying tissue structure [10].

Its ability to quantify diffusion in neural tissue has made dMRI a useful technique to investigate the healthy and diseased brain. In addition, it has been used to assess muscles and other organs, including kidney and prostate. Diffusion-weighted MRI has been particularly useful in the management of acute ischemia and the assessment of brain lesions. Because it allows for the visualization and segmentation of white matter fiber bundles, dMRI can be used in the planning of neurosurgery [10].

## Diffusion

Diffusion is the random Brownian motion of particles. At room temperature, water molecules are constantly moving because of their intrinsic thermal energy. They collide with other water molecules and change direction. In a free body of water, the molecules are free to move, only hindered by other water molecules. This is called free diffusion. The displacement of the molecules follows a zero-mean Gaussian distribution, i.e., shorter displacements are more likely to occur and, most likely, the total displacement will be zero. Because the diffusion is not hindered, it is independent of direction. This is called isotropic diffusion. In the brain, boundaries are present that restrict diffusion. This can be detected with diffusion-weighted MRI. At room temperature, water molecules move about  $25 \mu\text{m}$  in 50 ms, a relevant time window in dMRI. This length is similar to the size of many cellular structures in the brain.

This allows for the detection of the geometric properties and structure of tissue using dMRI [10, 11].

In biological tissue, two more types of diffusion occur: restricted diffusion and hindered diffusion. Diffusion is called restricted when the movement of water molecules is impeded by impermeable boundaries. In the brain, restricted diffusion occurs when water molecules are trapped within a cell boundary, i.e., in the intracellular space. The molecules can still move, but only within the cell. Diffusion is called hindered when water molecules are obstructed by an obstacle but are not entirely trapped. In this case, diffusion is reduced perpendicularly to the obstacle. In the brain, this occurs in the extracellular space. Restricted and hindered diffusion are illustrated in Figure 3.7. Cylindrical boundaries, which are numerous in the brain, reduce the amount of diffusion perpendicular to its axis, while diffusion along the axis is unhindered. This means that diffusion is directionally dependent, which is called anisotropic diffusion [10].

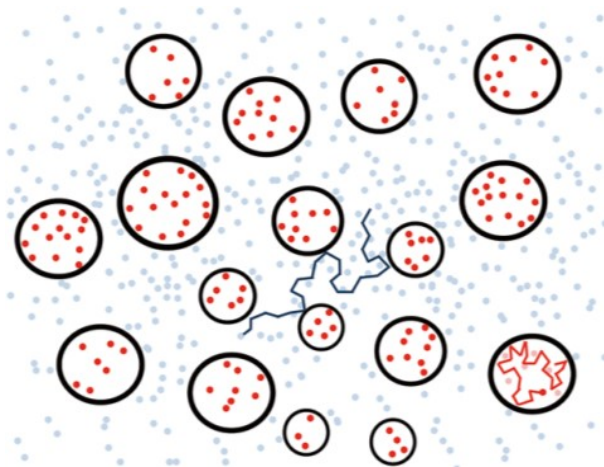


**Figure 3.7:** Restricted (red) and hindered (blue) diffusion. Red molecules can only move within the boundaries. Blue molecules can move around freely, but are hindered by the boundaries [10].

Diffusion in the brain depends on the presence of cellular structures that create boundaries. Several characteristics such as the cell membrane, viscosity of the intracellular space and subcellular structures can affect the diffusion of water molecules inside and outside the cell. Grey matter has a very complicated organization, containing neuron bodies and a mesh of dendrites and glial cells. This means that the diffusion properties in grey matter are very complex as well, so it is difficult to interpret dMRI results in grey matter. White matter, on the other hand, consists of tight bundles of thousands or millions of coherent and tightly packed axons. The water molecules in the intra-axonal space diffuse mainly in the direction of the axon bundle. These molecules are confined by the cell boundaries, so diffusion is restricted. In the extracellular space, the movement of water molecules is influenced by the lattice structure of the axons. Here, the diffusion is hindered. Imaging the diffusion of water in white matter can provide information about the location and orientation of axon bundles in the brain. As such, structural connectivity in the brain can be investigated using dMRI [10].

### **Diffusion-weighted imaging**

To detect diffusion in the MRI signal, a Pulsed Gradient Spin Echo (PGSE) sequence can be used (Figure 3.8). In this sequence, an extra magnetic field gradient is applied before and after the refocusing pulse. Protons precess at a frequency that is proportional to the magnetic field they are subjected to, so when a magnetic field gradient is applied, the precession frequency varies along the direction of the gradient. In a PGSE sequence, first an excitation rf pulse is applied that flips the magnetization to the transverse plane (Figure 3.9(a)). Then, a short pulsed gradient is applied which causes the spin magnetization to dephase, because the precession frequency depends on the position along the gradient (Figure 3.9(b)). Next, the refocusing pulse rotates the spins  $180^\circ$  (Figure 3.9(c)). The second pulsed gradient then rephases the spins. If there is no diffusion, the magnetization will rephase completely because the molecules experience the same magnetic field. If there is free diffusion, the molecules move between the start of the first and the second gradi-

ent. This means they experience a different magnetic field and precess at a different frequency, so the phase of their magnetization is different after the second gradient than after the first one. Because the molecules can move freely in all directions, the net magnetization is reduced and the acquired signal will be attenuated (Figure 3.9(d)) [12].

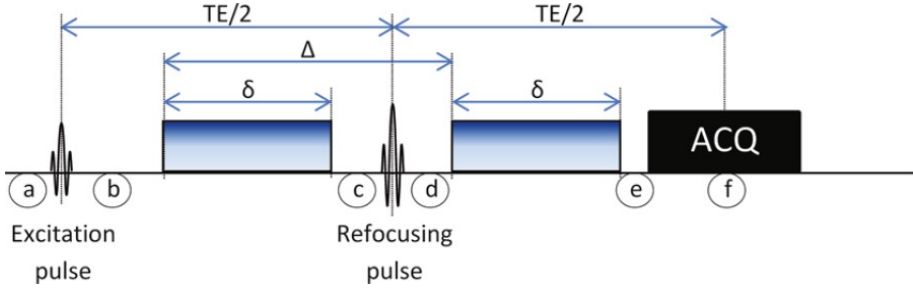


**Figure 3.8:** Pulsed Gradient Spin Echo (PGSE) sequence. An extra magnetic field gradient is applied before and after the refocusing pulse [10].

The signal acquired using a PGSE sequence follows the Stejskal-Tanner equation [12]:

$$\frac{S}{S_0} = e^{-(\gamma^2 G^2 \delta^2 (\Delta - \frac{\delta}{3})) D} \quad (3.1)$$

With  $\delta$  the gradient duration,  $\Delta$  the time between the start of the gradients,  $G$  the gradient strength,  $\gamma$  the gyromagnetic ratio,  $S$  the signal,  $S_0$  the signal without diffusion weighting and  $D$  the diffusion constant. This formula can be simplified using the b-value, a combination of  $G$ ,  $\delta$  and  $\Delta$ :

$$\frac{S}{S_0} = e^{-bD} \text{ with } b = \gamma^2 G^2 \delta^2 (\Delta - \frac{\delta}{3}) \quad (3.2)$$

The signal decays exponentially depending on the properties of the gradients and the diffusion constant. The gradients applied for spatial localization can have an influence on the signal as well, but are often canceled out using b-zero images [10].

The amount of diffusion weighting that is applied is determined by the b-value, expressed in  $\text{s}/\text{mm}^2$ . The higher the b-value, the more diffusion-weighted the image, but also the more the signal is attenuated. A b-value

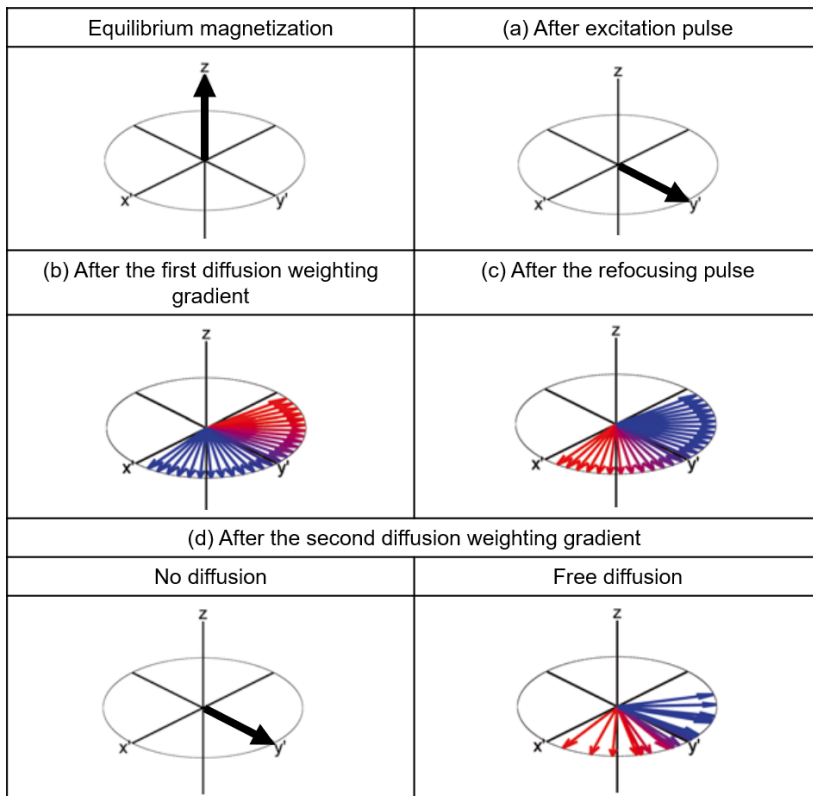


**Figure 3.9:** Magnetization during PGSE sequence. First an excitation rf pulse is applied that flips the magnetization to the transverse plane (a). Then a short pulsed gradient is applied that causes the spin magnetization to dephase, because the precession frequency depends on the position along the gradient (b). Next, the refocusing pulse rotates the spins  $180^\circ$  (c). The second pulsed gradient then rephases the spins. If there is no diffusion, the magnetization will rephase completely because the molecules experience the same magnetic field. If there is free diffusion, the molecules move between the start of the first and the second gradient. This means they experience a different magnetic field and precess at a different frequency, so the phase of their magnetization is different after the second gradient than after the first one. Because the molecules can move freely in all directions, the net magnetization is reduced and the acquired signal will be attenuated (d) (Adapted from [10]).

of zero means there is no diffusion weighting. Usually one or more images with zero b-value (b-zero images) are acquired at the beginning of a scan for normalization. Choosing the b-value is a compromise between the signal-to-noise ratio and contrast. Higher b-values can provide more details on tissue structure, but the signal-to-noise ratio is lower [13].

In free diffusion, the diffusion constant  $D$  corresponds with the self-diffusion coefficient, which quantifies the freedom of movement of a water molecule. At room temperature, the diffusion constant of water is about  $2.2 \cdot 10^{-3} \text{ mm}^2/\text{s}$ . In the brain, free diffusion only occurs in a few locations, such as the ventricles that are filled with cerebrospinal fluid (CSF). In other tissues, intra- and extracellular components and cellular membranes cause hindered and restricted diffusion. This means that the diffusion constant no longer represents the self-diffusion coefficient, but an apparent diffusion coefficient (ADC). The ADC varies as a function of the b-value and is lower than the self-diffusion coefficient, because hindered and restricted water molecules can diffuse less than freely moving molecules. The attenuation of the ADC is more prominent for higher b-values, because a longer diffusion time allows for more collisions of water molecules with boundaries, which increases the difference with free diffusion. Since the ADC is sensitive to the amount of hindered and restricted diffusion, it can be used to examine the cells that make up the boundaries. This way the properties and microstructure of tissues can be investigated [11].

The MRI signal is only sensitive to diffusion along the direction of the applied magnetic field gradient. In the case of free diffusion, such as in CSF, this is not a problem, because free diffusion is independent of direction. However, in white matter, diffusion is anisotropic. Water molecules diffuse more easily in the direction of the axon bundles than perpendicular to them. Depending on the direction of the magnetic field gradient, different diffusion-weighted images will be obtained. This means that by applying gradients in different directions, information about the anisotropy of tissue microstructure can be obtained. For example, Figure 3.10 shows diffusion-weighted images (DWIs) acquired along the x-axis (left to right), y-axis (back to front) and z-axis (bottom to top). The red

arrow indicates the genu of the corpus callosum. In this region, DWI-intensity is low along the x-axis and higher along the y- and z-axis. This indicates that diffusion is higher along x and lower along y and z, which suggests that there is an axon bundle that runs along the left-right axis. This is indeed true, as the corpus callosum is a white matter tract that connects the left and right hemispheres. In practice, more than three gradient directions are used to acquire a diffusion-weighted image. The more directions, the more accurate the DWI, but the longer the scanning time. The information about the directions of the magnetic field gradients is summarized in a gradient table. In this table, each row represents a DWI and its corresponding gradient direction and b-value [10].



**Figure 3.10:** Diffusion-weighted images (DWIs) acquired along the x-axis (left to right), y-axis (back to front) and z-axis (bottom to top). The red arrow indicates the genu of the corpus callosum. In this region, DWI-intensity is low along the x-axis and higher along the y- and z-axis [10].

DWIs are affected by T2 shine-through, i.e., high intensity can be caused by a high T2 intensity rather than hindered or restricted diffusion. That is why DWIs are first normalized using the b-zero images. To visualize the information of DWIs acquired with multiple gradient direction, a spherical polar plot can be used (Figure 3.11). In this plot, each voxel is represented as a sphere of which the radius corresponds with the MRI signal along a three-dimensional angle. In addition, colors are used to indicate directions: red corresponds with left to right, green with back to front and blue with bottom to top. A plot of the DWIs can be confusing,

because a higher intensity corresponds with less diffusion. Therefore, ADC plots are often used. In these plots, a higher value corresponds with more free diffusion [10].

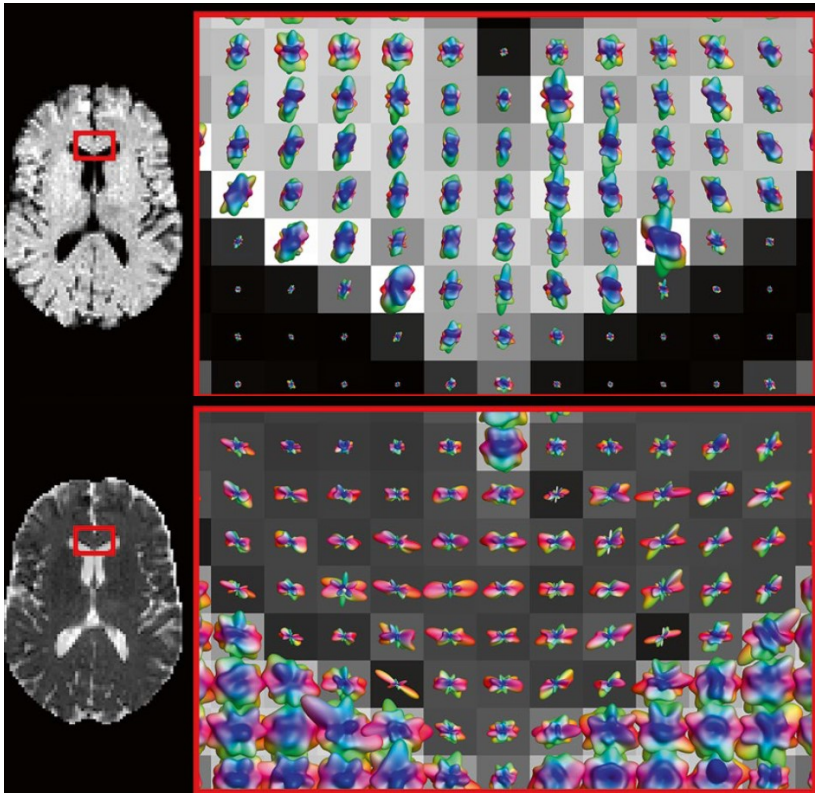


**Figure 3.11:** Spherical polar plot of DWIs (top) and ADC (bottom). In this plot, each voxel is represented as sphere of which the radius corresponds with the MRI signal along a three-dimensional angle. Colors indicate directions: red corresponds with left to right, green with back to front and blue with bottom to top. In the DWI plot, a higher intensity corresponds with less diffusion. In the ADC plot, a higher value corresponds with more free diffusion. The red rectangle shows the genu of the corpus callosum [10].

### 3.2.2 Diffusion-weighted MRI analysis methods

#### Preprocessing

Diffusion-weighted MRI is affected by typical artifacts, for which some corrections are needed during image preprocessing. Some of the most common artifacts in dMRI and their corrections are discussed below [10].

**Correction for eddy current-induced distortions** During the acquisition of dMRI images, diffusion-sensitizing gradients are switched on and off very fast. This creates a changing magnetic field, which induces current in conductors in the field. These currents are called eddy currents, since they are similar to swirling eddies in a river. The eddy currents induce additional magnetic gradient fields which influence the diffusion gradient. The overlap between the altered diffusion gradient and the spatial encoding gradient can produce geometric distortions and lead to misalignment of the DWIs. Because the diffusion gradient is different from what is expected, diffusion may be estimated incorrectly. The geometric distortions in the DWIs are visible in the phase-encoding direction and depend on the direction of the eddy current gradient. The misalignment can be seen as increased fractional anisotropy at the edges of the brain, typically in the phase-encoding direction. Several methods can be used to correct for eddy current-induced distortions during image preprocessing. The DWIs are usually registered to the b-zero image using mutual information. In Figure 3.12a, the effect of eddy current-induced distortion is visible on a directionally encoded color (DEC) map of diffusion as high anisotropy at the edges of the brain in the phase-encoding direction (i.e., x-direction). The DEC map after correction for eddy current-induced distortion is visualized in Figure 3.12b [14, 15].

**Correction for subject motion** Because of the long acquisition time of DWIs, subject motion is almost impossible to avoid. Motion occurs in six directions: three translations (x-, y- and z-direction) and three rotations (yaw, pitch and roll), and leads to misregistration of the DWI volumes. Similarly to eddy current-induced distortions, this can be seen

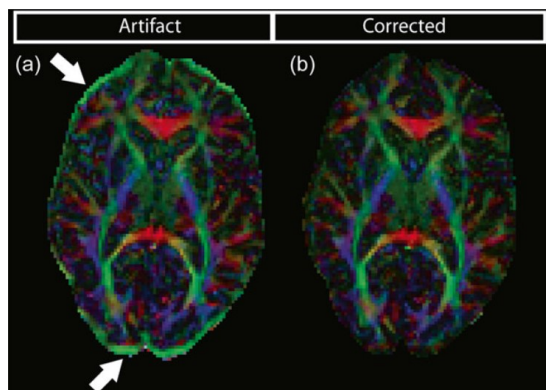


**Figure 3.12:** The effect of eddy current-induced distortion on a DEC map: (a) distortions are visible as high anisotropy at the edges of the brain in the phase-encoding direction, (b) the DEC map after correction for eddy current-induced distortions [10].

as high anisotropy at the edges of the brain, but it is present on all sides of the brain, not just in the phase-encoding direction. Correction for subject motion usually consists of image registration using six parameters for translation and rotation. This correction is typically performed at the same time as the correction for eddy currents. It is important to take into account that a DWI contains information about the gradient directions, so if a DWI is rotated, the b-matrix should be rotated as well. In Figure 3.13, the effect of subject motion on a DEC map is visualized. Anisotropy can be high at the edges of the brain or there can be an overall change in anisotropy. Misalignment can also be seen as an increased standard deviation across the DWIs at the edges of the brain. The effect of correction for subject motion on the DEC maps and standard deviation are visualized as well [14, 15].

**Correction for susceptibility-induced distortions** Different tissues have different magnetic susceptibilities, which can cause variations in the magnetic field  $B_0$ . Differences in susceptibility are most prominent where air-filled sinuses are close to bone or tissue. Especially echo-planar images (EPI) are highly affected by differences in susceptibility, because an entire image volume is acquired within a single excitation. Susceptibility-induced distortions can cause the signal of several voxels to

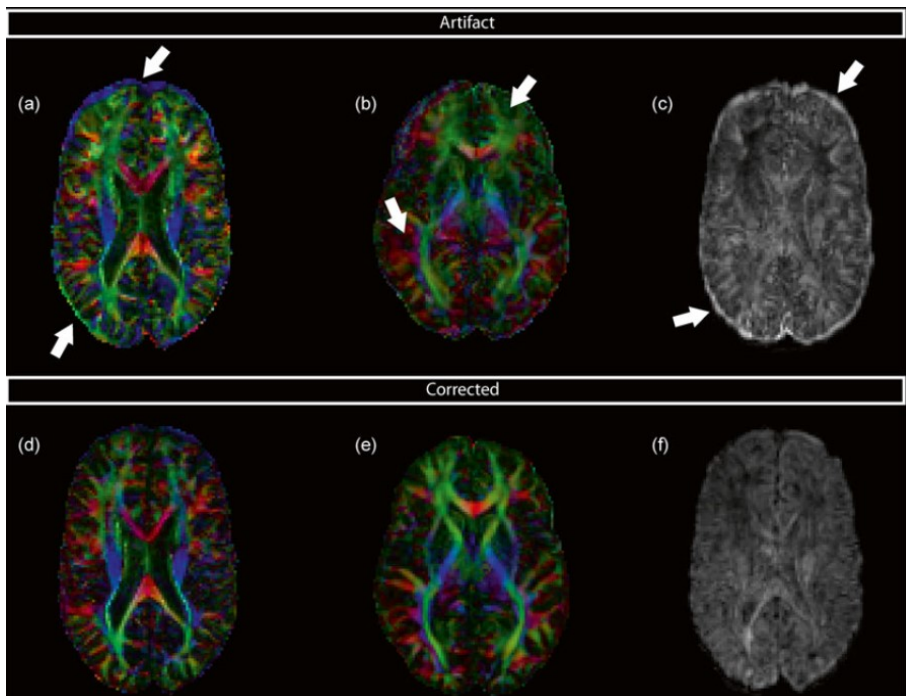


**Figure 3.13:** The effect of subject motion on a DEC map: (a) anisotropy is high at the edges of the brain or (b) there is an overall change in anisotropy, (c) standard deviation across the DWIs is high at the edges of the brain and (d), (e) and (f) show the effect of correction for subject motion on (a), (b) and (c), respectively [10].

be compressed into one voxel (signal pile up) or they can cause the signal from one voxel to be stretched out over multiple voxels (signal smearing). Distortions on the DWIs become visible when the images are fused with an anatomical image, such as a T1- or T2-weighted image, which is affected less by susceptibility differences. This anatomical image can also be used to correct for susceptibility-induced distortions using non-rigid image registration. In Figure 3.14, a DEC map is overlaid on an undistorted anatomical image. The white arrows indicate misalignments near the brain stem and corpus callosum due to susceptibility-induced distortions in the DWI (a). In (b), the misalignments are resolved after correction for susceptibility-induced distortions [15].

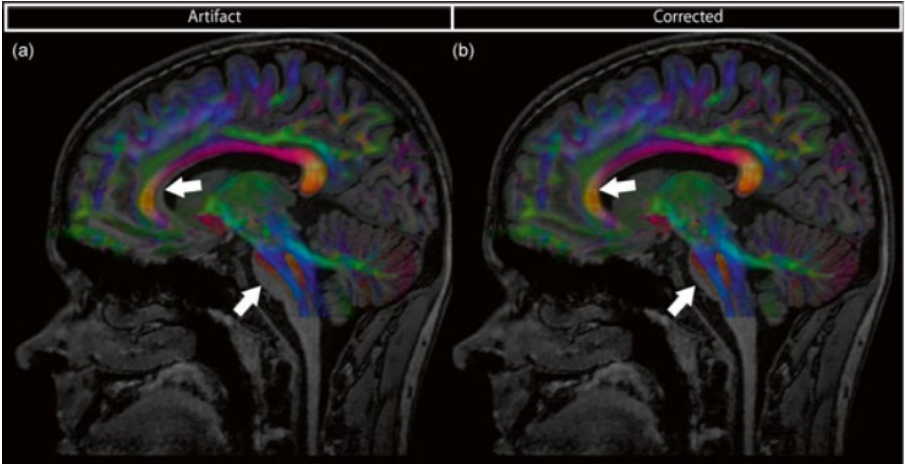


**Figure 3.14:** A color FA map overlaid on an undistorted anatomical image. White arrows indicate misalignments near the brain stem and corpus callosum due to susceptibility-induced distortions in the DWI (a). In (b), the misalignments are resolved after correction for susceptibility-induced distortions [10].

**Correction for Nyquist ghosting** A hardware related DWI artifact is Nyquist ghosting. Because there is a time difference of a few microseconds between the application of the readout gradient and the acquisition of the image, the data is shifted in the k-space, which can be seen in the image as a “ghost”, i.e., the image contains a copy of the subject shifted by half the field of view [10]. To correct for Nyquist ghosting, a reference scan can be acquired during the scanning session. Based on this reference scan, which contains several readouts through the center of the k-space, the difference between positive and negative readouts can be determined. For longer scans, multiple reference images need to be acquired throughout the scan. It is also possible to correct for Nyquist ghosting during preprocessing. First, separate images are generated from the odd and even echoes. Then, the phase maps of these images can be used to compute a phase correction and one corrected image can be reconstructed [16]. In Figure 3.15, a DWI with Nyquist ghosting (left) and after correction (right) is visualized.

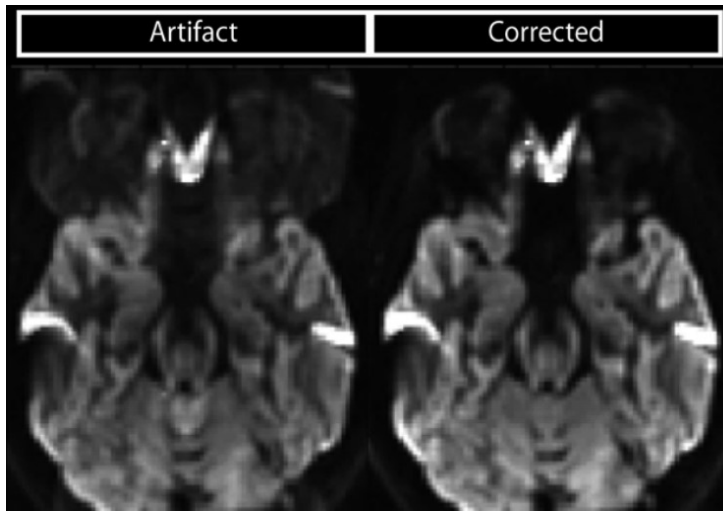


**Figure 3.15:** A DWI with Nyquist ghosting (left) and after correction (right). Nyquist ghosting can be seen as a copy of the subject shifted by half of the field of view [10].

**Gibbs ringing correction** A common artifact in MRI is Gibbs ringing. High frequencies are needed to visualize the transition between tissues with a very different intensity, such as CSF and white matter. However, during the acquisition of the k-space, very high frequencies that exceed the acquisition window are assumed to be zero. This causes a ringing artifact in the image. Gibbs ringing artifacts are most pronounced in non-DWIs, since they have the largest intensity differences. In Figure 3.16, a ringing artifact can be seen at the transition between CSF and white matter on a b-zero image (a) and a DEC map (b).

Gibbs ringing artifacts can be visualized by calculating voxels with physically implausible signals. In these voxels, signal intensity is higher in the DWIs than the non-DWI, which is not correct, because diffusion leads to signal decay. In Figure 3.16, these voxels are visualized overlaid on a map of fractional anisotropy (described below) (c).

One way to correct for Gibbs ringing artifacts is the total variation approach. In this approach, a term that preserves edge information but minimizes the contribution of transitions with large intensity differences, is used to correct the images [10].

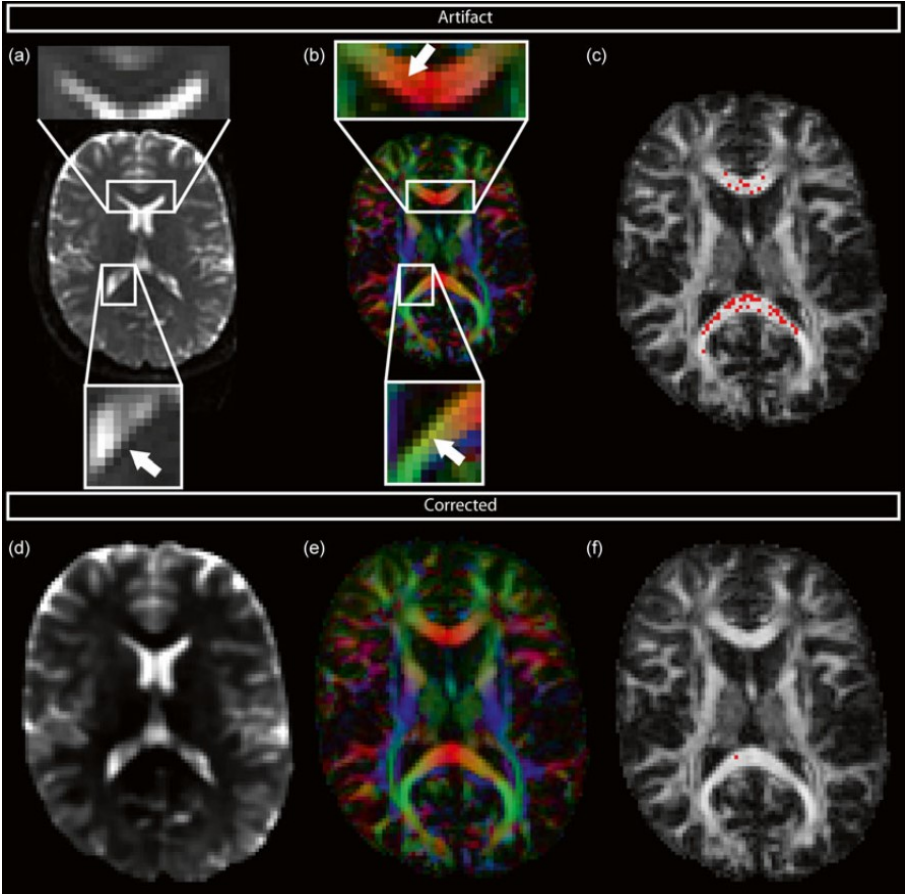


**Figure 3.16:** Gibbs ringing artifact. A ringing artifact can be seen at the transition between CSF and white matter on a b-zero image (a) and a DEC map (b). In (c), voxels with physically implausible signals (red) are overlaid on a map of fractional anisotropy. In (d-f), the same images are shown, but after Gibbs ringing correction [10].

An alternative approach is based on local subvoxel-shifts. The idea behind this approach is that the k-space can be seen as a convolution of the image and a sinc-function. If the image is reconstructed on a discrete grid, the severity of the ringing artifacts in the image depends on the location of a transition between tissues with a high intensity difference (edge) with respect to the sampling of the sinc-function. The ringing artifacts will be more severe if the side lobes of the sinc-function are sampled

at their extrema (Figure 3.17a) and disappear when the side lobes are sampled at the zero crossings (Figure 3.17b). To minimize the ringing artifacts, the images can be re-interpolated based on local, subvoxel-shifts so that the ringing pattern is sampled at the zero-crossings of the sinc-function [17].

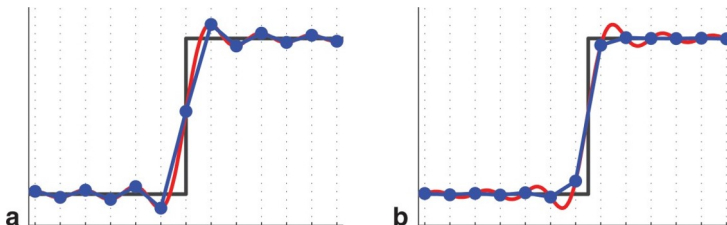


**Figure 3.17:** An image with a transition between tissues with a high intensity difference (black edge) is reconstructed from the k-space. The image is reconstructed on a discrete grid (blue). Ringing artifacts are more severe if the side lobes of the sinc-function are sampled at their extrema (a) and are minimal when the side lobes are sampled at the zero crossings (b) [17].

**Denosing** DWIs typically have a low signal-to-noise (SNR) ratio because the diffusion-weighting causes signal-attenuation and the long echo time causes T2 relaxation. The images are often affected by thermal noise that interferes with a visual inspection of the image and with quantitative interpretation of diffusion processes. Therefore, a common preprocessing step is denoising, i.e., minimizing the variance of the DWI signals. One way to do this is to use weighted averages of voxels based on metric similarity, however, this can lead to a lower spatial resolution and an increase in partial volume effects. Another approach is total variation minimization, which can remove local noise variation while the edges in the images are preserved. However, this technique is not ideal, since it depends on a regularization term, reconstruction artifacts can be introduced, only thermal noise is removed, and fine anatomical details may be lost. Alternatively, principal component analysis can be used to remove noise. The idea behind this is that only a few components will contain signal-related variance, while noise will be present in all components, so only those components which contribute most to the total variance are

used for further analysis. The number of relevant components depends on several factors including resolution, b-value and SNR, so it is difficult to determine objectively how many components should be selected. Veraart et al. [18] describe a method to objectify this selection based on random matrix theory.

### Diffusion tensor imaging

The most commonly used model for the analysis of DWIs is diffusion tensor imaging (DTI). In this model, the ADC values in function of the gradient direction are represented as a tensor  $\mathbf{D}$ . This tensor is a symmetric 3 X 3 matrix with 6 free parameters:

$$\mathbf{D} = \begin{bmatrix} D_{xx} & D_{xy} & D_{xz} \\ D_{xy} & D_{yy} & D_{yz} \\ D_{xz} & D_{yz} & D_{zz} \end{bmatrix} \quad (3.3)$$

The tensor can be evaluated for a gradient direction, represented by a three-element unit column vector  $\mathbf{g}$  (Equation 3.4), using the expression in Equation 3.5, with  $\mathbf{g}^T$  the transpose of  $\mathbf{g}$ .

$$\mathbf{g} = \begin{bmatrix} g_x \\ g_y \\ g_z \end{bmatrix} \quad (3.4)$$

$$\mathbf{g}^T \mathbf{D} \mathbf{g} = g_x^2 D_{xx} + g_y^2 D_{yy} + g_z^2 D_{zz} + 2g_x g_y D_{xy} + 2g_x g_z D_{xz} + 2g_y g_z D_{yz} \quad (3.5)$$

This results in one scalar number, which is the value of the tensor model along the direction  $\mathbf{g}$ . The tensor, which represents the ADC values, can then be filled in in the Stejskal-Tanner equation (Equation 3.2):

$$\frac{S}{S_0} = e^{-b\mathbf{g}^T \mathbf{D} \mathbf{g}} \quad (3.6)$$

This is the basis of DTI and shows the relationship between the experimental parameter  $b$ , and  $\mathbf{g}$ , the measured signals  $S$  and  $S_0$ , and the diffusion tensor model  $\mathbf{D}$ . If a DWI image is acquired, all parameters in Equation 3.6 can be filled in, except for the diffusion tensor model  $\mathbf{D}$ . To

obtain the six parameters of  $\mathbf{D}$ , at least six equations are necessary, so at least six DWIs with different gradient directions and a b-zero image need to be acquired. If more than 6 DWIs are acquired, the equation system is overdetermined, so it is no longer possible to obtain a single solution, but it can help to reduce noise [10].

The parameters of  $\mathbf{D}$  can be split up in three diagonal parameters ( $D_{xx}$ ,  $D_{yy}$  and  $D_{zz}$ ) and three off-diagonal parameters ( $D_{xy}$ ,  $D_{xz}$  and  $D_{yz}$ ). The diagonal parameters correspond with the ADC values along the x-, y- and z-axis. The off-diagonal parameters are the covariance between the pairs of axes, because the diffusion tensor is a covariance matrix. These parameters do not have a direct practical meaning. If the off-diagonal parameters are zero, the tensor is aligned with the x-, y- and z-axis. In this case, the diagonal parameters describe the shape and size of the tensor in a meaningful way. If the tensor is not aligned with these predefined axes, a new set of axes can be determined using eigendecomposition. In eigendecomposition, the original tensor is rewritten as:

$$\mathbf{D} = \begin{bmatrix} \vdots & \vdots & \vdots \\ \epsilon_1 & \epsilon_2 & \epsilon_3 \\ \vdots & \vdots & \vdots \end{bmatrix} \cdot \begin{bmatrix} \lambda_1 & 0 & 0 \\ 0 & \lambda_2 & 0 \\ 0 & 0 & \lambda_3 \end{bmatrix} \cdot \begin{bmatrix} \dots & \epsilon_1 & \dots \\ \dots & \epsilon_2 & \dots \\ \dots & \epsilon_3 & \dots \end{bmatrix} \quad (3.7)$$

The diagonal elements  $\lambda_1$ ,  $\lambda_2$  and  $\lambda_3$  are called eigenvalues. Each of these corresponds with an eigenvector  $\epsilon_1$ ,  $\epsilon_2$  and  $\epsilon_3$ . The eigenvalues are the ADC values along the eigenvectors and describe the shape and size of the tensor. The eigenvector  $\epsilon_1$  corresponds with the largest eigenvector  $\lambda_1$  and is referred to as the principal eigenvector. This eigenvector indicates the local orientation of the axon bundle. The eigenvectors can be visualized in a DEC map (Figure 3.18). This map only provides information about the orientation of the eigenvectors, not about the magnitude, since all eigenvectors have unit length. The orientation is visualized using colors: red corresponds with the left-right direction, green with front to back and blue with bottom to top.

A more common and simple visualization that only shows the most important characteristics of the diffusion tensor is tensor glyphs. Glyphs

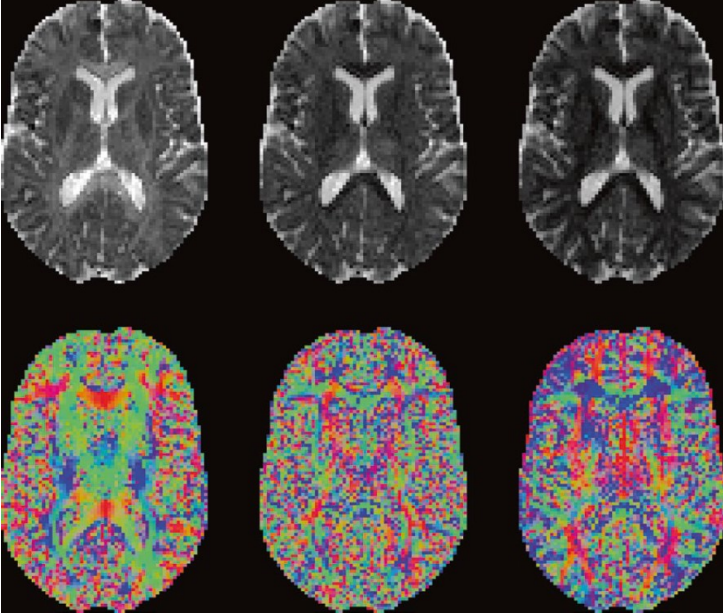


**Figure 3.18:** Top: Maps of the eigenvalues ( $\lambda_1, \lambda_2, \lambda_3$ ). Bottom: Directionally encoded color (DEC) maps of the eigenvectors ( $\epsilon_1, \epsilon_2, \epsilon_3$ ).

can be cuboids or ellipsoids, but ellipsoids are used most often. The dimensions of the ellipsoid are aligned with the eigenvectors and correspond to the eigenvalues. This type of visualization is more practical than the spherical polar plot because the ellipsoids are actually meaningful when they are scaled using the square roots of the eigenvalues (Figure 3.19). In this case, a water molecule that starts to diffuse from the center of the ellipsoid has an equal chance of arriving at any point on the surface of the ellipsoid after a fixed time period [10].

From the eigenvalues, several diffusion tensor measures can be derived. These measures provide information about the size or shape of the diffusion tensor, but are rotationally invariant, i.e., they do not depend on the orientation. The first measure is mean diffusivity (MD):

$$MD = \frac{\lambda_1 + \lambda_2 + \lambda_3}{3} = \frac{D_{xx} + D_{yy} + D_{zz}}{3} \quad (3.8)$$

MD is the average of the eigenvalues and is related to the size of the tensor. It represents the overall mean squared displacement of water

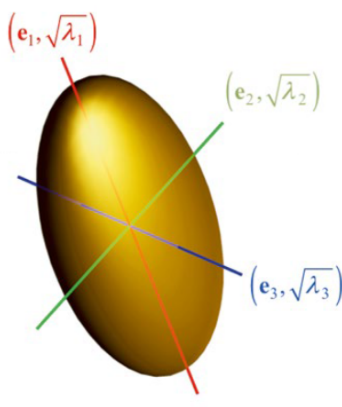


**Figure 3.19:** Visualization of the diffusion tensor as an ellipsoid, of which the dimensions are aligned with the eigenvectors and correspond with square roots of the eigenvalues.

molecules or the overall diffusivity in a voxel. MD is low in white and grey matter and high in the ventricles, where there is free diffusion. Related measures are axial diffusivity, which is equal to the first eigenvalue, and radial diffusivity, which is the average of the second and third eigenvalue. Axial diffusivity, also called longitudinal or parallel diffusivity, is the diffusivity along the principal eigenvector. Radial diffusivity, or transverse or perpendicular diffusivity, corresponds with the diffusivity perpendicular to the principal eigenvector. Axial diffusivity is sometimes associated with axonal damage and radial diffusivity with axonal density, myelin integrity, axonal diameter and fiber coherence, but diffusion directions can change in pathological tissue, so the biological interpretation of these measures should be done with caution [19].

Another measure is fractional anisotropy (FA):

$$FA = \sqrt{\frac{3}{2}} \cdot \frac{\sqrt{(\lambda_1 - \lambda)^2 + (\lambda_2 - \lambda)^2 + (\lambda_3 - \lambda)^2}}{\sqrt{\lambda_1^2 + \lambda_2^2 + \lambda_3^2}} \quad \text{with } \lambda = \frac{\lambda_1 + \lambda_2 + \lambda_3}{3} \quad (3.9)$$

This is the standard deviation of the eigenvalues divided by their root mean square and is related to the shape of the tensor. It quantifies the ratio between the anisotropic component of the diffusion tensor and the complete tensor. FA is a value between zero and one, with zero cor-

responding with completely isotropic diffusion and one with completely anisotropic diffusion. FA is highest in white matter [19]. The FA values can also be used as a weight for the DEC map (Figure 3.20). FA can be seen as a quantitative biomarker of white matter integrity. A reduction in FA is often associated with neurodegenerative processes, while FA seems to increase during development and improved performance. However, FA is influenced by several factors, such as the degree of myelination, axon packing, membrane permeability, internal axonal structure and tissue water content. Because of this, it is difficult to determine to which of these factors a change in FA can be attributed. Additionally, crossing fiber bundles can lead to a lower FA [10].

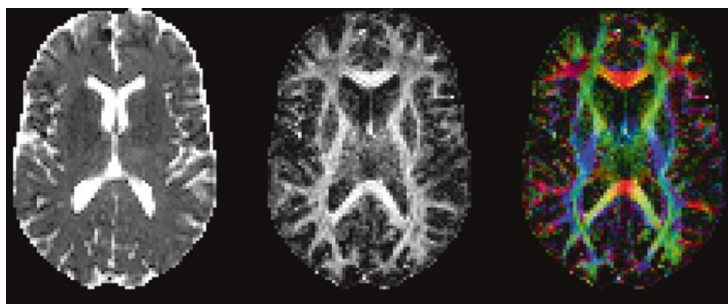


**Figure 3.20:** Maps of mean diffusivity (MD), fractional anisotropy (FA) and DEC FA.

The main advantage of DTI is that it reduces complex information into a few simple, sensitive and useful measures. However, this also leads to some limitations. First, there is the lack of specificity of the DTI measures. It is not possible to attribute changes in DTI measures to one biological or pathophysiological factor, which complicates the interpretation of these changes. In addition, the simplification of the DTI model requires several assumptions that are not met in reality. For example, the model assumes that the diffusion has a Gaussian distribution, which is not the case for intracellular water. A model that does take non-Gaussianity into account is diffusion kurtosis imaging (DKI), which will be described in the next paragraph. The DTI model also assumes that all voxels contain a single fiber direction, while in reality, many voxels contain crossing fibers. The crossing fiber problem and an analysis

method that can resolve it, will be described later. The presence of crossing fibers can affect the DTI measures, and fractional anisotropy in particular. Another factor which influences the DTI measures is the partial volume effect. This is the presence of different tissue organizations, such as CSF and white matter, in one voxel. In the DTI model, the contributions of the different tissue types are averaged out and result in a single dominant diffusion direction. Depending on the location of a voxel, it will be affected more or less by the partial volume effect. A voxel in the middle of a white matter bundle will be affected less than a voxel close to the ventricles. Partial volume contamination by CSF in particular, can greatly affect the DTI measures [10].

### **Diffusion kurtosis imaging**

In free diffusion, the displacement of water molecules follows a Gaussian distribution. Small displacements are more likely to occur than larger ones and on average, the total displacement is zero. In the brain, free diffusion only occurs in the CSF in the ventricles. In other brain tissues, diffusion is hindered or restricted. Hindered diffusion follows a Gaussian distribution as well, but restricted diffusion does not. In Figure 3.21, the squared displacement in function of the diffusion time is visualized. For both free and hindered diffusion, the squared displacement increases linearly with diffusion time. The slope is smaller for hindered diffusion, because the displacement is slowed down by obstacles. For restricted diffusion, the squared displacement reaches a maximum. This is the maximum displacement that is allowed within the boundaries. Most voxels contain tissue with both hindered and restricted diffusion, so the assumption of Gaussian diffusion does not hold. A more advanced model which takes the deviation from the Gaussian distribution, called excess kurtosis, into account, is diffusion kurtosis imaging (DKI). Describing kurtosis in addition to the diffusion coefficient leads to a better model of the diffusion process [20].

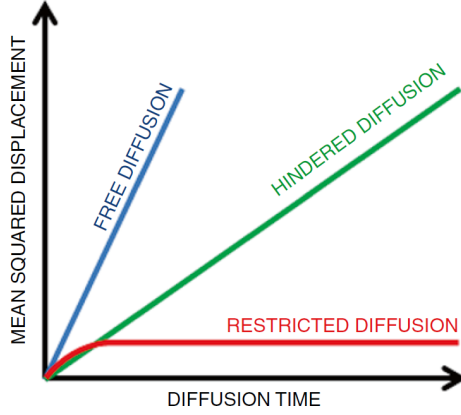


**Figure 3.21:** The squared displacement in function of diffusion time. For free and hindered diffusion, the squared displacement increases linearly with diffusion time. The slope is smaller for hindered diffusion, because the displacement is slowed down by obstacles. For restricted diffusion, the squared displacement reaches a maximum. This is the maximum displacement allowed within the boundaries [10].

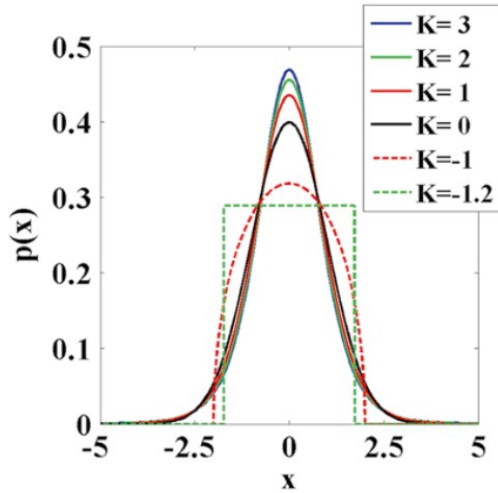


**Figure 3.22:** Distributions with a different kurtosis. If kurtosis is zero, the distribution is Gaussian. If kurtosis is positive, the distribution is more peaked and if kurtosis is negative, it is less peaked [10].

The dimensionless parameter kurtosis quantifies the deviation of a distribution from a Gaussian distribution. It indicates the peakedness or sharpness of the distribution. In Figure 3.22, several distributions with a different kurtosis are visualized. If kurtosis is zero, the distribution is Gaussian. If kurtosis is positive, the distribution is more peaked and if kurtosis is negative, it is less peaked. Because in DWI, voxels contain both hindered and restricted diffusion, kurtosis will only be positive. In the Stejskal-Tanner equation (Equation 3.2), kurtosis can be taken into account by adding an extra kurtosis term:

$$\frac{S}{S_0} = e^{-bD_{app} + \frac{1}{6}b^2D_{app}^2K_{app}} \quad (3.10)$$

The parameter  $K_{app}$  is the apparent kurtosis coefficient, the kurtosis equivalent of the apparent diffusion coefficient  $D_{app}$ . Like  $D_{app}$ ,  $K_{app}$  depends on the diffusion time and characterizes kurtosis in the direction of the magnetic field gradient. The kurtosis term depends on  $b$  squared, so the diffusion-weighted signal will decay non-mono-exponentially. Because diffusion in white matter is anisotropic, a single  $D_{app}$  and  $K_{app}$  value are not sufficient to accurately describe hindered diffusion. To take into account the directionality,  $D_{app}$  and  $K_{app}$  are replaced with a diffusion tensor  $\mathbf{D}$  and diffusion kurtosis tensor  $\mathbf{W}$ , respectively.  $\mathbf{W}$  is a symmetric fourth rank 3D tensor with 15 independent components.  $\mathbf{D}$  contains 6 independent parameters, so in total 21 independent parameters need to be calculated. Therefore, at least 21 DWIs in at least 15 different gradient directions and a  $b$ -zero image have to be acquired for DKI. In addition to this, at least three different  $b$ -values are needed, as well as typically higher values than used for DTI.

As described previously, using DTI, several diffusion measures can be calculated based on the eigenvalues and eigenvectors of the diffusion tensor, such as MD, AD, RD and FA. Using DKI, these measures can be quantified more objectively and more accurately because the influence of the  $b$ -value is reduced. In addition, several kurtosis measures can be calculated, such as axial, radial and mean kurtosis. Axial kurtosis is kurtosis evaluated along the principal diffusion direction, radial kurtosis is the mean kurtosis in the plane perpendicular to the principal diffusion

direction, and mean kurtosis is the average apparent diffusion kurtosis coefficient. Kurtosis measures seem more sensitive to properties of tissue microstructure and less sensitive to confounders. Therefore, they are thought to be a more robust biomarker [20].

A limitation of DKI is the risk of over-interpretation. DKI is a mathematical model and does not include biophysical modeling. The only thing that can be concluded from changes in DTI or DKI measures is that there is a change in the tissue microstructure that affects diffusion of water molecules. A way to obtain more information about the biophysical meaning of the DKI metrics is to use a two-compartment model. In this type of model, a distinction is made between two non-exchanging compartments in white matter: the intra-axonal space and extra-axonal space [10]. Several of these models have been described, but here, only the white matter tract integrity (WMTI) model developed by Fieremans et al. [21] will be discussed in more detail. In the WMTI model, it is assumed that white matter contains two non-exchanging compartments: the intra-axonal space (IAS) and the extra-axonal space (EAS). The IAS consists of myelinated axons that are modeled as long impermeable cylinders. Unmyelinated axons, dendrites and glial processes can contribute slightly to IAS as well. The protons in myelin are invisible on DWI because of their short T2 relaxation times. The EAS is modeled as an effective medium. Glial cells in the EAS are highly permeable, so they do not restrict diffusion. The diffusion in IAS and EAS is assumed to be Gaussian, and can be modeled by the compartmental diffusion tensors  $D_a$  and  $D_e$  respectively. This leads to the following equation to describe the DWI signal intensity:

$$\frac{S}{S_0} = f e^{-bn^T D_a n} + (1 - f) e^{-bn^T D_e n} \quad (3.11)$$

In this formula,  $f$  is the axonal water fraction (AWF), which is the ratio of intra-axonal water visible on DWI to the total amount of visible water signal. It gives an indication of the IAS water volume compared to the EAS water volume. Myelin water is neglected since it is invisible on DWIs. Other measures can be calculated as well. The IAS diffusivity is the trace of the intra-axonal diffusion tensor. Axial EAS diffusivity is the

principal eigenvalue of the EAS diffusion tensor. It is typically higher in the EAS than in the IAS, because cytoplasm and organelles slow down diffusion in the IAS. Radial EAS diffusivity is the average of the second and third eigenvalue of the EAS diffusion tensor. It is usually a lot smaller than axial EAS diffusivity, since diffusion perpendicular to the direction of the axons is much more restricted. The tortuosity of the EAS is the ratio of axial EAS diffusivity and radial EAS diffusivity, and gives an indication of the myelinated axonal fraction. IAS diffusivity and axial EAS diffusivity correspond with the intrinsic intra- and extra-axonal diffusion coefficient of water in white matter. These microstructural parameters can provide more insight into the meaning of changes in DKI metrics [21].

### **Constrained spherical deconvolution**

An important limitation of DTI is that it does not take into account crossing fibers, i.e., when different fiber populations are present in one voxel. The crossing fiber problem involves any combination of white matter fibers in a voxel that is more complicated than one straight fiber population, such as fanning, bending, diverging and crossing fibers. Since clinical scanners have a spatial resolution of about 2 to 3 mm, and white matter bundles are much smaller, crossing fibers occur in more than 90% of voxels in white matter. Crossing fibers have a big influence on the DTI measures, and especially on FA. Fractional anisotropy is reduced in voxels with crossing fibers, since the diffusion profiles of the different fiber populations are averaged out, so there is no longer a dominant diffusion direction. In the presence of crossing fibers, mean diffusivity is typically reduced as well. When radial diffusivity increases in one of the fiber populations, axial diffusivity of the other fiber population in the same voxel increases as well. When AD is reduced in one of the fiber populations, the RD of the other fiber population in the same voxel decreases as well. The influence of crossing fibers on DTI metrics becomes especially important for DTI-based tractography. If fiber orientations are estimated incorrectly, this will cause the tractography algorithm to deviate from the actual white matter tracts. Because FA is affected by

the crossing fiber problem, it is not an ideal biomarker for white matter integrity. For example, if one of the fiber populations in a voxel is affected in a neurodegenerative disease, the other fiber population could become more dominant, which could lead to an increase in FA, when neurodegeneration is expected to cause a decrease in FA [10].

To solve the crossing fiber problem, more advanced models are needed. Most of these models are based on high angular resolution diffusion-weighted imaging (HARDI). In this technique, DWIs are acquired in many directions with the same b-value to obtain a dense sampling on the sphere. This is a very efficient way to acquire data for fiber orientation estimation and tractography. HARDI acquisitions are the same as DTI acquisitions, but more gradient directions are used and the b-value can be larger as well.

The idea behind HARDI is that if a voxel contains crossing fibers, the DWI signal in this voxel will approximately be the sum of the DWI signals of each separate fiber bundle in the voxel (Figure 3.23). To resolve the crossing fiber problem, the contributions of the individual fiber bundles need to be separated. To do this, the problem can be described as a set of equations with a number of DWI acquisitions and a number of model parameters that have to be estimated. These parameters can be the orientations and volume fractions of fiber populations or the coefficients of a continuous characterization of diffusion or fiber organization, depending on the model [10].

The simplest method to resolve the crossing fiber problem is the multi-tensor approach. In this approach, it is assumed that a voxel contains two fiber populations and each of them is modeled using a separate diffusion tensor. Then, the volume fraction of each population, i.e., the relative amount of each population in the voxel, and its orientation need to be estimated (Figure 3.23). The disadvantage of this approach is that the problem is nonlinear, so it is computationally intensive. It is also ill-conditioned, because it is difficult to differentiate between changes in anisotropy and volume fraction [10].

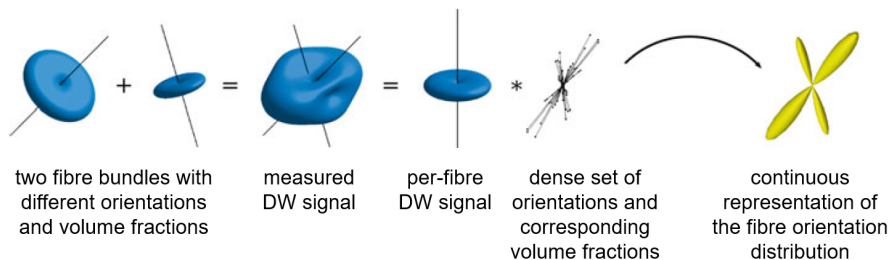


**Figure 3.23:** The idea behind HARDI is that if a voxel contains crossing fibers, the DWI signal in this voxel will approximately be the sum of the DWI signals of each separate fiber bundle in the voxel. In the multi-tensor approach (left), it is assumed that a voxel contains two fiber populations and each of them is modeled using an separate diffusion tensor. Then, the volume fraction and orientation of each fiber population need to be estimated. In spherical deconvolution, the measured DWI signal is a spherical convolution of the DWI signal per fiber and a dense set of orientations and the corresponding volume fraction, which corresponds with the FOD (right) [10].

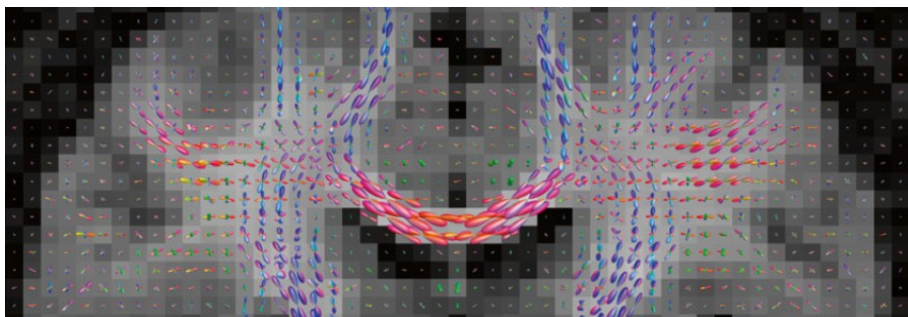


**Figure 3.24:** Example of fiber orientation distributions estimated using constrained spherical deconvolution, overlaid on a mean DWI image [10].

An extension of the multi-tensor model is spherical deconvolution. In this approach, a continuous representation of the fiber orientation information is used instead of a discrete number of fiber populations. Instead of trying to estimate the volume fraction and orientation of the fiber populations, many fiber populations with a fixed orientation are modeled.

Then, only their volume fractions need to be estimated. These volume fractions can be visualized as a distribution over the sphere, which is called the fiber orientation density function (fODF) or fiber orientation distribution (FOD). The measured DWI signal is then assumed to be a spherical convolution of the single-fiber response function, which models the DWI signal expected for a voxel containing a single coherently oriented bundle of axons, with the FOD. This is represented in Figure 3.23. The measured DWI signal is a spherical convolution of the DWI signal per fiber and a dense set of orientations and the corresponding volume fraction, which corresponds with the FOD. To estimate the FOD, a spherical deconvolution of the response function from the measured DWI signal needs to be performed [22]. The FOD corresponds with the amount of fibers aligned with each orientation on the sphere, and can be visualized as an orientation plot, as seen in Figure 3.24. Peaks in the FOD indicate specific fiber orientations [23].

The advantages of this method include that the relationship between the DWI signal and the FOD is linear, so it is possible to use more efficient reconstruction algorithms using linear algebra. Furthermore, it is not necessary to predefine a number of fiber orientations. The FOD is continuous and fiber orientations can be detected as peaks in the FOD. Finally, it is possible to model other types of complex fiber organizations using FOD, such as bending or fanning fibers. Based on FOD, a more accurate tractography is possible. Often, a non-negativity constraint is imposed on the FOD, since it is not physically possible to have negative volume fractions. This leads to a more stable estimation, which is more robust to noise. This method is called constrained spherical deconvolution. In (constrained) spherical deconvolution, it is assumed that the intrinsic anisotropy is the same in all fiber bundles. In other words, the response function, which models the DWI signal expected for a voxel containing a single coherently oriented bundle of axons, is the same for all fiber populations. While this seems like a huge oversimplification, it actually holds in most cases. The idea behind the constant anisotropy assumption is that anisotropy differences in the brain are only caused by crossing fibers or other partial volume effects. This corresponds with DTI literature,

where it was found that pathological changes in anisotropy were usually not large enough to affect the results and, if they were, they would mainly affect estimated volume fractions rather than fiber orientations. A limitation of this assumption is that it is not possible to obtain information about white matter integrity. However, the estimated volume fractions can be seen as measures of fiber density, which is a clinically relevant parameter [10]. Apparent fiber density is related to the intra-axonal water volume fraction. It can be calculated for each fiber population in a voxel separately, so it is more biologically interpretable and specific than DTI measures in voxels with crossing fibers [22].

A limitation of CSD is that it was designed for single-shell DWI data, i.e., data acquired with one non-zero b-value. If multi-shell data, i.e., data acquired with multiple different non-zero b-values, were acquired, usually only the shell with the highest b-value was used for CSD. The other shells, which might provide useful information as well, were discarded. In addition, while FOD can be estimated very well using CSD in white matter voxels, the FOD estimation in voxels containing grey matter or cerebrospinal fluid is less accurate or even unreliable, because the response functions in these tissues are different than in white matter. To resolve these limitations, Jeurissen et al. [22] developed the multi-shell multi-tissue CSD (MSMT-CSD) method. This method uses the unique b-value dependencies of white matter, grey matter and CSF to determine the contributions of each tissue type. For each tissue type and each b-value, a separate response function is estimated (Figure 3.25). These response functions are then used to estimate FODs in the different tissue types [22].

An advantage of the MSMT-CSD method compared to the single-shell CSD method is that the FODs are estimated with a lot more precision, and spurious peaks are suppressed. In addition, the FOD amplitudes are scaled to the white matter volume fractions, which leads to more accurate amplitudes and fiber orientations. This substantially improves fiber tracking. Tractograms are less noisy at transitions between white matter and CSF and white and grey matter. Because the FOD amplitudes correspond with the white matter volume fractions, a more reliable stopping

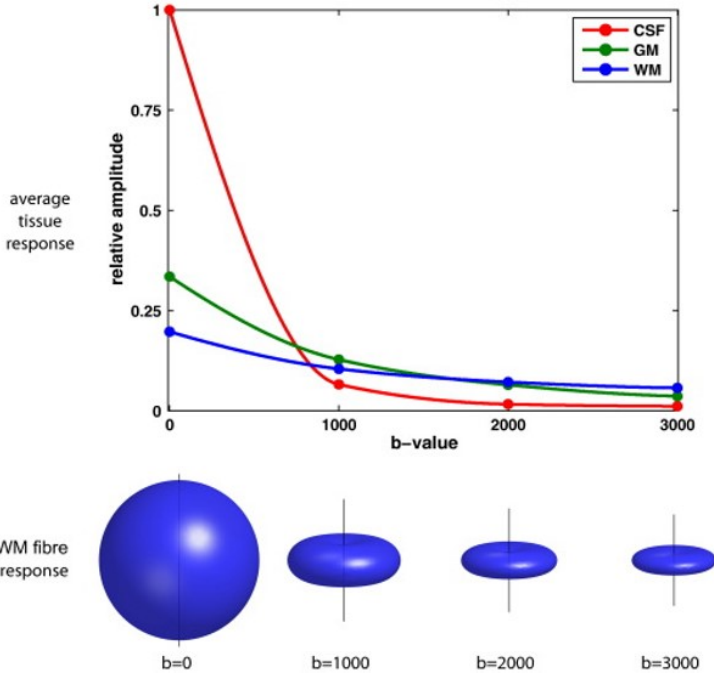


**Figure 3.25:** Estimation of response functions of white matter, grey matter and CSF for different b-values [22].

criterion can be used for fiber tracking. A lower FOD threshold can be used, so small white matter structures can be detected. An advantage of the distinction between the different tissue types is that the volume fractions of CSF, and grey matter might provide quantitative information as well. For example, the CSF volume fraction could be an indication of the volume of free water and might be used as a biomarker for edema. A limitation of the MSMT-CSD method is that the same response functions are used for all voxels of a specific tissue type, and the same FOD response is used for all fiber populations, while in reality, there could be a difference depending on cell sizes, densities, permeabilities and packing configurations. Because of this simplification, the reconstructions are better conditioned, so it is considered acceptable [22].

### Fixel-based analysis

In DWI, white matter is usually investigated on a voxel-level. However, since white matter voxels can contain crossing fibers, the information of the different fiber populations in a voxel is averaged and the voxel-level measures are not fiber-specific. To obtain information about the individual fiber populations in a voxel, more advanced diffusion models are necessary. A fiber population within a voxel is called a fixel. Using fixel-based analysis (FBA), fiber-specific characteristics can be detected, even in the presence of crossing fibers. In FBA, parameters are calculated that give an indication of the ability of local white matter to relay information. It is assumed that diffusion in axons only occurs along the direction of the axons and that there is almost no exchange of water between the intra- and extra-axonal space during a DWI scan. The volume of intra-axonal water depends on the number of axons and is related to the ability to relay information of the local white matter. Therefore, intra-axonal water is a biologically interesting quantitative parameter. The ability to relay information also depends on the axon diameter, but because of the small size of axons, it is not possible to estimate axon diameter in a fixel yet. The degree of myelination has an influence on the ability to relay information as well, and can be estimated using T1 relaxometry, but this requires a very long acquisition time that is not feasible in a clinical setting [24].

Several methods have been described to estimate measures of intra-axonal water and several names have been used to describe it, including population fraction of the restricted compartment, restricted fraction, axonal density, partial volume fraction, fiber density, apparent fiber density, neurite density, intra-axonal volume fraction, fiber volume fraction, and fascicle fraction of occupancy. In FBA, the measure related to intra-axonal water volume is referred to as fiber density (FD). Changes in intra-axonal volume in a fiber bundle can manifest in different ways (Figure 3.26). Intra-axonal water volume can be reduced in all voxels of the fiber bundle, as is the case for pathological axonal loss. This type of change causes a decrease in FD (Figure 3.26a). Intra-axonal volume can also be reduced if a fiber bundle consists of less voxels. This can happen

as a result of axon loss, after which the extra-axonal space is filled with extracellular matrix and cells associated with inflammation or gliosis. Eventually, the fiber bundle can become atrophic. A decrease in the number of voxels a fiber bundle consists of, is reflected as a decrease in fiber cross-section (FC) (Figure 3.26b). It is important to note that a decrease in intra-axonal water volume does not necessarily correspond with a decrease in the number of axons. Only a difference in volume perpendicular to the fiber orientation, i.e., a difference in fiber-bundle cross-section, is related to the number of axons and the ability to relay information. It is important to take into account fiber orientation in the calculation of parameters reflecting white matter morphology. Changes in white matter can also present as changes in both FD and FC. A parameter that combines the information of FD and FC would provide a more complete measure of the total intra-axonal water volume in a fiber bundle and its ability to relay information. For example, in a neurodegenerative disease, a decrease in FC could reflect accumulated axon loss, while a decrease in FD could provide information about the remaining white matter. A parameter that combines FD and FC is fiber-density-and-cross-section (FDC) (Figure 3.26c) [24].

One way to calculate fiber density is based on FOD images. At high b-values and long TE (as is the case in DWI acquisitions), the FOD amplitude is proportional to the intra-axonal volume of axons in a certain direction. The lobes of the FOD correspond with the fiber orientations in the voxel (Figure 3.27). For each of the lobes of fiber orientations, FD is calculated as the non-parametric numerical integration of that lobe. Fiber-bundle cross-section can be calculated based on the non-linear warp that matches a template to the subject space. Based on this transformation, information about local differences in volume can be obtained. Changes in volume perpendicular to the fixel orientation are related to differences in the number of axons. The relative measure FC is then calculated as the change in FC in a specific fixel orientation that is needed to spatially normalize the subject to the template. If the relative measure FC is higher than 1, the FC of the subject is larger than that of the template. If the relative measure FC is lower than 1,

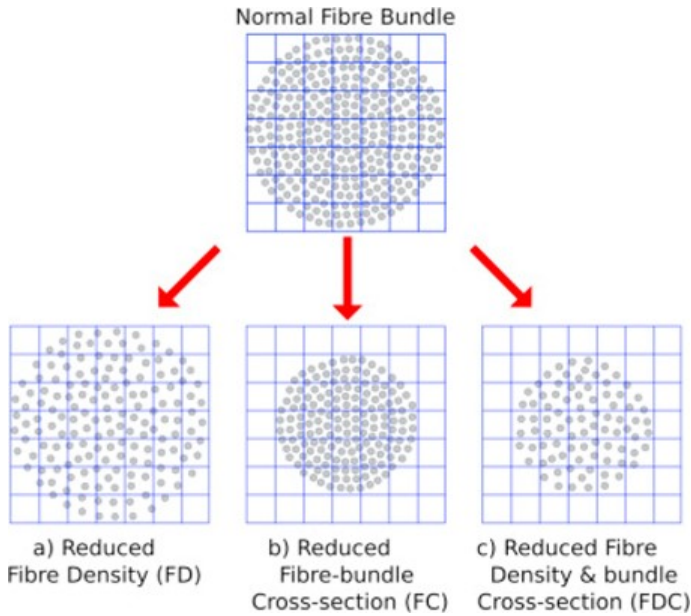


**Figure 3.26:** A schematic of a fiber bundle consisting of axons (grey) that spans several voxels (blue). A change in intra-axonal volume can be detected as a change in fiber density (FD), fiber-bundle cross-section (FC) or fiber-density-and-cross-section (FDC) [24].

FC is smaller in the subject compared to the template. Fiber-density-and-cross-section (FDC) is calculated as the fixel-wise multiplication of FD by FC. This parameter combines the information of the microscopic FD and macroscopic FC. It reflects the total intra-axonal volume in a fiber bundle during a transformation [24].

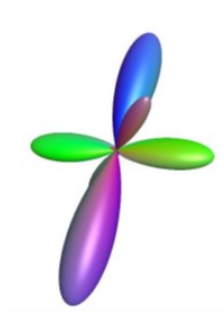


**Figure 3.27:** FOD with three lobes, corresponding with the three fiber orientations/populations in the voxel.

Pathological changes in intra-axonal volume can manifest as changes in FD, FC or FDC. The way these changes manifest can also change over time. For example, a decrease in the number of axons can initially be observed as a decrease in FD, but at a later stage, when atrophy occurs, as a decrease in FC. In fiber bundles with a small cross-section compared to the voxel size, changes in FC can be detected as changes in FD. Since FD is the intra-axonal water per volume, it can be smaller in voxels or fixels at the border of a fiber bundle compared to voxels or fixels in the center of the bundle. In other words, voxels at the edge of a fiber bundle contain a larger fraction of extra-axonal water compared to voxels in the center of a bundle. If FC decreases in a fiber bundle, there will be more fixels at the border compared to the center of the bundle, so FD will decrease. This shows that while FD and FC can provide biologically interesting information about changes in white matter tracts, care has to be taken when interpreting them separately. It is important to investigate FDC as well, as its interpretation is more straightforward [24].

### **Tractography**

Tractography or fiber tracking can be used to estimate and visualize white matter bundles in the brain. The estimated bundles or tracts are not a direct representation of individual axons, but are a result of combining diffusion orientation information in neighboring voxels. White matter tracts reconstructed through the use of tractography, typically correspond well with histological findings. However, false positive or false negative tracts can occur, so it is important to have prior anatomical knowledge [10].

In deterministic tractography, the orientation and shape of the diffusion profiles are used to estimate fiber tracts. First, a starting point or seed voxel is selected. In this voxel, a tract is produced in both diffusion orientation directions. From this point on, the direction of the tract is updated continuously depending on the diffusion orientation direction in the following voxels. This way, part of a white matter bundle can be obtained (Figure 3.28). To reconstruct an entire white matter bundle,

streamlines need to be generated from several seed points on the intersection of the bundle. The complete bundle is then represented by the combination of streamlines. To make sure the reconstructed tracts are anatomically plausible, several criteria can be defined. To prevent sharp bending of a tract, a curvature threshold can be set, usually between 30 and 70°. A threshold on fractional anisotropy can be used to restrict the tract to white matter. This threshold is typically set at  $FA > 0.2$ . The thresholds are usually determined empirically to minimize the amount of false positive and false negative streamlines. Other criteria can be minimal and maximal tract length, and seed point density, depending on the algorithm that is used. An alternative approach to seed-based tractography is whole-brain tractography. In this approach, streamlines are generated in all voxels that meet certain criteria (Figure 3.29). A specific white matter bundle can then be selected using (a) region(s) of interest through which it traverses. To this end, it is important to have prior anatomical knowledge about the trajectory of the bundle. Regions of interest can be selected based on anatomical scans or FA maps color-coded for orientation. The advantage of whole-brain tractography is that it is symmetric, which leads to a more robust tracking [25].

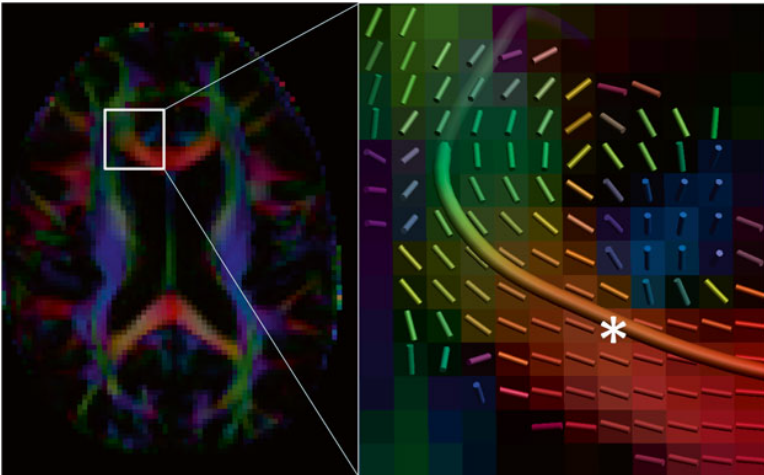


**Figure 3.28:** One streamline in corpus callosum generated starting from a seed voxel, indicated by an asterisk [10].

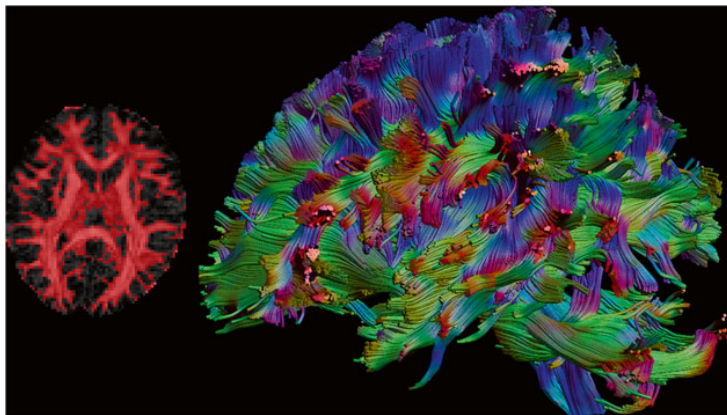


**Figure 3.29:** Whole-brain tractography generated from voxels with  $FA > 0.2$  (red on left image) [10].

While deterministic tractography uses the principal diffusion orientation to estimate the trajectory of white matter bundles, probabilistic tractography is based on the principle that the diffusion orientation cannot be estimated 100% accurately and that there is always some uncertainty. For example, if the noise level is higher, because there are fewer gradient directions or the diffusion anisotropy is lower, the amount of uncertainty will increase. With each step in a deterministic tracking algorithm, the uncertainties accumulate, and the estimated tracts deviate further from the actual white matter bundles. In probabilistic tractography, the amount of uncertainty in the estimation of the diffusion orientation is used to track white matter tracts more accurately. In each voxel, the orientation distribution is estimated. The width of this distribution corresponds with the amount of uncertainty. From the seed voxels, tens of thousands of streamlines are generated, each following a different trajectory depending on the orientation distributions. Then, a tract probability map can be calculated based on how many streamlines overlap with each voxel. If the uncertainty is low, the streamlines will have a similar trajectory. If the uncertainty is higher, the streamlines will be more spread out and the estimated tract will be more diffuse. Unlike deterministic tractography, probabilistic tractography can be used to map connections from gray matter regions, where the uncertainty in the principal diffusion orientation is higher. Because of the more complex

tracking algorithm, probabilistic tractography is computationally more challenging than deterministic tractography [26].

The principal diffusion orientation is often estimated using DTI, assuming each voxel contains only one fiber population. Even though most white matter voxels contain crossing fibers, DTI tractography can be used to reconstruct the main white matter bundles in the brain. However, for most clinical applications, this is not sufficient and more advanced models are required, such as constrained spherical deconvolution [10].

To obtain reliable tractography, the quality of the data needs to be high enough. First, it is important to have a good spatial resolution. A low resolution will lead to a coarse sampling of the white matter bundle, and partial volume effects. In voxels that contain crossing fibers, the principal diffusion orientation cannot be estimated correctly using DTI, which leads to problems with tractography. If the resolution is low, the curvature threshold needs to be lower as well because bends are sharper when more coarsely sampled. This leads to an increase in the number of false positive and false negative streamlines. Second, the sensitivity of orientation encoding, quantified by the b-value, should be high enough. Typically, b-values of at least  $1000 \text{ s/mm}^2$  should be used. To identify different diffusion orientations in one voxel in the case of crossing fibers, even higher b-values are necessary and a more advanced diffusion model such as CSD should be used. Furthermore, it is necessary to acquire DWIs in sufficient gradient directions to estimate the diffusion profile more accurately. At least 30 gradient directions should be used, but 60 to 80 directions are advised. The gradient directions should also be distributed optimally over the unit sphere. Finally, it is important to have a high signal-to-noise ratio. This can be obtained by increasing the number of signal averages, however, this also increases the scanning time. Using a higher field strength leads to a higher measured signal as well [10].

### Structural connectivity

Based on tractography, more information can be obtained about structural connectivity in the brain. However, it is difficult to compare measures of structural connectivity between individuals or over time.

From a neurobiological point of view, the strength of a structural connection between two brain regions depends on the number of axons that are present between them. The structure of the myelin sheath and cell membranes can influence structural connectivity as well. Structural connectivity based on tractography is related to the probability of reconstructing a tract based on diffusion. Based on deterministic tractography it is only possible to know whether a connection exists or not, but not how strong the connection is. In addition, anatomically implausible connections can be generated. Non-existing connections can also be found using probabilistic tractography. Therefore, it is not meaningful to derive measures of structural connectivity from tractography without taking into account anatomical information. While the number of streamlines between two brain regions, or the fiber count, seems to be related to the number of axons, in reality it is not, since tractography is performed on a different measurement scale. Furthermore, the fiber count can be affected by several factors, such as the length of the tract, fractional anisotropy, data quality and brain atrophy. The tract probability map generated in probabilistic tractography is not a good measure of structural connectivity either, as it does not represent the probability that a connection exists, but the variation in the results. Additionally, the variation is lower, close to the seed voxels, which introduces a bias [10].

A better approach to assess structural connectivity based on tractography is to use global tractography, not to be confused with whole-brain tractography. In global tractography, the entire tractogram is reconstructed simultaneously by determining the optimal trajectories through the diffusion field, that correspond best with the underlying data. During this process, neighboring tracts can affect each other. Because global tractography is less sensitive to local perturbations in the diffusion sig-

nal and to the build-up of errors during fiber tracking, it can be used to investigate structural connectivity. However, this approach is computationally challenging [27].

An alternative approach is spherical-deconvolution informed filtering of tractograms (SIFT), which includes anatomical information in the calculation of the tractogram. In this approach, the streamlines generated during tractography are mapped to the diffusion data and adapted, so that the number of streamlines between two brain regions corresponds with the estimated cross-section of the white matter tract that connects the regions. In this case, the number of streamlines is a meaningful measure of structural connectivity [28].

### Graph theory

Complex systems can be characterized using a mathematical representation, called a graph. A graph consists of a number of individual components, or nodes, and relations of connections between the components, called edges (Figure 3.30). Edges can be directed, when they represent a causal relationship between nodes, or undirected, when the relationship is symmetrical. They can also be weighted or unweighted. Weighted edges reflect stronger and weaker connections, while in an unweighted or binary graph, the connection strength between the nodes is assumed to be equal [29]. The number of edges connected to a node is called the degree. The nearest neighbors of a node are the nodes that are directly connected to it. Two important metrics that can be used to characterize the topology of a graph are the minimum path length and the clustering coefficient. The path length between two nodes is the minimum number of edges needed to form a direct connection between the nodes, and the clustering coefficient represents the number of connections between the neighbors of a node [29]. A random graph is a graph in which the edges are chosen randomly. In this type of graph, both the minimum path length and average clustering coefficient are small. A regular graph, on the other hand, is a graph in which each node is only connected to its four nearest neighbors. This graph has a highly clustered structure, so a high clustering coefficient, but no long-range connections, so a high

minimum path length. By randomly rewiring some of the edges in a regular graph to form long-range connections, it is possible to greatly reduce the path length. This type of graph, with a high clustering coefficient and short path length, is called a small-world graph or network (Figure 3.31). Small-world networks can be used to describe a myriad of complex systems, ranging from the Internet to biochemical systems [29]. For this dissertation, the ability of small-world networks to characterize brain network connectivity, is of special interest. Processes in the brain, such as sensorimotor or cognitive processing, take place locally in separate, specialized regions, but also in large-scale distributed systems. The high clustering coefficient of a small-world network corresponds with the specialized information processing, while the short path length is in line with the integrated or distributed information processing. Additionally, it is important for optimal functioning of the brain to maximize the efficiency and minimize the cost of information processing. This can also be modelled using a small-world network [29].

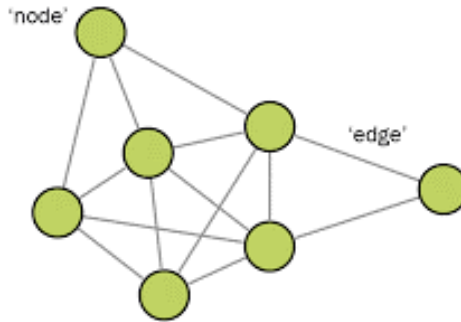


**Figure 3.30:** A graph consisting of nodes (yellow spheres) and edges (grey lines).

Graph theory can be used to investigate brain connectivity on a whole-brain level. In graph theory, the brain is viewed as a graph with a combination of nodes, i.e., brain regions, and edges, i.e., interactions between the nodes. The nodes in the graph can be defined using brain mapping, parcellated atlases and/or connectivity measures. It is important that the choice of nodes is biologically meaningful. Heterogeneously connected brain regions should not be combined into a single node, the

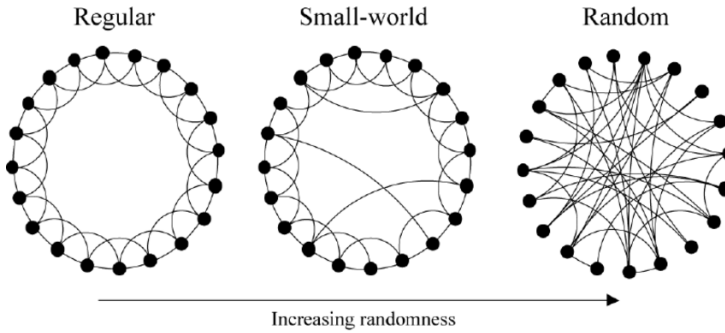


**Figure 3.31:** Different network topologies: a regular network with high clustering and long path length, a small-world network with high clustering and short path length, and a random network with low clustering and short path length [29].

complete surface of the cortex needs to be included in the parcellation, and nodes should not overlap. The edges can be anatomical, functional or effective connections between nodes: anatomical connections are usually white matter tracts between regions of interest. Functional connections are temporal correlations between brain activity in (un)connected brain regions. Effective connections reflect the causal influence of one brain region over another [30].

Structural connectivity is usually assessed based on whole-brain streamline tractography. Different measures of structural connectivity can be used, such as the number, length, volume or probability of the streamlines between two brain regions, or a diffusion measure calculated along the streamlines between two brain regions, derived from DTI or more advanced diffusion models. The structural connectome is more relevant if the measures used to assess structural connectivity are biologically meaningful. Therefore, anatomically-constrained tracking algorithms can be used, which take anatomy into account when selecting streamlines. Methods that filter the tractogram, such as SIFT, are especially useful, since the resulting number of streamlines is related to quantitative measures that are biologically meaningful, such as apparent fiber density. In this case, the number of streamlines between two brain regions can be used as a biologically meaningful measure of struc-

tural connectivity. The whole-brain connectivity can be summarized in a connectivity matrix, in which the rows and columns correspond with the regions of interest, or nodes, and the elements with the measure of structural connectivity, or edges (Figure 3.32) [31].

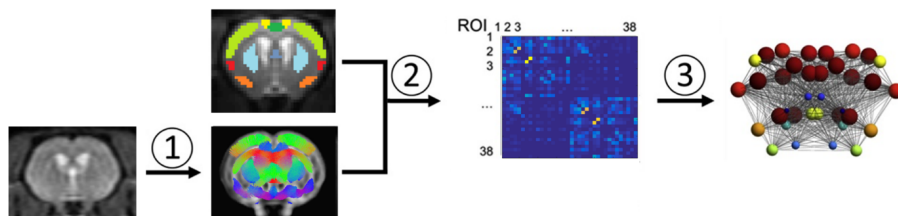


**Figure 3.32:** Construction of a structural network and graph. 1) Whole-brain streamline tractography is performed. 2) The number of streamlines in the (filtered) tractogram between predefined regions of interest (ROIs) is calculated and a connectivity matrix is obtained. 3) The connectivity matrix can be visualized as a graph in which the nodes represent the ROIs and the edges the measure of connectivity, e.g. the number of streamlines, between them.

Edges can be binary or weighted. Binary edges only indicate whether a connection is present in the graph or not, while weighted edges also take into account the strength of the connection. Binary graphs are easier to characterize and to compare between groups, but, using weighted graphs, different aspects of the brain network can be characterized and the weakest connections can be removed from the network. Finally, edges can be directed, when the directionality of the connection is known, or undirected [30]. Structural connections assessed using dMRI are always undirected [31].

Graphs can be characterized using network measures of global or local connectivity. These measures give an indication of integration and segregation, or of the importance of a brain region in the network.

Integration indicates how fast the brain can combine information from spatially dispersed regions. This is usually determined based on paths,

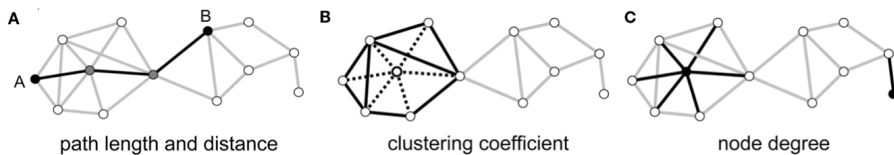


**Figure 3.33:** Common network measures: A) path length, a measure of integration, B) clustering coefficient, a measure of segregation, and C) degree, a measure of centrality (Adapted from [32]).

which are sequences of edges that reflect routes of information flow between brain regions (Figure 3.33A). Characteristic path length is the average shortest path length between two nodes in the network. In weighted graphs, the length of an edge is the inverse of its weight. A similar measure is global efficiency: the average inverse shortest path length. The advantage of using global efficiency is that the efficiency between unconnected brain regions is zero, a meaningful value, while the path length between unconnected regions is infinite [30].

Segregation reflects the ability for specialized processing in closely interconnected groups of brain regions, called clusters or modules. The amount of such clusters in the brain is an indication of the amount of segregated neural processing. A measure of segregation is the clustering coefficient (Figure 3.33B). This is the proportion of neighbors of a node, i.e., nodes connected to that node, that are also connected to one another. This gives an indication of the amount of clustered connectivity around the nodes. Another measure of segregation is local efficiency. Local efficiency is similar to global efficiency, but calculated within the neighborhood of a node, i.e., the nodes connected to that node. A more sophisticated measure of segregation is modularity. This measure indicates not only the presence of clusters, but also their size and composition. To calculate modularity, the network is divided into nonoverlapping groups of nodes based on a maximum number of within-group connections and a minimum number of between-group connections. Modularity is the degree to which the network can be divided in such groups. Brain networks have a small-world organization, meaning there is a balance between integration and segregation. Small-world networks are typically

highly integrated and segregated, and the ratio between segregation and integration is called small-worldness [30].

**Table 3.1:** Formulas to calculate network measures [30].

Calculation of network measures		
<hr/>		
Integration		
<hr/>		
Distance: shortest path between nodes i and j	$d_{ij} = \sum_{a_{uv} \in g_{i \leftrightarrow j}} f(w_{uv})$	f: map from weight to length (e.g. inverse)
Characteristic path length	$Lp = \frac{1}{n} \sum_{i \in N} \frac{\sum_{j \in N, j \neq i} d_{ij}}{n-1}$	
Global efficiency	$Eg = \frac{1}{n} \sum_{i \in N} \frac{\sum_{j \in N, j \neq i} (d_{ij})^{-1}}{n-1}$	
<hr/>		
Segregation		
<hr/>		
Number of triangles around node i	$t_i = \frac{1}{2} \sum_{j, h \in N} (w_{ij} w_{ih} w_{jh})^{1/3}$	
Clustering coefficient	$Cp = \frac{1}{n} \sum_{i \in N} \frac{2t_i}{k_i(k_i-1)}$	
Local efficiency	$Eloc = \frac{1}{2} \sum_{i \in N} \frac{\sum_{j, h \in N, j \neq i} (w_{ij} w_{ih} [d_{jh}(N_i)]^{-1})^{1/3}}{k_i(k_i-1)}$	$d_{jh}(N_i)$ : length of the shortest path between j and h that contains only neighbors of i
Modularity	$Q = \frac{1}{l} \sum_{i, j \in N} [w_{ij} - \frac{k_i k_j}{l}] \delta_{m_i, m_j}$	$l = \sum_{i, j \in N} w_{ij}$ : sum of all weights, $\delta_{m_i, m_j} = 1$ if $m_i = m_j$ and 0 otherwise
Small-worldness	$S = \frac{Cp/Cp_{rand}}{Lp/Lp_{rand}}$	
<hr/>		
Centrality		
<hr/>		
Degree	$k_i = \sum_{j \in N} w_{ij}$	
Participation coefficient	$y_i = 1 - \sum_{m \in M} (\frac{k_i(m)}{k_i})^2$	$k_i(m)$ : number of links between i and all nodes in module m
Betweenness	$b_i = \frac{1}{(n-1)(n-2)} \sum_{h, j \in N, h \neq j, h \neq i, j \neq i} \frac{\rho_{hj}(i)}{\rho_{hj}}$	$\rho_{hj}$ : the number of shortest paths between h and j

Regions that play an important role in the network are called hubs. These regions interact with a lot of other regions, which promotes integration. Measures of centrality reflect whether or not a node is a hub. The most common measure of centrality is degree (Figure 3.33C). The degree of a node is the number of edges connected to that node. A high degree indicates that a node has connections with a lot of other nodes. The participation coefficient reflects the amount of connections of a node with other clusters. Nodes with a high degree but low participation coefficient are called provincial hubs and play a role in segregation, while nodes with a high participation coefficient, called connector hubs, play a role in integration. Betweenness centrality is the proportion of shortest paths in the network that cross a certain node. Nodes with a high betweenness typically connect separate parts of the network. The calculation of network measures of integration, segregation and centrality is summarized in Table 3.1 [30].

## 3.3 Functional magnetic resonance imaging

### 3.3.1 Basic principles of functional MRI

#### Introduction

Functional MRI is a hemodynamic-based imaging technique. It is based on the idea that an increase in regional cerebral blood flow (CBF) can reflect neuronal activity, since CBF changes are coupled to glucose metabolism (CMR<sub>glu</sub>; cerebral metabolic rate of glucose) and cerebral metabolic rate of oxygen (CMRO<sub>2</sub>). Brain activity can be mapped using the venous blood oxygenation level-dependent (BOLD) contrast. The contrast in BOLD fMRI is created by changes in the ratio of oxyhemoglobin to deoxyhemoglobin in venous blood. Deoxyhemoglobin is paramagnetic, so alterations in its local concentration will cause changes in signal intensity of fMRI images. Because it has a high sensitivity and is easy to implement, BOLD fMRI is used extensively. However, the BOLD signal depends on several anatomical, physiological and imaging parameters, so it is difficult to compare signal changes in brain regions, between imaging facilities and between field strengths, and its interpretation is qualitative

or semi-quantitative. It is also possible to measure changes in cerebral blood volume (CBV) directly using a contrast agent. Then, the fMRI signal is related to one physiological parameter, making quantification and interpretation easier, however this technique is more complicated and not often used [4, 33].

Functional MRI is a very useful technique to map brain functions and has a good spatial and temporal resolution. It has been used widely for studying several brain functions, such as vision, motor, language and cognition [4]. In addition, fMRI has been used to investigate neurological disorders. It has helped to obtain more insight in neuroanatomical and pathophysiological changes in several diseases, such as brain tumors, epilepsy, dementia, movement disorders and traumatic brain injury. It can also be used to define targets for functional neurosurgery. Finally, it has the potential to be used as a biomarker for monitoring diseases and assessing treatment options [34].

### **Physiological background**

Functional MRI does not measure brain activity directly, but is based on the principle of neurovascular coupling, i.e., an increase in neuronal activation leads to an increase in cerebral blood flow (CBF). An increase in neural activity is accompanied by an increase in  $CMR_{glu}$  and  $CMRO_2$ , which leads to less oxygenated hemoglobin and more deoxygenated hemoglobin in the venous blood. To supply more glucose and oxygen to the tissue, both CBF and CBV will increase. The increase in CBF is much higher than the increase in  $CMRO_2$ , which means that the effect of the oxygen extraction fraction is reduced and the venous blood has a higher oxygenation level. Oxygenated blood is diamagnetic, while deoxygenated blood is paramagnetic. This means that deoxygenated blood leads to magnetic susceptibility artifacts around the vessels, which decreases the MRI signal. This is visualized in Figure 3.34. Using a pulse sequence that is very sensitive to magnetic susceptibility, BOLD imaging can detect subtle changes in blood oxygenation following neuronal activation [33, 35].

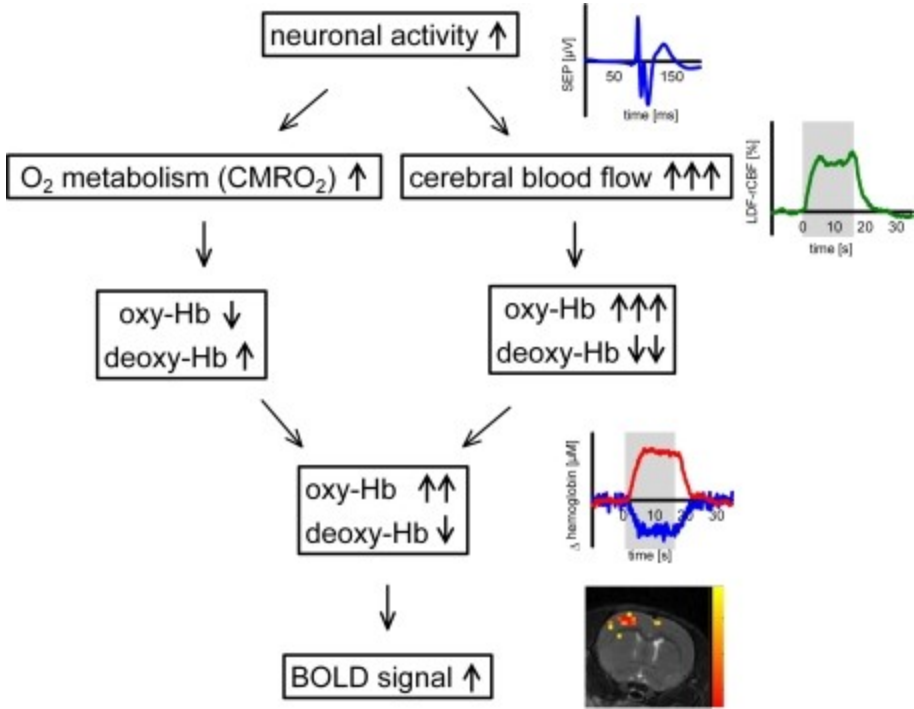


**Figure 3.34:** Physiological background of fMRI. An increase in neural activity is accompanied by an increase in CMRO<sub>2</sub>, which leads to less oxygenated hemoglobin and more deoxygenated hemoglobin in the venous blood. CBF increases as well, leading to more oxygenated hemoglobin and less deoxygenated hemoglobin. The increase in CBF is much higher than the increase in CMRO<sub>2</sub>, so overall the venous blood will have a higher oxygenation level, which leads to an increase in the BOLD signal [36].

### Evoked fMRI

The most common technique to investigate brain functioning using fMRI is to apply a certain stimulus and map which brain regions are activated following this stimulus. This is called evoked fMRI. The stimulus can be applied in a block design or event-related design. In a block design, periods during which a stimulus is applied are alternated with baseline periods. In an event-related design, very short stimuli are alternated with inter-stimulus intervals. The BOLD response to a stimulus has a specific shape called the hemodynamic response function (HRF) (Figure

3.35). Immediately after the stimulus, there is a dip in the HRF. This is the response to the increase in  $CMRO_2$ , which decreases the blood oxygenation level. Then the BOLD response increases when a large increase in CBF increases the blood oxygenation level. There can be a post-stimulus undershoot in the HRF, most likely because CBV decreases more slowly, which means there is a higher amount of deoxyhemoglobin in the blood compared to baseline. An estimated BOLD response is calculated by convolving the stimulus paradigm with the HRF. By correlating the estimated BOLD response with the actual BOLD response that was detected, voxels that are activated during the stimulus can be identified [35]. In Figure 3.36, an example of evoked fMRI with a block design is visualized. The blue line indicates the block design, which consists of alternating blocks during which the subjects open or close their eyes. The purple line is the BOLD time series in a voxel of the primary visual cortex. It is clear that this time series is correlated with the block design. By calculating correlations between the BOLD time series of all brain voxels and the applied block design, brain regions that are activated during the task (according to statistical inference) can be identified. On the right, the activated brain voxels, which are located in the primary visual cortex are visualized [37].

### Resting state fMRI

Instead of using a task or stimulus to investigate brain function, fMRI can also be acquired at rest. This is called resting state fMRI (rsfMRI). RsfMRI signals are consistent low frequency fluctuations between 0.01 and 0.08 Hz, which only occur in distinct cortical network systems. In task-based fMRI, these signals are discarded, but they are taken into account in rsfMRI. RsfMRI has several advantages over task-based fMRI. RsfMRI is acquired in the absence of a task or stimulus. This means it can also be acquired in patient populations in which task-based fMRI is difficult or not possible, such as children, unconscious patients and patients with a low intelligence quotient. During rest, the brain uses 60 to 80% of its energy for neuronal communication, while energy consumption only increases 5% during evoked activity. In task-based fMRI, 80% of

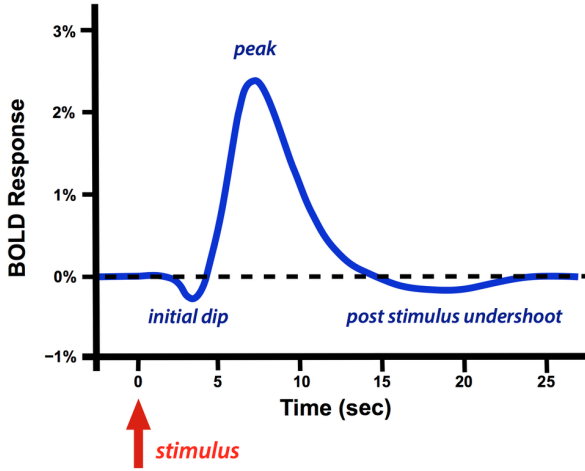


**Figure 3.35:** Hemodynamic response function (HRF). Immediately after the stimulus, there is a dip in the HRF because of an increase in  $CMRO_2$ , which decreases the blood oxygenation level. Then the BOLD response increases when a large increase in CBF increases the blood oxygenation level. There can be a post-stimulus undershoot in the HRF, most likely because CBV decreases more slowly, which means there is a higher amount of deoxyhemoglobin in the blood compared to baseline (Courtesy of Allen D. Elster, MRIquestions.com).

the signal is rejected as noise, while this is used as the main signal in rsfMRI. This also means that rsfMRI has a better signal-to-noise ratio than task-based fMRI. To investigate different brain functions using task-based fMRI, different tasks are needed. Using rsfMRI, different brain functions can be investigated with one "taskless" acquisition [38, 39].

Based on correlations between the low frequency fluctuations in spatially distinct brain regions, functional connections between regions can be identified [38]. Functional connectivity is the temporal dependency between spontaneous fluctuations in neuronal activity in spatially separated brain regions and gives an indication of the functional communication between these regions. The underlying neuronal basis of these spontaneous fluctuations is not yet completely understood. While some believe the fluctuations to be a result of physiological processes, such

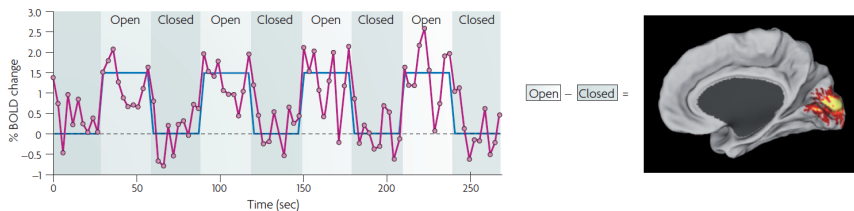


**Figure 3.36:** Example of evoked fMRI with a block design. The blue line indicates the block design, which consists of alternating blocks during which the subjects open or close their eyes. The purple line is the BOLD time series in a voxel of the primary visual cortex. It is clear that this time series is correlated with the block design. By calculating correlations between the BOLD time series of all brain voxels and the applied block design, brain regions that are activated during the task can be identified. On the right, the activated brain voxels, which are located in the primary visual cortex are visualized [37].

as cardiac and respiratory oscillations, there is more and more support for a neurological basis. Arguments for this are the observation that correlations between the fluctuations are found in brain regions with similar function and anatomy, the finding that mainly lower frequencies ( $<0.1$  Hz) occur in the BOLD signal while the higher frequencies of cardiac and respiratory fluctuations ( $>0.3$  Hz) rarely occur, and the report of associations between the rsfMRI fluctuations and electrophysiological recordings. However, non-neuronal fluctuations can still affect the rsfMRI signal, so it is important to reduce the influence of these signals using preprocessing techniques [40].

The main network found using rsfMRI is the default-mode network (DMN). This is a network of brain regions which are active during rest, but become less active during cognitive tasks [40]. The three main subdivisions of the DMN in humans are the ventral medial prefrontal cortex (VMPC), the dorsal medial prefrontal cortex (DMPC), and the posterior cingulate cortex, the adjacent precuneus and the lateral parietal cortex. The entorhinal cortex is often linked to the DMN as well. This suggests that the DMN plays a role in emotional processing (VMPC),

self-referential mental activity (DMPC) and the recollection of prior experiences (posterior regions) [41]. Other resting state networks are task-based or task-positive, i.e., their activity increases when a specific task is performed. These networks include the somatosensory network, visual network, language network and attention network [38]. Several resting state networks, which have been consistently identified by different research groups, in different subject groups and using different analysis methods, are visualized in Figure 3.37. These networks are the primary sensorimotor network, the primary visual and extra-striate visual network, a network comprised of bilateral temporal and insular and anterior cingulate cortex regions, left and right parietal-frontal network, the default-mode network and the frontal network [40].

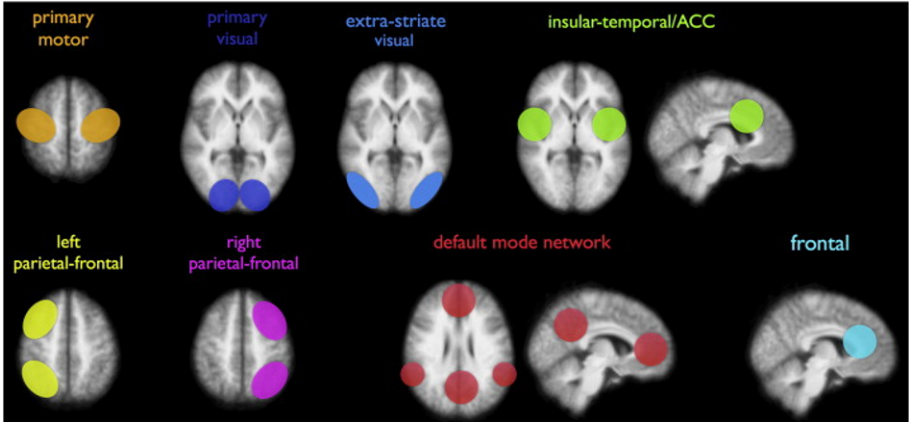


**Figure 3.37:** Overview of resting state networks that have been consistently identified by different research groups, in different subject groups and using different analysis methods: the primary sensorimotor network, the primary visual and extra-striate visual network, a network comprised of bilateral temporal and insular and anterior cingulate cortex regions, left and right parietal-frontal network, the default-mode network and the frontal network (Adapted from [40]).

### 3.3.2 Resting state fMRI analysis methods

#### Preprocessing

Before fMRI data can be analyzed, several preprocessing steps have to be performed. The main purpose of these steps is to correct temporal or spatial displacements that may have happened during image acquisition and to improve the detection of widespread signals within or across subjects [4].

**Slice timing correction** An fMRI image is acquired one slice at a time, so there is a slight time difference between the slices. This means that the signal of brain activity originating in a region that spans several slices will have a different time delay on each slice. To correct for this, slice timing correction is used. In this preprocessing step, the fMRI signal in each slice is calculated as if the slice was acquired first [4].

**Motion correction** There will always be some head motion in fMRI images, so motion correction is a common preprocessing step. In this step, the fMRI images at each time point are realigned with the first fMRI image. This is usually done using a six-parameter rigid body transformation. Three translations ( $x$ ,  $y$ ,  $z$ ) and three rotations (pitch, roll, yaw) are calculated to minimize the difference between the images. These parameters can also be used as covariates during the statistical analysis of the data to further reduce motion artifacts [4].

**Spatial normalization** Before a group analysis can be performed, images of different subjects or acquired at different time points, need to be matched to each other, so that all brain regions are positioned in the same location in all images. This can be done by warping the fMRI images of each subject to a template image. A possible difficulty is that there may be differences in brain anatomy between subjects that remain even after warping to a template. Even if a brain structurally matches a template, differences in brain function may still occur [4]. Spatial normalization is especially challenging when structural lesions are present in the brain. In this case, more advanced normalization

methods may be required [42].

**Spatial smoothing** Functional MR images are typically spatially smoothed before statistical analysis is done. During this preprocessing step, the images are convolved with a Gaussian kernel. This reduces noise in the images and corrects for some residual differences in anatomy between subjects [43].

**Temporal filtering** Depending on the following analysis method, a final preprocessing step is temporal filtering. The images are bandpass (0.01 to 0.08 or 0.1 Hz) filtered to reduce physiological noise. Within this frequency range, most meaningful low frequency fluctuations occur in the rsfMRI signal. Respiratory and aliased cardiac signals have a higher frequency and are filtered out in this preprocessing step [44].

### **Regional homogeneity and amplitude of low frequency fluctuations**

Regional homogeneity (ReHo) and amplitude of low frequency fluctuations (ALFF) are techniques used to investigate regional spontaneous brain activity, rather than functional connectivity. ReHo is a voxel-based method, which examines the degree of regional synchronization of the BOLD time series. Kendall's coefficient of concordance is calculated between the time series of a voxel and that of its neighbors. The higher this coefficient, the higher the regional synchronization, which is often associated with a higher activity [44]. The idea behind this technique is that significant brain activity is more likely to appear in clusters rather than in one voxel [45]. ReHo is most often computed within a low frequency band, usually 0.01 to 0.1 Hz, but can also be calculated within a subdivision of this band. For example, cortical activity can be more easily detected in the range of 0.01 to 0.04 Hz. However, the biological meaning of ReHo is still relatively unclear.

The ALFF is the average power of the BOLD signal within a low frequency band, usually 0.01 to 0.08 or 0.1 Hz, and indicates the magnitude of neural activity. Because ALFF is quite sensitive to large fluctuations

of high frequency noise, fractional ALFF (fALFF) has been introduced. This is the ratio of the amplitude within the low frequency span (0.01 to 0.08 Hz) to the amplitude of the whole frequency range [44]. An example of an ALFF map and a ReHo map is given in Figure 3.38, where rsfMRI was acquired in healthy volunteers. ALFF and ReHo are mainly increased in regions of the DMN [46]. ALFF and fALFF can also be investigated in different frequency ranges which all have different properties and physiological functions [44]. For example, frequencies between 0.01 and 0.027 Hz may correspond with cortical activity, frequencies between 0.027 and 0.073 Hz with basal ganglia activity, frequencies between 0.073 and 0.198 Hz with physiological noise, and frequencies between 0.198 and 0.25 Hz with white matter signal [46]. The advantages of ReHo and ALFF are that they have a high test-retest reliability, that there is no need for a priori definition of regions of interest and that they can be used to investigate whole-brain regional activity. While ALFF focuses more on strength or regional brain activity, ReHo looks at its coherence and centrality. Both techniques can be used to select ROIs for connectivity analysis or they can be used independently [46].

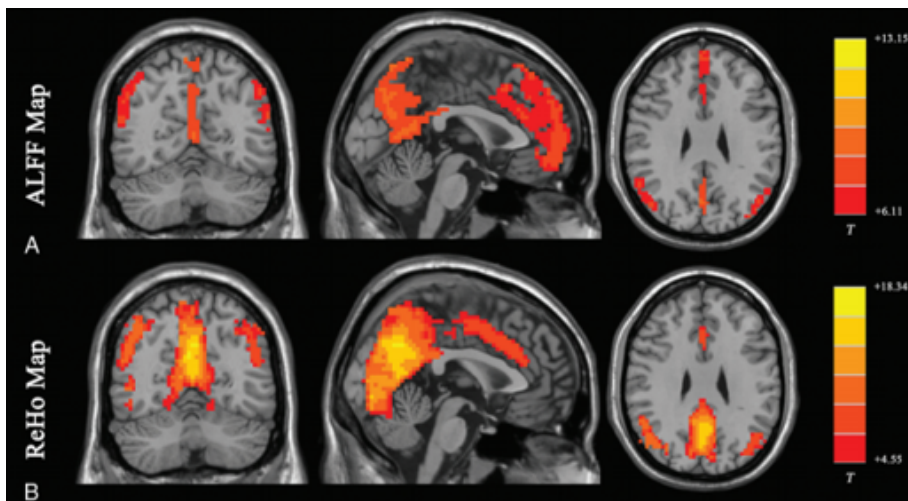


**Figure 3.38:** An example of an ALFF map and a ReHo map in healthy volunteers, reflecting regional neural activity. Increased ALFF and ReHo occur mainly in regions of the default-mode network [46].

### Seed-based analysis

The most basic method to assess functional connectivity in rsfMRI is a seed-based analysis. In this analysis method, the fMRI time series of each voxel is correlated with the time series of a predefined brain region, called a seed. This way a functional connectivity map is obtained that shows which regions are functionally connected to the seed region. Several metrics can be used to assess functional connectivity, such as the Pearson correlation coefficient, cross-correlation coefficient, partial correlation, multiple regressions and synchronized likelihood. The details of these metrics are beyond the scope of this thesis (for review, see [47]). Brain regions that are highly correlated are supposed to be involved in the same underlying functional process and are thus considered to be functionally connected. This does not necessarily mean they are structurally connected. The connections between several seed regions can be summarized in a connectivity matrix. Advantages of the seed-based analysis are that it is quite simple and the results are easy to interpret. Disadvantages are that the seed regions need to be defined a priori, which can induce bias, and that only connections of the seed regions can be identified, so it is not possible to investigate whole-brain connectivity [39, 40, 46]. In Figure 3.39, an example of a seed-based functional connectivity analysis is visualized. Here, the left Brodmann area 44 was used as a seed region [39].

### Independent component analysis

Whole-brain functional connectivity can be investigated using model-free methods. These methods search for patterns of functional connectivity across brain regions. The most commonly used model-free analysis method is independent component analysis (ICA). The fMRI signal can be seen as a combination of signals of interest and noise. ICA looks for a combination of sources that can explain this signal. The signal is decomposed into independent components, each with specific temporal and spatial characteristics. This way rsfMRI networks can be extracted. Each of these networks is characterized by a spatial map of z-scores obtained from the fMRI time series of each voxel and the average time series

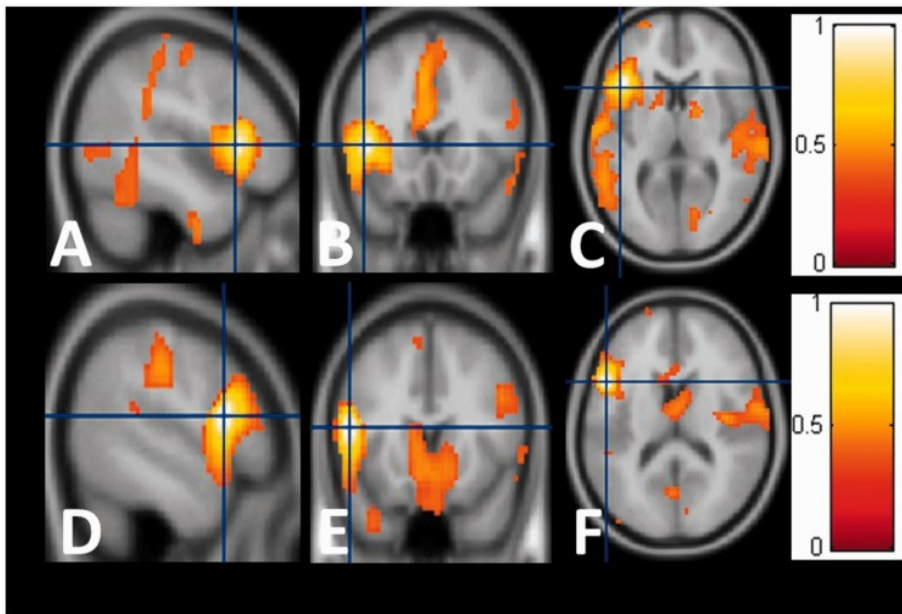


**Figure 3.39:** Example of a seed-based functional connectivity analysis with a seed in the left Brodmann area 44, indicated by the cross-hairs. Regions that are functionally connected to the seed region are indicated in color [39].

of the network. The average z-score of a network reflects the functional connectivity within that network [39, 40].

Several networks have been consistently found using ICA, including the DMN, the language network, and the auditory network [39, 40]. ICA is usually performed on a group level using the dual regression approach. This approach consists of three steps. First the concatenated fMRI signals of all subjects are decomposed into patterns of functional connectivity. Then, a subject-specific spatial map and time course is identified for each component. Finally, the component maps of the subjects are combined for non-parametric analysis to identify significant differences between and within groups [39]. Advantages of ICA include that it can be applied to whole-brain voxel-wise data, the temporal signals of the component can be used for further analysis, and direct comparison between groups is possible. Drawbacks are that it is more difficult to understand and interpret, the representation is more complex, and the amount of

subnetworks that can be detected depends on the number of independent components that are specified [39, 40, 46]. In Figure 3.40, an example is given of resting state networks identified using independent component analysis in healthy volunteers: A) the default-mode network, B) auditory network, C) medial visual network, D) lateral visual network, E) sensorimotor network, F) precuneus network, G) frontoparietal attention network, H) basal ganglia network, I) executive control network and J) visuospatial network [46].

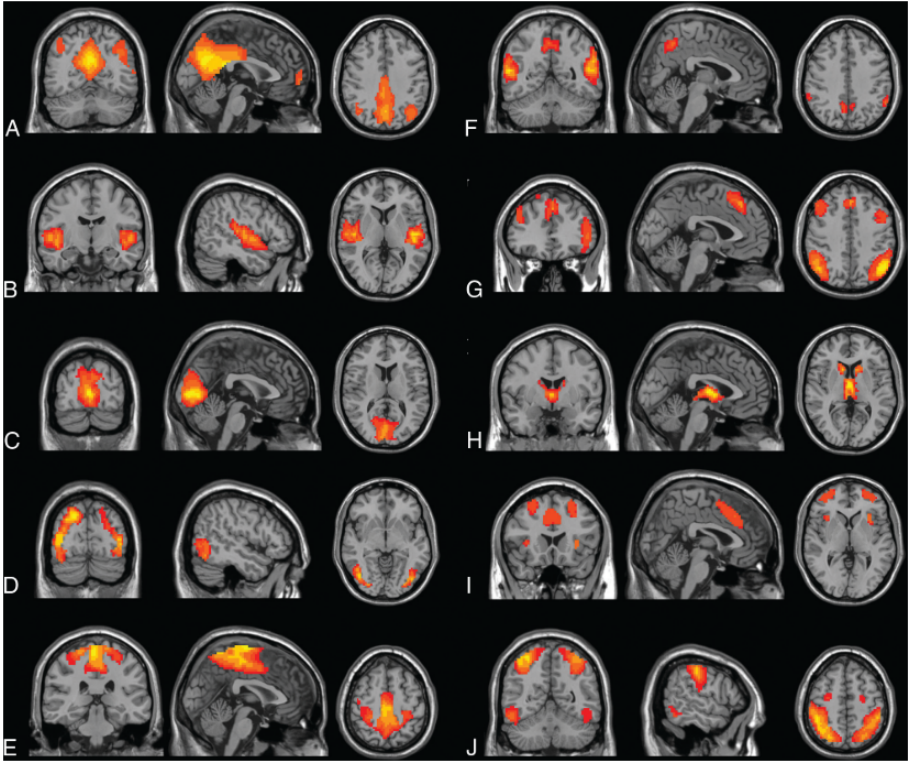


**Figure 3.40:** Example of resting state networks identified using independent component analysis in healthy volunteers: A) the default-mode network, B) auditory network, C) medial visual network, D) lateral visual network, E) sensorimotor network, F) precuneus network, G) frontoparietal attention network, H) basal ganglia network, I) executive control network and J) visuospatial network [46].

## Graph theory

Functional connectivity can be investigated on a whole-brain level using graph theory. As described in section 3.2.2, the brain can be seen as a graph consisting of nodes, i.e., brain regions, and edges, i.e., interactions between the nodes. The edges can be anatomical, functional or effective connections between nodes. In the context of rsfMRI, edges usually represent functional connections, assessed using the Pearson correlation coefficient. Functional connections are temporal correlations between brain activity in (un)connected brain regions. The functional network is represented by its connectivity or correlation matrix, in which the rows and columns correspond with the nodes or brain regions, and the elements with the correlation between them. In Figure 3.41, the construction of a functional brain network and the corresponding graph is visualized. The Pearson correlation coefficient is calculated between the time series of pairs of regions of interest and the results are summarized in a correlation matrix. This matrix is then represented by a graph in which the nodes correspond with the regions of interest and the edges with the correlation coefficients [30].

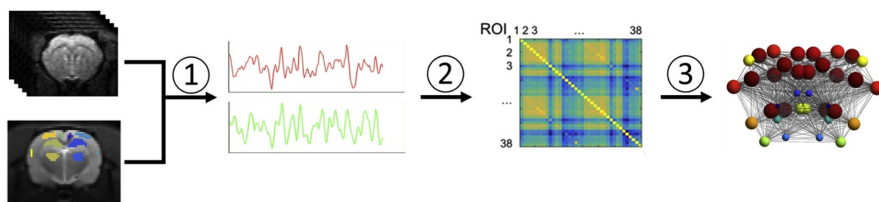


**Figure 3.41:** Construction of a functional network and graph. 1) The mean time series of predefined regions of interest (ROIs) are extracted from the rsfMRI images. 2) The Pearson correlation coefficient between each pair of ROIs is calculated and a correlation matrix is obtained. 3) The correlation matrix can be visualized as a graph in which the nodes represent the ROIs and the edges the correlation coefficients between them (Adapted from [48]).

Network measures of global or local connectivity can be calculated to characterize graphs. Measures of functional integration give an indication of overall communication efficiency in the brain. Examples are

characteristic path length, the average shortest path length between two nodes in the network, and global efficiency, the average inverse shortest path length. Measures of functional segregation reflect local interconnectivity. Clustering coefficient, which is the proportion of neighbors of a node that are also connected to one another, is the main measure of segregation. Other measures include local efficiency, which is similar to global efficiency but calculated within the neighborhood of a node, and modularity, which indicates the size and composition of clusters. The ratio between segregation and integration is called small-worldness. Functional brain networks typically have a small-world organization [30]. Measures of centrality reflect the importance of a node in the network. The most common measure of centrality is degree, i.e., the number of edges connected to a node. Other measures of centrality are the participation coefficient, which reflects the amount of connections of node with other clusters, and betweenness centrality, which is the proportion of shortest paths in the network that cross a certain node. These network measures are described in more detail in section 3.2.2 [30].

Some methodological considerations have to be taken into account when applying graph theory to the analysis of rsfMRI. Methodological decisions such as the selection of the nodes, definition of the edges and thresholding of the correlation matrix can affect the results, and can make it difficult to compare different experimental studies. The nodes used to construct a functional brain network can be based on structural information, such as an anatomical atlas, or based on functional information. In the latter case, components derived from independent component analysis can be used to determine the nodes, or they can be selected using a task- or stimulus-based fMRI protocol. Node selection based on functional information tends to minimize confounds and allows for a more accurate estimates of functional connectivity [49]. Edges can be defined based on different correlation measures. The most simple and most common measure is the Pearson correlation, that evaluates the similarity between two signals. Other measures are coherence, that assesses the similarity between two signals with a time lag, partial correlation, that controls for nuisance factors, and mutual information, that deter-

mines how much information can be obtained about one signal based on another signal. Simulation studies have reported that the simple methods, such as Pearson correlation and partial correlation, have the best performance [50]. Edges can be weighted or binary, with weighted edges representing the strength of the connection. The advantages of binary networks are that they are easier to characterize and to compare statistically. However, they contain less detailed information. Weighted networks take into account pairwise regional strength. They also tend to be more sensitive to network changes after a brain injury. Therefore, the use of weighted edges is preferred [49]. Connections in the functional network with a low strength or non-significant correlation can be spurious connections, and influence the topology of the strong and significant connection. Therefore, these connections are often removed by applying a threshold. The threshold can be absolute, discarding all connections below a certain strength, or they can be proportional, leading to networks with the same number of edges [30]. An absolute threshold can lead to a different number of edges between networks, and can cause significant differences in network topology between groups. Therefore, proportional thresholding is preferred. However, this type of thresholding may not be ideal in certain brain pathologies, where only regional differences in connectivity occur. If local increases in functional connectivity are detected, other connections that did not change may be erroneously removed from the network to maintain the same number of edges [51]. While most correlations in the functional brain network are positive, there are some negative correlations as well. Using Pearson correlation, the number of negative correlations is small, but when partial correlation is used, the number of positive and negative correlations is similar. Global signal regression to remove nuisance signals leads to a higher number of negative correlations as well. Currently, there is no consensus for handling negative correlations, or how to interpret them. It is not clear what negative correlations represent. They might be statistical artifacts, but could also reflect NMDA action in cortical inhibition [51]. Negative correlations are typically removed from the network [30]. In this dissertation, nodes were selected based on an anatomical atlas and edges were defined using Pearson's correlation coefficient. A weighted network was

used, and weak connections were removed using proportional thresholds to obtain a network density ranging from 20% to 50%. Only positive correlations were taken into account.

### **Dynamic functional connectivity**

In functional connectivity analysis, correlations between brain regions are typically calculated over the entire scan time, which is usually 5 to 20 minutes. Functional connectivity is thus assumed to be stationary [52]. However, several fMRI and electrophysiological studies have demonstrated that functional connectivity fluctuates within shorter time scales of seconds [52, 53]. To capture these fast changes, dynamic functional connectivity can be used [54].

The most common strategy to investigate dynamic functional connectivity is using a sliding window approach [52, 55]. In this approach, a functional connectivity metric, usually the Pearson correlation coefficient, is calculated between pairs of fMRI time series within a time window with length  $W$ . Then the time window is shifted by a time interval  $T$ , and again the functional connectivity metric is calculated within the window, which now spans from  $\text{time}=t_i+1+T$  to  $\text{time}=t_i+W+T$ , with  $t_i$  a time point within the fMRI time series. This is repeated for the entire fMRI time series, leading to a time series of functional connectivity. Correlations are calculated for each pair of time series of regions of interest, so a time series of  $N \times N$  connectivity matrices is obtained, with  $N$  the number of regions of interest (Figure 3.42) [52].

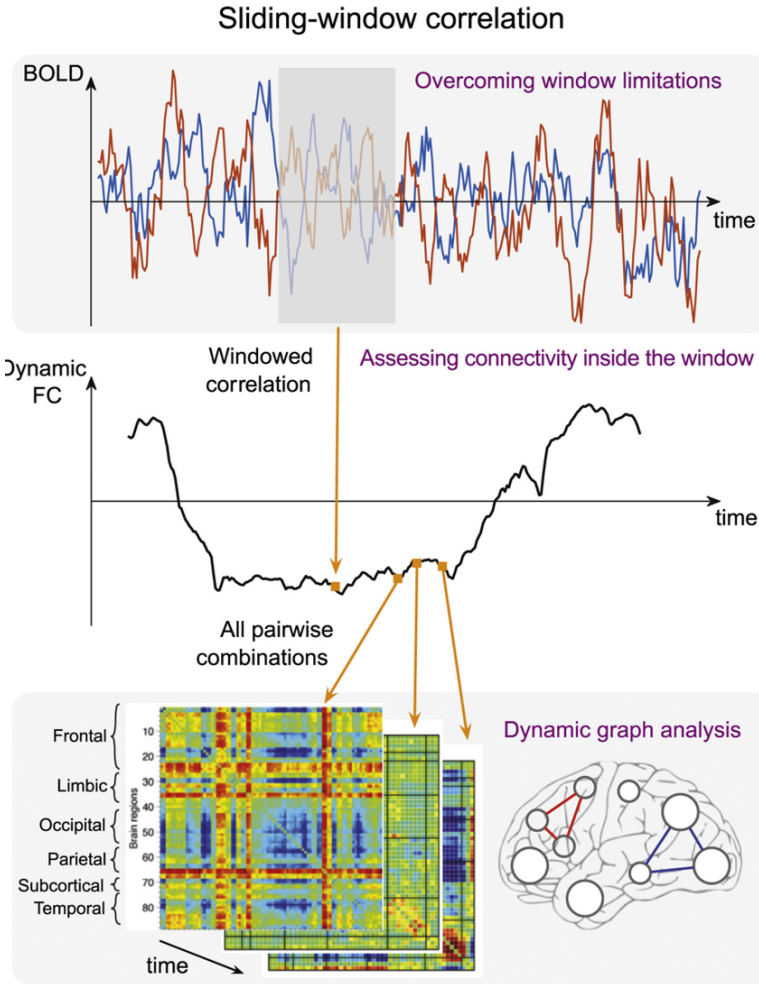


**Figure 3.42:** Sliding window approach. A functional connectivity metric is calculated between pairs of fMRI time series within a time window. Then the time window is shifted and again, the functional connectivity metric is calculated within the window. This is repeated for the entire fMRI time series, leading to a time series of functional connectivity. Connectivity is calculated for each pair of time series of regions of interest, so a time series of  $N \times N$  connectivity matrices is obtained, with  $N$  the number of regions of interest. Graph theory can be used to obtain more information about the dynamic functional connectivity. Graph metrics are calculated for each connectivity matrix, leading to a time series of graph metrics (Adapted from [52]).

It is important to use an appropriate window length  $W$ . If  $W$  is too short, spurious fluctuations can occur in the dynamic functional connectivity or there may not be enough time points within the window to reliably calculate correlations. If  $W$  is too long, not all fluctuations in dynamic functional connectivity will be detected [52]. Typically, windows of 30 to 60 s are used [52, 55]. A limitation of using a rectangular window is that all time points within the window contribute equally to the correlation, which can lead to outliers in the dynamic functional connectivity. To solve this, tapered windows, which disregard time points at the boundaries of the window, can be used [52].

While the Pearson correlation coefficient is used most often to assess functional connectivity in the sliding window approach, higher order analysis techniques can be used as well. Using ICA, the windows of the fMRI time series are decomposed into spatial components, and the temporal evolution of these components can be further analysed [52].

Graph theory is often used to obtain more information about the dynamic functional connectivity. Graph metrics are calculated for each connectivity matrix, leading to a time series of graph metrics. These metrics have been shown to vary over time, which indicates that brain networks are functionally disconnected one moment and interact with each other the next. Graph metrics can thus provide more insight into network integration and segregation (Figure 3.42) [52].

Dynamic functional connectivity metrics can be quantified using their standard deviation, coefficient of variation, or amplitude of low frequency fluctuations. Additionally, matrix factorization techniques such as k-means clustering or ICA can be used to decompose the metric into patterns or states of functional connectivity. For a group analysis, the connectivity time series of all subjects are concatenated before they are further analyzed. Using k-means clustering, recurrent patterns, which do not overlap in time, can be obtained. Temporal ICA can be used to identify maximally mutually temporally independent states. These states can overlap in time and each state contributes differently to functional connectivity at each time point [52].

Functional connectivity is known to differ in different frequency bands. To investigate dynamic functional connectivity in different frequency bands, a time-frequency analysis, such as wavelet transform coherence (WTC), can be used. In this type of analysis, the coherence and phase lag between two time series are estimated as a function of time and frequency. An advantage of this technique is that you do not need a fixed window length, but the window depends on the frequency. Shorter window lengths are used for higher frequencies, and longer window lengths for lower frequencies [52]. The details of WTC are beyond the scope of this thesis and can be found in [53].

An alternative view on dynamic functional connectivity suggests that meaningful information can be obtained from a single time point. In this approach, specific time points or events are selected, for example time points where the fMRI time series exceeds a threshold or time points where the fMRI signal is spatially similar. These clusters of time points are called co-activation patterns and characterize a specific configuration of BOLD activity (Figure 3.43) [52, 55].

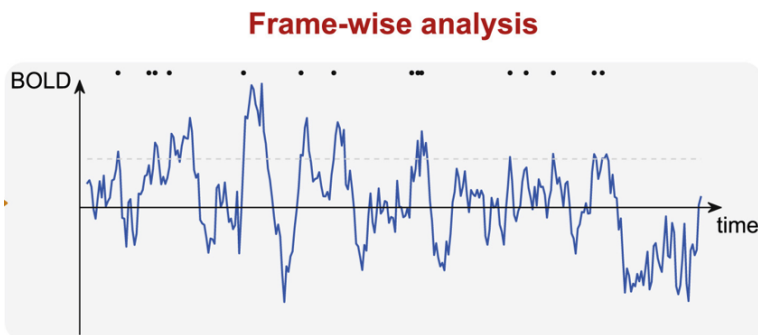


**Figure 3.43:** Frame-wise analysis. Time points where the fMRI time series exceeds a threshold are selected (dots). These clusters of time points are called co-activation patterns and characterize a specific configuration of BOLD activity (Adapted from [52]).

Another approach on dynamic functional connectivity is to analyse recurring spatiotemporal patterns that occur in the fMRI signal. Unlike the co-activation patterns, which reflect BOLD activity at a single time point, the spatiotemporal patterns are sequences of consecutive time

points. Majeed et al. [56] developed a method to identify these patterns and found patterns that were reproducible across subjects and species. These patterns included the DMN and attention network, which had opposed activity levels. An overview of the method is given in Figure 3.44. A series of consecutive images at a random time point is used as a template (a). Sliding correlations are calculated between the template and the fMRI time series (b). Peaks with a correlation that exceeds a threshold are identified (c). The series of images that correspond with these peaks are averaged to obtain an updated template (d). This process (b-d) is repeated until the template remains the same for two repetitions [52, 55, 56].

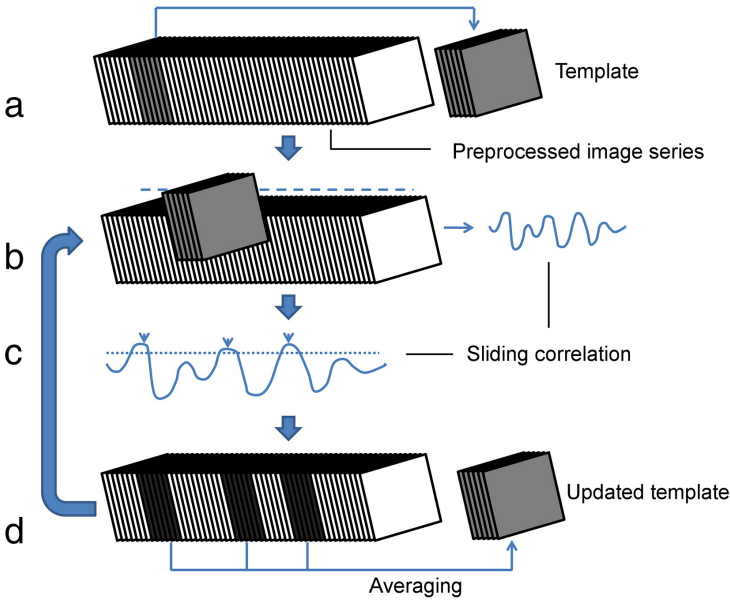


**Figure 3.44:** Method of Majeed et al. [56] to identify spatiotemporal patterns in the rsfMRI signal. A series of consecutive images at a random time point is used as a template (a). Sliding correlations are calculated between the template and the fMRI time series (b). Peaks with a correlation that exceeds a threshold are identified (c). The series of images that correspond with these peaks are averaged to obtain an updated template (d). This process (b-d) is repeated until the template remains the same for two repetitions [56].

## 3.4 Diffusion-weighted and resting state functional MRI in temporal lobe epilepsy

### 3.4.1 White matter and microstructural integrity in TLE

Diffusion-weighted MRI studies in patients with TLE have reported widespread changes in white matter integrity using the DTI model. Fractional anisotropy (FA) was reduced in several white matter regions, and mean diffusivity (MD) and radial diffusivity (RD) were increased [57–59]. Reduced FA, and to a lesser extent increased MD, were found in most association, commissural and projection fibers, in particular in fronto-central regions such as the genu and body of the corpus callosum, anterior corona radiata, cingulum and external capsule [57]. White matter changes were not restricted to the ipsilateral hemisphere but extended contralaterally [58]. However, white matter in the temporal lobe was more affected than white matter further away from the epileptogenic zone [57–59]. In a sub-group of TLE patients with hippocampal sclerosis, white matter changes were more severe, especially in hippocampal afferent and efferent tracts, such as cingulum, fornix and uncinate [57]. In addition, white matter changes were associated with age at epilepsy onset, epilepsy duration, and male sex [59]. Onset of epilepsy at a younger age and a longer disease duration resulted in larger changes in FA and MD in white matter bundles, which indicates that the white matter changes might be caused by recurrent seizures [57, 59].

A reduction in FA typically corresponds with a loss of axons and myelin sheaths, while increased MD and RD are associated with myelin disruption and increased extracellular space [57, 58]. Studies combining dMRI with histology found increased extra-axonal fraction, reduced axonal membrane circumference and reduced myelination in postsurgical fimbriae specimens. Presurgical FA was correlated with the reduction in axonal membrane circumference, and almost significantly correlated with decreased myelin thickness [58, 60].

The pathophysiological mechanisms underlying the changes in white matter structures in TLE are still largely unknown [58, 59]. The changes

could be related to the initial lesion or epileptogenic process, widespread axonal damage due to repetitive seizure spread, systemic effects of seizures like hypoxia and vasoconstriction, anti-epileptic drugs, altered brain development or neuroplasticity [58]. Because white matter changes are more severe close to the epileptogenic zone, it is more likely that they are caused by intrinsic processes, such as frequent seizure propagation, than external factors, such as anti-epileptic drugs [57, 59].

Additional clinical and preclinical studies are necessary to further investigate the underlying mechanisms of white matter changes [58]. These studies could also provide insight into the cognitive comorbidities of TLE, such as impaired memory and altered executive functioning [59]. Most studies investigating white matter integrity in patients with TLE use the DTI model. As already mentioned, the main limitation of this model is that it does not take into account crossing fibers. While decreased FA and increased MD are assumed to be associated with demyelination and axonal injury, FA can also be decreased in the presence of crossing fibers, because of extracellular diffusion, or because of other technical or biological factors. More advanced diffusion sequences and analysis methods could provide more insight into the biological meaning of white matter changes [57].

### 3.4.2 Structural and functional networks in TLE

Diffusion-weighted MRI also revealed changes in the structural network organization of the brain in TLE [61], but the results from the literature are not always consistent. Most studies reported decreased structural connectivity, and decreased network integration or communication efficiency. However, some studies found an increase in average clustering coefficient, indicating increased network segregation or local interconnectivity [61, 62], while others reported a decreased clustering coefficient [63].

The changes in white matter integrity also affect the functional network organization of the brain. Using resting state fMRI, studies found decreased functional connectivity, mainly in temporolimbic regions and

regions of the default mode network (DMN) [62, 63]. In a study by Bernhardt et al. [64], more severe structural changes in hippocampus were associated with a larger reduction in functional connectivity. Studies investigating functional network topology reported a decreased clustering coefficient in TLE patients, while network integration or communication efficiency appeared to be both increased or decreased [63].

### 3.4.3 Potential clinical and preclinical applications

Diffusion and resting state functional MRI have the potential to be valuable tools in the diagnosis and treatment of epilepsy, especially in presurgical planning. RsfMRI can be used to identify seizure foci, either on its own or in combination with EEG. Regions of increased functional connectivity, identified using rsfMRI and graph theory, were shown to overlap with epileptogenic areas identified using invasive EEG [38]. Both functional and structural network measures can be used to lateralize seizure focus [62]. In addition, changes in brain connectivity in spatially remote regions may provide new targets for surgical intervention or brain stimulation [65].

Task-based fMRI can be used in presurgical evaluation to localize eloquent cortex. Using a task protocol, motor areas and cortical areas involved in speech and language can be identified. In addition, cognitive functions can be mapped [34]. Alternatively, rsfMRI can be used to localize eloquent cortex as well. The advantage of rsfMRI over task-based fMRI is that it is less demanding and can be carried out on patients who are unable to execute a task-based protocol, such as young children, sedated patients, patients who are paretic or aphasic or patients with an altered mental status. It is also possible to detect several resting state networks at the same time, which reduces scanning time [38]. Using diffusion MRI tractography, important white matter tracts, such as the optic tract, can be mapped. This can help to predict functional deficits after surgery [62].

An application of structural and functional network analysis in epilepsy could be to predict and evaluate outcome after surgery [38, 62]. Us-

ing structural connectome measures and deep learning, predictive values for postoperative outcome could be obtained [66]. A rsfMRI analysis revealed that increased thalamic hubness was associated with seizure recurrence after surgery [67]. More diffuse functional epileptogenic networks seemed to predict a negative postoperative outcome [65].

An important future application of diffusion and resting state functional MRI is to better understand how a normal brain changes into an epileptic brain [65] and which brain regions play an important role during this highly dynamic biological process. This could help to improve the diagnosis and treatment of epilepsy [62]. Longitudinal preclinical studies that perform structural and functional network analysis can help to identify valuable biomarkers, i.e., objective measures of biological processes, that might be excellent tools for monitoring epileptogenesis and the dynamics of increased seizure propensity, as well as the potential to interfere with these key pathological aspects of epilepsy.

## Bibliography

- [1] D. W. McRobbie, E. A. Moore, M. J. Graves, and M. R. Prince, *MRI from Picture to Proton*, 2nd ed. Cambridge University Press, 2006.
- [2] M. A. Brown and R. C. Semelka, *MRI: Basic principles and Applications*, 3rd ed. Hoboken, N.J.: Wiley-Liss, 2003.
- [3] G. Huang, C.-H. Lu, and H.-H. Yang, “Magnetic nanomaterials for magnetic bioanalysis,” in *Novel Nanomaterials for Biomedical, Environmental and Energy Applications*. Elsevier, 2019, pp. 89–109.
- [4] S. H. Faro and F. B. Mohamed, *BOLD fMRI: A guide to functional imaging for neuroscientists*. Springer Science & Business Media, 2006. [Online]. Available: <https://books.google.com/books?hl=nl&lr=&id=MkjTO4wx-bkC&oi=fnd&pg=PR1&dq=BOLD+fMRI:+A+guide+to+functional+imaging+for+neuroscientists&ots=ozRiC-W2uY&sig=mb1etGpUXyin73GxNrthkc3iDHs>
- [5] J. P. Ridgway, “Cardiovascular magnetic resonance physics for clinicians: part i,” *Journal of cardiovascular magnetic resonance*, vol. 12, no. 1, pp. 1–28, 2010.
- [6] A. D. Sodickson and D. K. Sodickson, “Introductory Magnetic Resonance Imaging Physics,” in *Handbook of Neuro-Oncology Neuroimaging: Second Edition*. Elsevier Inc., apr 2016, pp. 157–166.
- [7] E. A. El-Dahshan, H. M. Mohsen, K. Revett, and A. B. M. Salem, “Computer-aided diagnosis of human brain tumor through MRI: A survey and a new algorithm,” *Expert Systems with Applications*, vol. 41, no. 11, pp. 5526–5545, sep 2014.
- [8] C. Hoyer, N. Gass, W. Weber-Fahr, and A. Sartorius, “Advantages and Challenges of Small Animal Magnetic Resonance Imaging as a Translational Tool,” *Neuropsychobiology*, vol. 69, no. 4, pp. 187–201, 2014. [Online]. Available: <https://www.karger.com/Article/FullText/360859>

- [9] J. L. Tremoleda, A. Kerton, and W. Gsell, “Anaesthesia and physiological monitoring during in vivo imaging of laboratory rodents: considerations on experimental outcomes and animal welfare,” *EJN-MMI research*, vol. 2, no. 1, pp. 1–23, 2012.
- [10] W. Van Hecke, L. Emsell, and S. Sunaert, Eds., *Diffusion Tensor Imaging*. New York, NY: Springer New York, 2016. [Online]. Available: <http://link.springer.com/10.1007/978-1-4939-3118-7>
- [11] D. Le Bihan and H. Johansen-Berg, “Diffusion MRI at 25: Exploring brain tissue structure and function,” pp. 324–341, jun 2012.
- [12] E. O. Stejskal and J. E. Tanner, “Spin diffusion measurements: spin echoes in the presence of a time-dependent field gradient,” *The journal of chemical physics*, vol. 42, no. 1, pp. 288–292, 1965.
- [13] D. Le Bihan and E. Breton, “Imagerie de diffusion in vivo par résonance magnétique nucléaire,” *Comptes rendus de l’Académie des sciences. Série 2, Mécanique, Physique, Chimie, Sciences de l’univers, Sciences de la Terre*, vol. 301, no. 15, pp. 1109–1112, 1985.
- [14] G. K. Rohde, A. S. Barnett, P. J. Basser, S. Marenco, and C. Pierpaoli, “Comprehensive Approach for Correction of Motion and Distortion in Diffusion-Weighted MRI,” *Magnetic Resonance in Medicine*, vol. 51, no. 1, pp. 103–114, 2004. [Online]. Available: <https://pubmed.ncbi.nlm.nih.gov/14705050/>
- [15] D. K. Jones and M. Cercignani, “Twenty-five pitfalls in the analysis of diffusion MRI data,” *NMR in Biomedicine*, vol. 23, no. 7, pp. 803–820, sep 2010. [Online]. Available: <http://doi.wiley.com/10.1002/nbm.1543>
- [16] Y. Zhang and F. W. Wehrli, “Reference-scan-free method for automated correction of nyquist ghost artifacts in echoplanar brain images,” *Magnetic Resonance in Medicine*, vol. 51, no. 3, pp. 621–624, mar 2004. [Online]. Available: <http://doi.wiley.com/10.1002/mrm.10724>

- [17] E. Kellner, B. Dhital, V. G. Kiselev, and M. Reiser, "Gibbs-ringing artifact removal based on local subvoxel-shifts," *Magnetic resonance in medicine*, vol. 76, no. 5, pp. 1574–1581, 2016.
- [18] J. Veraart, E. Fieremans, and D. S. Novikov, "Diffusion mri noise mapping using random matrix theory," *Magnetic resonance in medicine*, vol. 76, no. 5, pp. 1582–1593, 2016.
- [19] P. J. Basser, "New histological and physiological stains derived from diffusion-tensor mr images," *Annals of the New York Academy of Sciences*, vol. 820, no. 1, pp. 123–138, 1997.
- [20] E. S. Hui, M. M. Cheung, L. Qi, and E. X. Wu, "Towards better mr characterization of neural tissues using directional diffusion kurtosis analysis," *Neuroimage*, vol. 42, no. 1, pp. 122–134, 2008.
- [21] E. Fieremans, J. H. Jensen, and J. A. Helpert, "White matter characterization with diffusional kurtosis imaging," *Neuroimage*, vol. 58, no. 1, pp. 177–188, 2011.
- [22] B. Jeurissen, J.-D. Tournier, T. Dhollander, A. Connelly, and J. Sijbers, "Multi-tissue constrained spherical deconvolution for improved analysis of multi-shell diffusion mri data," *NeuroImage*, vol. 103, pp. 411–426, 2014.
- [23] J.-D. Tournier, F. Calamante, and A. Connelly, "Robust determination of the fibre orientation distribution in diffusion mri: non-negativity constrained super-resolved spherical deconvolution," *Neuroimage*, vol. 35, no. 4, pp. 1459–1472, 2007.
- [24] D. A. Raffelt, J.-D. Tournier, R. E. Smith, D. N. Vaughan, G. Jackson, G. R. Ridgway, and A. Connelly, "Investigating white matter fibre density and morphology using fixel-based analysis," *Neuroimage*, vol. 144, pp. 58–73, 2017.
- [25] J.-D. Tournier, S. Mori, and A. Leemans, "Diffusion tensor imaging and beyond," *Magnetic resonance in medicine*, vol. 65, no. 6, p. 1532, 2011.

- [26] T. E. Behrens, H. J. Berg, S. Jbabdi, M. F. Rushworth, and M. W. Woolrich, “Probabilistic diffusion tractography with multiple fibre orientations: What can we gain?” *Neuroimage*, vol. 34, no. 1, pp. 144–155, 2007.
- [27] J.-F. Mangin, P. Fillard, Y. Cointepas, D. Le Bihan, V. Frouin, and C. Poupon, “Toward global tractography,” *Neuroimage*, vol. 80, pp. 290–296, 2013.
- [28] R. E. Smith, J.-D. Tournier, F. Calamante, and A. Connelly, “The effects of SIFT on the reproducibility and biological accuracy of the structural connectome,” *Neuroimage*, vol. 104, pp. 253–265, 2015.
- [29] D. S. Bassett and E. Bullmore, “Small-world brain networks,” *The neuroscientist*, vol. 12, no. 6, pp. 512–523, 2006.
- [30] M. Rubinov and O. Sporns, “Complex network measures of brain connectivity: uses and interpretations,” *Neuroimage*, vol. 52, no. 3, pp. 1059–1069, 2010.
- [31] C.-H. Yeh, D. K. Jones, X. Liang, M. Descoteaux, and A. Connelly, “Mapping structural connectivity using diffusion mri: Challenges and opportunities,” *Journal of Magnetic Resonance Imaging*, 2020.
- [32] O. Sporns, “The non-random brain: efficiency, economy, and complex dynamics,” *Frontiers in computational neuroscience*, vol. 5, p. 5, 2011.
- [33] S. Ogawa, T.-M. Lee, A. R. Kay, and D. W. Tank, “Brain magnetic resonance imaging with contrast dependent on blood oxygenation,” *proceedings of the National Academy of Sciences*, vol. 87, no. 24, pp. 9868–9872, 1990.
- [34] D. Orringer, D. R. Vago, and A. J. Golby, “Clinical applications and future directions of functional mri,” in *Seminars in neurology*, vol. 32, no. 4. NIH Public Access, 2012, p. 466.
- [35] K. Uludag, D. J. Dubowitz, and R. B. Buxton, “Basic principles of functional mri,” *Clinical MRI. Elsevier, San Diego*, pp. 249–287, 2005.

- [36] U. Lindauer, U. Dirnagl, M. Füchtemeier, C. Böttiger, N. Offenhauser, C. Leithner, and G. Royl, “Pathophysiological interference with neurovascular coupling—when imaging based on hemoglobin might go blind,” *Frontiers in neuroenergetics*, vol. 2, p. 25, 2010.
- [37] M. D. Fox and M. E. Raichle, “Spontaneous fluctuations in brain activity observed with functional magnetic resonance imaging,” *Nature reviews neuroscience*, vol. 8, no. 9, pp. 700–711, 2007.
- [38] M. H. Lee, C. D. Smyser, and J. S. Shimony, “Resting-state fmri: a review of methods and clinical applications,” *American Journal of neuroradiology*, vol. 34, no. 10, pp. 1866–1872, 2013.
- [39] K. Smitha, K. Akhil Raja, K. Arun, P. Rajesh, B. Thomas, T. Kapilamoorthy, and C. Kesavadas, “Resting state fmri: A review on methods in resting state connectivity analysis and resting state networks,” *The neuroradiology journal*, vol. 30, no. 4, pp. 305–317, 2017.
- [40] M. P. Van Den Heuvel and H. E. H. Pol, “Exploring the brain network: a review on resting-state fmri functional connectivity,” *European neuropsychopharmacology*, vol. 20, no. 8, pp. 519–534, 2010.
- [41] M. E. Raichle, “The brain’s default mode network,” *Annual review of neuroscience*, vol. 38, pp. 433–447, 2015.
- [42] J. Crinion, J. Ashburner, A. Leff, M. Brett, C. Price, and K. Friston, “Spatial normalization of lesioned brains: Performance evaluation and impact on fMRI analyses,” *NeuroImage*, vol. 37, no. 3, pp. 866–875, sep 2007. [Online]. Available: [/pmc/articles/PMC3223520//pmc/articles/PMC3223520/?report=abstracthttps://www.ncbi.nlm.nih.gov/pmc/articles/PMC3223520/](https://www.ncbi.nlm.nih.gov/pmc/articles/PMC3223520/)
- [43] J. Ashburner, G. Barnes, C.-C. Chen, J. Daunizeau, G. Flandin, K. Friston, S. Kiebel, J. Kilner, V. Litvak, R. Moran *et al.*, “Spm12 manual,” *Wellcome Trust Centre for Neuroimaging, London, UK*, vol. 2464, 2014.

- [44] C. Yan and Y. Zang, "Dparsf: a matlab toolbox for" pipeline" data analysis of resting-state fmri," *Frontiers in systems neuroscience*, vol. 4, p. 13, 2010.
- [45] Y. Liu, K. Wang, Y. Chunshui, Y. He, Y. Zhou, M. Liang, L. Wang, and T. Jiang, "Regional homogeneity, functional connectivity and imaging markers of alzheimer's disease: a review of resting-state fmri studies," *Neuropsychologia*, vol. 46, no. 6, pp. 1648–1656, 2008.
- [46] H. Lv, Z. Wang, E. Tong, L. M. Williams, G. Zaharchuk, M. Zeineh, A. N. Goldstein-Piekarski, T. M. Ball, C. Liao, and M. Wintermark, "Resting-state functional mri: everything that nonexperts have always wanted to know," *American Journal of Neuroradiology*, vol. 39, no. 8, pp. 1390–1399, 2018.
- [47] S. M. Smith, K. L. Miller, G. Salimi-Khorshidi, M. Webster, C. F. Beckmann, T. E. Nichols, J. D. Ramsey, and M. W. Woolrich, "Network modelling methods for fmri," *Neuroimage*, vol. 54, no. 2, pp. 875–891, 2011.
- [48] J. Wang, X. Zuo, and Y. He, "Graph-based network analysis of resting-state functional mri," *Frontiers in systems neuroscience*, vol. 4, p. 16, 2010.
- [49] K. Caeyenberghs, H. Verhelst, A. Clemente, and P. H. Wilson, "Mapping the functional connectome in traumatic brain injury: What can graph metrics tell us?" *Neuroimage*, vol. 160, pp. 113–123, 2017.
- [50] A. Fornito, "Graph theoretic analysis of human brain networks," in *FMRI techniques and protocols*. Springer, 2016, pp. 283–314.
- [51] M. N. Hallquist and F. G. Hillary, "Graph theory approaches to functional network organization in brain disorders: A critique for a brave new small-world," *Network Neuroscience*, vol. 3, no. 1, pp. 1–26, 2018.

- [52] M. G. Preti, T. A. Bolton, and D. Van De Ville, "The dynamic functional connectome: State-of-the-art and perspectives," *Neuroimage*, vol. 160, pp. 41–54, 2017.
- [53] C. Chang and G. H. Glover, "Time–frequency dynamics of resting-state brain connectivity measured with fmri," *Neuroimage*, vol. 50, no. 1, pp. 81–98, 2010.
- [54] J. Grandjean, M. G. Preti, T. A. Bolton, M. Buerge, E. Seifritz, C. R. Pryce, D. Van De Ville, and M. Rudin, "Dynamic reorganization of intrinsic functional networks in the mouse brain," *Neuroimage*, vol. 152, pp. 497–508, 2017.
- [55] R. M. Hutchison, T. Womelsdorf, E. A. Allen, P. A. Bandettini, V. D. Calhoun, M. Corbetta, S. Della Penna, J. H. Duyn, G. H. Glover, J. Gonzalez-Castillo *et al.*, "Dynamic functional connectivity: promise, issues, and interpretations," *Neuroimage*, vol. 80, pp. 360–378, 2013.
- [56] W. Majeed, M. Magnuson, W. Hasenkamp, H. Schwarb, E. H. Schumacher, L. Barsalou, and S. D. Keilholz, "Spatiotemporal dynamics of low frequency bold fluctuations in rats and humans," *Neuroimage*, vol. 54, no. 2, pp. 1140–1150, 2011.
- [57] S. N. Hatton, K. H. Huynh, L. Bonilha, E. Abela, S. Alhusaini, A. Altmann, M. K. M. Alvim, A. R. Balachandra, E. Bartolini, B. Bender, N. Bernasconi, A. Bernasconi, B. Bernhardt, N. Bargallo, B. Caldairou, M. E. Caligiuri, S. J. A. Carr, G. L. Cavalleri, F. Cendes, L. Concha, E. Davoodi-bojd, P. M. Desmond, O. Devinsky, C. P. Doherty, M. Domin, J. S. Duncan, N. K. Focke, S. F. Foley, A. Gambardella, E. Gleichgerrcht, R. Guerrini, K. Hamandi, A. Ishikawa, S. S. Keller, P. V. Kochunov, R. Kotikalapudi, B. A. K. Kreilkamp, P. Kwan, A. Labate, S. Langner, M. Lenge, M. Liu, E. Lui, P. Martin, M. Mascalchi, J. C. V. Moreira, M. E. Morita-Sherman, T. J. O'Brien, H. R. Pardoe, J. C. Pariente, L. F. Ribeiro, M. P. Richardson, C. S. Rocha, R. Rodríguez-Cruces, F. Rosenow, M. Severino, B. Sinclair,

- H. Soltanian-Zadeh, P. Striano, P. N. Taylor, R. H. Thomas, D. Tortora, D. Velakoulis, A. Vezzani, L. Vivash, F. von Podewils, S. B. Vos, B. Weber, G. P. Winston, C. L. Yasuda, A. H. Zhu, P. M. Thompson, C. D. Whelan, N. Jahanshad, S. M. Sisodiya, and C. R. McDonald, "White matter abnormalities across different epilepsy syndromes in adults: an ENIGMA-Epilepsy study," *Brain*, vol. 143, no. 8, pp. 2454–2473, aug 2020. [Online]. Available: <https://academic.oup.com/brain/article/143/8/2454/5894684>
- [58] W. M. Otte, P. van Eijsden, J. W. Sander, J. S. Duncan, R. M. Dijkhuizen, and K. P. J. Braun, "A meta-analysis of white matter changes in temporal lobe epilepsy as studied with diffusion tensor imaging," *Epilepsia*, vol. 53, no. 4, pp. 659–667, apr 2012. [Online]. Available: <http://doi.wiley.com/10.1111/j.1528-1167.2012.03426.x>
- [59] G. Slinger, M. R. Sinke, K. P. Braun, and W. M. Otte, "White matter abnormalities at a regional and voxel level in focal and generalized epilepsy: A systematic review and meta-analysis," *NeuroImage: Clinical*, vol. 12, pp. 902–909, feb 2016.
- [60] L. Concha, D. J. Livy, C. Beaulieu, B. M. Wheatley, and D. W. Gross, "In vivo diffusion tensor imaging and histopathology of the fimbria-fornix in temporal lobe epilepsy," *Journal of Neuroscience*, vol. 30, no. 3, pp. 996–1002, jan 2010. [Online]. Available: [www.jneurosci.org](http://www.jneurosci.org)
- [61] E. van Diessen, S. J. H. Diederer, K. P. J. Braun, F. E. Jansen, and C. J. Stam, "Functional and structural brain networks in epilepsy: What have we learned?" *Epilepsia*, vol. 54, no. 11, pp. 1855–1865, nov 2013. [Online]. Available: <http://doi.wiley.com/10.1111/epi.12350>
- [62] S. Tavakol, J. Royer, A. J. Lowe, L. Bonilha, J. I. Tracy, G. D. Jackson, J. S. Duncan, A. Bernasconi, N. Bernasconi, and B. C. Bernhardt, "Neuroimaging and connectomics of drug-resistant epilepsy at multiple scales: From focal lesions to macroscale networks," *Epilepsia*, vol. 60, no. 4, pp. 593–604, apr 2019.

- [Online]. Available: <https://onlinelibrary.wiley.com/doi/abs/10.1111/epi.14688>
- [63] S. Chiang and Z. Haneef, "Graph theory findings in the pathophysiology of temporal lobe epilepsy," *Clinical Neurophysiology*, vol. 125, no. 7, pp. 1295–1305, jul 2014. [Online]. Available: <http://linkinghub.elsevier.com/retrieve/pii/S1388245714001928>
- [64] B. C. Bernhardt, A. Bernasconi, M. Liu, S.-J. Hong, B. Caldairou, M. Goubran, M. C. Guiot, J. Hall, and N. Bernasconi, "The spectrum of structural and functional imaging abnormalities in temporal lobe epilepsy," *Annals of Neurology*, vol. 80, no. 1, pp. 142–153, jul 2016. [Online]. Available: <http://doi.wiley.com/10.1002/ana.24691>
- [65] S. Chiang, Z. Haneef, J. M. Stern, and J. Engel, "Use of resting-state fmri in planning epilepsy surgery," *Neurology India*, vol. 65, no. 7, p. 25, 2017.
- [66] E. Gleichgerrcht, B. Munsell, S. Bhatia, W. A. Vandergrift, C. Rorden, C. McDonald, J. Edwards, R. Kuzniecky, and L. Bonilha, "Deep learning applied to whole-brain connectome to determine seizure control after epilepsy surgery," *Epilepsia*, vol. 59, no. 9, pp. 1643–1654, sep 2018. [Online]. Available: <http://doi.wiley.com/10.1111/epi.14528>
- [67] X. He, G. E. Doucet, D. Pustina, M. R. Sperling, A. D. Sharan, and J. I. Tracy, "Presurgical thalamic "hubness" predicts surgical outcome in temporal lobe epilepsy," *Neurology*, vol. 88, no. 24, pp. 2285–2293, jun 2017. [Online]. Available: <https://n.neurology.org/content/88/24/2285><https://n.neurology.org/content/88/24/2285.abstract>



## 4 | Research aims

The main aim of this dissertation is to gain more insight into the mechanisms of epileptogenesis, with the ultimate goal of finding a biomarker to predict which patients will develop epilepsy after an initial precipitating injury. To this end, alterations in structural and functional brain networks during epileptogenesis are investigated in a rat model of TLE using advanced magnetic resonance imaging (MRI).

Structural connectivity can be assessed using diffusion-weighted MRI (dMRI). This imaging technique detects the diffusion of water, based on which the microstructure and structural integrity of the brain can be mapped. The most basic and most commonly used model of diffusion is the diffusion tensor model. However, this model is not specific to microstructure and is not accurate in the presence of complex white matter configurations. A more advanced model that can overcome these limitations is multi-shell multi-tissue constrained spherical deconvolution (MSMT-CSD). Based on this model, a more accurate estimation of white matter structures in the brain (tractography) can be obtained. In addition, information about specific white matter fiber populations can be derived from this model using fixel-based analysis (FBA), and the structural integrity of these populations can be assessed. In Chapter 5, structural network topology and white matter integrity are investigated using dMRI, tractography and FBA based on the MSMT-CSD model in a rat model of TLE, to address the following research questions:

- How does the structural brain network change during epileptogenesis and which brain regions are affected most?

- Are changes in structural network topology related to changes in white matter integrity?

Resting state functional MRI (rsfMRI) is an imaging technique that allows visualisation of whole-brain activity and can be used to identify and investigate functional brain networks. The topology of these networks can be assessed using graph theory. In graph theory, the brain is represented as a network consisting of nodes, usually brain regions, and edges, which show the relationship between the nodes. Several graph theoretical measures can be calculated to describe and quantify the network. In Chapter 6, changes in functional network topology in a rat model of TLE are evaluated using rsfMRI and graph theory analysis. The following research questions are addressed:

- How does the functional organization of the rat brain change after status epilepticus and during the development of TLE?
- In which brain regions does the degree of functional connectivity change the most?
- Are changes in functional network topology associated with the occurrence of spontaneous epileptic seizures?

In most rsfMRI studies, one value of functional connectivity is calculated over an entire scan, which usually lasts 5 to 20 minutes. Functional connectivity is thus assumed to be stationary during this time period. However, in reality, functional connectivity fluctuates within shorter time scales of seconds. To capture these fast changes, dynamic functional connectivity analysis can be used. In Chapter 7, changes in dynamic functional connectivity and network topology during epileptogenesis are investigated in a rat model of TLE, to address the following research questions:

- How do dynamic functional connectivity and network topology of the rat brain change after status epilepticus and during the development of TLE?
- Are the changes in dynamic functional connectivity and network topology associated with the occurrence of spontaneous seizures?

## 5 | White matter integrity in a rat model of epileptogenesis: structural connectomics and fixel-based analysis

This chapter is based on: Christiaen, E., Goossens, M. G., Descamps, B., Delbeke, J., Wadman, W., Vonck, K., Boon, P., Raedt, R., & Vanhove, C. (2021). White matter integrity in a rat model of epileptogenesis: structural connectomics and fixel-based analysis. *Brain Connectivity*.

### Abstract

**Introduction** Electrophysiological and neuroimaging studies have demonstrated that large-scale brain networks are affected during the development of epilepsy. These networks can be investigated using diffusion magnetic resonance imaging (dMRI). The most commonly used model to analyze dMRI is diffusion tensor imaging (DTI). However, DTI metrics are not specific to microstructure or pathology and the DTI model does not take into account crossing fibers, which may lead to erroneous results. To overcome these limitations, a more advanced model based on multi-shell multi-tissue constrained spherical deconvolution was used in this study to perform tractography with more precise fiber orientation estimates and to assess changes in intra-axonal volume using fixel-based analysis.

**Methods** Diffusion MRI images were acquired before and at several time points after induction of status epilepticus in the intraperitoneal kainic acid (IPKA) rat model of temporal lobe epilepsy. Tractography

was performed and fixel metrics were calculated in several white matter tracts. The tractogram was analyzed using graph theory.

**Results** Global degree, global and local efficiency were decreased in IPKA animals compared to controls during epileptogenesis. Nodal degree was decreased in the limbic system and default-mode network, mainly during early epileptogenesis. Furthermore, fiber density (FD) and fiber-density-and-cross-section (FDC) were decreased in several white matter tracts.

**Discussion** These results indicate a decrease in overall structural connectivity, integration and segregation and decreased structural connectivity in the limbic system and default-mode network. Decreased FD and FDC point to a decrease in intra-axonal volume fraction during epileptogenesis, which may be related to neuronal degeneration and gliosis.

## 5.1 Introduction

Epilepsy is a neurological disorder characterized by recurrent epileptic seizures, which affects more than 50 million people worldwide [1, 2]. In about one third of patients, seizures cannot be suppressed with anti-epileptic drugs, i.e., they suffer from drug-resistant epilepsy. One of the most prevalent types of drug-resistant epilepsy is temporal lobe epilepsy (TLE) [3]. This type of epilepsy is often the result of an initial precipitating insult, such as stroke, head trauma, infection, brain tumor, or status epilepticus (SE), i.e., a prolonged, uncontrolled seizure. The transformation process of a normal brain into an epileptic brain is called epileptogenesis [4]. Studies investigating brain connectivity have demonstrated that large-scale brain networks are affected during epileptogenesis. Obtaining more knowledge about these networks could improve our understanding of the disease mechanisms and help to develop new therapies [5].

When investigating brain connectivity, a distinction can be made between structural connectivity, the “hardware” of the brain, and functional connectivity, the “software” that uses the hardware to execute

specific tasks. Many studies have investigated functional connectivity in epilepsy (for review, see [6]), but the research into structural connectivity is more limited, even though integrating the functional and structural changes could provide more accurate information about the epileptogenic process. In this paper we will focus on structural connectivity, assessed using diffusion MRI (dMRI). Diffusion MRI is an imaging technique that can be used to map the microstructure and structural integrity of the brain. Using diffusion tensor imaging (DTI), studies investigating epilepsy found extensive and bilateral alterations in white matter tracts and mainly reported decreased fractional anisotropy (FA) and increased diffusivity [5, 7, 8]. Using DTI-based tractography, most studies found decreased structural connectivity and decreased global and local efficiency in the structural brain network [9–12].

Disadvantages of DTI are that the metrics are not specific to microstructure or pathology and difficult to interpret [13]. In addition, this model does not take into account that many voxels contain crossing or kissing fibers, leading to diffusion metrics that may not be fiber-specific and even erroneous [14, 15]. A model that can overcome this limitation is multi-shell multi-tissue constrained spherical deconvolution (MSMT-CSD). Using this model, fiber orientation distribution functions can be estimated and whole-brain fiber tractography can be performed with more precise fiber orientation estimates [14]. Based on the tractography, structural brain networks can be investigated. The few studies that investigated epilepsy using this technique reported decreased structural connectivity in patients with TLE [16].

Using the MSMT-CSD model, it is also possible to obtain information about specific fiber populations within a voxel, referred to as a fixel (fiber population in voxel). Fixel-based analysis (FBA) can be used to detect white matter changes that are related to brain connectivity, such as fiber density (FD), which reflects the intra-axonal volume fraction within voxels [15]. A fixel-based metric for macroscopic white matter tract morphology is fiber-bundle cross-section (FC), which is related to volume differences perpendicular to the fiber orientation [15]. These metrics can also be combined (multiplied) as fiber-density-and-cross-section (FDC),

which is related to the total intra-axonal volume and is a more comprehensive measure of the ability of white matter to relay information than fiber density or fiber-bundle cross-section separately (Figure 5.1) [15]. The very few studies that have used FBA to investigate epilepsy reported decreased FD and FDC in patients with epilepsy [17, 18].

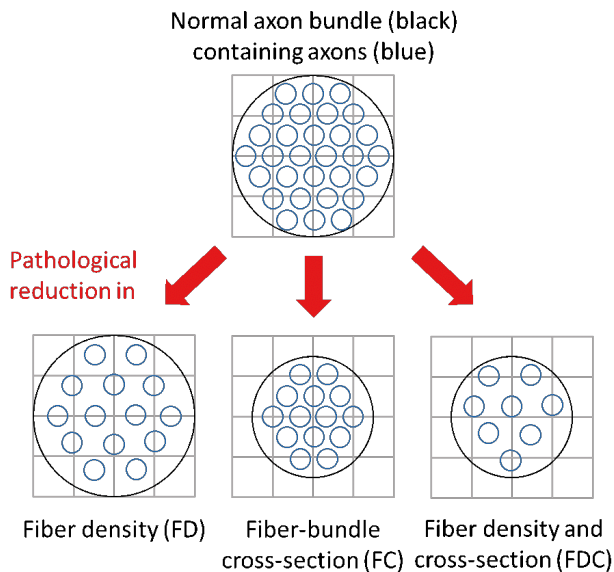


**Figure 5.1:** Representation of a normal axon bundle (black) containing axons (blue). The grid (grey) represents imaging voxels. In this example of pathological changes in fixel metrics, fiber density (FD), fiber-bundle cross-section (FC) and fiber-density-and-cross-section (FDC) are decreased compared to a normal axon bundle. Adapted from Raffelt et al. [15].

In this study, changes in structural brain connectivity and white matter integrity during epileptogenesis were investigated using whole-brain tractography and FBA based on the MSMT-CSD model in the intraperitoneal kainic acid (IPKA) rat model for TLE. Diffusion MR images were acquired before SE and at multiple time points (1, 3, 11 and 16 weeks) post-SE in IPKA animals and age-matched controls. The aim of this study was twofold: to investigate 1) how the structural brain network changes during epileptogenesis and which brain regions are affected most

and 2) whether the changes in network topology are related to changes in white matter integrity, assessed using FBA. To the best of our knowledge, this is the first longitudinal dMRI study that combines analysis of structural connectivity and FBA in a rat model of TLE.

## 5.2 Materials and methods

### 5.2.1 Animals

Sixteen adult male Sprague-Dawley rats ( $238 \pm 11$  g body weight at SE induction; Envigo, The Netherlands) were included in this study. All animals were treated according to European guidelines (directive 2010/63/EU) and the protocol was approved by the local Ethical Committee on Animal Experiments of Ghent University (ECD 16/31). The animals were housed under controlled laboratory conditions (12 h normal light/dark cycles, 20–23 C and 40–60% relative humidity) with food (Rats and Mice Maintenance, Carfil, Belgium) and water *ad libitum*. The animals were housed individually in type III H cages (Tecniplast, Australia) on wood-based bedding (Carfil, Belgium). Paper nesting material (Nesting, Carfil, Belgium) and a piece of gnawing wood (M-brick, Carfil, Belgium) were added to the cages for enrichment.

### 5.2.2 Status epilepticus

In 9 animals (8 weeks old), kainic acid (KA; Tocris Bioscience, UK) was injected intraperitoneally (i.p., 5 mg/kg/h) according to the protocol of Hellier et al. [19]. KA was injected every hour until motor seizures were induced for 3 hours or longer, called status epilepticus (SE). On average, 13.6 mg/kg KA (range: 10–20 mg/kg) was administered to the animals. The remaining 7 animals were used as control group.

### 5.2.3 Image acquisition

Anatomical and diffusion-weighted MR images were acquired in 9 IPKA animals and 7 control animals before the induction of SE, twice during early (1 and 3 weeks post-SE, seizures are rare) and twice during late epileptogenesis (11 and 16 weeks post-SE, frequent seizures). One of the

IPKA animals died before the final scanning session. During the scanning sessions, the animals were anesthetized with isoflurane (5% for induction, 2% for maintenance; Isoflo, Zoetis, USA) and O<sub>2</sub>. If necessary, isoflurane was lowered gradually to a minimum of 0.5% to maintain a respiratory rate of 0.7 to 1 per second. Respiration was monitored using a pressure sensor, and a circulating-water heating pad and bubble wrap were used to control body temperature. The MRI scans were performed on a 7T system (PharmaScan, Bruker, Germany) using a transmit-receive volume coil (Bruker, Germany). First, a T2-weighted anatomical image was acquired using a Rapid Acquisition with Refocused Echoes (RARE) sequence with TR 5.5 s, TE 37 ms, RARE factor 8, FOV 25 x 25 mm<sup>2</sup>, in-plane resolution 109 x 109 μm<sup>2</sup>, slice thickness 600 μm, 45 slices, acquisition time 12 min. Then, 3 diffusion-weighted MR images were acquired using spin-echo echo-planar imaging (EPI) with 32, 46 and 64 gradient directions, b-values of 800, 1500 and 2000 s/mm<sup>2</sup>, and 5, 5 and 7 b<sub>0</sub> images, respectively, with TR 6.250 s, TE 24 ms, 4 EPI segments, FOV 30 x 30 mm<sup>2</sup>, in-plane resolution 333 x 333 μm<sup>2</sup>, slice thickness 500 μm, interslice distance 600 μm, 25 slices and total acquisition time 65 min.

#### 5.2.4 Electrode implantation and EEG recording

To record electroencephalography (EEG), electrodes were implanted in both hippocampi on average 22 weeks post-SE (range 21 to 23 weeks) in the IPKA group (n=8). Bipolar recording electrodes were placed stereotactically in both hippocampi (AP -5.3 mm, ML +&-3.2 mm relative to bregma, DV about -3.0 mm relative to brain surface). The Rat Brain Atlas by Paxinos and Watson [20] was used to select the coordinates.

To ensure that all animals in the IPKA group had spontaneous seizures, EEG was recorded for eight consecutive days in awake and freely moving animals. The IPKA animals were connected to the EEG setup two to three weeks after surgery. Electrographic seizures, defined as a repetitive pattern (>2 Hz) of complex, high amplitude EEG spikes, longer than 5 seconds, were annotated by an experienced investigator. The first 36 hours of EEG recording were considered an acclimatization pe-

riod and were not included in further analysis. The average number of seizures/day was calculated based on the last six days of EEG recording.

### 5.2.5 Image preprocessing

The diffusion-weighted images were preprocessed using MRtrix3 [21] and the ExploreDTI toolbox version 4.8.6. [22]. First, the three shells were concatenated and noise correction and Gibbs ringing correction were performed using the *dwidenoise* and *mrdegibbs* commands in MRtrix3. Next, the images were corrected for EPI, eddy current and motion distortion in ExploreDTI. In MRtrix3, response functions were estimated for white matter, grey matter and cerebrospinal fluid using the command *dwi2response dhollander*. Then, fiber orientation distributions (FOD) were estimated using MSMT-CSD with the MRtrix3 command *dwi2fod*. Bias field correction and intensity normalization were performed on the FOD images using the command *mtnormalise*. Next, the images were registered and warped to an FOD template with reorientation. This template was calculated based on the FOD images of the IPKA animals 3 weeks post-SE.

### 5.2.6 Structural connectome

Whole-brain tractography was performed with the *tckgen* command in MRtrix using the probabilistic iFOD2 algorithm. Streamlines were seeded from 5 million seeds, the FOD cutoff value was set at 0.25 and a step size of 15  $\mu\text{m}$  was used. Then, the command *tcksift2* was used to filter out streamlines to obtain a better match between the tractogram and fixel-wise fiber densities.

A structural connectome, or graph, was constructed with 38 predefined regions of interest (ROIs) as nodes and the number of streamlines that cross each pair of ROIs as edges. The ROIs, listed in Table 5.1, were drawn manually based on T2-weighted anatomical images and FOD template. Each region has a component on the left and right side of the brain. The number of streamlines crossing each pair of ROIs was calculated using the command *tck2connectome* in MRtrix3.

**Table 5.1:** Regions of interest (ROIs) used for the construction of the structural brain network.

<b>Regions of interest (ROIs)</b>			
<b>Full name</b>	<b>Abbreviation</b>	<b>Full name</b>	<b>Abbreviation</b>
Auditory Cortex	Au	Piriform Cortex	Pir
Caudate Putamen	CPu	Posterior Parietal Cortex	PtP
Cingulate Cortex	Cg	Retrosplenial Cortex	RSC
Dorsolateral Orbitofrontal Cortex	DLO	Septum	Sep
Globus Pallidus	GP	Somatosensory Cortex	SSC
Hippocampus	Hip	Subiculum	Sub
Insula	Ins	Temporal Association Cortex	TeA
Motor Cortex	MC	Thalamus	Th
Nucleus Accumbens	NAC	Visual Cortex	Vis
Parietal Association Cortex	PtA		

Graph theoretical network metrics were calculated for each graph using a Graph Theoretical Analysis Toolbox (GRETNA) [23]. First, a threshold was applied to the network to remove the weakest connections. Several thresholds were used to obtain a network density (i.e., the number of remaining connections divided by the maximum number of possible connections) ranging from 20 to 50% with a 5% interval. The following weighted network metrics were then calculated for each network density and averaged: degree, characteristic path length, global efficiency, clustering coefficient and local efficiency. Degree or connection strength is the sum of the edges linked to a node. It is an indication of centrality or the importance of a region in the structural network. Characteristic path length is the mean number of edges between two nodes in the network, and global efficiency is the mean inverse path length between two regions. These are measures of integration in the network or the overall

efficiency of the network. Clustering coefficient is the ratio of neighbors of a node that are also linked to one another and local efficiency is the average inverse path length within the neighborhood of a node, i.e., the nodes linked to that node. These are measures of segregation or local interconnectivity [24, 25].

### 5.2.7 Tractometry-based DTI analysis

The DTI metrics fractional anisotropy (FA), axial diffusivity (AD), radial diffusivity (RD) and mean diffusivity (MD) were calculated on a whole-brain level using the *dwi2tensor* and *tensor2metric* commands in MRtrix3. From the whole-brain tractography of the individual animals, six white matter tracts were extracted using the *tck2connectome* command: anterior commissure, corpus callosum, cingulum, internal and external capsule, and fimbria. These tracts were selected because they were the most prominent white matter bundles in the whole-brain tractography. Along each tract, DTI metrics were evaluated using the *tckresample* and *tcksample* commands in MRtrix3. Then, the median of each DTI metric was calculated for each tract.

### 5.2.8 Fixel-based analysis

For the fixel-based analysis, a new FOD template was constructed based on the baseline images of all animals. To obtain an isotropic resolution, voxel size of the template was changed to  $0.3 \times 0.3 \times 0.3 \text{ mm}^3$ . The individual normalized FOD images were registered and warped to the template without reorientation using the *mrregister* and *mrtransform* commands in MRtrix3. Then, a fixel mask was constructed using the *fod2fixel* command. For each scan, fiber density was calculated using the *fod2fixel* command and fiber-bundle cross-section was calculated based on the warp that was computed during the image registration using the *warp2metric* command. In addition, the combined metric fiber-density-and-cross-section was calculated. These metrics were analyzed at two levels: using fixel-based analysis (FBA) and using ROI-based analysis. For FBA, whole-brain tractography was performed on the baseline template using an FOD cutoff value of 0.325 and step size of  $15 \text{ }\mu\text{m}$ , leading

to 2 million streamlines. The tractogram was filtered using the command `tcksift`. For the ROI-based analysis, six white matter tracts were extracted from the tractogram using the `tck2connectome` command: anterior commissure, corpus callosum, cingulum, internal and external capsule, and fimbria. The tracts were converted to ROIs using the `tckmap` command and manually corrected for stray streamlines and enlarged ventricles at later time points. Then, average FD, FC and FDC were calculated for each ROI.

### 5.2.9 Volume of enlarged ventricles

On the T2-weighted images, it was clear that the size of the ventricles increased during epileptogenesis. To measure the change in ventricular volume, ventricles were manually delineated on the T2-weighted images using `mrview` in `MRtrix3`.

### 5.2.10 Statistical analysis

The global and nodal network metrics, the tractography-based and fixel-based metrics in white matter tracts were analyzed using the MIXED procedure (linear mixed-effects model) in IBM SPSS Statistics for Windows, version 26 (IBM Corp., N.Y., USA) using the protocol of Duricki et al. [26]. The covariance structure was ‘compound symmetry’, and group (IPKA and control animals), time (baseline, 1, 3, 11 and 16 weeks post-SE) and group-by-time interaction were fixed factors. Ventricular volume was used as covariate. Significant effects and interactions were investigated using least-significant-difference tests, and to correct for multiple comparisons, the Bonferroni correction was used. A significance level of 0.05 was used for main effects and interactions for the analysis of the global metrics, while for nodal degree, a significance level of 0.0026 was used to correct for multiple comparisons between nodes and for the fixel metrics in white matter tracts, and a significance level of 0.0083 was used to correct for multiple comparisons between tracts. Ventricular volume was analyzed in the same way, but without covariate and with a significance level of 0.05.

For FBA, differences in fixel metrics between groups were analyzed at each time point using the *fixelcfstats* command in MRtrix3, which uses connectivity-based fixel enhancement and non-parametric permutation testing. The significance level after family-wise error rate (FWE) correction was 0.05.

Correlations between global degree, global and local efficiency post-SE on the one hand and FD, FC and FDC post-SE, averaged over the white matter tracts, on the other hand were analyzed using the Pearson correlation coefficient. A significance level of 0.008 was used to correct for multiple comparisons between parameters. Correlations of global network metrics, nodal network metrics and fixel metrics with seizure frequency were assessed using Spearman's rank correlation coefficient.

## 5.3 Results

### 5.3.1 Ventricular volume

In Figure 5.2A, a T2 scan of a representative animal of each group at each time point is shown with delineation of the ventricles. Statistical analysis of the ventricular volume showed a significant group-by-time interaction ( $F_{4,57.835}=4.426$ ,  $p=0.003$ ). Ventricular volume was significantly higher in the IPKA group compared to the control group during early epileptogenesis (1 and 3 weeks post-SE). During late epileptogenesis (11 and 16 weeks post-SE), ventricular volume was still increased in the IPKA group. In addition, there was a significant increase in ventricular volume in the control group (Figure 5.2B).

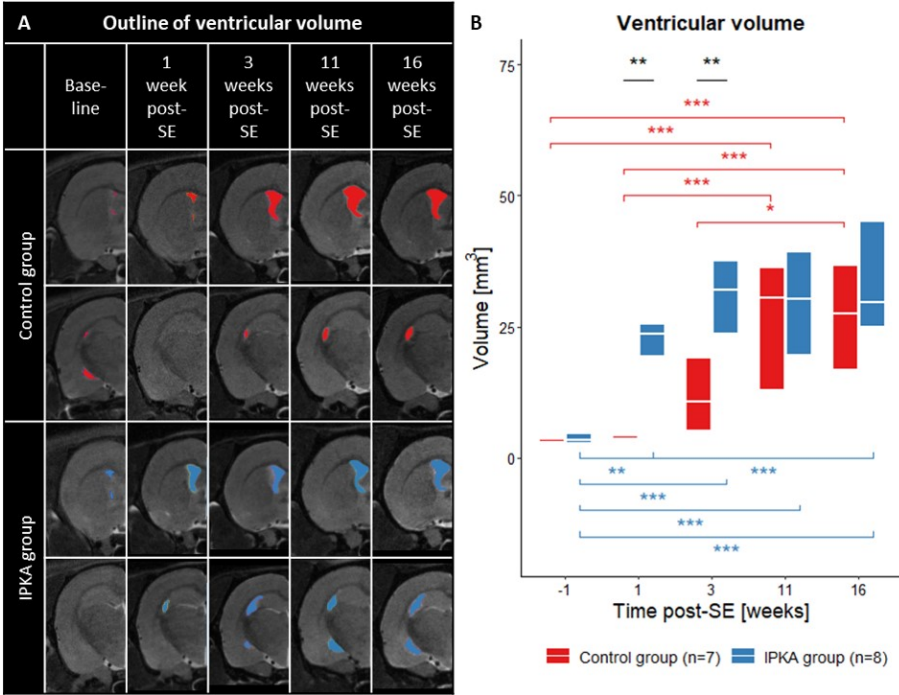


**Figure 5.2:** A) Outline of ventricular volume on T2 image of representative IPKA animal (KADTI5) and control animal (MG008) and B) Changes in ventricular volume during epileptogenesis in IPKA group and control group. Data are visualized as a boxplot with median and interquartile range (\*  $p < 0.05$ , \*\*  $p < 0.01$ , \*\*\*  $p < 0.001$ ).

### 5.3.2 Global network metrics

Changes in global network metrics during epileptogenesis are visualized in Figure 5.3. A significant group-by-time interaction was found for global degree, characteristic path length, global and local efficiency ( $F_{4,47.315} = 7.919$ ,  $p < 0.001$ ;  $F_{4,46.555} = 9.196$ ,  $p < 0.001$ ;  $F_{4,46.808} = 6.840$ ,  $p < 0.001$ ;  $F_{4,47.264} = 7.086$ ,  $p < 0.001$ , respectively), but not for  $C_p$  ( $F_{4,47.779} = 0.978$ ,  $p = 0.429$ ). Degree, global and local efficiency were significantly lower and characteristic path length significantly higher in the IPKA group compared to the control group 1, 3 and 16 weeks post-SE.

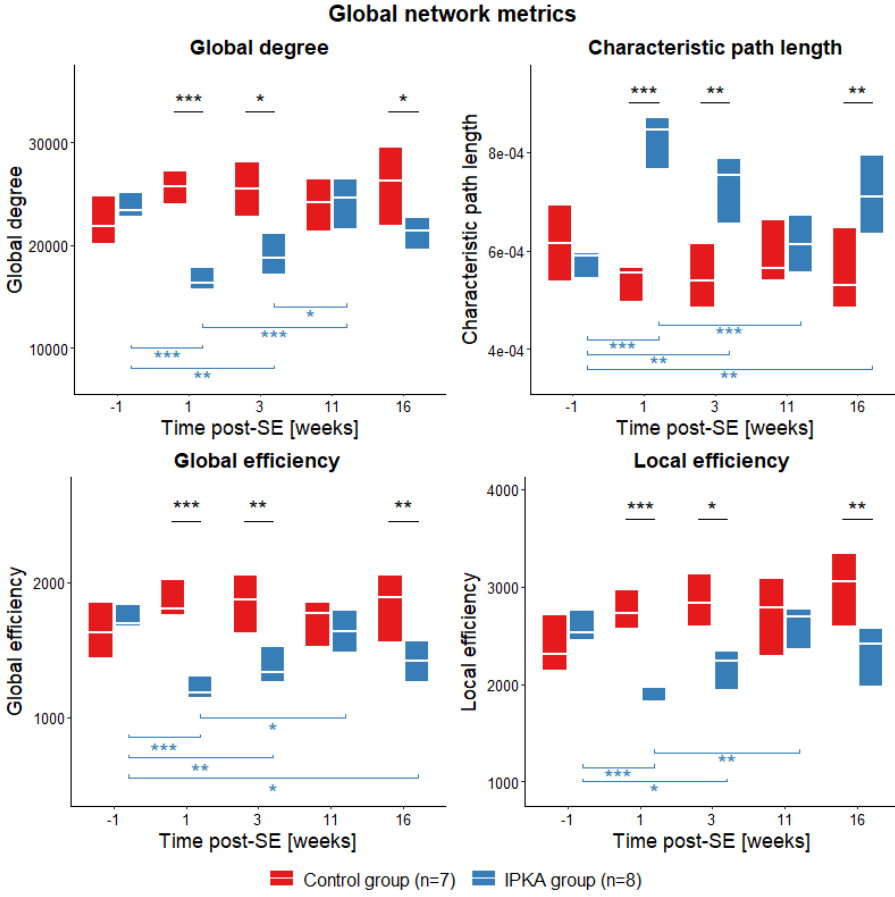


**Figure 5.3:** Changes in global network metrics during epileptogenesis in IPKA group and control group: global degree, characteristic path length, global efficiency and local efficiency. Data are visualized as a boxplot with median and interquartile range (\*  $p < 0.05$ , \*\*  $p < 0.01$ , \*\*\*  $p < 0.001$ ).

### 5.3.3 Nodal degree

A significant group-by-time interaction was found for nodal degree in hippocampus, subiculum, thalamus, septum, dorsolateral orbitofrontal cortex, globus pallidus, nucleus accumbens, somatosensory cortex, cingulate cortex, and caudate putamen (Table 5.2). In hippocampus, subiculum, thalamus, septum, dorsolateral orbitofrontal cortex, globus pallidus, and

**Table 5.2:** Results of statistical analysis using linear mixed-effects model of nodal degree in cingulum (Cg), caudate putamen (CPu), dorso-lateral orbitofrontal cortex (DLO), hippocampus (Hip), nucleus accumbens (NAc), septum (Sep), somatosensory cortex (SSC), subiculum (Sub) and thalamus (Thal).

ROI	Group-by-time interaction		ROI	Group-by-time interaction	
Cg	$F_{4,55.9}=8.39$	$p<0.001$	NAc	$F_{4,57.0}=12.9$	$p<0.001$
CPu	$F_{4,56.2}=6.17$	$p<0.001$	Sep	$F_{4,56.4}=19.0$	$p<0.001$
DLO	$F_{4,56.8}=7.21$	$p<0.001$	SSC	$F_{4,56.0}=6.01$	$p<0.001$
GP	$F_{4,55.8}=10.9$	$p<0.001$	Sub	$F_{4,52.7}=14.6$	$p<0.001$
Hip	$F_{4,54.6}=7.13$	$p<0.001$	Thal	$F_{4,54.5}=9.18$	$p<0.001$

nucleus accumbens (Figure 5.4A), nodal degree was significantly lower in the IPKA group compared to the control group during early epileptogenesis. During late epileptogenesis, degree increased significantly in these regions in the IPKA group compared to early epileptogenesis. In somatosensory cortex, cingulate cortex, and caudate putamen (Figure 5.4B), degree was significantly lower in the IPKA group compared to the control group or significantly decreased during both early and late epileptogenesis.

### 5.3.4 DTI metrics in white matter tracts

A significant group-by-time interaction was found for RD in external capsule ( $F_{4,44.0}=4.16$ ,  $p=0.006$ ), MD in internal capsule ( $F_{4,45.9}=3.99$ ,  $p=0.007$ ), and FA and RD in fimbria ( $F_{4,44.9}=4.39$ ,  $p=0.004$  and  $F_{4,44.6}=4.69$ ,  $p=0.003$ , respectively) (Figure 5.5). In the IPKA group, RD is significantly higher in external capsule and fimbria, and MD in internal capsule, during early and late epileptogenesis compared to the control group. In fimbria, FA is significantly lower in the IPKA group compared to the control group during late epileptogenesis.

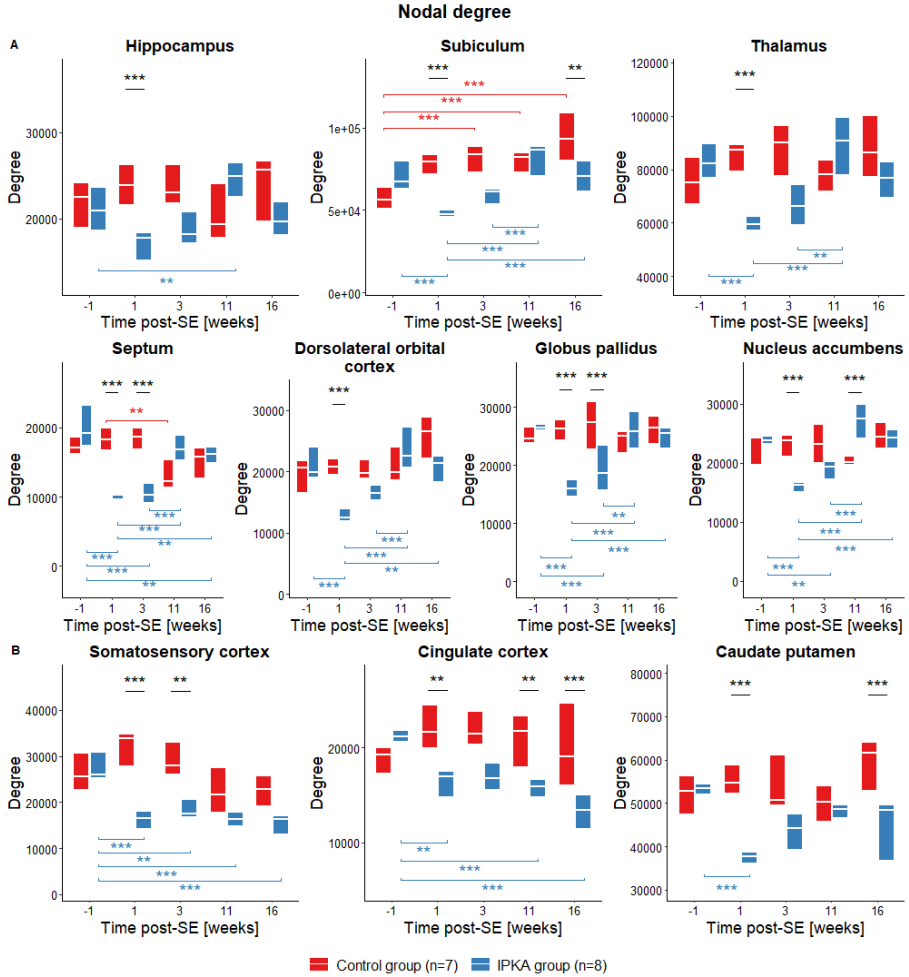


**Figure 5.4:** Changes in nodal degree during epileptogenesis in IPKA group and control group in A) hippocampus, subiculum, thalamus, septum, dorsolateral orbitofrontal cortex, globus pallidus and nucleus accumbens, and B) somatosensory cortex, cingulate cortex and caudate putamen. Data are visualized as a boxplot with median and interquartile range (\*  $p < 0.05$ , \*\*  $p < 0.01$ , \*\*\*  $p < 0.001$ ).

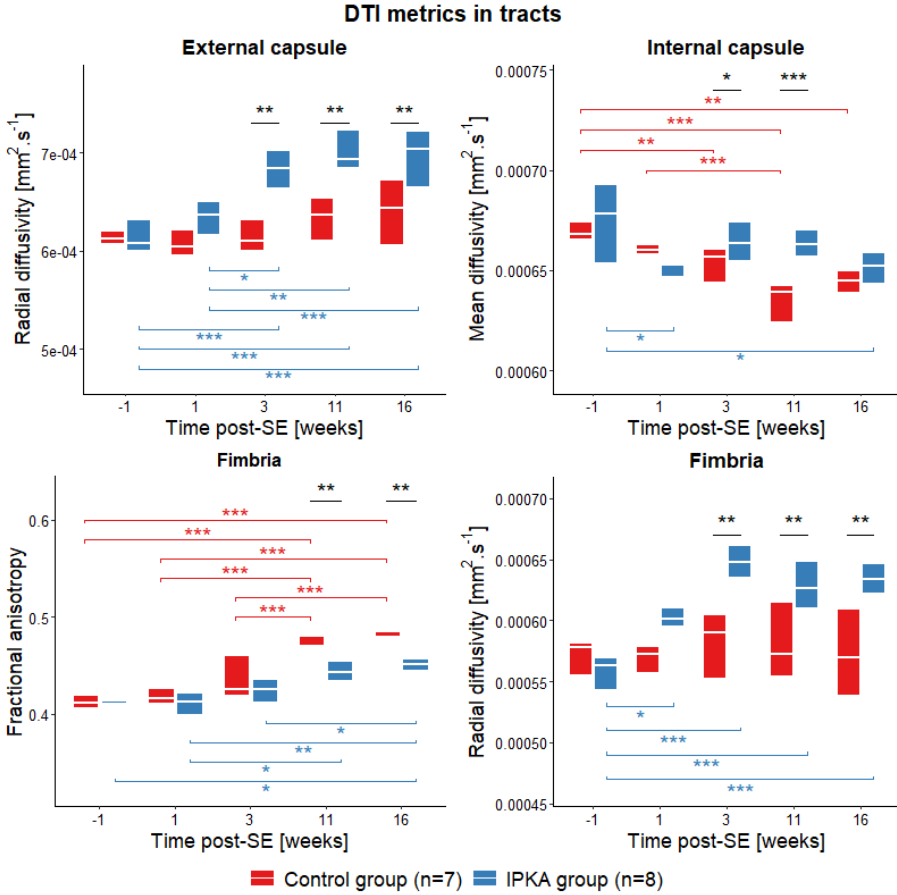


**Figure 5.5:** Significant changes in DTI metrics in white matter tracts during epileptogenesis. Data are visualized as a boxplot with median and interquartile range (\*  $p < 0.05$ , \*\*  $p < 0.01$ , \*\*\*  $p < 0.001$ ).

### 5.3.5 Fixel metrics in white matter tracts

Fixel metrics were analyzed using FBA and ROI-based analysis. The white matter tracts under investigation are visualized in Figure 5.6, overlaid on the template FOD image. Using FBA, fixels in which FD, FC and FDC were significantly different between IPKA animals and controls during early (1 and/or 3 weeks post-SE) and late epileptogenesis (11 and/or 16 weeks post-SE) were identified. The white matter tracts containing these fixels are visualized in Figure 5.7. Changes in fixel met-

rics in white matter tracts over time were assessed using a ROI-based analysis. Average FD, FC and FDC were calculated for each tract and significant differences were identified using a linear mixed-effects model (LMEM). In Figure 5.8, changes in FDC during epileptogenesis in anterior commissure, corpus callosum and fimbria are visualized.

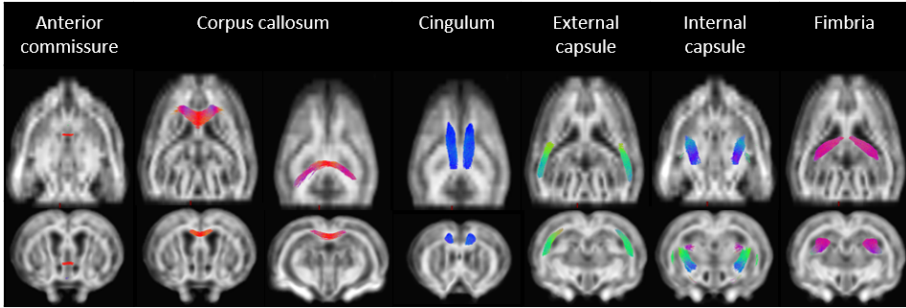


**Figure 5.6:** White matter tracts overlaid on FOD image of template: anterior commissure, corpus callosum, cingulum, external capsule, internal capsule and fimbria.

FBA revealed a significantly lower FC in the IPKA group in anterior commissure during early epileptogenesis (Figure 5.7). Using ROI-based analysis, a significant group-by-time interaction was found for FC and FDC ( $F_{4,49.6}=4.76$ ,  $p=0.002$  and  $F_{4,49.6}=4.44$ ,  $p=0.004$ , respectively). FC and FDC were significantly lower in the IPKA group compared to the control group during early epileptogenesis (Figure 5.8).

In corpus callosum, FBA showed that FD was significantly lower in the IPKA group compared to the control group during early epileptogenesis, while FDC was significantly lower in the IPKA group during both early and late epileptogenesis (Figure 5.7). This was also observed using ROI-based analysis, as there was a significant group-by-time interaction for FD and FDC ( $F_{4,49.4}=7.45$ ,  $p<0.001$  and  $F_{4,50.3}=5.69$ ,  $p=0.001$ , respectively) (Figure 5.8).

In cingulum, FBA revealed that FC was significantly lower in the IPKA group compared to the control group during early and late epileptogenesis, and that FDC was significantly lower in the IPKA group during late

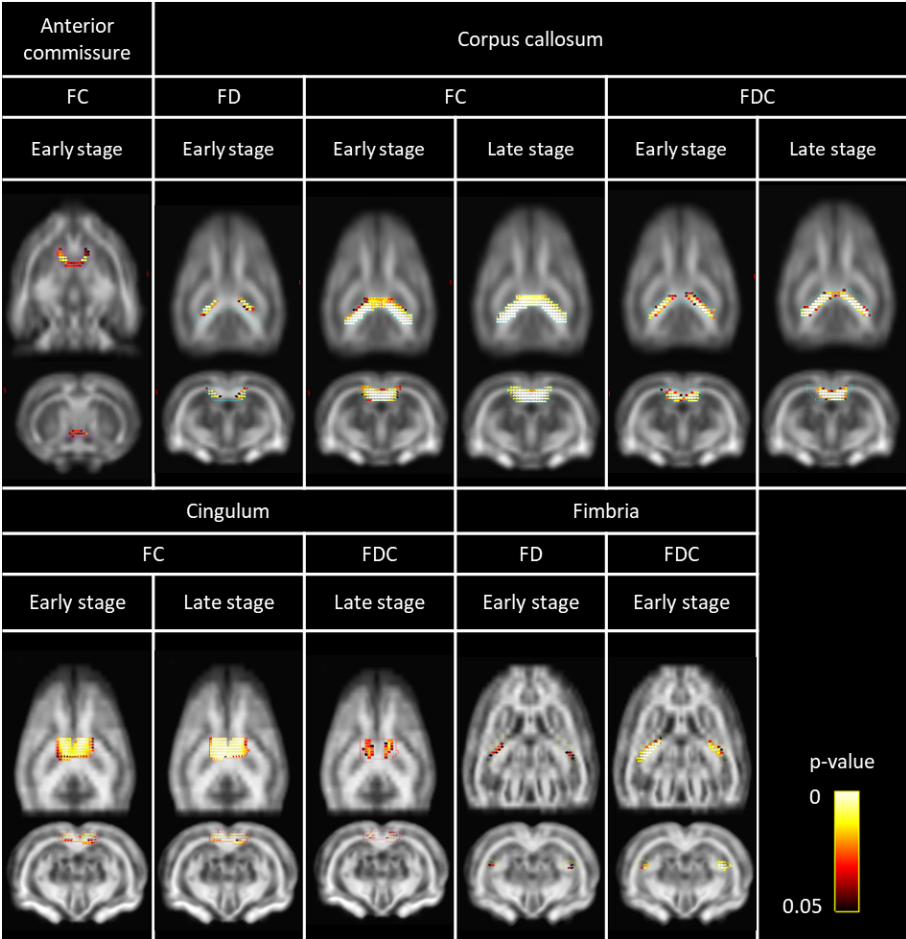


**Figure 5.7:** White matter tracts containing fixels in which FD, FC and FDC are significantly lower in the IPKA group compared to controls during early (1 and/or 3 weeks post-SE) and late epileptogenesis (11 and/or 16 weeks post-SE), identified using FBA. Colors represent FWE-corrected p-values.

epileptogenesis (Figure 5.7). No significant group-by-time interaction was found for cingulum using ROI-based analysis.

Neither FBA nor ROI-based analysis revealed any significant differences or changes in external capsule.

In internal capsule, no significant differences in fixel metrics could be demonstrated using FBA. However, a significant group-by-time inter-

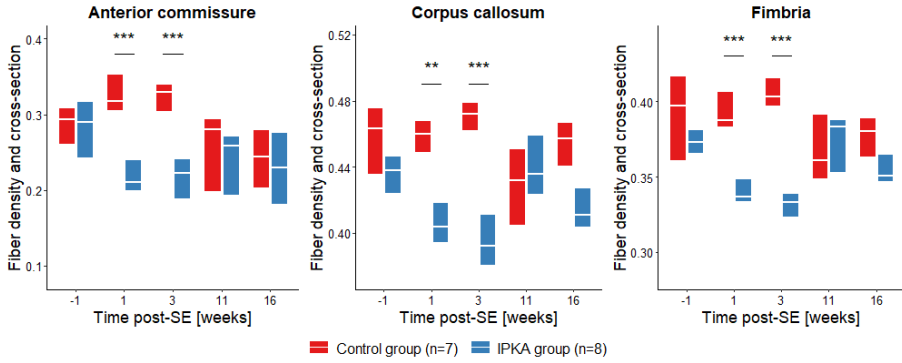


**Figure 5.8:** Changes in fiber density and cross-section (FDC) during epileptogenesis in anterior commissure, corpus callosum and fimbria. Data are visualized as a boxplot with median and interquartile range (\*\*  $p < 0.01$ , \*\*\*  $p < 0.001$ ).

action was found for FD ( $F_{4,48.6} = 0.007$ ) using ROI-based analysis. FD was significantly lower in the IPKA group compared to the control group during late epileptogenesis.

FBA revealed that in fimbria, FD and FDC were significantly lower in the IPKA group compared to the control group during early epileptogenesis (Figure 5.7). This was also demonstrated using ROI-based analysis, where a significant group-by-time interaction was found for FD and FDC ( $F_{4,49.9} = 7.55$ ,  $p < 0.001$  and  $F_{4,50.1} = 4.43$ ,  $p = 0.003$ , respectively) (Figure 5.8).

### 5.3.6 Correlations between network metrics and fixel metrics

In Figure 5.9, correlations between the network metrics global degree, global and local efficiency post-SE, and the fixel metrics FD, FC and FDC are visualized. Degree, and global and local efficiency were positively correlated with FC and FDC in the IPKA group and with FD and FDC in the control group. In both groups, the correlation between network metrics and FDC was strongest.

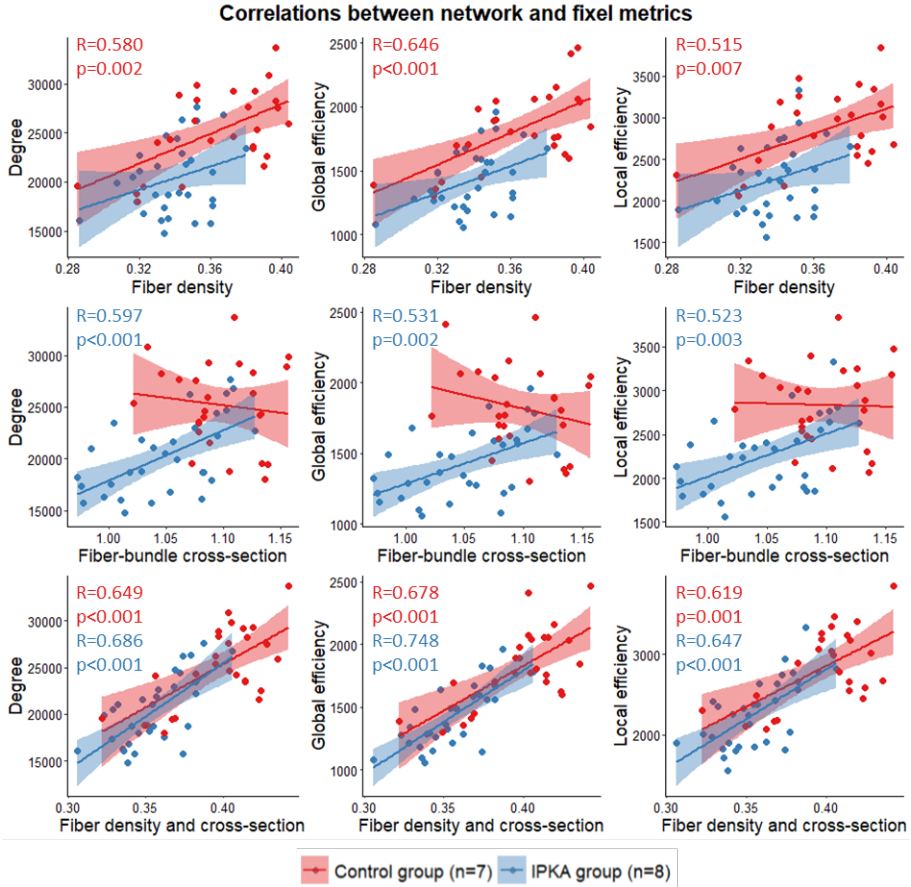


**Figure 5.9:** Correlations between network metrics (degree, global efficiency and local efficiency) and fixel metrics (FD, FC and FDC) at all time points post-SE. Data are visualized as a scatter plot with regression line and 95% confidence interval. When significant correlations were observed, R- and p-values are added to the scatter plot. FC and FDC were significantly correlated with network metrics in the IPKA group, and FD and FDC were significantly correlated with network metrics in the control group.

### 5.3.7 EEG recording

EEG was recorded in 8 IPKA animals for 6 consecutive days. All animals displayed epilepsy with spontaneous seizures. On average, the animals had a total of 127 seizures (range: 31 to 218) during the entire recording

period, or 23 seizures per day. However, we could not demonstrate any significant correlations between seizure frequency and global or nodal network metrics, nor with any fixel metric or ventricular volume.

## 5.4 Discussion

The objectives of this study were twofold: to investigate 1) how the structural brain network changes during epileptogenesis in the IPKA rat model, and which brain areas are most affected and 2) whether the changes in network topology are related to changes in the integrity of the white matter assessed using fixel-based analysis.

### 5.4.1 Disruption of the structural brain network during epileptogenesis

Using diffusion-weighted MRI in combination with the multi-shell multi-tissue constrained spherical deconvolution model, we found that global degree and local efficiency, measures of structural connectivity and segregation or local interconnectivity, respectively, significantly decreased in the IPKA group. In addition, global efficiency decreased and characteristic path length increased, which points to a decrease in integration or overall communication efficiency.

Nodal degree decreased significantly during early epileptogenesis in hippocampus, subiculum, thalamus, septum, dorsolateral orbitofrontal cortex, globus pallidus and nucleus accumbens. In cingulate cortex, caudate putamen, and somatosensory cortex, nodal degree decreased during early epileptogenesis and remained decreased during late epileptogenesis. Many of these regions (hippocampus, thalamus, septum, dorsolateral orbitofrontal cortex, cingulate cortex, and somatosensory cortex) are also part of the rat default-mode network (DMN) [27, 28]. This indicates that mainly regions of the limbic system and the DMN are affected during epileptogenesis.

Our results are in line with most patient studies investigating structural connectivity in TLE using DTI-based tractography, where TLE patients

are compared to controls at one specific time point. Kamiya et al. [12] found network alterations in the ipsilateral temporoparietal lobe, including regions of the DMN, in patients with TLE. They reported decreased local efficiency and degree in multiple brain regions, including posterior cingulate gyrus, cuneus, and hippocampus [12]. Bernhardt et al. [10] reported decreased global and local efficiency in TLE patients, suggesting decreased connectivity, mainly within temporolimbic networks that are strongly connected to hippocampus. Liao et al. [9] found decreased structural connectivity in the DMN in TLE. DeSalvo et al. [11] reported decreased structural connectivity in orbitofrontal, temporal and posterior cingulate cortex, and precuneus, but increased local efficiency in frontal, insular, posterior cingulate and occipital cortex, and precuneus, in patients with TLE. Bonilha et al. [29] found decreased fiber density in patients with TLE, but increased clustering in the limbic network and increased local efficiency, degree and clustering coefficient in insula, superior temporal regions, and thalamus. In hippocampus, clustering coefficient and local efficiency were decreased, while nodal degree was increased [29]. To the best of our knowledge, the study of Besson et al. [16] is the only one using probabilistic tractography based on FOD to investigate structural connectivity in TLE. They reported decreased connectivity in left TLE patients compared to controls and found that mainly the inferolateral cortex, temporal pole, and perisylvian cortex were affected in these patients. In patients with right TLE, connectivity was decreased to a lesser extent, only affecting limbic structures and ipsilateral temporal cortex [16].

Our study is the first to investigate structural network topology in a rat model of TLE using longitudinal multi-shell dMRI and FOD-based tractography. However, several studies have investigated functional network topology in this model. Pirttimäki et al. [30] found altered functional connectivity in several brain regions 1 week post-SE in the IPKA rat model for TLE. One or two months post-SE, functional connectivity was decreased, mainly between somatosensory cortex and thalamus, and perirhinal and piriform cortices [30]. In the same model, Gill et al. [31] reported increased functional connectivity within the temporal regions,

limbic network and DMN 4 to 5 weeks post-SE. In the pilocarpine rat model of TLE, Jiang et al. [32] found decreased functional connectivity within the hippocampal network, mainly in hippocampus, amygdala, thalamus, motor cortex, and somatosensory cortex, and increased functional connectivity in visual cortex, mesencephalon, and insula. Bernhardt et al. [10] reported that functional connectivity was altered in several regions of the DMN and found wide-spread network connectivity hyposynchrony 2 weeks post-SE in the IPKA rat model for TLE. In the same model, we previously reported that functional connectivity, segregation and integration decreased 3 weeks post-SE and remained decreased during epileptogenesis. Regions of the DMN were affected most, retrosplenial cortex in particular [33]. Using dynamic functional connectivity analysis, we demonstrated that functional connectivity states with a lower mean functional connectivity, integration, and segregation, occurred more often in IPKA animals compared to controls [34].

Overall, our findings are in line with studies investigating structural connectivity in patients with TLE where structural connectivity, global efficiency or integration, and local efficiency or segregation, are decreased in TLE patients, and that mainly regions of the DMN and the limbic network are affected. In addition, our results correspond with findings of reduced functional connectivity in animal models of TLE. Our longitudinal study design also demonstrates that changes in structural connectivity are dynamic and therefore vary with time. In most regions that are part of the DMN, structural connectivity is decreased in early epileptogenesis. During late epileptogenesis, structural connectivity remains low in some brain regions (somatosensory cortex, cingulate cortex, and caudate putamen), while it increases again in other brain regions (hippocampus, subiculum, thalamus, septum, dorsolateral orbitofrontal cortex, globus pallidus, and nucleus accumbens).

Whether these changes in network topology are related to changes in white matter integrity was the second objective of our study. Our hypothesis is that these changes might be related to neuronal degeneration and gliosis, the two main neuropathological changes during epileptogenesis in the IPKA model [35], which could be further clarified by fixel-based

analysis as explained below.

### **5.4.2 Increased diffusivity in white matter tracts during epileptogenesis**

Our results indicate that diffusivity increases in white matter tracts during early and late epileptogenesis, especially in fimbria and external capsule. In control animals, FA increased over time in fimbria, which is most likely related to normal maturation of the brain, in particular myelination, since the animals are only six weeks old during the first scanning session [36]. In IPKA animals, FA increased more slowly, leading to a decreased FA compared to control animals during late epileptogenesis. Our results are partly in line with other DTI studies in animal models of epilepsy, which reported decreased diffusivity during epileptogenesis. FA is typically increased in dentate gyrus, which may reflect mossy fiber sprouting and reorganization of axons [35]. On the other hand, DTI studies in TLE patients found that FA was reduced in several white matter regions, and diffusivity was increased [7, 37, 38], which is consistent with our results. However, DTI metrics are not specific to microstructure or pathology and may be erroneous in the presence of crossing fibers [14, 15], and more advanced analysis methods, such as fixel-based analysis, could provide more information about the underlying microstructural changes during epileptogenesis.

### **5.4.3 Decrease in FD and FDC in white matter tracts during epileptogenesis**

The analysis of the fixel metrics revealed that FD was decreased during early and late epileptogenesis in the IPKA group in corpus callosum, internal capsule, and fimbria. FDC was decreased during early epileptogenesis in anterior commissure, corpus callosum and fimbria, and in corpus callosum and cingulum during late epileptogenesis. This indicates that there is a decrease in intra-axonal volume fraction. This is in line with the neuropathological changes that are known to occur after SE in the IPKA model. Following the initial insult, it has been shown that neuronal loss occurs in hippocampus, entorhinal cortex, subiculum,

and amygdala, but also in some extratemporal regions including thalamus, caudate putamen, and cerebral cortex, and especially piriform cortex. During this early phase, gliosis also takes place in hippocampus, piriform cortex, entorhinal cortex, olfactory bulb, substantia nigra, thalamus, and mesencephalon [35, 39, 40]. Both neuronal loss and gliosis will be reflected as a decrease in intra-axonal volume fraction.

During late epileptogenesis, there is less (micro)gliosis compared to the early phase [35, 39]. In this study, we have observed that in fimbria, and to a lesser extent in corpus callosum, FDC seems to increase during late epileptogenesis, which may be related to reduced gliosis. On the other hand, it could also be associated with the occurrence of spontaneous seizures during this stage. The animals had on average 23 seizures per day, meaning it is likely that they had a seizure within hours before the scanning session. During the periictal period, cerebral edema and cell swelling can cause a temporary decrease in diffusivity [41, 42], which may be reflected in an increase in FDC.

These findings are also in line with those of Vaughan et al. [18], who investigated tract-specific atrophy in focal epilepsy and reported decreased FDC in fornix, uncinate, inferior longitudinal, inferior fronto-occipital and arcuate fasciculus, cingulum, anterior commissure, tapetum, and corpus callosum in patients with TLE. The decrease in FDC was accompanied by a decrease in both FD and FC and was most pronounced in the temporal pole, inferior temporal white matter and anterior commissure [18]. Feshki et al. [17] reported decreased FD and FDC in white matter in both hemispheres in TLE patients.

Moreover, we also found that global degree and global and local efficiency in the structural brain network were positively correlated with FC and FDC in IPKA animals. This further indicates that decreased degree, integration and segregation post-SE are likely related to decreased axonal density or decreased white matter integrity in the main white matter tracts in the rat brain.

#### 5.4.4 Decreased FD in control group: related to social isolation?

Fixel metrics also seemed to change over time in the control group. During the later time points, FD was decreased in corpus callosum, internal capsule, and fimbria, and FC was increased in anterior commissure. This indicates that the intra-axonal volume fraction decreases, while the total intra-axonal volume remains stable. During these later time points, we also see an increase in ventricular volume in this group. Since the animals were first scanned when they were only six weeks old, brain maturation might play a role. However, this would lead to a decrease in diffusivity, related to myelination, which does not correspond with our findings [36]. Another reason for these changes could be social isolation. To match the housing situation of the IPKA animals, control animals were housed separately. In the later phase of the experiment, the animals have therefore been housed separately for more than 10 weeks. Social isolation is known to cause depression in rats and is even used to create a rat model for depression [43–45]. In the chronic mild stress (CMS) model, another rat model for depression, a dMRI study found increased mean and radial diffusivity and decreased fractional anisotropy, which could be related to demyelination and possibly edema or inflammation [46, 47]. Several other studies reported alterations in diffusion tensor and kurtosis metrics and in neurite density in this model, mainly in hippocampus, amygdala, and caudate putamen, which were thought to be related to atrophy in hippocampus and hypertrophy or arborization in amygdala [48–50]. This indicates that social isolation and/or depression might be related to the changes in fixel metrics in the control group in the late stage of the experiment.

#### 5.4.5 Limitation

A possible limitation of this study is the small sample size that was used for data analysis. Future studies with larger sample sizes are required to validate the results.

## 5.5 Conclusion

In this longitudinal multi-shell dMRI study, changes in structural network topology and white matter integrity during epileptogenesis in the IPKA rat model for TLE were assessed using a combination of whole-brain tractography, graph theory and fixel-based analysis. We found a decrease in structural connectivity, integration and segregation in IPKA animals compared to controls during both early and late epileptogenesis. Structural connectivity was predominantly decreased in regions of the limbic system and DMN, mainly during early epileptogenesis. In addition, FD and FDC decreased post-SE in several white matter tracts, including anterior commissure, corpus callosum, cingulum, internal capsule, and fimbria indicating intra-axonal volume fraction decreased, which may be related to neuronal degeneration and gliosis.

## Bibliography

- [1] R. S. Fisher, W. V. E. Boas, W. Blume, C. Elger, P. Genton, P. Lee, and J. Engel Jr, “Epileptic seizures and epilepsy: definitions proposed by the international league against epilepsy (ILAE) and the international bureau for epilepsy (IBE),” *Epilepsia*, vol. 46, no. 4, pp. 470–472, 2005.
- [2] P. Kwan and M. J. Brodie, “Early identification of refractory epilepsy,” *New England Journal of Medicine*, vol. 342, no. 5, pp. 314–319, 2000.
- [3] J. Engel Jr, “Approaches to refractory epilepsy,” *Annals of Indian Academy of Neurology*, vol. 17, no. Suppl 1, p. S12, 2014.
- [4] E. M. Goldberg and D. A. Coulter, “Mechanisms of epileptogenesis: a convergence on neural circuit dysfunction,” *Nature Reviews Neuroscience*, vol. 14, no. 5, pp. 337–349, 2013.
- [5] S. Tavakol, J. Royer, A. J. Lowe, L. Bonilha, J. I. Tracy, G. D. Jackson, J. S. Duncan, A. Bernasconi, N. Bernasconi, and B. C. Bernhardt, “Neuroimaging and connectomics of drug-resistant epilepsy at multiple scales: From focal lesions to macroscale networks,” *Epilepsia*, vol. 60, no. 4, pp. 593–604, apr 2019. [Online]. Available: <https://onlinelibrary.wiley.com/doi/abs/10.1111/epi.14688>
- [6] F. Xiao, D. An, and D. Zhou, “Functional mri-based connectivity analysis: a promising tool for the investigation of the pathophysiology and comorbidity of epilepsy,” *Seizure*, vol. 44, pp. 37–41, 2017.
- [7] W. M. Otte, R. M. Dijkhuizen, M. P. van Meer, W. S. van der Hel, S. A. Verlinde, O. van Nieuwenhuizen, M. A. Viergever, C. J. Stam, and K. P. Braun, “Characterization of functional and structural integrity in experimental focal epilepsy: reduced network efficiency coincides with white matter changes,” *PloS one*, vol. 7, no. 7, p. e39078, 2012.

- [8] D. W. Gross, “Diffusion tensor imaging in temporal lobe epilepsy,” *Epilepsia*, vol. 52, no. SUPPL. 4, pp. 32–34, jul 2011. [Online]. Available: <https://onlinelibrary.wiley.com/doi/full/10.1111/j.1528-1167.2011.03149.x><https://onlinelibrary.wiley.com/doi/abs/10.1111/j.1528-1167.2011.03149.x><https://onlinelibrary.wiley.com/doi/10.1111/j.1528-1167.2011.03149.x>
- [9] W. Liao, Z. Zhang, Z. Pan, D. Mantini, J. Ding, X. Duan, C. Luo, Z. Wang, Q. Tan, G. Lu *et al.*, “Default mode network abnormalities in mesial temporal lobe epilepsy: a study combining fmri and dti,” *Human brain mapping*, vol. 32, no. 6, pp. 883–895, 2011.
- [10] B. C. Bernhardt, F. Fadaie, M. Liu, B. Caldairou, S. Gu, E. Jefferies, J. Smallwood, D. S. Bassett, A. Bernasconi, and N. Bernasconi, “Temporal lobe epilepsy: Hippocampal pathology modulates connectome topology and controllability,” *Neurology*, vol. 92, no. 19, pp. E2209–E2220, may 2019. [Online]. Available: <https://n.neurology.org/content/92/19/e2209><https://n.neurology.org/content/92/19/e2209.abstract>
- [11] M. N. DeSalvo, L. Douw, N. Tanaka, C. Reinsberger, and S. M. Stuffebeam, “Altered Structural Connectome in Temporal Lobe Epilepsy,” *Radiology*, vol. 270, no. 3, pp. 842–848, mar 2014. [Online]. Available: <http://pubs.rsna.org/doi/10.1148/radiol.13131044>
- [12] K. Kamiya, S. Amemiya, Y. Suzuki, N. Kunii, K. Kawai, H. MORI, A. Kunimatsu, N. Saito, S. Aoki, and K. Ohtomo, “Machine Learning of DTI Structural Brain Connectomes for Lateralization of Temporal Lobe Epilepsy,” *Magnetic Resonance in Medical Sciences*, vol. 15, no. 1, pp. 121–129, 2016. [Online]. Available: <https://www.jstage.jst.go.jp/article/mrms/15/1/15{ }2015-0027/{ }article>
- [13] D. K. Jones, T. R. Knösche, and R. Turner, “White matter integrity, fiber count, and other fallacies: the do’s and don’ts of diffusion mri,” *Neuroimage*, vol. 73, pp. 239–254, 2013.

- [14] B. Jeurissen, J.-D. Tournier, T. Dhollander, A. Connelly, and J. Sijbers, “Multi-tissue constrained spherical deconvolution for improved analysis of multi-shell diffusion mri data,” *NeuroImage*, vol. 103, pp. 411–426, 2014.
- [15] D. A. Raffelt, J.-D. Tournier, R. E. Smith, D. N. Vaughan, G. Jackson, G. R. Ridgway, and A. Connelly, “Investigating white matter fibre density and morphology using fixel-based analysis,” *Neuroimage*, vol. 144, pp. 58–73, 2017.
- [16] P. Besson, V. Dinkelacker, R. Valabregue, L. Thivard, X. Leclerc, M. Baulac, D. Sammler, O. Colliot, S. Lehericy, S. Samson, and S. Dupont, “Structural connectivity differences in left and right temporal lobe epilepsy,” *NeuroImage*, vol. 100, pp. 135–144, oct 2014.
- [17] M. Feshki, E. Parham, and H. Soltanin-Zadeh, “Fixel-Based Analysis of White Matter in Temporal Lobe Epilepsy,” in *2018 25th Iranian Conference on Biomedical Engineering and 2018 3rd International Iranian Conference on Biomedical Engineering, ICBME 2018*. Institute of Electrical and Electronics Engineers Inc., jul 2018.
- [18] D. N. Vaughan, D. Raffelt, E. Curwood, M.-H. Tsai, J.-D. Tournier, A. Connelly, and G. D. Jackson, “Tract-specific atrophy in focal epilepsy: Disease, genetics, or seizures?” *Annals of Neurology*, vol. 81, no. 2, pp. 240–250, feb 2017. [Online]. Available: <http://doi.wiley.com/10.1002/ana.24848>
- [19] J. L. Hellier, P. R. Patrylo, P. S. Buckmaster, and F. E. Dudek, “Recurrent spontaneous motor seizures after repeated low-dose systemic treatment with kainate: assessment of a rat model of temporal lobe epilepsy,” *Epilepsy research*, vol. 31, no. 1, pp. 73–84, 1998.
- [20] G. Paxinos and C. Watson, *The Rat Brain in Stereotaxic Coordinates*, 7th ed. Elsevier Science, 2013.
- [21] J.-D. Tournier, R. Smith, D. Raffelt, R. Tabbara, T. Dhollander, M. Pietsch, D. Christiaens, B. Jeurissen, C.-H. Yeh, and A. Connelly, “Mrtrix3: A fast, flexible and open software framework for

- medical image processing and visualisation,” *NeuroImage*, vol. 202, p. 116137, 2019.
- [22] A. Leemans, B. Jeurissen, J. Sijbers, and D. K. Jones, “ExploreDTI: a graphical toolbox for processing, analyzing, and visualizing diffusion MR data,” *17th Annual Meeting of Intl Soc Mag Reson Med*, p. 3537, 2009. [Online]. Available: <http://www.exploredti.com>.
- [23] J. Wang, X. Wang, M. Xia, X. Liao, A. Evans, and Y. He, “Gretna: a graph theoretical network analysis toolbox for imaging connectomics,” *Frontiers in human neuroscience*, vol. 9, p. 386, 2015.
- [24] M. Rubinov and O. Sporns, “Complex network measures of brain connectivity: uses and interpretations,” *Neuroimage*, vol. 52, no. 3, pp. 1059–1069, 2010.
- [25] J. Wang, X. Zuo, and Y. He, “Graph-based network analysis of resting-state functional mri,” *Frontiers in systems neuroscience*, vol. 4, p. 16, 2010.
- [26] D. A. Duricki, S. Soleman, and L. D. Moon, “Analysis of longitudinal data from animals with missing values using spss,” *Nature protocols*, vol. 11, no. 6, pp. 1112–1129, 2016.
- [27] H. Lu, Q. Zou, H. Gu, M. E. Raichle, E. A. Stein, and Y. Yang, “Rat brains also have a default mode network,” *Proceedings of the National Academy of Sciences*, vol. 109, no. 10, pp. 3979–3984, 2012.
- [28] A. Sierakowiak, C. Monnot, S. N. Aski, M. Uppman, T.-Q. Li, P. Damberg, and S. Brené, “Default Mode Network, Motor Network, Dorsal and Ventral Basal Ganglia Networks in the Rat Brain: Comparison to Human Networks Using Resting State-fMRI,” 2015. [Online]. Available: <http://dx.doi.org/10>.
- [29] L. Bonilha, T. Nesland, G. U. Martz, J. E. Joseph, M. V. Spampinato, J. C. Edwards, and A. Tabesh, “Medial temporal lobe epilepsy is associated with neuronal fibre loss and paradoxical increase in structural connectivity of limbic structures,” *Journal of*

- Neurology, Neurosurgery and Psychiatry*, vol. 83, no. 9, pp. 903–909, sep 2012. [Online]. Available: <http://www.fmrib.ox.ac.uk/fsl>
- [30] T. Pirttimäki, R. A. Salo, A. Shatillo, M. I. Kettunen, J. Paasonen, A. Sierra, K. Jokivarsi, V. Leinonen, P. Andrade, S. Quittek *et al.*, “Implantable rf-coil with multiple electrodes for long-term eeg-fmri monitoring in rodents,” *Journal of neuroscience methods*, vol. 274, pp. 154–163, 2016.
- [31] R. S. Gill, S. M. Mirsattari, and L. S. Leung, “Resting state functional network disruptions in a kainic acid model of temporal lobe epilepsy,” *NeuroImage: Clinical*, vol. 13, pp. 70–81, 2017.
- [32] Y. Jiang, C.-L. Han, H.-G. Liu, X. Wang, X. Zhang, F.-G. Meng, and J.-G. Zhang, “Abnormal hippocampal functional network and related memory impairment in pilocarpine-treated rats,” *Epilepsia*, vol. 59, no. 9, pp. 1785–1795, 2018.
- [33] E. Christiaen, M.-G. Goossens, R. Raedt, B. Descamps, L. E. Larsen, E. Craey, E. Carrette, K. Vonck, P. Boon, and C. Vanhove, “Alterations in the functional brain network in a rat model of epileptogenesis: A longitudinal resting state fmri study,” *Neuroimage*, vol. 202, p. 116144, 2019.
- [34] E. Christiaen, M. G. Goossens, B. Descamps, L. E. Larsen, P. Boon, R. Raedt, and C. Vanhove, “Dynamic functional connectivity and graph theory metrics in a rat model of temporal lobe epilepsy reveal a preference for brain states with a lower functional connectivity, segregation and integration,” *Neurobiology of Disease*, vol. 139, jun 2020.
- [35] D. Bertoglio, H. Amhaoul, A. Van Eetveldt, R. Houbrechts, S. Van De Vijver, I. Ali, and S. Dedeurwaerdere, “Kainic acid-induced post-status epilepticus models of temporal lobe epilepsy with diverging seizure phenotype and neuropathology,” *Frontiers in neurology*, vol. 8, p. 588, 2017.
- [36] L. Mengler, A. Khmelinskii, M. Diedenhofen, C. Po, M. Staring, B. P. Lelieveldt, and M. Hoehn, “Brain maturation of the adoles-

- cent rat cortex and striatum: Changes in volume and myelination,” *NeuroImage*, vol. 84, pp. 35–44, jan 2014.
- [37] S. N. Hatton, K. H. Huynh, L. Bonilha, E. Abela, S. Alhusaini, A. Altmann, M. K. M. Alvim, A. R. Balachandra, E. Bartolini, B. Bender, N. Bernasconi, A. Bernasconi, B. Bernhardt, N. Bargallo, B. Caldairou, M. E. Caligiuri, S. J. A. Carr, G. L. Cavalleri, F. Cendes, L. Concha, E. Davoodi-bojd, P. M. Desmond, O. Devinsky, C. P. Doherty, M. Domin, J. S. Duncan, N. K. Focke, S. F. Foley, A. Gambardella, E. Gleichgerrcht, R. Guerrini, K. Hamandi, A. Ishikawa, S. S. Keller, P. V. Kochunov, R. Kotikalapudi, B. A. K. Kreilkamp, P. Kwan, A. Labate, S. Langner, M. Lenge, M. Liu, E. Lui, P. Martin, M. Mascalchi, J. C. V. Moreira, M. E. Morita-Sherman, T. J. O’Brien, H. R. Pardoe, J. C. Pariente, L. F. Ribeiro, M. P. Richardson, C. S. Rocha, R. Rodríguez-Cruces, F. Rosenow, M. Severino, B. Sinclair, H. Soltanian-Zadeh, P. Striano, P. N. Taylor, R. H. Thomas, D. Tortora, D. Velakoulis, A. Vezzani, L. Vivash, F. von Podewils, S. B. Vos, B. Weber, G. P. Winston, C. L. Yasuda, A. H. Zhu, P. M. Thompson, C. D. Whelan, N. Jahanshad, S. M. Sisodiya, and C. R. McDonald, “White matter abnormalities across different epilepsy syndromes in adults: an ENIGMA-Epilepsy study,” *Brain*, vol. 143, no. 8, pp. 2454–2473, aug 2020. [Online]. Available: <https://academic.oup.com/brain/article/143/8/2454/5894684>
- [38] G. Slinger, M. R. Sinke, K. P. Braun, and W. M. Otte, “White matter abnormalities at a regional and voxel level in focal and generalized epilepsy: A systematic review and meta-analysis,” *NeuroImage: Clinical*, vol. 12, pp. 902–909, feb 2016.
- [39] M. Drexel, A. P. Preidt, and G. Sperk, “Sequel of spontaneous seizures after kainic acid-induced status epilepticus and associated neuropathological changes in the subiculum and entorhinal cortex,” *Neuropharmacology*, vol. 63, no. 5, pp. 806–817, oct 2012.
- [40] M. Lévesque and M. Avoli, “The kainic acid model of temporal lobe

- epilepsy,” *Neuroscience & Biobehavioral Reviews*, vol. 37, no. 10, pp. 2887–2899, 2013.
- [41] J.-A. Kim, J. I. Chung, P. H. Yoon, D. I. Kim, T.-S. Chung, E.-J. Kim, and E.-K. Jeong, “Transient mr signal changes in patients with generalized tonicoclonic seizure or status epilepticus: periictal diffusion-weighted imaging,” *American journal of neuroradiology*, vol. 22, no. 6, pp. 1149–1160, 2001.
- [42] M. Yogarajah and J. S. Duncan, “Diffusion-based magnetic resonance imaging and tractography in epilepsy,” *Epilepsia*, vol. 49, no. 2, pp. 189–200, 2008.
- [43] J. Djordjevic, A. Djordjevic, M. Adzic, and M. B. Radojicic, “Effects of chronic social isolation on wistar rat behavior and brain plasticity markers,” *Neuropsychobiology*, vol. 66, no. 2, pp. 112–119, aug 2012.
- [44] M. E. Fox, R. Isaac Studebaker, N. J. Swofford, and R. M. Wightman, “Stress and drug dependence differentially modulate norepinephrine signaling in animals with varied HPA axis function,” *Neuropsychopharmacology*, vol. 40, no. 7, pp. 1752–1761, feb 2015. [Online]. Available: [www.neuropsychopharmacology.org](http://www.neuropsychopharmacology.org)
- [45] D. L. Wallace, M.-H. Han, D. L. Graham, T. A. Green, V. Vialou, S. D. Iñiguez, J.-L. Cao, A. Kirk, S. Chakravarty, A. Kumar, V. Krishnan, R. L. Neve, D. C. Cooper, C. A. Bolaños, M. Barrot, C. A. Mcclung, and E. J. Nestler, “CREB regulation of nucleus accumbens excitability mediates social isolation-induced behavioral deficits,” *NATURE NEUROSCIENCE*, vol. 12, no. 2, 2009.
- [46] B. S. Hemanth Kumar, S. K. Mishra, R. Trivedi, S. Singh, P. Rana, and S. Khushu, “Demyelinating evidences in CMS rat model of depression: A DTI study at 7T,” *Neuroscience*, vol. 275, pp. 12–21, sep 2014.
- [47] A. C. Rossetti, M. Papp, P. Gruca, M. S. Paladini, G. Racagni, M. A. Riva, and R. Molteni, “Stress-induced anhedonia is associated with the activation of the inflammatory system in the rat brain:

- Restorative effect of pharmacological intervention,” *Pharmacological Research*, vol. 103, pp. 1–12, jan 2016.
- [48] A. R. Khan, B. Hansen, J. Danladi, A. Chuhutin, O. Wiborg, J. R. Nyengaard, and S. N. Jespersen, “Neurite atrophy in dorsal hippocampus of rat indicates incomplete recovery of chronic mild stress induced depression,” *NMR in Biomedicine*, vol. 32, no. 3, p. e4057, mar 2019. [Online]. Available: <http://doi.wiley.com/10.1002/nbm.4057>
- [49] R. D. Y. Palacios, M. Verhoye, K. Henningsen, O. Wiborg, and A. Van Der Linden, “Diffusion kurtosis imaging and high-resolution mri demonstrate structural aberrations of caudate putamen and amygdala after chronic mild stress,” *PLoS ONE*, vol. 9, no. 4, apr 2014. [Online]. Available: [/pmc/articles/PMC3989315/?report=abstracthttps://www.ncbi.nlm.nih.gov/pmc/articles/PMC3989315/](https://www.ncbi.nlm.nih.gov/pmc/articles/PMC3989315/)
- [50] P. Vestergaard-Poulsen, G. Wegener, B. Hansen, C. R. Bjarkam, S. J. Blackband, N. C. Nielsen, and S. N. Jespersen, “Diffusion-Weighted MRI and quantitative biophysical modeling of hippocampal neurite loss in chronic stress,” *PLoS ONE*, vol. 6, no. 7, p. 20653, 2011. [Online]. Available: [/pmc/articles/PMC3128590/?report=abstracthttps://www.ncbi.nlm.nih.gov/pmc/articles/PMC3128590/](https://www.ncbi.nlm.nih.gov/pmc/articles/PMC3128590/)



## 6 | Alterations in the functional brain network in a rat model of epileptogenesis: A longitudinal resting state fMRI study

This chapter is based on: Christiaen, E. & Goossens, M. G., Raedt, R., Descamps, B., Larsen, L. E., Craey, E., Carrette, E., Vonck, K., Boon, P., & Vanhove, C. (2019). Alterations in the functional brain network in a rat model of epileptogenesis: A longitudinal resting state fMRI study. *Neuroimage*, 202, 116144.

### Abstract

Epilepsy is a neurological disorder characterized by recurrent epileptic seizures. Electrophysiological and neuroimaging studies in patients with epilepsy suggest that abnormal functional brain networks play a role in the development of epilepsy, i.e., epileptogenesis, resulting in the generation of spontaneous seizures and cognitive impairment. In this longitudinal study, we investigated changes in functional brain networks during epileptogenesis in the intraperitoneal kainic acid (IPKA) rat model of temporal lobe epilepsy (TLE) using resting state functional magnetic resonance imaging (rsfMRI) and graph theory. Additionally, we investigated whether these changes are related to the frequency of the occurrence of spontaneous epileptic seizures in the chronic phase of epilepsy. Using a 7T MRI system, rsfMRI images were acquired under medetomidine anaesthesia before and 1, 3, 6, 10 and 16 weeks after status epilepticus (SE) induction in 20 IPKA animals and 7 healthy control

animals. To obtain a functional network, the correlation between the fMRI time series of 38 regions of interest (ROIs) was calculated. Then, several graph theoretical network measures were calculated to describe and quantify the network changes. At least 17 weeks post-SE, IPKA animals were implanted with electrodes in the left and right dorsal hippocampus, EEG was measured for 7 consecutive days, and spontaneous seizures were counted. Our results show that correlation coefficients of fMRI time series shift to lower values during epileptogenesis, indicating weaker whole brain network connections. Segregation and integration in the functional brain network also decrease, indicating a lower local interconnectivity and a lower overall communication efficiency. Secondly, this study demonstrates that the largest decrease in functional connectivity is observed for the retrosplenial cortex. Finally, post-SE changes in functional connectivity, segregation and integration are correlated with seizure frequency in the IPKA rat model.

## 6.1 Introduction

Blood oxygenation level dependent (BOLD) functional magnetic resonance imaging (fMRI) detects changes in blood oxygenation that are related to neuronal activity. It is a neuroimaging technique that allows for the visualisation of whole-brain activity and can be used to identify and investigate functional brain networks [1]. During rest, basic neuronal activity is believed to induce low frequency fluctuations in the BOLD signal that can be detected by performing resting state fMRI (rsfMRI). Calculating the correlation between the low frequency fluctuations, a technique called functional connectivity analysis, allows for the identification of brain regions that are functionally connected [2]. The functional organization of the brain can be investigated using different analysis methods, including seed-based correlation, independent component analysis (ICA) and graph theory [3]. In graph theory, the brain is represented as a network consisting of nodes, usually brain regions, and edges that show the relationship between the nodes. Several graph theoretical measures can be calculated to describe and quantify the network [4]. Changes in these measures, and thus in functional connectivity,

have been found in various pathologies, including Alzheimer's disease, schizophrenia, attention-deficit hyperactivity disorder, traumatic brain injury, and epilepsy [2].

Epilepsy is a neurological disorder characterized by recurrent epileptic seizures [5]. It is one of the most common brain disorders and in about one third of patients, seizures cannot be controlled with anti-epileptic drugs. These patients suffer from drug-resistant epilepsy (DRE) [6]. In DRE, epilepsy is often caused by an initial precipitating insult (IPI) such as stroke, infection, trauma, brain tumor, or (febrile) status epilepticus (SE). An IPI is typically followed by a latent period, during which the brain is transformed into an epileptic brain, finally leading to chronic acquired epilepsy. This process is called epileptogenesis [7].

In temporal lobe epilepsy (TLE), the most common type of acquired DRE [8], structural abnormalities have been demonstrated in both patients and rodent models [9–12]. The volume of the hippocampus and the entorhinal, perirhinal, and temporopolar cortices is lower in patients with TLE compared to healthy controls [13–17]. In addition, significant differences in functional connectivity have been found [18–23].

Studies combining rsfMRI with graph theory in patients with established epilepsy have shown abnormalities in the topological organization of the brain network. Most studies found a lower segregation in patients with TLE [18, 21, 23], while integration was either increased [18, 21] or decreased [23]. Functional connectivity was altered within the epileptic network, but also between the presumed epileptic network and the rest of the brain, including the contralateral equivalent of the epileptic network and the default-mode network (DMN) [18–20, 22]. Preclinical rsfMRI studies, in various rat models for acquired epilepsies, have demonstrated changes in functional brain networks compared to healthy rats [24–29]. In the intraperitoneal kainic acid (IPKA) rat model for TLE, Pirttimäki et al. [29] found decreased functional connectivity, mainly between the somatosensory cortex and thalamus, and between the perirhinal and piriform cortices, 1 or 2 months post-SE. Bertoglio et al. [24] found a wide-spread network connectivity hyposynchrony 2 weeks post-SE and a

severely affected functional connectivity in several regions of the DMN, including cingulate, parietal association, and posterior parietal cortex. On the other hand, Gill et al. [25] found a higher functional connectivity within the temporal regions, such as hippocampus and amygdala, and the limbic network and between the anterior and posterior DMN. However, there is still a need for longitudinal rsfMRI studies investigating network reorganisation during epileptogenesis to provide more insight into the mechanisms of action of epilepsy.

In this study, graph theory analysis of rsfMRI-based functional brain networks was performed before and multiple times during SE-induced epileptogenesis and compared to healthy control rats. During the chronic epilepsy phase, at least 19 weeks post-SE, electroencephalography (EEG) monitoring was performed to quantify the frequency of occurrence of spontaneous seizures. The aim of this study was threefold: 1) to characterize how the functional organization of the rat brain changes after SE and during the development of TLE; 2) to identify the brain regions with the highest degree of connectivity changes; 3) to evaluate whether connectivity changes are associated with the occurrence of spontaneous seizures. To the best of our knowledge, this is the first longitudinal rsfMRI study, combined with graph theory analysis, in a rat model of TLE.

## 6.2 Materials and Methods

### 6.2.1 Animals

Twenty-seven adult male Sprague-Dawley rats ( $276 \pm 15$  g body weight; Envigo, The Netherlands) were used in this study. They were treated according to European guidelines (directive 2010/63/EU). The protocol was approved by the local Ethical Committee on Animal Experiments of Ghent University (ECD 16/31). For practical reasons, animals were divided over 3 batches ( $n_{B1} = 10$ ,  $n_{B2} = 5$ ,  $n_{B3} = 12$ ) but experiments were performed at a fixed age. Each batch included control animals. The animals were kept under environmentally controlled conditions (12 h normal light/dark cycles, 20–23 °C and 40–60% relative humidity) with

food (Rats and Mice Maintenance, Carfil, Belgium) and water ad libitum. The animals were housed individually in type III H cages (Tecniplast, Australia) on wood-based bedding (Carfil, Belgium). Cages were enriched with paper nesting material (Nesting, Carfil, Belgium) and a piece of gnawing wood (M-brick, Carfil, Belgium).

### 6.2.2 Status epilepticus

Twenty animals (8 weeks old) were intraperitoneally (i.p., 5 mg/kg/h) injected with kainic acid (KA; Tocris Bioscience, UK) according to the protocol of Hellier et al. [30]. KA was administered hourly until motor seizures were elicited for 3 h or longer, referred to as status epilepticus (SE). The other 7 animals were injected similarly with saline and used as control group. On average, the animals were injected with 12.2 mg/kg KA (range: 5–20 mg/kg). Two animals died during or within 4 h after SE induction.

### 6.2.3 Image acquisition

Anatomical and resting state functional MR images were acquired twice before the induction of SE and at 5 time points during the development of epilepsy: 1, 3, 6, 10 and 16 weeks after SE (Figure 6.1). The two baseline scans, acquired 2–5 days apart, were used to assess the test-retest reliability of our methods and to obtain a better characterization of the baseline functional brain network. The animals were scanned in a random order, leading to an average difference in time of the day of 2 h and 53 min (range: 12 min–8 h and 6 min) between the baseline scans. Animals were transported to the MR facility one day before scanning. One IPKA rat was excluded 3 weeks after SE, because a metal fragment lodged behind its teeth caused a large artifact on the MR images.

During acquisition of the functional MR images the animals were sedated with medetomidine [31]. First, the animals were anesthetized with isoflurane (5% for induction, 2% for maintenance; Isoflo, Zoetis, USA) and O<sub>2</sub>. Then, a bolus of medetomidine (0.05 mg/kg; Domitor, Orion Pharma, Finland) was injected subcutaneously and 10 min later, isoflurane anaesthesia was stopped. Fifteen minutes after the bolus injection,



**Figure 6.1:** Timeline of the protocol. Anatomical and resting state fMRI were acquired 1 week before and 1, 3, 6, 10 and 16 after SE induction. On average 19.5 weeks after SE, electrodes were implanted in both hippocampi and 1 week later EEG was recorded in the animals for 7 consecutive days.

continuous subcutaneous infusion of medetomidine (0.1 mg/kg/h) was started and 25 min later functional MR images were acquired. After the image acquisition, anaesthesia was reversed with a subcutaneous injection of atipamezole (0.1 mg/kg; Antisedan, Orion Pharma, Finland).

The MR images were acquired on a 7T system (PharmaScan, Bruker, Germany) using a transmit volume coil (Rapid Biomedical, Germany) and an actively-decoupled rat head surface coil (Rapid Biomedical, Germany) to receive the signal. The body temperature of the animals was controlled using a circulating-water heating pad and respiration was measured using a pressure sensor. After optimizing the magnetic field homogeneity, TurboRARE T2-weighted anatomical images (TR 3661 ms, TE 37 ms, 30 slices, FOV 35 x 35 mm<sup>2</sup>, in-plane slice resolution 109 x 109  $\mu\text{m}^2$ , slice thickness 0.6 mm, acquisition time 9 min 46 s) were acquired. Then, 3 resting state fMRI scans per session were acquired using single-shot gradient echo echo-planar imaging (GE-EPI) with TR 2000 ms, TE 20 ms, 16 slices, FOV 30 x 30 mm<sup>2</sup> and voxel size 0.375 x 0.375 x 1 mm<sup>3</sup>. Each scan comprised 300 repetitions and lasted 10 min. Examples of a GE-EPI scan of a representative IPKA animal at baseline and 16 weeks post-SE are shown in Figure 6.14 and Figure 6.15.

## 6.2.4 Electrode implantation

On average 19.5 weeks after SE (range 17–23 weeks), electrodes were implanted in both hippocampi for EEG recording. The rats were anesthetized with a mixture of isoflurane (5% for induction, 2% for maintenance) and medical O<sub>2</sub>. After exposure of the skull, 13 small burr

holes were drilled: 9 for the positioning of stainless steel anchor screws (1.75 mm diameter; PlasticsOne, USA), 2 for the epidural ground/reference electrodes above the right and left frontal cortex respectively, 1 for a left-sided hippocampal EEG recording electrode, and 1 for a right-sided hippocampal EEG recording electrode. Epidural anchor screws were implanted to ensure sufficient fixation of the head cap during EEG monitoring in freely moving animals. Epidural electrodes were custom-made by attaching an insulated copper wire to an anchor screw. Bipolar recording electrodes were custom-made by twisting two polyimide-coated stainless steel wires (70  $\mu\text{m}$  bare diameter; California Fine Wire, USA) around each other. The distance between wire tips was set at 900  $\mu\text{m}$ .

Recording electrodes were inserted stereotactically in both hippocampi (AP -3.8 mm, ML  $\pm$ 2.2 mm relative to bregma, DV about -3.3 mm relative to brain surface). The coordinates were selected based on the Rat Brain Atlas by Paxinos and Watson [32] and the T2-weighted anatomical MR images obtained 16 weeks after SE were used to ensure electrodes were placed outside KA-induced lesions. During the electrode implantation, the position of the electrodes was verified by visual and auditive monitoring of real time electrophysiological recording, so that one tip of the electrode was positioned in the subgranular layer of the dentate gyrus, while the other tip was situated in the pyramidal cell layer of the CA1 region. All electrode leads ended in a connector that was fixed to the skull and anchor screws with acrylic dental cement. At the end of the surgery, rats were subcutaneously injected with the nonsteroidal anti-inflammatory drug meloxicam (1 mg/kg, Boehringer Ingelheim, Germany) and lidocaine (2% Xylocaine gel, AstraZeneca, UK) was locally applied to the wound to minimize discomfort. Twenty-four hours after surgery, rats received a second injection of meloxicam.

### 6.2.5 EEG recording

After a recovery period of one to two weeks, rats (IPKA group:  $n = 17$ , control group:  $n = 7$ ) were connected to the EEG set up. The first 3 days of EEG recording served as an acclimatization period and were not used for further analysis. The EEG set up consisted of a custom-built head

stage with unity gain preamplifier (based on TI TL074 JFET OpAmps), shielded 12-channel cables (363/2-000; PlasticsOne, USA), a 12-channel commutator (SL12C; PlasticsOne, USA) and a custom-built 512x amplifier (based on TI TL074 JFET OpAmps and a first order high-pass filter with a time constant of 1s). Recordings were performed while rats were awake and freely moving. Signals were sampled at 2 kHz by a 16-bit resolution data acquisition card (USB-6259, National Instruments, USA) and stored on the computer for offline analysis by a Matlab-based script (MathWorks, USA). Seizures were visually annotated by experienced investigators. An electrographic seizure was defined as a repetitive pattern ( $>2$  Hz), of complex, high amplitude EEG spikes that lasts for a minimum of 5 s (Figure 6.16). The average number of seizures/day and mean seizure duration were calculated based on 7 consecutive days of EEG recording.

## 6.2.6 Data analysis

### Preprocessing

The functional MRI data were preprocessed using SPM12 (<https://www.fil.ion.ucl.ac.uk/spm/software/spm12/>). First, the images were corrected for differences in slice acquisition time; then, they were realigned to their mean image using a least squares approach and a 6 parameter (rigid body) spatial transformation to remove movement artifacts. Afterwards, the images were normalized to an EPI template and spatially smoothed using a Gaussian kernel with a Full Width at Half Maximum of 0.8 mm. Finally, a band pass filter (0.01 Hz–0.1 Hz) was applied to filter out low frequency and physiological noise.

### Functional network construction

A parcellated atlas containing 38 cortical and subcortical regions of interest (ROIs) was manually constructed based on T2 anatomical images of the local population using SPM12 and Matlab. The ROIs are listed in Table 6.1. The atlas was adapted to the IPKA model. Structural damage visible on the T2 images as hyperintensity was excluded from the ROIs. Due to the resolution of the fMRI images, it was not useful to

divide the hippocampus into its subregions. It was not possible to make an ROI of the entorhinal cortex, a brain region that is structurally damaged during epileptogenesis, because of EPI signal dropout as a result of air in the ear canal.

**Table 6.1:** List of ROIs. Each ROI has a component on the left and right side of the brain.

ROIs			
Full name	Abbreviation	Full name	Abbreviation
Auditory Cortex	Au	Piriform Cortex	Pir
Caudate Putamen	CPu	Posterior Parietal Cortex	PtP
Cingulate Cortex	Cg	Prelimbic Cortex	PrL
Dorsolateral Orbitofrontal Cortex	DLO	Retrosplenial Cortex	RSC
Globus Pallidus	GP	Septum	Sep
Hippocampus	Hip	Somatosensory Cortex	SSC
Insula	Ins	Temporal Association Cortex	TeA
Motor Cortex	MC	Thalamus	Th
Nucleus Accumbens	Acb	Visual Cortex	Vis
Parietal Association Cortex	PtA		

A Graph Theoretical Analysis Toolbox (GRETNA) [33] was used to extract the mean time series of each ROI and to calculate the Pearson correlation coefficient between each pair. In this way a 38 x 38 correlation matrix was obtained. Thresholds were applied to this matrix to remove the weakest connections. These thresholds were chosen based on network density (i.e., the number of remaining connections divided by the maximum number of possible connections). Different thresholds were used to obtain correlation matrices with a density ranging from 20% to 50%. For further analysis, the correlation coefficients were Fisher r-to-z transformed to obtain a normal distribution. Based on the correlation

matrices, functional networks or graphs were constructed, in which each node represents a ROI and each edge a correlation coefficient. In Figure 6.2 an overview of the methodology for network construction is given.

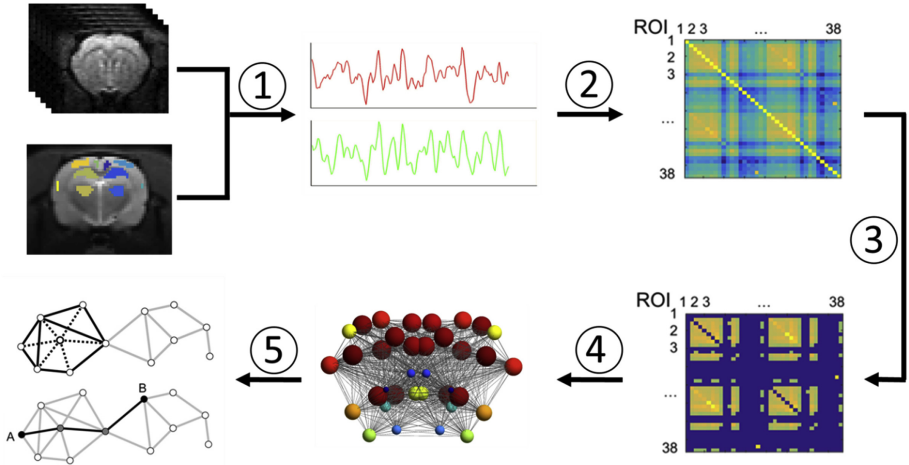
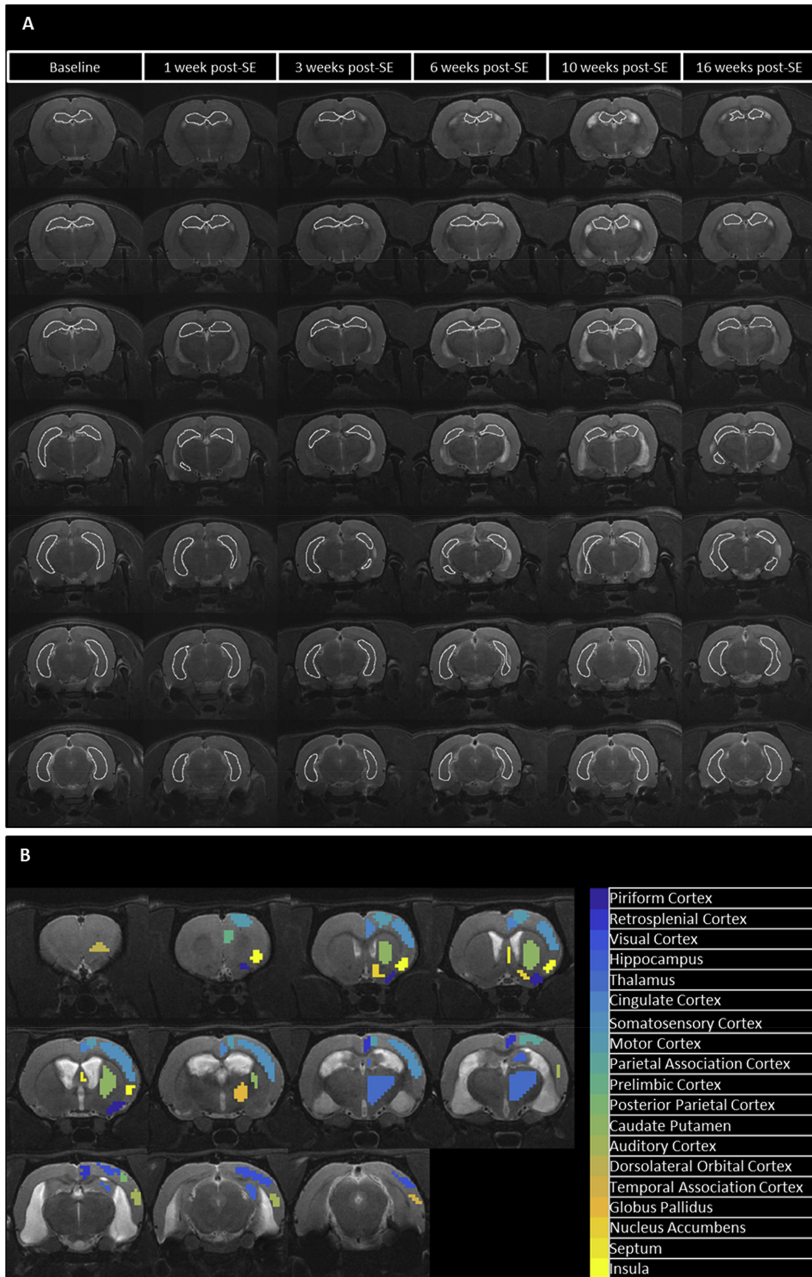


**Figure 6.2:** Construction of a functional network and graph. 1) The mean time series of each ROI is extracted from the preprocessed rsfMRI images. 2) The Pearson correlation coefficient between each pair of ROIs is calculated and a correlation matrix is obtained. 3) A threshold is applied to remove the weakest connections. 4) The correlation matrix can be visualized as a graph in which the nodes (dots) represent the ROIs and the edges (lines) the correlation coefficients between them. 5) Several network measures can be calculated (Adapted from [2, 4]).



### Graph theoretical analysis

For each graph several network measures were calculated using GREYNET: degree was investigated on a nodal level, and characteristic path length ( $L_p$ ), clustering coefficient ( $C_p$ ), global efficiency ( $E_g$ ) and local efficiency ( $E_{loc}$ ) on a global level. Degree or connection strength is the number of edges connected to a node, and is a measure for centrality or the importance of a node in the network. Characteristic path length is the average number of edges connecting two nodes in the network, and global efficiency is the average inverse path length between two nodes. Both are measures of functional integration or overall communication efficiency in the network. Clustering coefficient is the fraction of neighbours of a node that are also connected to one another, and local efficiency is global efficiency calculated within the neighbourhood of a node, i.e., the nodes connected to that node. Both are measures of functional segregation or local interconnectivity [2, 4].

Network measures were calculated at each matrix density, from 20% to 50% density with a 1% interval, and averaged over these densities. Then the measures were averaged over the 3 scans acquired within one scanning session to obtain one value per animal per time point.

The test-retest reliability of the network measures was assessed by calculating the coefficient of variation between scans in the same scanning session, between different sessions, and between different animals (Table 6.3).

### Amplitude of low frequency fluctuations

The analysis of resting state fMRI using graph theory is based on the correlations of low frequency fluctuations in the BOLD signal. The amplitude of these fluctuations could have an influence on functional connectivity and should be taken into account when analysing resting state networks [34]. Therefore, the mean amplitude of low frequency fluctuations (ALFF) in the frequency range 0.01–0.1 Hz was calculated in all ROIs using the Resting-State fMRI Data Analysis Toolkit (REST)

[35] and used as a covariate in the statistical analysis of the network measures.

### **Volumetric analysis of hippocampus**

The hippocampus is one of the brain structures that is affected most by cell damage in the IPKA rat model [36] and hippocampal volume loss is a known feature of IPKA animals [11, 12]. We investigated volume loss in the hippocampus during epileptogenesis. The volume of the hippocampus was measured on the T2-weighted MR images using the image processing package Fiji, a distribution of ImageJ [37, 38]. The hippocampus was drawn manually and its volume was calculated (Figure 6.3A). Hyper- and hypointensities were considered damage and excluded from the volume. In other words, we calculated the volume of the hippocampus that appeared undamaged on the T2-weighted MR images, or the T2-normal hippocampal volume [12]. To avoid false correlations due to this structural damage, visible damage was excluded from all ROIs used to construct the functional brain network. The ROIs were adapted based on the T2 image of the animal with the most extensive structural damage (KAC4, 16 weeks post-SE), as can be seen in Figure 6.3B. These ROIs were used in all animals, at all time points. We chose to use fixed ROIs because the size of an ROI can have an influence on its connectivity and larger ROIs tend to be more highly correlated [39]. If variable ROIs are used, a decreased hippocampal volume could falsely induce a lower correlation. The effect of using a reduced hippocampal ROI on the control animals' outcome values is minimal, as similar results were obtained using a hippocampal ROI that encompasses the whole hippocampus (data not shown).

### **Statistical analysis**

The mean correlation coefficient, and nodal and global network measures were analysed using the MIXED procedure in IBM SPSS Statistics for Windows, version 25 (IBM Corp., N.Y., USA) according to the protocol for the analysis of longitudinal data from animals with missing values using SPSS, described by [40]. The covariance structure was the 'com-

pound symmetry' structure, fixed factors were group (IPKA animals and control animals), time (baseline, 1, 3, 6, 10 and 16 weeks after SE) and group-by-time interaction. Mean ALFF in all ROIs was used as covariate. Least-significant-difference tests were used to explore significant effects and interactions, a significance level of 0.05 was used for main effects and interactions, and the Bonferroni correction was used to correct for multiple comparisons. For the analysis of nodal measures, an extra correction for multiple nodal comparisons was done using the false discovery rate (FDR) at  $q = 0.05$ . T2-normal hippocampal volume was analysed in the same way, but without mean ALFF as a covariate.

The Pearson correlation coefficient was calculated between seizure frequency, i.e., the average number of seizures per day during 7 days, and mean seizure duration on the one hand, and the network measures at each time point on the other hand. In addition, the Pearson correlation was calculated between T2-normal hippocampal volume on the one hand and network measures and seizure frequency on the other hand.

### **Network-based statistic**

The individual network connections were analysed with network-based statistic (NBS) using the NBS Connectome toolbox [41]. This is a non-parametric statistical method that allows for the correction for multiple comparisons in a graph. The family-wise error rate is controlled when mass univariate testing is done on all connections.

The strongest network connections at baseline were identified using the One Sample Test. This test flips the sign of the data points at random for each permutation and corresponds to a one-sided One Sample t-test. It tests the null hypothesis that the connectivity is equal to zero. The test statistic threshold was set to 1.2 to obtain the 20% connections that differed most from zero. The ROIs present in the resulting subnetwork were used for further statistical analysis. The network connections that were different between IPKA and control animals were identified using the F-test with a threshold of 25.9 to obtain the 10% connections that differed the most between the groups.



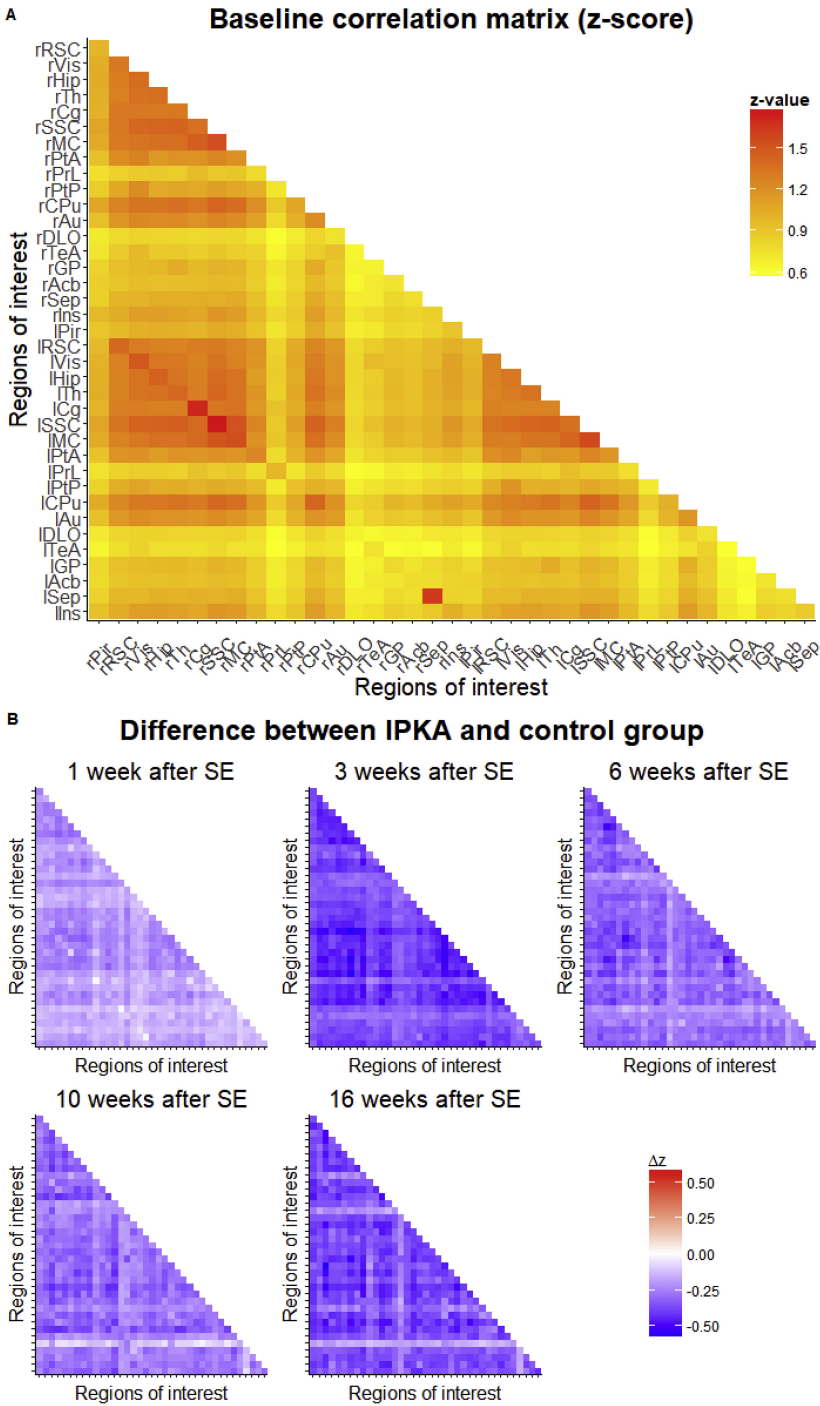


**Figure 6.5:** Correlation matrices. A) Correlation matrix at baseline. B) Difference in correlation matrices between IPKA and control animal. All values are negative, indicating that the correlation coefficients are lower in the IPKA animals.

### 6.3.2 Decrease in correlation coefficients during epileptogenesis

The difference in correlation matrices between IPKA animals and control animals is visualized in Figure 6.5. All difference values were negative, indicating that the correlation coefficient between each pair of ROIs is lower in IPKA animals compared to control animals.

A similar evolution was observed in the distribution of the correlation coefficients in Figure 6.6. The correlation coefficients shifted to smaller values during the development of epilepsy. This shift was already observed 1 week after status epilepticus, but the largest shift occurred 3 weeks post-SE. Later on, the distribution remained stable.

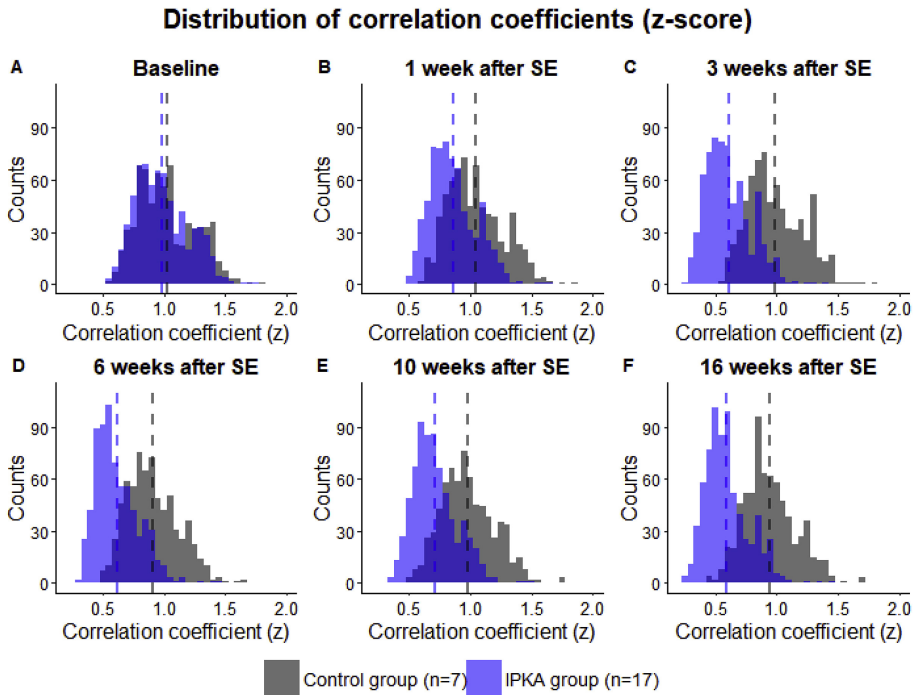


**Figure 6.6:** Distribution of correlation coefficients (z-score). During epileptogenesis the correlation coefficients shift towards lower values in the IPKA animals.

Statistical analysis of the mean correlation coefficient using LMEM showed a significant effect of group ( $F_{1,27.6} = 13.68$ ,  $p = 0.001$ ) and time in the IPKA group ( $F_{5,127} = 8.71$ ,  $p < 0.001$ ) but not in the control group ( $F_{5,123} = 0.735$ ,  $p = 0.598$ ). Pairwise comparison of the means showed that the mean correlation coefficient was significantly lower in IPKA animals than in controls at 3, 6, 10, and 16 weeks post-SE. In the IPKA animals, there was a significant decrease in mean correlation coefficient between baseline and 3, 6, 10, and 16 weeks post-SE and between 1 week and 3, 6, and 16 weeks post-SE. This is illustrated in Figure 6.7.

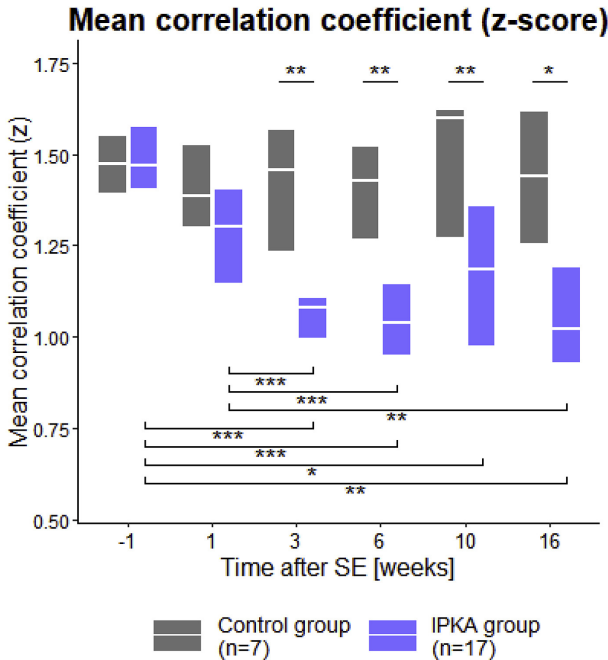


**Figure 6.7:** Mean correlation coefficient (z-score) in function of time. The mean correlation coefficient is significantly lower in IPKA animals than in controls at 3, 6, 10 and 16 weeks post-SE. In the IPKA animals, there is a significant decrease in mean correlation coefficient between baseline and 3, 6, 10 and 16 weeks post-SE and between 1 week and 3, 6 and 16 weeks post-SE. Data are presented as a boxplot with median and interquartile range, \* $p < 0.05$ , \*\* $p < 0.01$ , \*\*\* $p < 0.001$ .

### 6.3.3 Decrease in global functional segregation and integration

Significant decreases in measures of global functional segregation (i.e., clustering coefficient and local efficiency) and integration (characteristic path length and global efficiency) were observed during epileptogenesis with the largest changes occurring between 1 and 3 weeks after SE (Figure 6.8). Statistical analysis of the clustering coefficient showed a significant effect of group ( $F_{1,27.8} = 9.37$ ,  $p = 0.005$ ) and time in the IPKA group ( $F_{5,127} = 8.66$ ,  $p < 0.001$ ) but not in the control group ( $F_{5,123} = 0.457$ ,  $p = 0.807$ ). Pairwise comparison of the means showed that clustering coefficient was significantly lower in IPKA animals compared to control animals at 3, 6, 10, and 16 weeks post-SE. There was a significant decrease in clustering coefficient in the IPKA animals between baseline and 3, 6, 10, and 16 weeks post-SE and between 1 week and 3, 6, 10, and 16 weeks post-SE. Statistical analysis of the local efficiency also showed a significant effect of group ( $F_{1,26.8} = 9.96$ ,  $p = 0.004$ ) and time in the IPKA group ( $F_{5,126} = 8.44$ ,  $p < 0.001$ ) but not in the control group ( $F_{5,122} = 0.942$ ,  $p = 0.456$ ). Pairwise comparison of the means showed that local efficiency was significantly lower in IPKA animals than in controls at 3, 6, 10, and 16 weeks post-SE. There was a significant decrease in local efficiency in the IPKA animals between baseline and 3 and 6 weeks post-SE and between 1 week and 3, 6, 10, and 16 weeks post-SE.

Statistical analysis of the characteristic path length showed a significant effect of group ( $F_{1,26.7} = 6.70$ ,  $p = 0.015$ ) and time in the IPKA group ( $F_{5,126} = 10.3$ ,  $p < 0.001$ ), but not in the control group ( $F_{5,122} = 0.887$ ,  $p = 0.497$ ). Pairwise comparison of the means showed that characteristic path length was significantly higher in IPKA animals than in control animals at 3, 6, and 10 weeks post-SE. There was a significant increase in characteristic path length in the IPKA animals between baseline and 3 and 6 weeks post-SE and between 1 week and 3, 6, 10, and 16 weeks post-SE. Statistical analysis of the global efficiency showed a significant effect of group ( $F_{1,26.7} = 6.89$ ,  $p = 0.014$ ) and time in the IPKA group ( $F_{5,126} = 8.44$ ,  $p < 0.001$ ) but not in the control group ( $F_{5,122} = 0.942$ ,

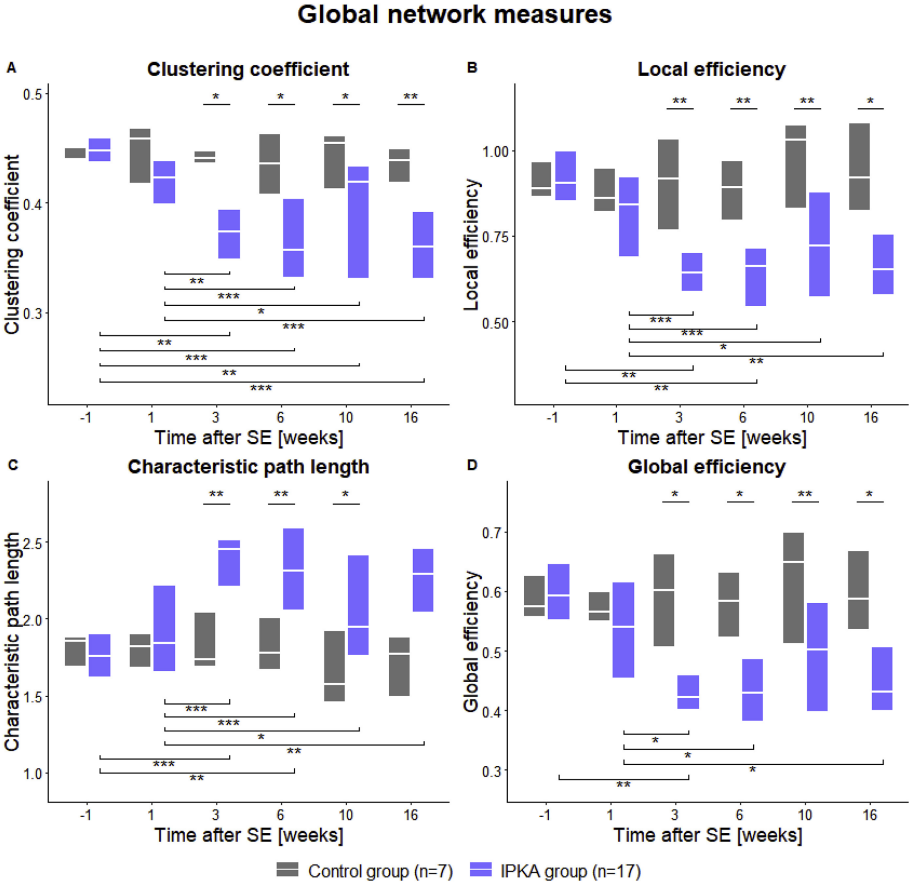


**Figure 6.8:** Global network measures in function of time. A) Clustering coefficient and B) Local efficiency decrease during epileptogenesis, indicating a decrease in segregation in the functional network. C) Characteristic path length increases and D) Global efficiency decreases during epileptogenesis, indicating a decrease in integration. Data are presented as a boxplot with median and interquartile range, \* $p < 0.05$ , \*\* $p < 0.01$ , \*\*\* $p < 0.001$ .

$p = 0.456$ ). Pairwise comparison of the means showed that global efficiency was significantly lower in IPKA animals than in controls at 3, 6, 10, and 16 weeks post-SE. There was a significant decrease in global efficiency in the IPKA animals between baseline and 3 weeks post-SE and between 1 week and 3, 6, and 16 weeks post-SE.

### 6.3.4 Decrease in connectivity strength in highly connected nodes

Figure 6.9 visualizes the nodal degree for each ROI at each time point. NBS was used to identify the 20% strongest connections in the network at baseline. The obtained subnetwork consisted of 20 nodes: at the left and right side of the brain; the somatosensory cortex (SSC), motor cortex (MC), caudate putamen (CPu), visual cortex (Vis), thalamus (Th), hippocampus (Hip), cingulate cortex (Cg), retrosplenial cortex (RSC), auditory cortex (Au), and parietal association cortex (PtA). These nodes were also the nodes with the highest degree at baseline and showing the largest decreases during epileptogenesis. Because the degree of each node was similar on the right and left side of the brain, the average degree of the right and left component of each node was calculated. There was a significant effect of group and time in the IPKA group, but not in the control group (FDR-corrected  $p > 0.05$ ) in the 10 strongest nodes. There was a significant decrease in degree during epileptogenesis and the degree was lower in the IPKA animals than in the control animals. The largest decrease happened between 1 and 3 weeks post-SE.

### 6.3.5 Decrease in connectivity in connections of the retrosplenial cortex

The most significant changes in functional connectivity take place between 1 and 3 weeks post-SE. To investigate functional connectivity changes at week 3 in more detail, NBS was used to identify which network connections differed the most between IPKA animals and controls. In Figure 6.10, the 10% connections that differed the most are visualized in a circular graph ( $F > 25.9$ ,  $p < 0.001$ ). The majority of these connections were connected to the retrosplenial cortex (10 out of 20). Eleven out of 20 connections were within one hemisphere, the other 9 were between hemispheres. None of the connections connected the right and left component of the same brain region.

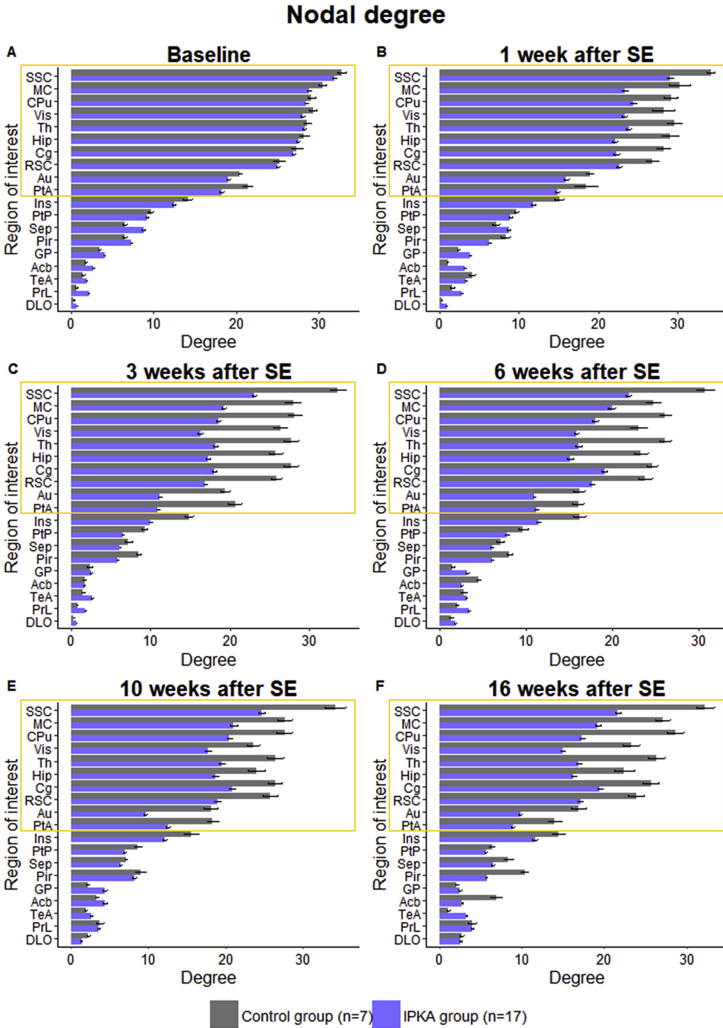


**Figure 6.9:** Nodal degree at each time point. At baseline (A) we can see that the nodes with the highest degree (yellow rectangle) are the somatosensory cortex (SSC), motor cortex (MC), caudate putamen (CPu), visual cortex (Vis), thalamus (Th), hippocampus (Hip), cingulate cortex (Cg), retrosplenial cortex (RSC), auditory cortex (Au) and parietal association cortex (PtA). Less important nodes are the insula (Ins), posterior parietal cortex (PtP), septum (Sep), piriform cortex (Pir), globus pallidus (GP), nucleus accumbens (Acb), temporal association cortex (TeA), prelimbic cortex (PrL) and dorsolateral orbital cortex (DLO). During epileptogenesis the degree decreases in most of the nodes, especially those with a higher degree at baseline. Data are presented as a bar graph with mean and standard error.

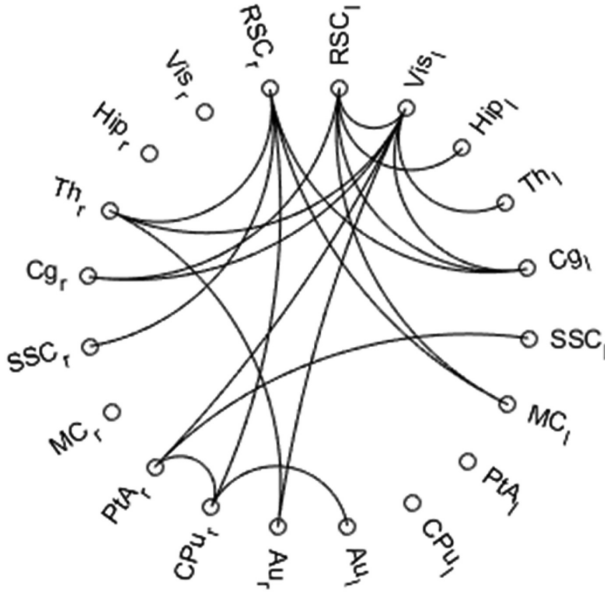


**Figure 6.10:** Circular visualisation of network with the 10% connections that differ the most between IPKA and control animals 3 weeks post-SE. Half of the connections are connections of the retrosplenial cortex.

### 6.3.6 Correlation between changes in network measures and seizure frequency

Based on 7 days of consecutive EEG monitoring, the average daily seizure frequency at least 19 weeks post-SE was calculated for each animal (Figure 6.11). The animal which had no seizures during the monitoring period (KAA2), did display occasional tonic-clonic seizures outside the EEG recording period (e.g. when entering the housing room). In addition, interictal epileptiform activity, such as epileptic spikes and pathological high frequency oscillations, were observed on the EEG signal (Figure 6.16D). Therefore, it was considered epileptic. The relationship between the number of seizures recorded at least 19 weeks post-SE and the functional network measures was evaluated using the Pearson correlation coefficient. The Shapiro-Wilk test showed that the seizure frequency data follow a normal distribution ( $W(17) = 0.953$ ,  $p = 0.514$ ). Seizure frequency was positively correlated with clustering coefficient at

week 1 and 16, local and global efficiency at week 1, and negatively with characteristic path length at week 1 and 16 post-SE (Figure 6.12, Figure 6.13). Seizure frequency was also positively correlated with mean nodal degree measured one week post-SE, and more specifically with the degree of the hippocampus ( $r = 0.591$ ,  $p = 0.013$ ), thalamus ( $r = 0.585$ ,  $p = 0.014$ ), cingulate cortex ( $r = 0.656$ ,  $p = 0.004$ ), somatosensory cortex ( $r = 0.617$ ,  $p = 0.008$ ), caudate putamen ( $r = 0.598$ ,  $p = 0.011$ ), auditory cortex ( $r = 0.544$ ,  $p = 0.024$ ), and insula ( $r = 0.653$ ,  $p = 0.004$ ). No significant correlation between mean seizure duration and any of the network measures could be found.

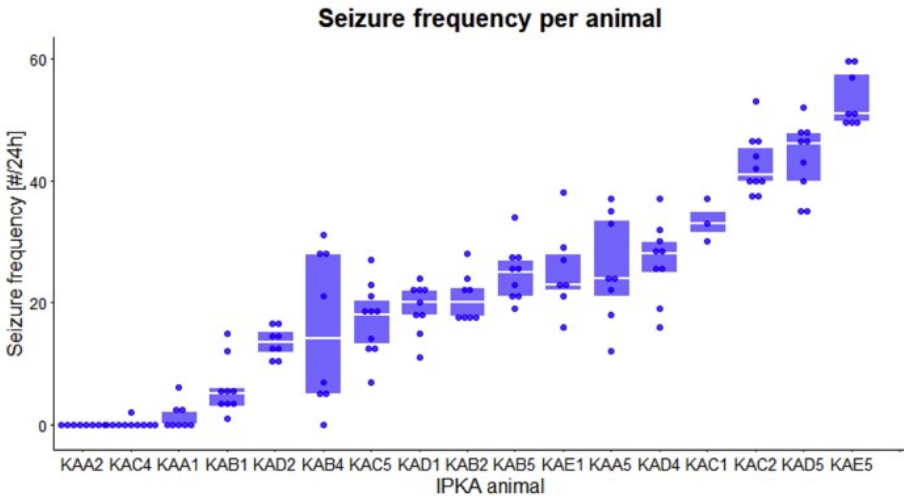


**Figure 6.11:** Seizure frequency (# per 24h) per animal. Data are presented as a boxplot with median, interquartile range and individual data points.

Seizure frequency was also positively correlated with T2-normal hippocampal volume 3, 6, 10, and 16 weeks post-SE (Figure 6.17). In addition, T2-normal hippocampal volume was correlated with several global network measures at all time points post-SE (Table 6.2).

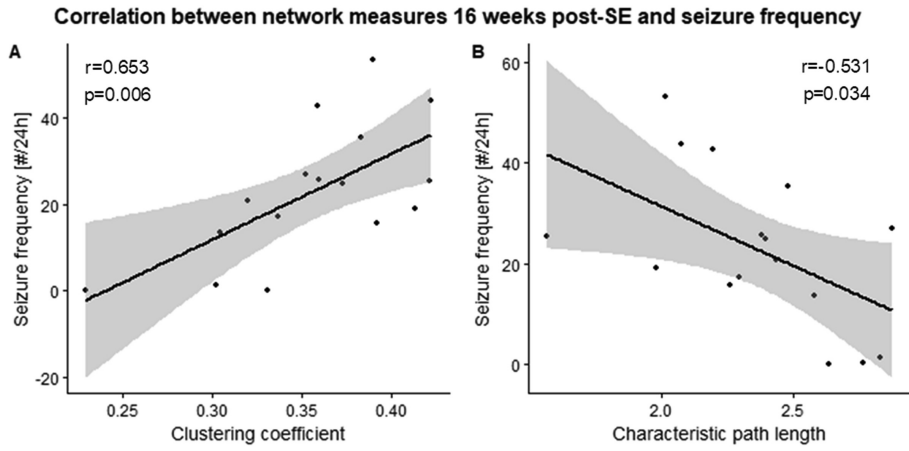


**Figure 6.12:** Correlation between network measures 16 weeks post-SE and seizure frequency (number per 24 h).

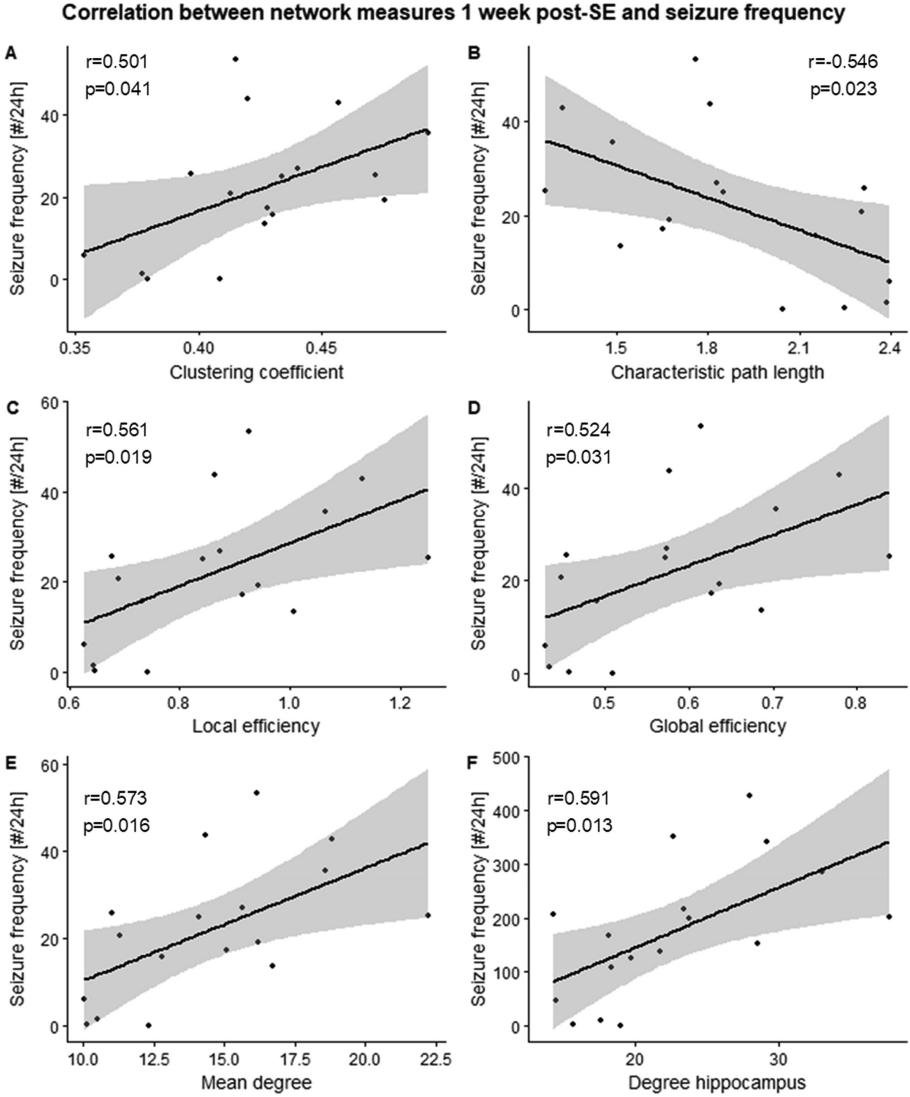


**Figure 6.13:** Correlation between network measures 1 week post-SE and seizure frequency (number per 24 h).

**Table 6.2:** Correlation between T2-normal hippocampal volume and seizure frequency and global network measures (\*p < 0.05, \*\*p < 0.01, \*\*\*p < 0.001).

		Correlation of T2-normal hippocampal volume with					
	Seizure frequency [#/#/24 h]	Mean degree	Clustering coefficient	Characteristic path length	Local efficiency	Global efficiency	
1 week post-SE							
1 week	r	0.501*	0.519*	-0.543*	0.542*	0.545*	
	p	0.034	0.027	0.020	0.020	0.019	
3 weeks post-SE							
3 weeks	r	0.451	0.389	-0.671**	0.502*	0.537*	
	p	0.070	0.123	0.003	0.040	0.026	
6 weeks post-SE							
6 weeks	r	0.579*	0.404	-0.598*	0.578*	0.566*	
	p	0.015	0.108	0.011	0.015	0.018	
10 weeks post-SE							
10 weeks	r	0.775***	0.777***	-0.823***	0.777***	0.786***	
	p	<0.001	<0.001	<0.001	<0.001	<0.001	
16 weeks post-SE							
16 weeks	r	0.636**	0.760***	-0.684**	0.674**	0.631**	
	p	0.006	<0.001	0.002	0.003	0.007	

## 6.4 Discussion

### 6.4.1 Temporal progression of network topology and link with time-dependent changes in structural lesions and seizure frequency

The aim of this study was to characterize how the topological organization of the rat brain changes after SE during the development of TLE. We found that during epileptogenesis, BOLD signal fluctuations were less correlated between brain areas, indicating decreased functional connectivity. Graph analysis revealed that segregation and integration in the functional brain network decreased during epileptogenesis. This indicates that there is a lower local interconnectivity and a lower overall communication efficiency. Nodal degree decreased significantly in the most highly connected ROIs in the baseline network, indicating a loss in connection strength. Most of these ROIs are part of the rat DMN, including cingulate cortex, retrosplenial cortex, visual cortex, auditory cortex, hippocampus, thalamus, motor cortex, and somatosensory cortex [42, 43]. Becerra et al. [42] identified a spatial resting-state network that had many brain regions in common with the DMN in humans. This network consisted of the retrosplenial cortex, thalamus, hippocampus, insula, motor cortex, somatosensory cortex, orbitofrontal cortex, septum, and periaqueductal gray [42]. Later, Lu et al. [43] demonstrated that rat brains have a DMN similar to that of humans. They identified the orbital cortex, prelimbic cortex, cingulum, auditory and temporal association cortex, posterior parietal cortex, retrosplenial cortex, hippocampus, and visual cortex as its key structures [43]. This was confirmed by Hsu et al. [44]. We also found small, non-significant changes in functional connectivity, integration, and segregation in the control group, most likely due to normal aging.

Functional connectivity, segregation and integration decreased most significantly between 1 and 3 weeks post-SE. Beyond this time point, the network connectivity remained unchanged. Sharma et al. [45] investigated the temporal progression of lesions in a kainic acid-induced rat (F-344) model of TLE. They found that neuronal degeneration can mainly

be seen during the first 4 weeks after SE in the hippocampus (CA1, CA3 and dentate gyrus), amygdala, thalamus, and cortex. Astrogliosis increased until 4 weeks after SE, while microgliosis peaked 1 week after SE. This gliosis remained elevated over time in these brain regions weeks after SE. Aberrant mossy fibre sprouting could be seen in the dentate gyrus 1 week after SE, reaching a maximum 2 weeks post-SE and decreasing afterwards [45]. This was confirmed by Bertoglio et al. [46], who found neuronal loss in CA3 and dentate hilus (DH) 1 weeks post-SE, and in CA3, DH and piriform cortex (Pir) 12 weeks post-SE in a kainic acid-induced rat (Sprague-Dawley) model of TLE. They also found microglial activation in CA3 and Pir 1 week post-SE, and in Pir 12 weeks post-SE [46]. Overall the dynamics of brain topology changes that we found correspond nicely with the temporal profiles of neuronal degradation and gliosis. This study showed, based on structural MRI, that T2-normal hippocampal volume loss was already maximal one week after SE, indicating that the most significant change in network topology is secondary to the loss of neuronal tissue. A decreased hippocampal volume has often been reported in patients with TLE [13, 14, 16, 17].

Van Nieuwenhuysse et al. [47] investigated how seizure frequency changes during epileptogenesis in the IPKA model and found that after a mean latency period of 7 days after SE, animals start to have spontaneous seizures at an increasing frequency until a plateau phase is reached 17 weeks after SE. While seizure frequency continues to increase 3 weeks after SE, functional connectivity, segregation, and integration reached stable but decreased levels, indicating that worsening of the epileptic condition is not associated with further decrease in functional connectivity of the brain. We cannot rule out that the animals had seizures during the image acquisition, since the used anaesthesia does not suppress seizure activity [48] and EEG was not monitored during the scanning sessions. However, because seizure frequency continues to increase while network measures have reached a plateau phase, it is very unlikely that the observed changes in functional connectivity, segregation, and integration are the mere result of spontaneous seizures during image acquisition.

### 6.4.2 Comparison with previous animal studies

Although there is a large variability in changes in functional connectivity and network topology during epileptogenesis between studies and animal models, most studies agree that functional connectivity is decreased in several brain regions, including hippocampus and thalamus, which corresponds with our results. Pirttimäki et al. [29] investigated dynamic network changes in the IPKA rat model for TLE and analysed longitudinal data by comparing z-scores of correlation coefficients. They found small increases and decreases in functional connectivity in several brain regions 1 week post-SE, although the average change was not significant. Similar to our study, they found decreased functional connectivity 1 or 2 months after SE, mainly between the somatosensory cortex and thalamus, and between the perirhinal and piriform cortices [29]. An rsfMRI study performed by Mishra et al. [27] demonstrated a lower functional connectivity between the ipsilateral and contralateral parietal cortex, and between the hippocampus and parietal cortex on the injured side in the lateral fluid-percussion rat model of post-traumatic epileptogenesis 4 months post-injury, using a comparison of z-scores. In the pilocarpine rat model of TLE, Jiang et al. [26] found a decreased connectivity of the hippocampal functional network in the hippocampus, amygdala, thalamus, motor cortex, and somatosensory cortex and increased connectivity in the visual cortex, mesencephalon, and insula, using ICA. In the IPKA model of TLE, Bertoglio et al. [24] found a wide-spread network connectivity hyposynchrony 2 weeks post-SE, using ICA and comparison of z-scores. In addition, they found that functional connectivity was severely affected in several regions of the DMN [24]. Interestingly, a study performed by Gill et al. [25] in the IPKA model for TLE found a higher functional connectivity within the temporal regions and the limbic network and between the anterior and posterior DMN together with an increased network segregation and integration 4–5 weeks post-SE.

Several factors might contribute to the discrepancy between our study and the study by Gill et al. [25], including different ROIs for the construction of the correlation matrix, a different animal strain (Long-Evans versus Sprague-Dawley) and the use of a different anaesthetic agent (isoflu-

rane versus medetomidine). Several studies have shown that different types of anaesthesia have an influence on spontaneous fluctuations in the BOLD signal and on functional connectivity [49–53]. Medetomidine, an  $\alpha$ 2-adrenergic agonist, has gained popularity in longitudinal fMRI studies, since it induces sedation rather than general anaesthesia and decreases global cerebral blood flow without dose-dependent vasodilation or neuronal suppression [54, 55].

### 6.4.3 Comparison with patient studies

Our findings are generally in line with most studies investigating functional connectivity and network topology in patients with TLE. Most studies agree that segregation is decreased in patients with TLE [18, 21, 23]. Integration has been found to be increased [18, 21] as well as decreased [23]. Liao et al. [18] found increased functional connectivity within the temporal lobe and decreased functional connectivity in the frontal and parietal lobe and in the DMN in patients with TLE. Additionally, they found a lower degree in nodes of the DMN [18]. Morgan et al. [19] found that functional connectivity between the seizure propagation network and its contralateral equivalent is decreased in TLE, and that functional connectivity within the seizure propagation network decreases linearly with increasing duration of epilepsy. Pittau et al. [20] found decreased connectivity of the hippocampus and amygdala with the DMN, ventromesial limbic prefrontal regions and contralateral mesial temporal structures including hippocampus. Song et al. [22] also found a decreased functional connectivity in the DMN in epilepsy patients.

### 6.4.4 Decrease in connectivity of the retrosplenial cortex

The brain region which changed most profoundly in functional connectivity in the IPKA model was the retrosplenial cortex. The retrosplenial cortex is one of the most important nodes of the rat DMN [42, 43]. Three weeks post-SE, when change in network connectivity had reached stable levels, half of the connections that differed most in strength between healthy and IPKA animals, included the retrosplenial cortex. This finding is in line with a study in TLE patients that demonstrated a decrease

in functional connectivity between the temporal lobe and the posterior cingulate cortex, the human equivalent of the rat retrosplenial cortex [56]. It is rather surprising that the retrosplenial cortex appears to be more affected than regions of the mesial temporal lobe (hippocampus, entorhinal and piriform cortices, and amygdala) which display most extensive cell loss [36, 45]. However, since the retrosplenial cortex plays a role in spatial navigation and episodic memory [57], the lower functional connectivity of this brain region could be a cause of the memory impairment seen in rats with TLE [26].

In addition to the retrosplenial cortex, the cingulum and parietal association cortex are affected during epileptogenesis as well. These brain regions have a high structural connectivity with other cortical regions, such as hippocampus and thalamus. Together, these regions form a connection between the primary sensory cortices [43, 44]. This could explain why the decrease in functional connectivity in the brain network is so extensive, rather than limited to structurally lesioned brain regions.

#### **6.4.5 Correlation between changes in network measures and seizure frequency**

Finally, we investigated whether the changes in network measures occurring during the development of epilepsy were associated with the occurrence of spontaneous epileptic seizures in the chronic epilepsy phase at least 19 weeks after SE. A positive correlation was found between the number of seizures on the one hand and clustering coefficient, local efficiency, global efficiency, and mean degree at 1 week post-SE and clustering coefficient at 16 weeks post-SE on the other hand. A negative correlation was found with characteristic path length 1 week and 16 weeks post-SE. Seizure frequency in the chronic epilepsy phase was positively correlated with the degree of several brain regions, determined 1 week after SE. These regions included the hippocampus and thalamus, two regions heavily affected by neurodegeneration and gliosis in response to SE. This means that the more functionally disconnected these brain regions are upon KA-induced SE, the less likely it is for seizures to occur in the chronic phase. These associations between seizure frequency and

functional connectivity measures all point out a quite unexpected finding, namely that the more profoundly the brain network is affected by the KA-induced SE, the less likely it is that spontaneous epileptic seizures are generated. Thus, it seems that the brain network needs to keep a minimal degree of organization to enable the emergence of seizures. This is in line with the potent therapeutic effects of resective/disconnective surgery as a treatment for epilepsy. Our findings correspond with those of Bertoglio et al. [24], who also found that functional connectivity is correlated with seizure frequency. In addition, we found that those animals with the largest T2-normal hippocampal volume loss displayed the lowest number of seizures. This could indicate that a sufficient amount of hippocampal tissue needs to be preserved as a substrate for seizure generation.

The correlation between network measures and seizure frequency 1 week after SE is very interesting, since we never recorded spontaneous epileptic seizures at that time point in the IPKA model for TLE. This indicates that network reorganisation upon an IPI might have a predictive value and could potentially be used as a biomarker for the development and progression of epilepsy.

#### 6.4.6 Study limitations

To calculate mean seizure frequency and duration, seizures were visually annotated by experienced investigators. Our study could have benefited from automated seizure detection. In preclinical epilepsy research, automatic seizure detection is rarely used and visual annotation remains the standard procedure. Seizures are easy to recognize by a trained researcher, but hard to describe in terms of parameters, because they are complex and slightly different in every animal. However, with recent advances in machine learning, automatic detection is starting to emerge.

EEG was recorded for 7 consecutive days and seizures were detected in all IPKA animals but one (KAA2). Since this animal did display occasional tonic-clonic seizures outside the EEG recording period, a longer recording period might be recommended to obtain a more accurate estimate of the

seizure frequency.

Another limitation of our study is that we did not do post-mortem histological analysis. Therefore, we could not confirm the extent of hippocampal volume loss calculated based on the T2 images, nor could we verify the exact location of the electrodes, which would have been particularly interesting in the animals with extensive damage. In addition, we could not investigate whether the changes in network topology during epileptogenesis were related to specific histopathological changes, such as neuronal loss or gliosis.

Finally, we calculated the volume of the hippocampus by delineating hippocampal tissue that looked normal on the T2-weighted MR images [12]. To avoid including ventricles in the volume of the hippocampus, all hyperintensities were excluded, since it was difficult to differentiate between enlarged ventricles and other reasons for hyperintensities, such as gliosis or inflammation. This means that we measured T2-normal hippocampal volume, and not the actual volume of the hippocampus. The T2-normal hippocampal volume is most likely an underestimation of the actual volume.

## 6.5 Conclusion

We investigated changes in functional brain networks during epileptogenesis in the IPKA rat model of TLE using longitudinal resting state fMRI and graph theory. First, we found that functional brain network connections become weaker during the development of epilepsy. On a global level, we found that segregation and integration in the functional brain network decrease during epileptogenesis. As hypothesized, the functional brain network was extensively disrupted during the development of epilepsy. The largest changes in functional connectivity, segregation and integration occurred between 1 and 3 weeks post-SE, which is when the animals start to have spontaneous seizures. A loss in connection strength could be seen in the most highly connected ROIs in the network, many of which are part of the rat DMN. Secondly, we found that 3 weeks post-SE, the connectivity of the retrosplenial cortex, one of

the most important nodes in the rat DMN, was highly affected. Lastly, as we hypothesized, the changes in functional connectivity, segregation, and integration were correlated with seizure frequency. A more profound topological reorganisation of the brain network corresponds with a lower frequency of spontaneous epileptic seizures. The findings of this study provide more insight into how the topological organization of the functional brain network changes during the development of epilepsy, which could lead to a better understanding of the underlying mechanisms of epilepsy and help the rational development of epilepsy therapies. To further elaborate on the link between changes in brain network topology and epileptogenesis, a follow-up study is planned using MR-compatible electrodes to enable longitudinal EEG-fMRI studies in various models for acquired epilepsy, including the IPKA animal model.

## Supplementary data

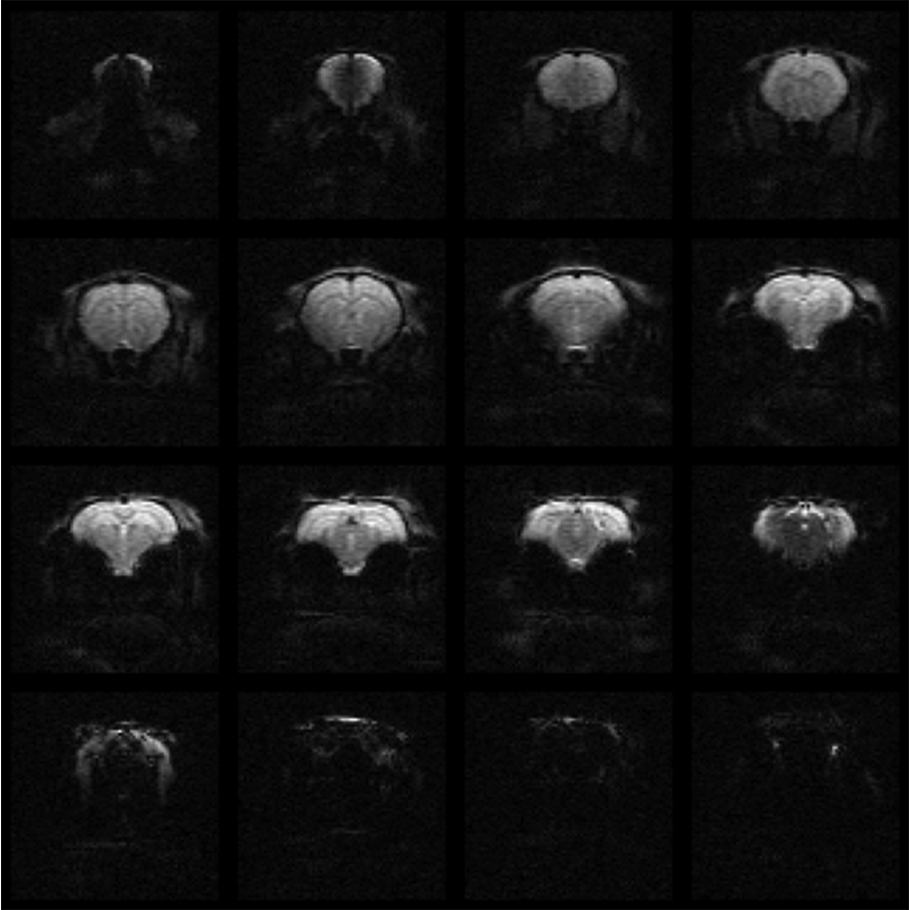


**Figure 6.14:** Example of a raw GE-EPI scan of a representative animal at baseline.

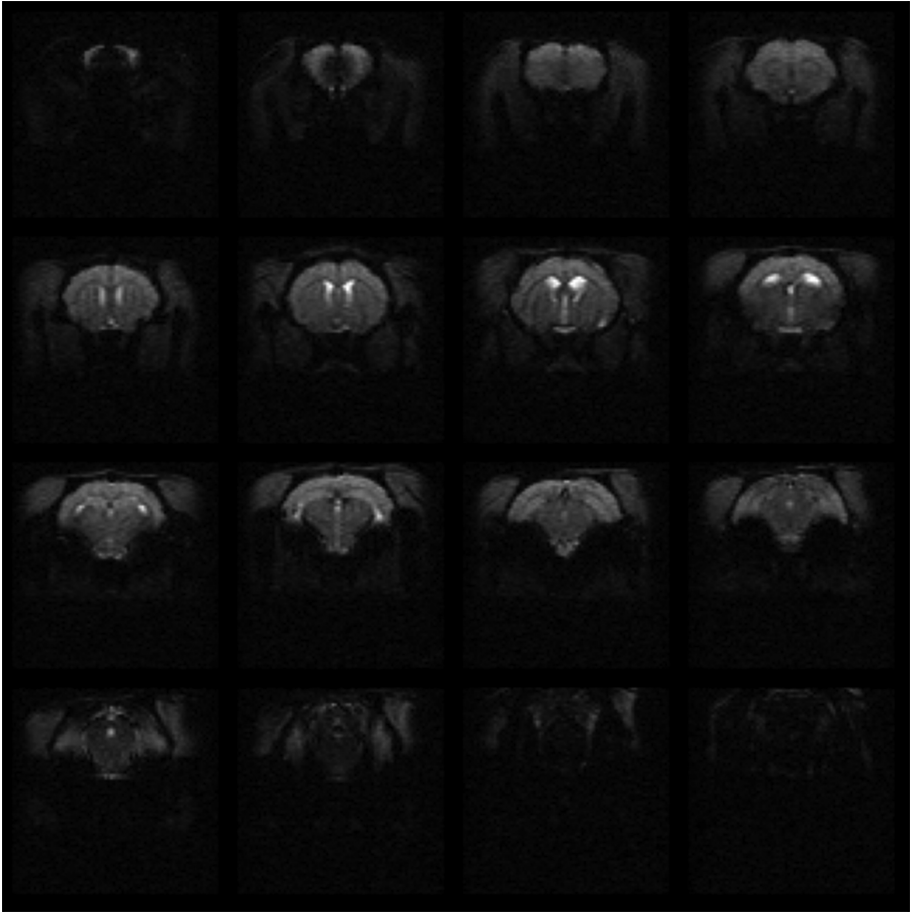


**Figure 6.15:** Example of a raw GE-EPI scan of a representative animal 16 weeks post-SE.

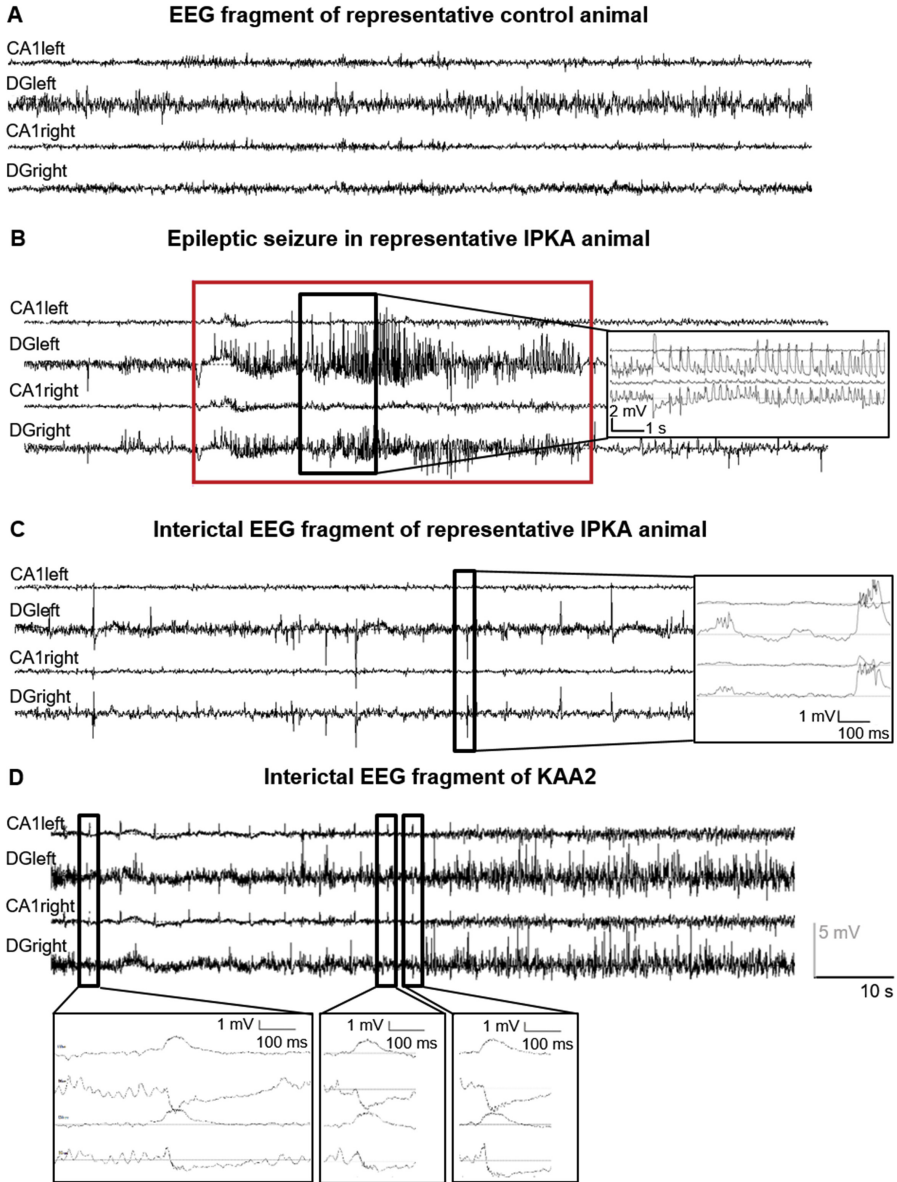


**Figure 6.16:** Examples of EEG recording. A) EEG fragment of a representative control animal, B) EEG fragment of an epileptic seizure and fast ripples in a representative IPKA animal, C) interictal EEG fragment, with typical epileptic discharges, of a representative IPKA animal, D) interictal EEG fragment, with typical epileptiform activity such as epileptic spikes and pathological high frequency oscillations, of KAA2, an animal that did not display any seizures on the EEG during the recording period.

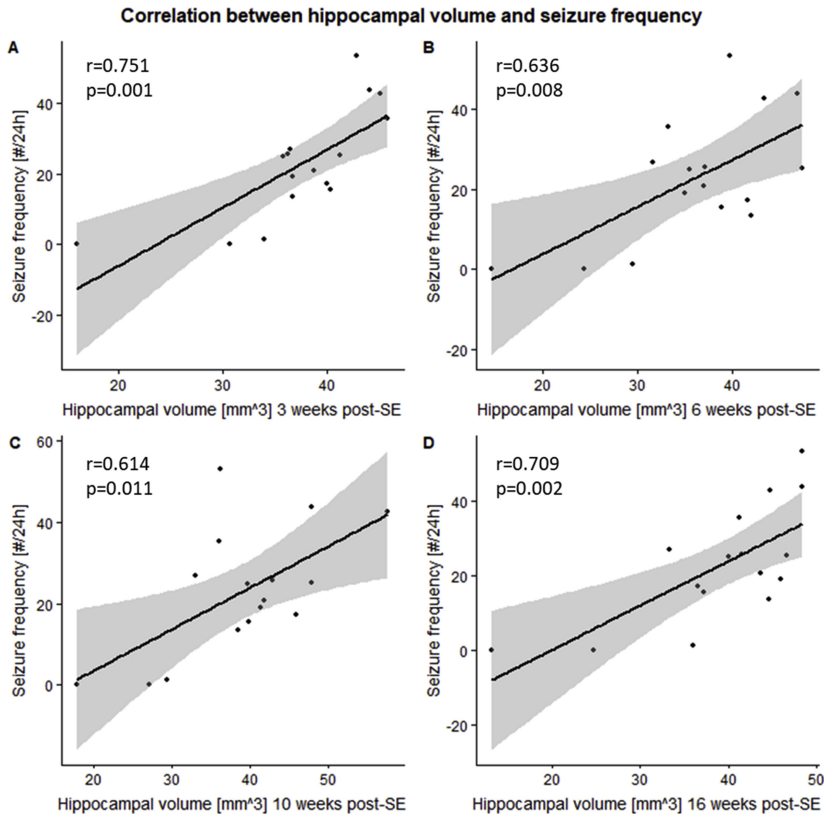


**Figure 6.17:** Correlation between T2-normal hippocampal volume and seizure frequency (number per 24 h).

**Table 6.3:** Test-retest reliability of graph theoretical network measures, assessed using the coefficient of variation [%] calculated between scans within one scanning session, between scans in different sessions and between scans in different animals.

	Mean	Standard deviation	Coefficient of variation [%]		
			Within-session	Between-sessions	Between subjects
<b>Degree</b>	13.1	1.64	8.65	5.12	12.5
<b>Clustering coefficient</b>	0.393	0.0180	4.17	2.39	4.58
<b>Characteristic path length</b>	2.55	0.282	8.81	5.79	11.1
<b>Local efficiency</b>	0.811	0.0958	8.80	5.57	11.8
<b>Global efficiency</b>	0.491	0.0609	8.96	6.52	12.4

## Bibliography

- [1] P. M. Matthews and P. Jezzard, “Functional magnetic resonance imaging,” *Journal of Neurology, Neurosurgery & Psychiatry*, vol. 75, no. 1, pp. 6–12, 2004.
- [2] J. Wang, X. Zuo, and Y. He, “Graph-based network analysis of resting-state functional mri,” *Frontiers in systems neuroscience*, vol. 4, p. 16, 2010.
- [3] K. Smitha, K. Akhil Raja, K. Arun, P. Rajesh, B. Thomas, T. Kapilamoorthy, and C. Kesavadas, “Resting state fmri: A review on methods in resting state connectivity analysis and resting state networks,” *The neuroradiology journal*, vol. 30, no. 4, pp. 305–317, 2017.
- [4] M. Rubinov and O. Sporns, “Complex network measures of brain connectivity: uses and interpretations,” *Neuroimage*, vol. 52, no. 3, pp. 1059–1069, 2010.
- [5] R. S. Fisher, W. V. E. Boas, W. Blume, C. Elger, P. Genton, P. Lee, and J. Engel Jr, “Epileptic seizures and epilepsy: definitions proposed by the international league against epilepsy (ILAE) and the international bureau for epilepsy (IBE),” *Epilepsia*, vol. 46, no. 4, pp. 470–472, 2005.
- [6] P. Kwan and M. J. Brodie, “Early identification of refractory epilepsy,” *New England Journal of Medicine*, vol. 342, no. 5, pp. 314–319, 2000.
- [7] E. M. Goldberg and D. A. Coulter, “Mechanisms of epileptogenesis: a convergence on neural circuit dysfunction,” *Nature Reviews Neuroscience*, vol. 14, no. 5, pp. 337–349, 2013.
- [8] J. Engel Jr, “Approaches to refractory epilepsy,” *Annals of Indian Academy of Neurology*, vol. 17, no. Suppl 1, p. S12, 2014.
- [9] J. Nairismägi, A. Pitkänen, M. I. Kettunen, R. A. Kauppinen, and H. Kubova, “Status epilepticus in 12-day-old rats leads to temporal

- lobe neurodegeneration and volume reduction: a histologic and mri study,” *Epilepsia*, vol. 47, no. 3, pp. 479–488, 2006.
- [10] H. G. Niessen, F. Angenstein, S. Vielhaber, C. Frisch, A. Kudin, C. E. Elger, H.-J. Heinze, H. Scheich, and W. S. Kunz, “Volumetric magnetic resonance imaging of functionally relevant structural alterations in chronic epilepsy after pilocarpine-induced status epilepticus in rats,” *Epilepsia*, vol. 46, no. 7, pp. 1021–1026, 2005.
- [11] R. S. Polli, J. M. Malheiros, R. Dos Santos, C. Hamani, B. M. Longo, A. Tannús, L. E. Mello, and L. Covolan, “Changes in hippocampal volume are correlated with cell loss but not with seizure frequency in two chronic models of temporal lobe epilepsy,” *Frontiers in neurology*, vol. 5, p. 111, 2014.
- [12] O. Wolf, V. Dyakin, A. Patel, C. Vadasz, M. De Leon, B. McEwen, and K. Bulloch, “Volumetric structural magnetic resonance imaging (mri) of the rat hippocampus following kainic acid (ka) treatment,” *Brain research*, vol. 934, no. 2, pp. 87–96, 2002.
- [13] N. Bernasconi, A. Bernasconi, Z. Caramanos, S. Antel, F. Andermann, and D. L. Arnold, “Mesial temporal damage in temporal lobe epilepsy: a volumetric mri study of the hippocampus, amygdala and parahippocampal region,” *Brain*, vol. 126, no. 2, pp. 462–469, 2003.
- [14] R. S. Briellmann, S. F. Berkovic, A. Syngeniotes, M. A. King, and G. D. Jackson, “Seizure-associated hippocampal volume loss: a longitudinal magnetic resonance study of temporal lobe epilepsy,” *Annals of neurology*, vol. 51, no. 5, pp. 641–644, 2002.
- [15] L. Jutila, A. Ylinen, K. Partanen, I. Alafuzoff, E. Mervaala, J. Partanen, M. Vapalahti, P. Vainio, and A. Pitkänen, “Mr volumetry of the entorhinal, perirhinal, and temporopolar cortices in drug-refractory temporal lobe epilepsy,” *American Journal of Neuroradiology*, vol. 22, no. 8, pp. 1490–1501, 2001.
- [16] T. Lencz, G. McCarthy, R. A. Bronen, T. M. Scott, J. A. Insigni, K. J. Sass, R. A. Novelly, J. H. Kim, and D. D. Spencer, “Quantita-

- tive magnetic resonance imaging in temporal lobe epilepsy: relationship to neuropathology and neuropsychological function,” *Annals of Neurology: Official Journal of the American Neurological Association and the Child Neurology Society*, vol. 31, no. 6, pp. 629–637, 1992.
- [17] L. Marsh, M. J. Morrell, P. K. Shear, E. V. Sullivan, H. Freeman, A. Marie, K. O. Lim, and A. Pfefferbaum, “Cortical and hippocampal volume deficits in temporal lobe epilepsy,” *Epilepsia*, vol. 38, no. 5, pp. 576–587, 1997.
- [18] W. Liao, Z. Zhang, Z. Pan, D. Mantini, J. Ding, X. Duan, C. Luo, G. Lu, and H. Chen, “Altered functional connectivity and small-world in mesial temporal lobe epilepsy,” *PLoS one*, vol. 5, no. 1, p. e8525, 2010.
- [19] V. L. Morgan, B. Abou-Khalil, and B. P. Rogers, “Evolution of functional connectivity of brain networks and their dynamic interaction in temporal lobe epilepsy,” *Brain connectivity*, vol. 5, no. 1, pp. 35–44, 2015.
- [20] F. Pittau, C. Grova, F. Moeller, F. Dubeau, and J. Gotman, “Patterns of altered functional connectivity in mesial temporal lobe epilepsy,” *Epilepsia*, vol. 53, no. 6, pp. 1013–1023, 2012.
- [21] J. Song, V. A. Nair, W. Gaggl, and V. Prabhakaran, “Disrupted brain functional organization in epilepsy revealed by graph theory analysis,” *Brain connectivity*, vol. 5, no. 5, pp. 276–283, 2015.
- [22] M. Song, H. Du, N. Wu, B. Hou, G. Wu, J. Wang, H. Feng, and T. Jiang, “Impaired resting-state functional integrations within default mode network of generalized tonic-clonic seizures epilepsy,” *PLoS One*, vol. 6, no. 2, p. e17294, 2011.
- [23] M. Vlooswijk, M. Vaessen, J. Jansen, M. De Krom, H. Majoie, P. Hofman, A. Aldenkamp, and W. Backes, “Loss of network efficiency associated with cognitive decline in chronic epilepsy,” *Neurology*, vol. 77, no. 10, pp. 938–944, 2011.

- [24] D. Bertoglio, E. Jonckers, I. Ali, M. Verhoye, A. Van der Linden, and S. Dedeurwaerdere, "In vivo measurement of brain network connectivity reflects progression and intrinsic disease severity in a model of temporal lobe epilepsy," *Neurobiology of disease*, vol. 127, pp. 45–52, 2019.
- [25] R. S. Gill, S. M. Mirsattari, and L. S. Leung, "Resting state functional network disruptions in a kainic acid model of temporal lobe epilepsy," *NeuroImage: Clinical*, vol. 13, pp. 70–81, 2017.
- [26] Y. Jiang, C.-L. Han, H.-G. Liu, X. Wang, X. Zhang, F.-G. Meng, and J.-G. Zhang, "Abnormal hippocampal functional network and related memory impairment in pilocarpine-treated rats," *Epilepsia*, vol. 59, no. 9, pp. 1785–1795, 2018.
- [27] A. M. Mishra, X. Bai, B. G. Sanganahalli, S. G. Waxman, O. Shatillo, O. Grohn, F. Hyder, A. Pitkänen, and H. Blumenfeld, "Decreased resting functional connectivity after traumatic brain injury in the rat," *PloS one*, vol. 9, no. 4, p. e95280, 2014.
- [28] W. M. Otte, R. M. Dijkhuizen, M. P. van Meer, W. S. van der Hel, S. A. Verlinde, O. van Nieuwenhuizen, M. A. Viergever, C. J. Stam, and K. P. Braun, "Characterization of functional and structural integrity in experimental focal epilepsy: reduced network efficiency coincides with white matter changes," *PloS one*, vol. 7, no. 7, p. e39078, 2012.
- [29] T. Pirttimäki, R. A. Salo, A. Shatillo, M. I. Kettunen, J. Paasonen, A. Sierra, K. Jokivarsi, V. Leinonen, P. Andrade, S. Quittek *et al.*, "Implantable rf-coil with multiple electrodes for long-term eeg-fmri monitoring in rodents," *Journal of neuroscience methods*, vol. 274, pp. 154–163, 2016.
- [30] J. L. Hellier, P. R. Patrylo, P. S. Buckmaster, and F. E. Dudek, "Recurrent spontaneous motor seizures after repeated low-dose systemic treatment with kainate: assessment of a rat model of temporal lobe epilepsy," *Epilepsy research*, vol. 31, no. 1, pp. 73–84, 1998.

- [31] R. Weber, P. Ramos-Cabrer, D. Wiedermann, N. Van Camp, and M. Hoehn, “A fully noninvasive and robust experimental protocol for longitudinal fmri studies in the rat,” *Neuroimage*, vol. 29, no. 4, pp. 1303–1310, 2006.
- [32] G. Paxinos and C. Watson, *The Rat Brain in Stereotaxic Coordinates*, 7th ed. Elsevier Science, 2013.
- [33] J. Wang, X. Wang, M. Xia, X. Liao, A. Evans, and Y. He, “Gretna: a graph theoretical network analysis toolbox for imaging connectomics,” *Frontiers in human neuroscience*, vol. 9, p. 386, 2015.
- [34] X. Di, E. H. Kim, C.-C. Huang, C.-P. Lin, and B. B. Biswal, “The influence of the amplitude of low-frequency fluctuations on resting-state functional connectivity,” *Frontiers in human neuroscience*, vol. 7, p. 118, 2013.
- [35] X.-W. Song, Z.-Y. Dong, X.-Y. Long, S.-F. Li, X.-N. Zuo, C.-Z. Zhu, Y. He, C.-G. Yan, and Y.-F. Zang, “Rest: a toolkit for resting-state functional magnetic resonance imaging data processing,” *PloS one*, vol. 6, no. 9, p. e25031, 2011.
- [36] M. Lévesque and M. Avoli, “The kainic acid model of temporal lobe epilepsy,” *Neuroscience & Biobehavioral Reviews*, vol. 37, no. 10, pp. 2887–2899, 2013.
- [37] C. T. Rueden, J. Schindelin, M. C. Hiner, B. E. DeZonia, A. E. Walter, E. T. Arena, and K. W. Eliceiri, “Imagej2: Imagej for the next generation of scientific image data,” *BMC bioinformatics*, vol. 18, no. 1, pp. 1–26, 2017.
- [38] J. Schindelin, I. Arganda-Carreras, E. Frise, V. Kaynig, M. Longair, T. Pietzsch, S. Preibisch, C. Rueden, S. Saalfeld, B. Schmid *et al.*, “Fiji: an open-source platform for biological-image analysis,” *Nature methods*, vol. 9, no. 7, pp. 676–682, 2012.
- [39] A. Fornito, A. Zalesky, and E. T. Bullmore, “Network scaling effects in graph analytic studies of human resting-state fmri data,” *Frontiers in systems neuroscience*, vol. 4, p. 22, 2010.

- [40] D. A. Duricki, S. Soleman, and L. D. Moon, "Analysis of longitudinal data from animals with missing values using spss," *Nature protocols*, vol. 11, no. 6, pp. 1112–1129, 2016.
- [41] A. Zalesky, A. Fornito, and E. T. Bullmore, "Network-based statistic: identifying differences in brain networks," *Neuroimage*, vol. 53, no. 4, pp. 1197–1207, 2010.
- [42] L. Becerra, G. Pendse, P.-C. Chang, J. Bishop, and D. Borsook, "Robust reproducible resting state networks in the awake rodent brain," *PloS one*, vol. 6, no. 10, p. e25701, 2011.
- [43] H. Lu, Q. Zou, H. Gu, M. E. Raichle, E. A. Stein, and Y. Yang, "Rat brains also have a default mode network," *Proceedings of the National Academy of Sciences*, vol. 109, no. 10, pp. 3979–3984, 2012.
- [44] L.-M. Hsu, X. Liang, H. Gu, J. K. Brynildsen, J. A. Stark, J. A. Ash, C.-P. Lin, H. Lu, P. R. Rapp, E. A. Stein *et al.*, "Constituents and functional implications of the rat default mode network," *Proceedings of the National Academy of Sciences*, vol. 113, no. 31, pp. E4541–E4547, 2016.
- [45] A. K. Sharma, W. H. Jordan, R. Y. Reams, D. G. Hall, and P. W. Snyder, "Temporal profile of clinical signs and histopathologic changes in an f-344 rat model of kainic acid-induced mesial temporal lobe epilepsy," *Toxicologic pathology*, vol. 36, no. 7, pp. 932–943, 2008.
- [46] D. Bertoglio, H. Amhaoul, A. Van Eetveldt, R. Houbrechts, S. Van De Vijver, I. Ali, and S. Dedeurwaerdere, "Kainic acid-induced post-status epilepticus models of temporal lobe epilepsy with diverging seizure phenotype and neuropathology," *Frontiers in neurology*, vol. 8, p. 588, 2017.
- [47] B. Van Nieuwenhuyse, R. Raedt, M. Sprengers, I. Dauwe, S. Gadeyne, E. Carrette, J. Delbeke, W. Wadman, P. Boon, and K. Vonck, "The systemic kainic acid rat model of temporal lobe epilepsy: long-term eeg monitoring," *Brain research*, vol. 1627, pp. 1–11, 2015.

- [48] A. M. Airaksinen, J.-P. Niskanen, R. Chamberlain, J. K. Huttunen, J. Nissinen, M. Garwood, A. Pitkänen, and O. Gröhn, “Simultaneous fmri and local field potential measurements during epileptic seizures in medetomidine-sedated rats using raser pulse sequence,” *Magnetic resonance in medicine*, vol. 64, no. 4, pp. 1191–1199, 2010.
- [49] J. Grandjean, A. Schroeter, I. Batata, and M. Rudin, “Optimization of anesthesia protocol for resting-state fmri in mice based on differential effects of anesthetics on functional connectivity patterns,” *Neuroimage*, vol. 102, pp. 838–847, 2014.
- [50] E. Jonckers, R. Delgado y Palacios, D. Shah, C. Guglielmetti, M. Verhoye, and A. Van der Linden, “Different anesthesia regimes modulate the functional connectivity outcome in mice,” *Magnetic resonance in medicine*, vol. 72, no. 4, pp. 1103–1112, 2014.
- [51] M. E. Magnuson, G. J. Thompson, W.-J. Pan, and S. D. Keilholz, “Time-dependent effects of isoflurane and dexmedetomidine on functional connectivity, spectral characteristics, and spatial distribution of spontaneous bold fluctuations,” *NMR in biomedicine*, vol. 27, no. 3, pp. 291–303, 2014.
- [52] J. Paasonen, P. Stenroos, R. A. Salo, V. Kiviniemi, and O. Gröhn, “Functional connectivity under six anesthesia protocols and the awake condition in rat brain,” *Neuroimage*, vol. 172, pp. 9–20, 2018.
- [53] K. A. Williams, M. Magnuson, W. Majeed, S. M. LaConte, S. J. Peltier, X. Hu, and S. D. Keilholz, “Comparison of  $\alpha$ -chloralose, medetomidine and isoflurane anesthesia for functional connectivity mapping in the rat,” *Magnetic resonance imaging*, vol. 28, no. 7, pp. 995–1003, 2010.
- [54] J. Paasonen, R. A. Salo, A. Shatillo, M. M. Forsberg, J. Närväinen, J. K. Huttunen, and O. Gröhn, “Comparison of seven different anesthesia protocols for nicotine pharmacologic magnetic resonance imaging in rat,” *European Neuropsychopharmacology*, vol. 26, no. 3, pp. 518–531, 2016.

- [55] W.-J. Pan, J. C. Billings, J. K. Grooms, S. Shakil, and S. D. Keilholz, “Considerations for resting state functional mri and functional connectivity studies in rodents,” *Frontiers in neuroscience*, vol. 9, p. 269, 2015.
- [56] W. Liao, Z. Zhang, Z. Pan, D. Mantini, J. Ding, X. Duan, C. Luo, Z. Wang, Q. Tan, G. Lu *et al.*, “Default mode network abnormalities in mesial temporal lobe epilepsy: a study combining fmri and dti,” *Human brain mapping*, vol. 32, no. 6, pp. 883–895, 2011.
- [57] S. D. Vann, J. P. Aggleton, and E. A. Maguire, “What does the retrosplenial cortex do?” *Nature reviews neuroscience*, vol. 10, no. 11, pp. 792–802, 2009.



## 7 | Dynamic functional connectivity and graph theory metrics in a rat model of temporal lobe epilepsy reveal a preference for brain states with a lower functional connectivity, segregation and integration

This chapter is based on: Christiaen, E., Goossens, M. G., Descamps, B., Larsen, L. E., Boon, P., Raedt, R., & Vanhove, C. (2020). Dynamic functional connectivity and graph theory metrics in a rat model of temporal lobe epilepsy reveal a preference for brain states with a lower functional connectivity, segregation and integration. *Neurobiology of disease*, 139, 104808.

### Abstract

Epilepsy is a neurological disorder characterized by recurrent epileptic seizures. The involvement of abnormal functional brain networks in the development of epilepsy and its comorbidities has been demonstrated by electrophysiological and neuroimaging studies in patients with epilepsy. This longitudinal study investigated changes in dynamic functional connectivity (dFC) and network topology during the development of epilepsy using the intraperitoneal kainic acid (IPKA) rat model of temporal lobe epilepsy (TLE). Resting state functional magnetic resonance images (rsfMRI) of 20 IPKA animals and 7 healthy control animals were acquired before and 1, 3, 6, 10 and 16 weeks after status epilepticus

(SE) under medetomidine anaesthesia using a 7 T MRI system. Starting from 17 weeks post-SE, hippocampal EEG was recorded to determine the mean daily seizure frequency of each animal. Dynamic functional connectivity was assessed by calculating the correlation matrices between fMRI time series of predefined regions of interest within a sliding window of 50 s using a step length of 2 s. The matrices were classified into 6 functional connectivity states, each characterized by a correlation matrix, using k-means clustering. In addition, several time-variable graph theoretical network metrics were calculated from the time-varying correlation matrices and classified into 6 states of functional network topology, each characterized by a combination of network metrics. Our results showed that functional connectivity states with a lower mean functional connectivity, and lower segregation and integration occurred more often in IPKA animals compared to control animals. Functional connectivity also became less variable during epileptogenesis. In addition, average daily seizure frequency was positively correlated with percentage dwell time (i.e., how often a state occurs) in states with high mean functional connectivity, high segregation and integration, and with the number of transitions between states, while negatively correlated with percentage dwell time in states with a low mean functional connectivity, low segregation, and low integration. This indicates that animals that dwell in states of higher functional connectivity, higher segregation and higher integration, and that switch more often between states, have more seizures.

## 7.1 Introduction

Functional magnetic resonance imaging (fMRI) is a neuroimaging technique that allows for non-invasive visualisation of whole-brain activity. It detects changes in the blood oxygenation level dependent (BOLD) signal, which reflects neuronal activity [1]. Generally, fMRI is used to construct maps indicating brain regions that are activated by a certain task. In contrast to task-based fMRI, resting-state fMRI (rsfMRI) does not require subjects to perform any specific task. During rest, background activity modulates the BOLD signal, inducing spontaneous low frequency fluctuations. Based on statistical dependencies between the

BOLD time series of brain regions of interest, functionally connected regions can be identified and functional brain networks can be detected [2]. Several techniques can be used to assess functional connectivity, such as seed-based correlation, independent component analysis (ICA), and graph theory [3]. Functional connectivity is affected in several neurological disorders, including Alzheimer's disease, depression, schizophrenia, attention-deficit hyperactivity disorder, and epilepsy [4].

In most rsfMRI studies, functional connectivity is calculated based on statistical dependencies between brain regions over the entire scan, which usually lasts 5 to 20 min, and is thus assumed to be stationary [5]. However, several fMRI and electrophysiological studies have demonstrated that functional connectivity fluctuates within shorter time scales of seconds [5, 6]. To capture these fast changes, dynamic functional connectivity (dFC) can be used [7]. The most common strategy to investigate dFC is using a sliding window approach where pairwise connectivity between brain regions or voxels is repeatedly evaluated for (non)overlapping time windows of data [5, 8]. Differences in dFC between patients and controls have been found in several neurological disorders, including schizophrenia, autism, mild cognitive impairment, Alzheimer's disease, post-traumatic stress disorder, and multiple sclerosis (for review see [5], but also in epilepsy [9–14].

Epilepsy is a neurological disorder characterized by recurrent epileptic seizures [15] and about one third of patients suffer from drug-resistant epilepsy, i.e., their seizures cannot be controlled with anti-epileptic drugs. The most common type of acquired drug-resistant epilepsy is temporal lobe epilepsy (TLE) [16]. Using different analysis techniques, dFC studies found several alterations in TLE patients, including altered mean and variance of the BOLD signal [17], and altered variability of functional connectivity and graph theory metrics [17–20].

Epilepsy is often caused by an initial precipitating insult (IPI) such as stroke, infection, trauma, brain tumor or (febrile) status epilepticus (SE). Following an IPI, functional and structural changes occur in the brain which in some patients are associated with the development of sponta-

neous epileptic seizures. The process where a healthy brain is transformed into an epileptic brain is called epileptogenesis [21].

In this study, changes in dynamic functional connectivity and network topology during the development of epilepsy were investigated in the intraperitoneal kainic acid (IPKA) rat model of TLE. The aim of this study was twofold: (1) to characterize how dFC and dynamic network topology of the rat brain change after SE and during the development of TLE, and (2) to evaluate whether these changes are associated with the occurrence of spontaneous seizures. To the best of our knowledge, no studies have investigated dFC and dynamic network topology in an animal model of epilepsy.

## 7.2 Materials and methods

### 7.2.1 Data set

The data set consisted of rsfMRI scans and EEG recordings of 27 adult male Sprague-Dawley rats ( $276 \pm 15$  g body weight; Envigo, The Netherlands), of which 20 were IPKA animals and 7 control animals. An extra data set was used to validate our methods. This validation data set consisted of rsfMRI scans of 8 adult male Sprague-Dawley rats ( $237 \pm 11$  g body weight; Envigo), all of which were IPKA animals.

### 7.2.2 Animals

The animals were treated according to European guidelines (directive 2010/63/EU). The local Ethical Committee on Animal Experiments of Ghent University (ECD 16/31) approved the protocol. The animals were housed individually in type III H cages (Tecniplast, Australia) on wood-based bedding (Carfil, Belgium), under environmentally controlled conditions (12 h normal light/dark cycles, 20–23 °C and 40–60% relative humidity) with food (Rats and Mice Maintenance, Carfil, Belgium) and water ad libitum. Paper nesting material (Nesting, Carfil, Belgium) and a piece of gnawing wood (M-brick, Carfil, Belgium) were used to enrich the cages.

### 7.2.3 Status epilepticus

Twenty animals of the main data set and all 8 animals of the validation data set were intraperitoneally (i.p., 5 mg/kg/h) injected with kainic acid (KA; Tocris Bioscience, UK) according to the protocol of Hellier et al. [22] at an age of 8 weeks. KA was administered every hour until motor seizures were elicited for at least 3 h, referred to as status epilepticus (SE). On average, the animals were injected with 12.7 mg/kg KA (range: 5–20 mg/kg). Two animals died during or within 4 h after SE induction. The other 7 animals of the main data set were injected similarly with saline and served as a control group.

### 7.2.4 Image acquisition

In the main data set, anatomical and resting state functional MRI was performed one week before and 1, 3, 6, 10, and 16 weeks after SE. One IPKA rat was excluded 3 weeks after SE, because of a large artifact on the MR images caused by a metal fragment lodged behind its teeth. Anatomical and resting state functional MR images were acquired 20 weeks post-SE in the animals in the validation data set. These animals had been intrahippocampally injected with the viral vector AAV2/7-CamKII $\alpha$ -hM4Di-mCherry (titer  $2.78 \times 10^{13}$  genome copies/ml) 16 weeks post-SE as part of an additional study. Animals were transported to the MR facility one day before scanning. They were sedated with medetomidine while the functional MR images were acquired [23]. First, the animals were anesthetized with isoflurane (5% for induction, 2% for maintenance; Isoflo, Zoetis, USA) and O<sub>2</sub>. Then, a bolus of medetomidine (0.05 mg/kg; Domitor, Orion Pharma, Finland) was injected subcutaneously and after 10 min, isoflurane anaesthesia was discontinued. Continuous subcutaneous infusion of medetomidine (0.1 mg/kg/h) was started 15 min after the bolus injection and 25 min later functional MR images were acquired. Anaesthesia was reversed after the image acquisition with a subcutaneous injection of atipamezole (0.1 mg/kg; Antisedan, Orion Pharma, Finland). The MR images were acquired on a 7 T system (PharmaScan, Bruker, Germany) using a transmit body volume coil (Rapid Biomedical, Germany) and an actively decoupled rat head surface

coil (Rapid Biomedical, Germany) to receive the signal. A circulating-water heating pad maintained the body temperature of the animals and respiration was measured using a pressure sensor. After optimizing the magnetic field homogeneity, TurboRARE T2-weighted anatomical images (TR: 3661 ms, TE: 37 ms, 30 slices, FOV: 35 x 35 mm<sup>2</sup>, in-plane slice resolution: 109 x 109  $\mu\text{m}^2$ , slice thickness: 0.6 mm, acquisition time: 9 min 46 s) were acquired. Next, 3 rsfMRI scans were acquired for the main data set and 2 for the validation data set using single-shot gradient echo echo-planar imaging (GE-EPI; TR: 2000 ms, TE: 20 ms, 16 slices, FOV: 30 x 30 mm<sup>2</sup> and voxel size: 0.375 x 0.375 x 1 mm<sup>3</sup>). Each rsfMRI scan consisted of 300 repetitions and lasted 10 min.

### 7.2.5 Electrode implantation

On average 19.5 weeks after SE (range 17 to 23 weeks), recording electrodes were implanted in both hippocampi in the animals of the main data set. The rats were anesthetized with a mixture of isoflurane (5% for induction, 2% for maintenance) and medical O<sub>2</sub>. After exposing the skull, 13 small burr holes were drilled: 9 for the positioning of stainless steel anchor screws (1.75 mm diameter; PlasticsOne, USA), 2 for the epidural ground/reference electrodes above the right and left frontal cortex respectively and 2 for bilateral hippocampal EEG recording electrodes. Epidural electrodes and bipolar recording electrodes were custom-made by connecting an insulated copper wire to an anchor screw and by twisting two polyimide-coated stainless steel wires (70  $\mu\text{m}$  bare diameter, 900  $\mu\text{m}$  distance between wire tips; California Fine Wire, USA) around each other, respectively. Recording electrodes were implanted in the left and right hippocampus using stereotactic coordinates based on the Rat Brain Atlas by Paxinos and Watson [24] (AP -3.8 mm, ML  $\pm$ 2.2 mm relative to bregma, DV about -3.3 mm relative to brain surface). The T2-weighted anatomical MR images, obtained 16 weeks post-SE, were used to check whether the implantation site was free of KA-induced lesions. Real time electrophysiological recordings were monitored visually and auditively during the positioning of the electrodes to ensure that one tip of the electrode was placed in the subgranular layer of the dentate

gyrus and the other in the pyramidal cell layer of the CA1 region. All electrode leads ended in a connector that was attached to the skull and the anchor screws using acrylic dental cement. Meloxicam (1 mg/kg, subcutaneously, Boehringer Ingelheim, Germany) was injected at the end of the surgery and lidocaine (2% Xylocaine gel, AstraZeneca, UK) was locally applied to the wound to minimize discomfort. Meloxicam was injected a second time 24 h after surgery.

### 7.2.6 EEG recording

EEG recordings were started after one to two weeks of recovery. The EEG set up consisted of a custom-built head stage with unity gain preamplifier (based on TI TL074 JFET OpAmps), shielded 12-channel cables (363/2-000; PlasticsOne), a 12-channel commutator (SL12C; PlasticsOne) and a custom-built 512 $\times$  amplifier (based on TI TL074 JFET OpAmps and a first order high-pass filter with a time constant of 1 s). Animals were awake and freely moving during the recording period. Signals were sampled at 2 kHz by a 16-bit resolution data acquisition card (USB-6259, National Instruments, USA) and stored on the computer for offline analysis by a Matlab-based script (MathWorks, USA). Experienced investigators annotated seizures visually. An electrographic seizure was defined as a repetitive pattern ( $>2$  Hz) of complex, high amplitude EEG spikes that lasts for minimally 5 s. Following an acclimatization period of 3 days, the average number of seizures per day was calculated based on 7 consecutive days of EEG recording.

### 7.2.7 Dynamic functional brain network

#### Parcellation

An in-house parcellated atlas containing 38 cortical and subcortical regions of interest (ROIs), constructed manually based on T2w anatomical images of part of the main data set (10 animals) using SPM12 (<https://www.fil.ion.ucl.ac.uk/spm/software/spm12/>) and Matlab, was used to construct the dynamic functional brain network. The ROIs included auditory cortex, caudate putamen, cingulate cortex, dorsolateral orbital cortex, globus pallidus, hippocampus, insula, motor cortex,

nucleus accumbens, parietal association cortex, piriform cortex, posterior parietal cortex, prelimbic cortex, retrosplenial cortex, septum, somatosensory cortex, temporal association cortex, thalamus, and visual cortex, each in the left and right hemisphere. The atlas was adapted to the IPKA model, i.e., hyperintensities visible on the T2w images indicative for structural damage were excluded from the ROIs.

### **Sliding window analysis**

The sliding window approach, implemented in the Graph Theoretical Network Analysis (GRETNA) toolbox [25], was used to calculate the dFC between the ROIs (Figure 7.1). The mean time series for each ROI were extracted and the Pearson correlation coefficient was calculated between each pair within a rectangular time window of 50 s. Then, the time window was shifted repeatedly with 2 s and each time the correlation coefficients were calculated. In this way, 276 correlation matrices (38 x 38) were obtained for each scan. For further analysis, the correlation coefficients were Fisher r-to-z transformed to obtain a normal distribution. In addition, graph theory was used to assess the functional organization of the brain within each time window [26]. The correlation matrices were represented as a graph with the ROIs as nodes, and the correlation coefficients between the ROIs as edges. The weakest edges were removed to obtain a 35% network density, i.e., the number of remaining connections divided by the maximum number of possible connections. Several graph theoretical metrics were calculated using GRETNA. On a global level, degree, characteristic path length, global efficiency, clustering coefficient, and local efficiency were determined, and degree was calculated for each node or ROI as well. Degree is the number of edges connected to a node. Characteristic path length is the average number of edges connecting two nodes in the graph, and global efficiency is the average inverse path length between two nodes. Clustering coefficient is the proportion of neighbours of a node that are also connected to one another, and local efficiency is global efficiency calculated within the neighbourhood of a node, i.e., the nodes connected to that node. Degree is a measure of the importance of a node in the graph, characteristic path length and global

efficiency are measures of functional integration or overall communication efficiency, and clustering coefficient and local efficiency are measures of functional segregation or local interconnectivity in the network [2, 26].

### 7.2.8 States of functional connectivity and functional network topology

The correlation matrices were classified into a subset of connectivity states. These states can be seen as recurring patterns of functional connectivity. A k-means clustering algorithm (kmeans function in Matlab) was used to partition the correlation matrices into a number of clusters and the optimal number of clusters was determined by the Elbow method [27]. In k-means clustering, the total intra-cluster variation is minimized. The Elbow method calculates the intra-cluster variation in function of the number of clusters and determines for which number of clusters, adding another cluster does not lead to a large decrease in intra-cluster variation. The clustering was performed on the entire data set containing 144,900 correlation matrices, consisting of the scans of all animals of the main data set at all time points. For each state of functional connectivity, mean, standard deviation, and maximum and minimum z-scores were calculated. These were then sorted from highest to lowest mean value. Additionally, the graph theoretical network metrics characteristic path length, clustering coefficient, global and local efficiency, and global and nodal degree were calculated for each state. These network metrics were calculated at different densities of the correlation matrices, from 20 to 50% density with a 5% interval, and averaged over these densities. Moreover, coreness of the nodes was used to assess the importance of the nodes in each functional connectivity state, regardless of the mean value of this state. A functional brain network usually consists of a core, i.e., a set of highly connected nodes, and a periphery, i.e., the other, weakly connected, nodes. Coreness indicates how often a node is part of the core and is a number between 0 (never in the core) and 1 (always in the core) [28]. To calculate coreness, all nodes are ranked from highest to lowest degree. Then, the connection strength with all nodes with a higher degree is calculated for each node. The node for which this value

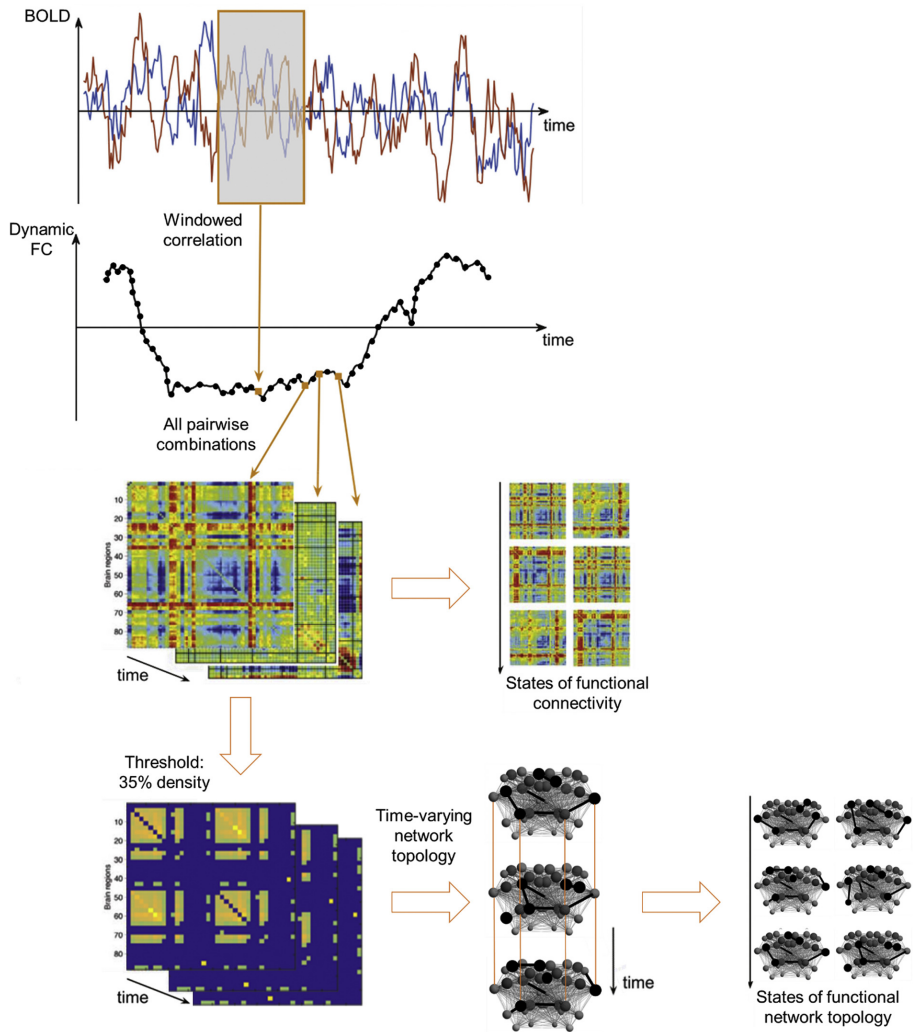


**Figure 7.1:** Construction and clustering of dynamic functional brain networks: Pearson correlation coefficient is calculated between each pair of ROIs within a rectangular time window of 50 s that is shifted repeatedly with 2 s, to obtain 276  $38 \times 38$  correlation matrices that are then clustered into 6 recurring states of functional connectivity. After applying a threshold to obtain a network density of 35%, several graph theoretical network metrics are calculated for each correlation matrix to quantify its topology. The different network topologies are then clustered into 6 states of functional network topology (Adapted from [5]).

is maximal is the limit of the core. All nodes with a higher degree are part of the core and are assigned coreness 1, all nodes with a lower degree are part of the periphery and are assigned coreness 0. This is done for all network densities and averaged, leading to a coreness between 0 and 1 for each node in the network.

To assess the variability in functional network topology, the standard deviation over the 276 time windows was calculated for all graph theoretical network metrics. Then, the time-varying network topology, characterized by a combination of the global network metrics degree, clustering coefficient, characteristic path length, and local and global efficiency, was classified into a subset of states as well.

### 7.2.9 Dwell time and number of transitions

For each animal and each time point, the percentage dwell time for each state of functional connectivity and network topology was determined. This was calculated as the ratio of the number of times a state occurs within a scan, to the total number of windows within the scan ( $n = 276$ ). In addition, the number of transitions was calculated. This is the number of times the functional connectivity changes between states within a scan, i.e., within 10 min. These parameters, and the variability in network topology, were statistically analysed using a linear mixed-effects model (LMEM) in IBM SPSS Statistics for Windows, version 26 (IBM Corp., N.Y., USA). The covariance structure was the ‘compound symmetry’ structure, fixed factors were group (IPKA animals and control animals), time (baseline, 1, 3, 6, 10 and 16 weeks after SE), and group-by-time interaction. Least-significant-difference tests were used to explore significant effects and interactions, a significance level of 0.05 was used for main effects and interactions, and the Bonferroni and false discovery rate (FDR) correction were used to correct for multiple comparisons between time points and variables, respectively. For some parameters, the assumption of normally distributed residuals was not met, most likely due to a large number of zero values in some states. In this case, the effect of group was evaluated using the non-parametric Mann-Whitney U test, and effect of time with the non-parametric Friedmann test. For pair-

wise comparisons, the Mann-Whitney U test and Wilcoxon signed-rank test were used for between-group and within-group statistical testing, respectively, and the Bonferroni correction was used to correct for multiple comparisons.

### 7.2.10 Correlation with seizure frequency

The Pearson correlation coefficient was calculated to assess the correlation between mean daily seizure frequency and dFC parameters such as dwell time in states of functional connectivity and network topology, number of transitions between states, and standard deviation of global network metrics at each time point. A significance level of 0.05 was used. If the one-sample Kolmogorov-Smirnov test showed that one of the variables was not normally distributed, Spearman's rank-order correlation was used instead of Pearson correlation. FDR correction was used to correct for multiple comparisons when calculating the correlation between seizure frequency and percentage dwell time in different states at the same time point.

### 7.2.11 Influence of window length

One of the limitations of a sliding window analysis, is that the window length has to be chosen a priori. If it is too short, false fluctuations can be observed in the dFC, but if the window length is too long, not all genuine fluctuations will be detected. A window length of 30 to 60 s is usually a good trade-off [5]. In this study, we chose a window length of 50 s or 25 TRs. To assess the influence of the choice of window length, we repeated the calculation of dwell time in, and number of transitions between states of functional connectivity using window lengths of 30 s (15 TRs) and 70 s (35 TRs).

### 7.2.12 Validation of epileptic dynamic functional connectivity

An extra data set was used to validate our results. This data set consisted of rsfMRI scans in 8 IPKA animals, acquired 20 weeks post-SE.

The dynamic functional brain network was constructed using the parcellated atlas of the main data set and a sliding window length of 50 s. Each correlation matrix was assigned to one of the states of functional connectivity of the main data set using the Matlab function *pdist2*. This function determines which functional connectivity state is the closest match to each matrix based on Euclidian distance. Again, percentage dwell time in each state and number of transitions were calculated. Then, a two-sample Kolmogorov-Smirnov test assessed whether these parameters came from the same distribution as those of the IPKA group in the main data set.

## 7.3 Results

### 7.3.1 States of functional connectivity and network topology

Using k-means clustering and the Elbow method, all time-varying correlation matrices were assigned to one of 6 recurring states of functional connectivity (Figure 7.2). For each state, mean, standard deviation, and maximum and minimum z-scores are listed in Table 7.1. The states were sorted from highest (State 1) to lowest mean value (State 6). In addition, 4 global network metrics were calculated and displayed in Figure 7.3. Characteristic path length was lowest in State 1 and highest in State 6, while clustering coefficient and local and global efficiency were highest in State 1 and lowest in State 6. In Figure 7.4, nodal degree and coreness are visualized for each state. Average degree decreased from State 1 to State 6, but the relative importance of the nodes in the network remained similar. For each state, the core consisted of somatosensory cortex, cingulate cortex, motor cortex, visual cortex, caudate putamen, thalamus, retrosplenial cortex, and hippocampus. Of these regions, visual cortex, thalamus, and hippocampus varied most between states.

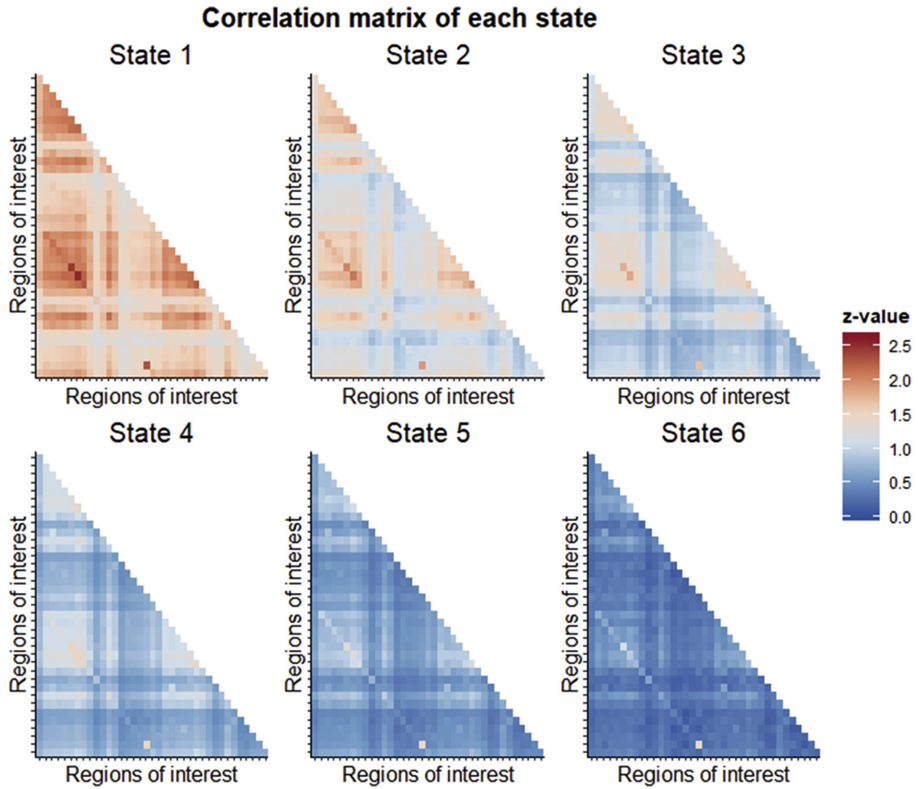


**Figure 7.2:** Correlation matrices (z-score) of 6 recurring states of functional connectivity, sorted from highest (State 1) to lowest (State 6) mean value.

**Table 7.1:** Characterization of 6 recurring states of functional connectivity determined using k-means clustering.

	State 1	State 2	State 3	State 4	State 5	State 6
Mean	1.65	1.28	1.03	0.80	0.58	0.35
Standard deviation	0.24	0.24	0.22	0.21	0.18	0.14
Maximum	2.53	2.11	1.81	1.55	1.42	1.35
Minimum	1.13	0.80	0.61	0.42	0.26	0.08

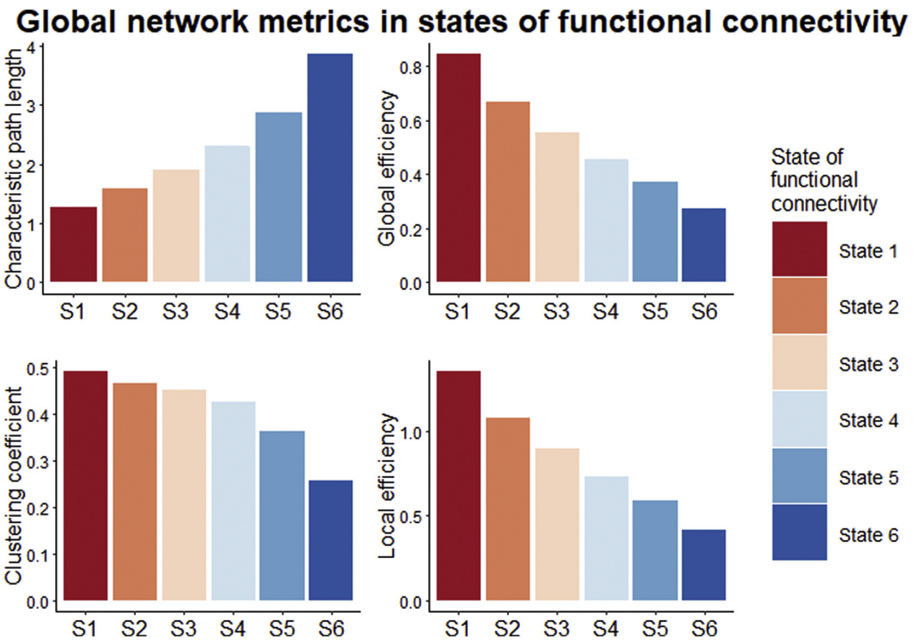


**Figure 7.3:** Global network metrics for each state of functional connectivity. Characteristic path length increases from State 1 to State 6, while clustering coefficient and local and global efficiency decrease.

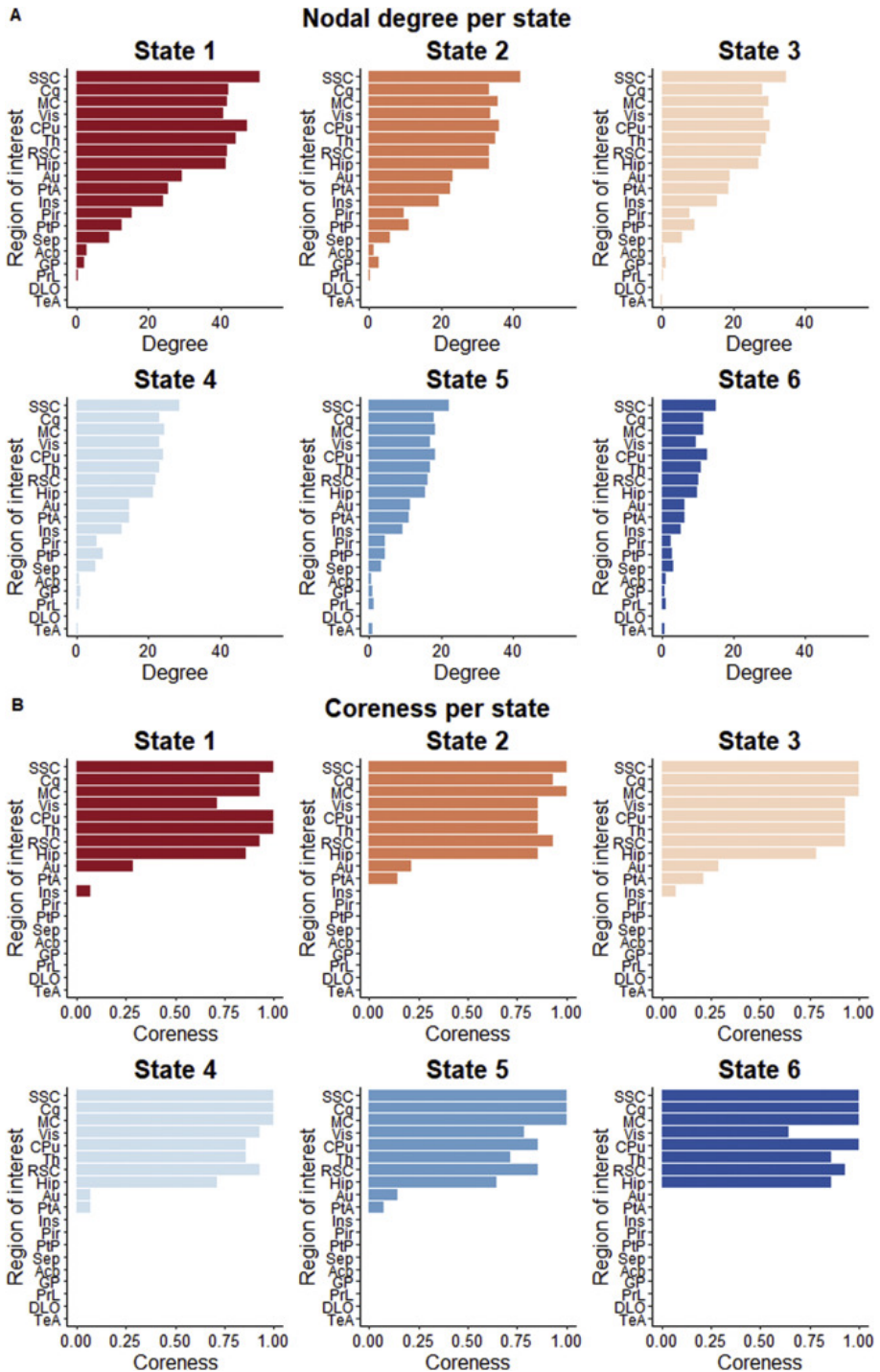


**Figure 7.4:** A) Nodal degree and B) coreness for each state. On average, degree decreases from State 1 to State 6, but the relative importance of the nodes in the network remains similar. Data are visualized as a bar graph with mean values.

Network metrics were not only calculated for the 6 functional connectivity states, but also for the time-varying correlation matrices. The standard deviation over the 276 time windows of global degree, clustering coefficient, and global efficiency is visualized in Figure 7.5. Statistical analysis showed that standard deviation of global degree and global efficiency was significantly lower in the IPKA group compared to the control group ( $U = 1.27 \cdot 10^3$ ,  $p < 0.001$  and  $U = 1.21 \cdot 10^3$ ,  $p < 0.001$ , respectively), while standard deviation of clustering coefficient was significantly higher ( $F_{1,24.3} = 12.5$ ,  $p = 0.002$ ). Standard deviation of global degree and global efficiency decreased significantly during epileptogenesis in the IPKA group ( $\chi^2 = 22.3$ ,  $p < 0.001$  and  $\chi^2 = 15.6$ ,  $p = 0.008$ , respectively), but not in the control group ( $\chi^2 = 1.61$ ,  $p = 0.900$  and  $\chi^2 = 3.08$ ,  $p = 0.687$ , respectively). There was a significant increase in standard deviation of clustering coefficient during epileptogenesis in the IPKA group ( $F_{5,123} = 3.93$ ,  $p = 0.002$ ), but not in the control group ( $F_{5,122} = 1.45$ ,  $p = 0.210$ ).

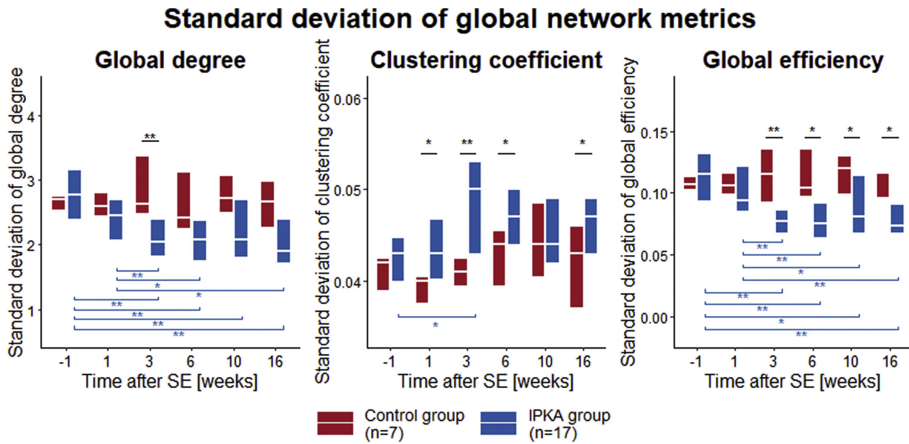


**Figure 7.5:** Standard deviation over 276 time windows for global degree, clustering coefficient and global efficiency. Data are presented as a boxplot with median and interquartile range, \* $p < .05$ , \*\* $p < .01$ , \*\*\* $p < .001$ .

The time-varying network metrics were also decomposed into 6 recurring states of functional network topology using k-means clustering in combination with the Elbow method. The states were sorted from highest

to lowest global degree. Clustering coefficient, and local and global efficiency were highest in State 1 and lowest in State 6, while characteristic path length was lowest in State 1 (Figure 7.6).

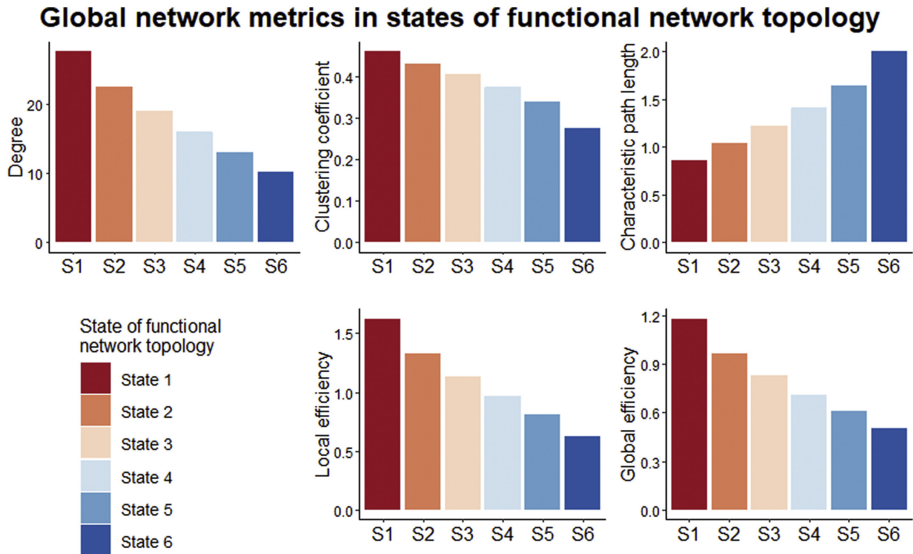


**Figure 7.6:** Global network metrics for each state of functional network topology. Degree, clustering coefficient, local and global efficiency decrease from State 1 to State 6, while characteristic path length increases.

### 7.3.2 Percentage dwell time in states of functional connectivity and network topology

Percentage dwell time was calculated for each state of functional connectivity and network topology and visualized as a function of time, i.e., the number of weeks post-SE, for the IPKA group and the control group. In Figure 7.7, each segment of a bar represents the percentage dwell time in a state averaged over the animals in the group (IPKA group or control group) at one time point. The 6 states always add up to 100%. Statistical analysis revealed a significant difference in percentage dwell time between the control and the IPKA group. The dwell time in State 1, 2 and 3 was significantly lower in the IPKA group compared to the control group, while dwell time in State 5 and 6 was significantly higher in the

IPKA group. A significant effect of time could be found in the IPKA group. There was a significant decrease in dwell time in State 1, 2, 3 and 4 and an increase in dwell time in State 5 and 6 during epileptogenesis in the IPKA group. No significant changes over time were found in the control group.

Similar results were obtained for percentage dwell time in states of functional network topology. In State 1, 2 and 3, dwell time was significantly lower in the IPKA group compared to the control group, while in State 5 and 6, dwell time was significantly higher in the IPKA group. Percentage dwell time in State 1, 2, 3 and 4 decreased significantly during epileptogenesis in the IPKA group, while it increased significantly in State 5 and 6. No significant changes over time were found in the control group. The results of the statistical analysis are summarized in 7.2.

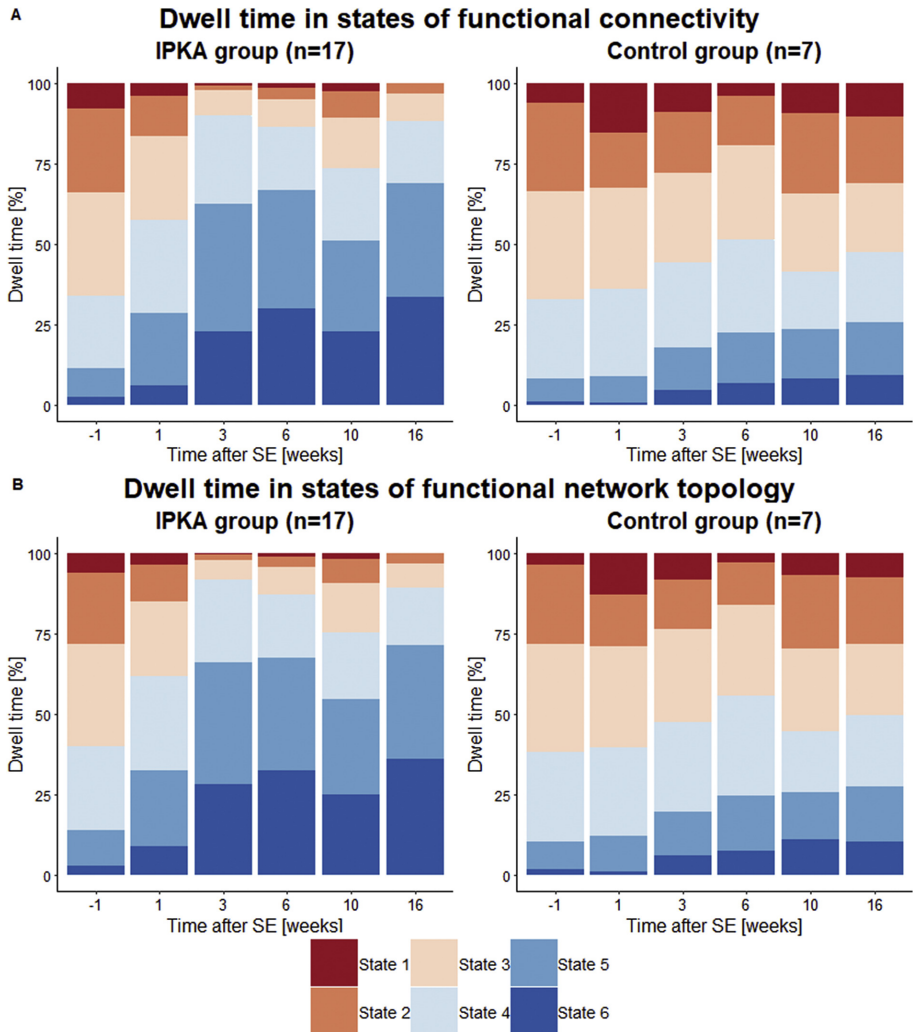


**Figure 7.7:** Percentage dwell time in states of A) functional connectivity and B) functional network topology, visualized as a function of time (weeks post-SE) for the IPKA group and the control group. Data are visualized as a stacked bar graph with mean values. Each segment of a bar represents the percentage dwell time in a state averaged over the animals in the group at one time point. The 6 segments always add up to 100%.

**Table 7.2:** Results of statistical analysis of percentage dwell time in states of functional connectivity and network topology, p-values are FDR-corrected for multiple comparisons.

Dwell time	Effect of group		Effect of time		Effect of time	
			IPKA group	control group		
States of functional connectivity						
State 1	U = 1.29 10 <sup>3</sup>	p < 0.001	$\chi^2 = 28.5$	p < 0.001	$\chi^2 = 3.39$	p = 0.768
State 2	U = 1.20 10 <sup>3</sup>	p < 0.001	$\chi^2 = 36.1$	p < 0.001	$\chi^2 = 3.96$	p = 1.00
State 3	F <sub>1,26.0</sub> = 14.6	p = 0.001	F <sub>5,125</sub> = 17.7	p < 0.001	F <sub>5,123</sub> = 1.22	p = 1.00
State 4	U = 2.14 10 <sup>3</sup>	p = 0.724	$\chi^2 = 11.1$	p = 0.050	$\chi^2 = 5.78$	p = 0.987
State 5	F <sub>1,26.0</sub> = 16.9	p = 0.001	F <sub>5,124</sub> = 16.9	p < 0.001	F <sub>5,123</sub> = 0.780	p = 0.849
State 6	U = 3.23 10 <sup>3</sup>	p < 0.001	$\chi^2 = 37.5$	p < 0.001	$\chi^2 = 2.57$	p = 0.766
States of functional network topology						
State 1	U = 1.45 10 <sup>3</sup>	p < 0.001	$\chi^2 = 30.5$	p < 0.001	$\chi^2 = 3.66$	p = 1.00
State 2	U = 1.16 10 <sup>3</sup>	p < 0.001	$\chi^2 = 35.2$	p < 0.001	$\chi^2 = 2.88$	p = 1.00
State 3	F <sub>1,24.8</sub> = 16.4	p = 0.001	F <sub>5,122</sub> = 15.6	p < 0.001	F <sub>5,121</sub> = 0.940	p = 1.00
State 4	F <sub>1,25.0</sub> = 0.692	p = 0.413	F <sub>5,122</sub> = 2.70	p = 0.024	F <sub>5,122</sub> = 1.16	p = 1.00
State 5	F <sub>1,24.4</sub> = 17.0	p = 0.001	F <sub>5,122</sub> = 12.6	p < 0.001	F <sub>5,121</sub> = 0.537	p = 0.898
State 6	U = 1.14 10 <sup>3</sup>	p < 0.001	$\chi^2 = 35.6$	p < 0.001	$\chi^2 = 2.19$	p = 0.822

### 7.3.3 Number of transitions between states of functional connectivity and network topology

The number of transitions between states of functional connectivity and states of functional network topology are visualized in Figure 7.8A and 7.8B, respectively. Each stacked bar represents the total number of transitions at one time point averaged over all animals within one group (IPKA group or control group). Each segment of a bar represents the number of transitions between two specific states. Only transitions between consecutive states are represented, since transitions between non-consecutive states were rare.

The total number of transitions between states of functional connectivity was significantly lower in the IPKA group compared to the control group and decreased significantly during epileptogenesis in the IPKA group. More specifically, the number of transitions between states 1 and 2, 2 and 3, and 3 and 4 was significantly lower in the IPKA compared to the control group and decreased significantly during epileptogenesis in the IPKA group. The number of transitions between states 5 and 6 was significantly higher in the IPKA group and the number of transitions between states 4 and 5, and 5 and 6 increased significantly during epileptogenesis in the IPKA group.

Similar results were obtained for the number of transitions between states of functional network topology. The total number of transitions was significantly lower in the IPKA group compared to the control group, but there was no significant effect of time in either group. In the IPKA group, the number of transitions between states 1 and 2, 2 and 3, and 3 and 4 was significantly lower, and between states 5 and 6 significantly higher compared to the control group. There was a significant decrease in the number of transitions between states 1 and 2, 2 and 3, and 3 and 4 during epileptogenesis in the IPKA group, while the number of transitions between states 5 and 6 increased significantly. The results of the statistical analysis are summarized in Table 7.3.

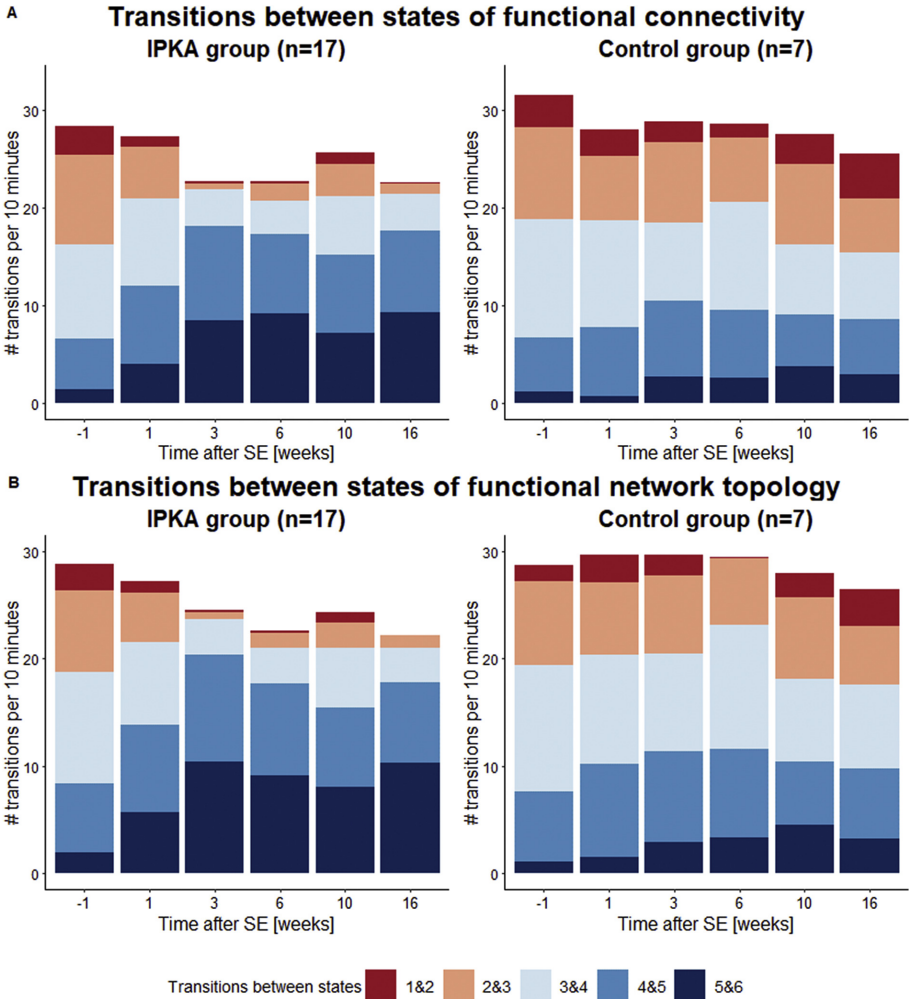


**Figure 7.8:** Number of transitions between states of A) functional connectivity and B) functional network topology, visualized as a function of time (weeks post-SE) for the IPKA group and the control group. Data are visualized as a stacked bar graph with mean values. Each segment of a bar represents the number of transitions between 2 specific states averaged over the animals in the group at one time point.

**Table 7.3:** Results of statistical analysis of number of transitions between states of functional connectivity and functional network topology, p-values are FDR-corrected for multiple comparisons.

Number of transitions	Effect of group		Effect of time		Effect of time	
			IPKA group	control group		
States of functional connectivity						
Total	U = 1.64 10 <sup>3</sup>	p = 0.016	$\chi^2 = 17.2$	p = 0.005	$\chi^2 = 8.03$	p = 0.465
State 1&2	U = 1.29 10 <sup>3</sup>	p < 0.001	$\chi^2 = 30.2$	p < 0.001	$\chi^2 = 4.22$	p = 1.00
State 2&3	U = 1.23 10 <sup>3</sup>	p < 0.001	$\chi^2 = 38.3$	p < 0.001	$\chi^2 = 3.79$	p = 0.870
State 3&4	F <sub>1,25.3</sub> = 11.2	p = 0.005	F <sub>5,124</sub> = 9.08	p < 0.001	F <sub>5,123</sub> = 2.38	p = 0.252
State 4&5	F <sub>1,26.1</sub> = 1.56	p = 0.222	F <sub>5,125</sub> = 2.81	p = 0.019	F <sub>5,123</sub> = 0.529	p = 0.754
State 5&6	U = 3.27 10 <sup>3</sup>	p < 0.001	$\chi^2 = 32.5$	p < 0.001	$\chi^2 = 2.97$	p = 0.846
States of functional network topology						
Total	U = 1.54 10 <sup>3</sup>	p = 0.006	$\chi^2 = 9.32$	p = 0.116	$\chi^2 = 4.71$	p = 1.00
State 1&2	U = 1.46 10 <sup>3</sup>	p < 0.001	$\chi^2 = 31.8$	p < 0.001	$\chi^2 = 1.79$	p = 0.877
State 2&3	U = 1.12 10 <sup>3</sup>	p < 0.001	$\chi^2 = 31.9$	p < 0.001	$\chi^2 = 1.90$	p = 1.00
State 3&4	U = 1.26 10 <sup>3</sup>	p < 0.001	$\chi^2 = 34.7$	p < 0.001	$\chi^2 = 6.40$	p = 1.00
State 4&5	F <sub>1,25.0</sub> = 0.264	p = 0.612	F <sub>5,122</sub> = 1.53	p = 0.185	F <sub>5,122</sub> = 0.665	p = 1.00
State 5&6	U = 1.07 10 <sup>3</sup>	p < 0.001	$\chi^2 = 28.3$	p < 0.001	$\chi^2 = 3.08$	p = 1.00

#### 7.3.4 Correlation of mean global network metrics, percentage dwell time and number of transitions with seizure frequency

During 7 days of consecutive EEG monitoring at least 19 weeks post-SE, the animals had a mean average daily seizure frequency of 22 seizures per 24 h (range: 0–53). One animal did not display any seizures on EEG during the recording period but did display occasional tonic-clonic seizures outside the recording period (e.g., when entering the housing room) and interictal epileptiform activity, such as epileptic spikes and pathological high frequency oscillations that could be observed on the EEG signal. Therefore, it was considered epileptic.

Seizure frequency was positively correlated with dwell time in the 2 higher states of functional connectivity one week post-SE, dwell time in State 4 16 weeks post-SE, and the total number of transitions between states of functional connectivity 16 weeks post-SE. Seizure frequency was negatively correlated with dwell time in State 5 of functional connectivity one week post-SE, and State 6 of functional connectivity 16 weeks post-SE (Figure 7.9).

Seizure frequency was also positively correlated with dwell time in the 3 higher states of functional network topology (State 1, 2 and 3) one week post-SE, but negatively correlated with dwell time in State 5 of functional network topology. Sixteen weeks post-SE, dwell time in State 4 and 6 of functional network topology were positively and negatively correlated with seizure frequency, respectively. At this time point, seizure frequency was positively correlated with the total number of transitions between states as well (Figure 7.10).

In addition, there was a positive correlation between average seizure frequency and the standard deviation over 276 time windows of global degree and local efficiency 1 week post-SE.

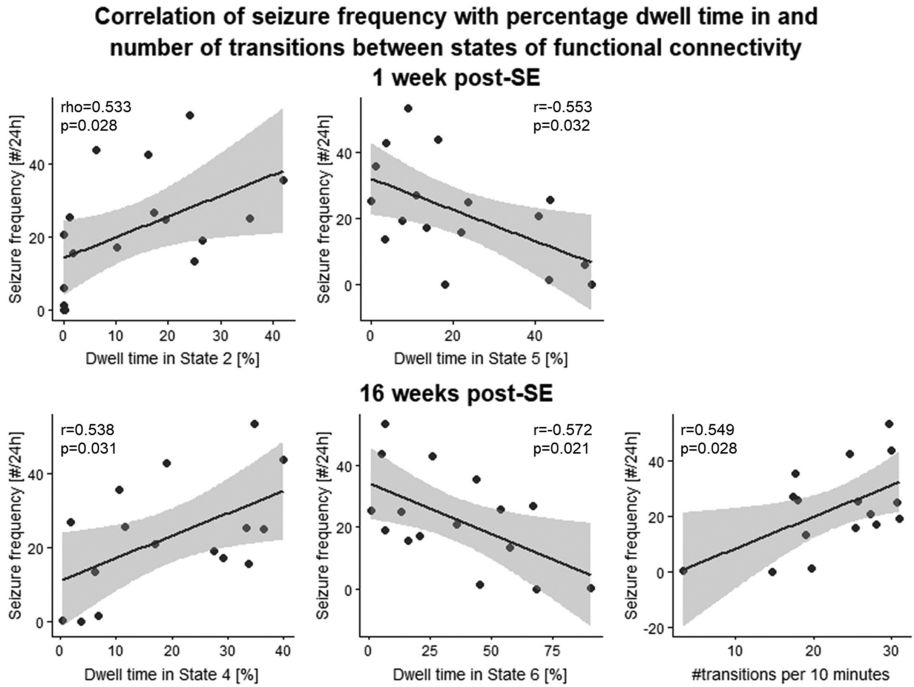


**Figure 7.9:** Correlation between average daily seizure frequency (number per 24 h) on the one hand and percentage dwell time in and total number of transitions per scan between states of functional connectivity 1 week and 16 weeks post-SE on the other hand.

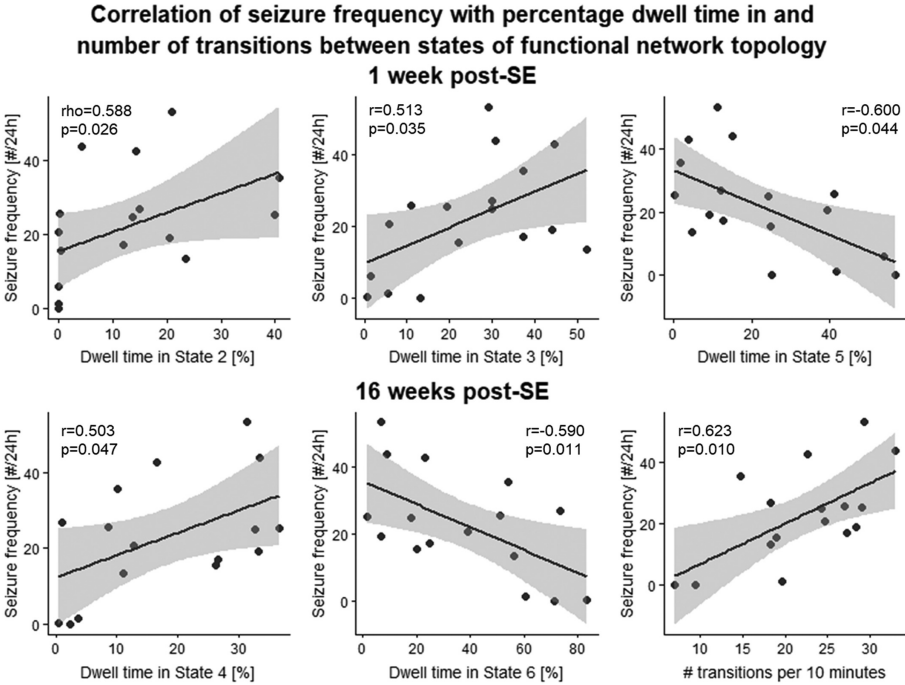


**Figure 7.10:** Correlation between average daily seizure frequency (number per 24 h) on the one hand and percentage dwell time in and total number of transitions per scan between states of functional network topology 1 week and 16 weeks post-SE on the other hand.

### 7.3.5 Influence of window length

Six states of functional connectivity were calculated using window lengths of 30 s (15 TRs) and 70 s (35 TRs). The mean value, standard deviation, and maximum and minimum of each state for each window length were similar for the different window lengths (Figure 7.12, Table 7.5). Similar changes in percentage dwell time and number of transitions were found for window lengths of 30 s and 70 s as for 50 s (Figure 7.13, Table 7.6). The different window lengths resulted in a similar correlation of percentage dwell time and number of transitions with average daily seizure frequency (Table 7.7).

**Table 7.4:** Results of two-sample Kolmogorov-Smirnov test to assess whether percentage dwell time and number of transitions differed significantly between the IPKA group 16 weeks post-SE and the validation group 20 weeks post-SE.

	State 1	State 2	State 3	State 4	State 5	State 6	Number of Transitions
<b>Z</b>	0.686	0.610	0.324	0.175	0.583	0.058	0.262
<b>p</b>	0.493	0.542	0.746	0.861	0.560	0.954	0.793

### 7.3.6 Validation of epileptic dynamic functional connectivity

A two-sample Kolmogorov-Smirnov test could not demonstrate a significant difference between the percentage dwell time in each state and number of transitions of the validation data set and those of the main data set (Table 7.4, Figure 7.11).

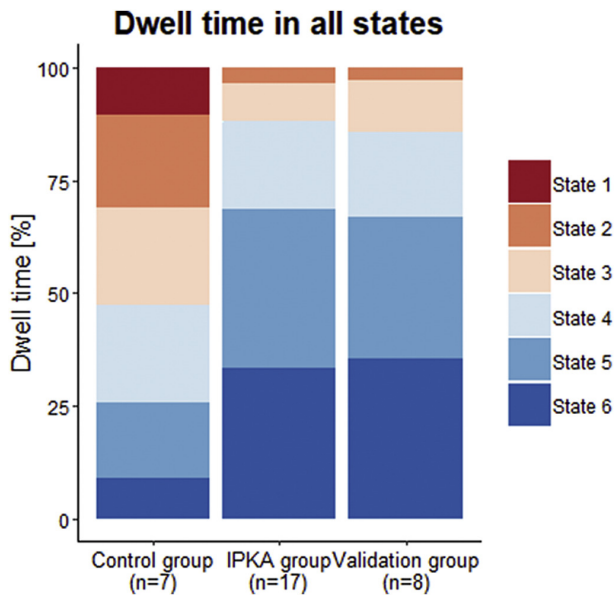


**Figure 7.11:** Percentage dwell time in each state for the control group and IPKA group 16 weeks post-SE and the validation group 20 weeks post-SE. Data are visualized as a stacked bar graph with mean values.

## 7.4 Discussion

### 7.4.1 Dwelling in states with a lower mean functional connectivity, segregation and integration

The aim of this study was to identify changes in dynamic functional connectivity and functional network topology during the development of epilepsy in the IPKA rat model of TLE, and to investigate whether these changes are associated with the occurrence of spontaneous seizures. In IPKA and control animals, 6 recurring states of functional connectivity could be distinguished. Percentage dwell time in the states with the highest mean functional connectivity was lower in the IPKA group compared to the control group, while dwell time was higher in the states with the lowest mean functional connectivity. In states with a higher mean functional connectivity, clustering coefficient and local efficiency were higher as well, indicating a high segregation or local interconnectivity. In these states, characteristic path length was lower and local efficiency higher, indicating a high integration or overall communication efficiency. Similarly, segregation and integration were lower in states with a lower mean functional connectivity. The decomposition of time-varying global graph theoretical network metrics into states of functional network topology led to similar results. Dwell time was lower in states with a higher functional connectivity, segregation and integration in the IPKA animals.

Significant changes in percentage dwell time could already be found 1 week post-SE, but the largest changes occurred between 1 and 3 weeks post-SE, after which dwell time remained constant. This timeline corresponds with the timing of structural changes during epileptogenesis in the IPKA rat model for TLE. During the first 4 weeks post-SE, neuronal degeneration can be found in hippocampus, amygdala, thalamus, piriform cortex, and cortex and there is an increase in astrogliosis. Microgliosis already reaches a maximum 1 week post-SE, after which it remains high [29, 30].

Our results indicate that the epileptic rat brain is characterized by states with a lower overall functional connectivity, segregation, and integration,

which is in line with studies investigating static functional connectivity in rat models of TLE. Christiaen et al. [31] found a decreased functional connectivity, segregation and integration in the IPKA rat model for TLE, mainly in regions of the default-mode network (DMN). In the same model, Pirttimäki et al. [32] reported small changes in functional connectivity in several brain regions 1 week post-SE, and decreased functional connectivity, predominantly between the somatosensory cortex and thalamus and between the perirhinal and piriform cortices, 1 or 2 months after SE. Bertoglio et al. [33] demonstrated a highly affected functional connectivity in multiple regions of the DMN, and a wide-spread network connectivity hyposynchrony 2 weeks post-SE. On the other hand, Gill et al. [34] found that functional connectivity was increased within the temporal regions and the limbic network, and between the anterior and posterior DMN 4 to 5 weeks post-SE. Jiang et al. [35] demonstrated that connectivity of the hippocampal functional network was decreased in several regions, including hippocampus, amygdala, thalamus, motor cortex, and somatosensory cortex, and increased in the visual cortex, mesencephalon, and insula in the pilocarpine rat model of TLE.

Overall, most of these studies found a decreased static functional connectivity in rat models of TLE. This is in agreement with our current findings regarding global changes in dynamic functional connectivity and network topology during epileptogenesis. In addition, it is in line with our finding that coreness, a measure for the relative importance of a node in the network, varies most between functional connectivity states in visual cortex, thalamus, and hippocampus, 3 regions of the rat DMN [36, 37]. Hippocampus and thalamus are also regions that are highly affected by neuronal degeneration in the IPKA rat model [29, 30].

#### **7.4.2 Changes in variability of functional connectivity, segregation and integration**

Furthermore, our study indicates that the total number of transitions between states of functional connectivity and network topology is lower in the IPKA group compared to the control group, i.e., the flexibility is lower. Variability in functional connectivity and integration, assessed

using the standard deviation over scanning time of network metrics, was lower in the IPKA animals compared to the control group, while variability in segregation was higher. This is in line with the findings of Douw et al. [38], who found a lower flexibility in functional connectivity of the posterior cingulate cortex in patients with TLE, which was correlated with disturbed memory functioning.

Since the functional connectivity states mostly differ in mean value rather than specific connections or ROIs, and transitions predominantly occur between neighbouring states, it is possible that there is a continuum between states and our classification is somewhat artificial. However, even if this would be the underlying truth, our main conclusions still stand, namely that functional connectivity, integration, and segregation are more often low and vary less in IPKA animals compared to control animals and that animals that dwell in states of high functional connectivity, have more chronic seizures.

### 7.4.3 Correlation with seizure frequency

Interestingly, average daily seizure frequency was positively correlated with percentage dwell time in states with a high mean functional connectivity and high segregation and integration, and negatively with dwell time in states with a low mean functional connectivity and low segregation and integration, 1 and 16 weeks post-SE. In other words, our findings indicate that animals that dwell in states with high functional connectivity, segregation, and integration have more chronic seizures. This is in line with the findings of Bertoglio et al. [33], who reported a positive correlation between functional brain connectivity and seizure frequency in the IPKA model for TLE. On the other hand, residing in states of low functional connectivity, associated with lower seizure frequencies, may reflect the protective effect and effectiveness of the treatment of epilepsy by means of resective/disconnective surgery [39]. Since functional connectivity is more restricted to the states with the lowest functional connectivity, integration, and segregation in animals that have fewer seizures, it is conceivable that temporary increases in functional connectivity might be necessary for seizures to be generated.

We also found a positive correlation between number of seizures on the one hand and the number of transitions 16 weeks post-SE and standard deviation over scanning time of global degree and local efficiency 1 week post-SE on the other hand, indicating that number of seizures is higher in animals with more variable functional connectivity.

#### 7.4.4 Dynamic functional connectivity in patients with TLE

In the last five years, several studies investigated dFC in patients with TLE. Laufs et al. [17] found that the BOLD signal variance was increased in the temporal pole, including the hippocampus, and reported greater variance in dFC between this brain region and the precuneus, sensory motor structures, and frontal cortices, using seed-based correlation and a sliding window analysis. Morgan et al. [20] calculated the standard deviation across 20 functional connectivity values of a network, obtained using a sliding window approach, and covariance of the functional connectivity time series between two networks. They found a nonsignificant decrease in functional connectivity in the cingulate midline network in TLE patients, and an increase in functional connectivity variability that was correlated with disease duration. Using a Bayesian hidden Markov model approach, Chiang et al. [19] found that small-world index was more stationary than characteristic path length in TLE patients, but less than clustering coefficient, suggesting that the balance between integration and segregation might be affected in these patients. Two years later, Chiang et al. [18] found decreased functional connectivity and several abnormal spectral features of functional connectivity between the DMN and the memory network in TLE patients, which indicated that functional connectivity fluctuated at lower frequencies and with less variability, using a Generalized Autoregressive Conditional Heteroskedasticity model and time-frequency analysis. They reported that this may lead to a lower flexibility for cognitive processing, which could be related to the memory impairment that is often seen in TLE patients [18]. Overall, these studies found that functional connectivity variability was both increased, which was correlated with disease duration, and decreased,

which was related to impaired cognitive processing. This is in line with our results, which show that variability in functional connectivity is lower in IPKA animals, but a higher variability is related to a higher seizure frequency.

#### **7.4.5 Validation data set**

We believe that this is the first study investigating dynamic functional connectivity in a rat model of epilepsy. To validate our findings, we repeated the analysis for a different data set consisting of rsfMRI scans of 8 IPKA animals acquired 20 weeks post-SE. Percentage dwell time in each state and the number of transitions in the validation data set were very similar to the ones in the IPKA group of the main data set 16 weeks post-SE, and statistically indistinguishable.

#### **7.4.6 Limitations**

To make sure that the fluctuations in functional connectivity are related to brain functions and are not artifacts, it is important to choose appropriate parameters, such as window length, and to use the right statistical tests [5]. We chose a window length based on the recommendations in literature and repeated our analysis using a longer and shorter window length, which led to similar results. Our dFC findings are also in line with previous findings using static functional connectivity analysis. Therefore, we believe that the fluctuations in functional connectivity we found, are related to underlying brain activity.

While we found clear differences in dynamic functional connectivity and network topology between IPKA animals and control animals, it is not easy to link them directly to specific mechanisms of epileptogenesis. It is clear that the timeline of our findings corresponds well with known structural changes in the IPKA model, such as neuronal degeneration and gliosis, which suggests that these are most likely related. Other imaging techniques, such as diffusion MR imaging, might help to elucidate the relationship between changes in (dynamic) functional connectivity and mechanisms of epileptogenesis.

### **7.4.7 Future work**

We found a lower flexibility in functional connectivity, which might be related to cognitive problems and memory impairment [5]. In future studies we aim to confirm this with behavioural testing. In addition, we would like to investigate changes in structural connectivity underlying alterations in (dynamic) functional connectivity. We believe this will improve the understanding of how altered functional connectivity is related to structural lesions during epileptogenesis. Therefore, we plan to do a longitudinal rsfMRI and diffusion MRI study, combined with behavioural testing.

## **7.5 Conclusion**

We investigated changes in dynamic functional connectivity and network topology during epileptogenesis in the IPKA rat model of TLE using longitudinal resting state fMRI. First, we found that functional connectivity states with a lower mean functional connectivity and network topologies with a lower segregation and integration, occur more often in IPKA animals compared to control animals. In addition, functional connectivity becomes less variable during epileptogenesis. Secondly, we found a positive correlation of the average daily seizure frequency with percentage dwell time in states with a high mean functional connectivity, high segregation, and high integration, and a higher number of transitions, and a negative correlation with percentage dwell time in states with a low mean functional connectivity and low segregation and integration. This indicates that animals that dwell in states of higher functional connectivity, segregation, and integration, and have a higher functional connectivity variability, have more chronic seizures.

## Appendix: Influence of window length

Table 7.5: Characterization of each state for each window length.

Window length	State 1	State 2	State 3	State 4	State 5	State 6
Mean	30 s 1.75	1.35	1.06	0.810	0.566	0.304
	50 s 1.65	1.28	1.03	0.798	0.580	0.350
	70 s 1.63	1.25	1.01	0.782	0.574	0.354
Standard deviation	30 s 0.244	0.242	0.231	0.212	0.185	0.139
	50 s 0.241	0.238	0.224	0.206	0.178	0.144
	70 s 0.241	0.235	0.222	0.204	0.174	0.144
Maximum	30 s 2.64	2.18	1.86	1.57	1.43	1.35
	50 s 2.53	2.11	1.81	1.55	1.42	1.35
	70 s 2.50	2.09	1.78	1.53	1.42	1.35
Minimum	30 s 1.22	0.859	0.623	0.419	0.233	0.056
	50 s 1.13	0.800	0.612	0.425	0.264	0.081
	70 s 1.12	0.782	0.594	0.416	0.263	0.086

**Table 7.6:** Results of statistical analysis of percentage dwell time (%DT) and number of transitions using LMEM, p-values are FDR-corrected for multiple comparisons.

	Window length	Effect of group		Effect of time		Effect of time		
				IPKA group		control group		
%DT in State 1	30 s	U=1.24	103	p<0.001	$\chi^2=27.4$	p<0.001	$\chi^2=3.02$	p=0.836
	50 s	U=1.29	$10^3$	p<0.001	$\chi^2=28.5$	p<0.001	$\chi^2=3.39$	p=0.768
	70 s	U=1.54	$10^3$	p<0.001	$\chi^2=31.1$	p<0.001	$\chi^2=3.89$	p=0.679
%DT in State 2	30 s	U=1.24	$10^3$	p<0.001	$\chi^2=33.9$	p<0.001	$\chi^2=2.09$	p=0.837
	50 s	U=1.20	$10^3$	p<0.001	$\chi^2=36.1$	p<0.001	$\chi^2=3.96$	p=1.00
	70 s	U=1.27	$10^3$	p<0.001	$\chi^2=38.2$	p<0.001	$\chi^2=3.21$	p=0.668
%DT in State 3	30 s	F <sub>1,26.3</sub>	14.1	p=0.001	F <sub>5,125</sub> =17.2	p<0.001	F <sub>5,123</sub> =0.988	p=1.00
	50 s	F <sub>1,26.0</sub>	14.6	p=0.001	F <sub>5,125</sub> =17.7	p<0.001	F <sub>5,123</sub> =1.22	p=1.00
	70 s	F <sub>1,25.8</sub>	16.2	p<0.001	F <sub>5,125</sub> =16.0	p<0.001	F <sub>5,123</sub> =1.44	p=1.00
%DT in State 4	30 s	F <sub>1,25.7</sub>	0.200	p=0.658	F <sub>5,124</sub> =1.71	p=0.137	F <sub>5,122</sub> =0.973	p=1.00
	50 s	U=8.24	103	p=0.724	$\chi^2=11.1$	p=0.050	$\chi^2=5.78$	p=0.987
	70 s	U=2.06	103	p=0.479	$\chi^2=10.0$	p=0.074	$\chi^2=6.11$	p=0.880
%DT in State 5	30 s	F <sub>1,26.4</sub>	17.2	p<0.001	F <sub>5,124</sub> =23.6	p<0.001	F <sub>5,123</sub> =0.660	p=0.983
	50 s	F <sub>1,26.0</sub>	16.9	p=0.001	F <sub>5,124</sub> =16.9	p<0.001	F <sub>5,123</sub> =0.780	p=0.849
	70 s	F <sub>1,25.9</sub>	17.5	p<0.001	F <sub>5,125</sub> =14.9	p<0.001	F <sub>5,123</sub> =0.992	p=0.850
%DT in State 6	30 s	U=3.23	$10^3$	p<0.001	$\chi^2=35.7$	p<0.001	$\chi^2=3.60$	p=1.00
	50 s	U=8.90	$10^3$	p<0.001	$\chi^2=37.5$	p<0.001	$\chi^2=2.57$	p=0.766
	70 s	U=3.35	$10^3$	p<0.001	$\chi^2=35.7$	p<0.001	$\chi^2=4.61$	p=0.698
Number of transitions	30 s	U=2.22	$10^3$	p=0.969	$\chi^2=6.59$	p=0.253	$\chi^2=2.35$	p=0.799
	50 s	U=1.64	$10^3$	p=0.013	$\chi^2=17.2$	p=0.004	$\chi^2=8.03$	p=0.155
	70 s	U=2.97	$10^3$	p=0.002	$\chi^2=12.2$	p=0.032	$\chi^2=5.96$	p=0.310

**Table 7.7:** Results of statistical analysis of correlation between percentage dwell time (%DT) and number of transitions per scan 1 week and 16 weeks post-SE, and average daily seizure frequency (number per 24 h). P-values are FDR-corrected for multiple comparisons.

		<b>Correlation with seizure frequency</b>		
		<b>30 s</b>	<b>50 s</b>	<b>70 s</b>
1 week post-SE	<b>Pearson's r</b>	0.513		
	<b>Spearman's <math>\rho</math></b>		0.533	0.532
	<b>p</b>	0.047	0.028	0.028
	<b>Pearson's r</b>	-0.585	-0.553	
	<b>p</b>	0.028	0.032	
	<b>Spearman's <math>\rho</math></b>	-0.491		
	<b>p</b>	0.045		
16 weeks post-SE	<b>Pearson's r</b>	0.528	0.538	0.540
	<b>p</b>	0.035	0.031	0.031
	<b>Pearson's r</b>	-0.591	-0.572	-0.571
	<b>p</b>	0.016	0.021	0.021
	<b>Pearson's r</b>		0.549	
	<b>p</b>		0.028	

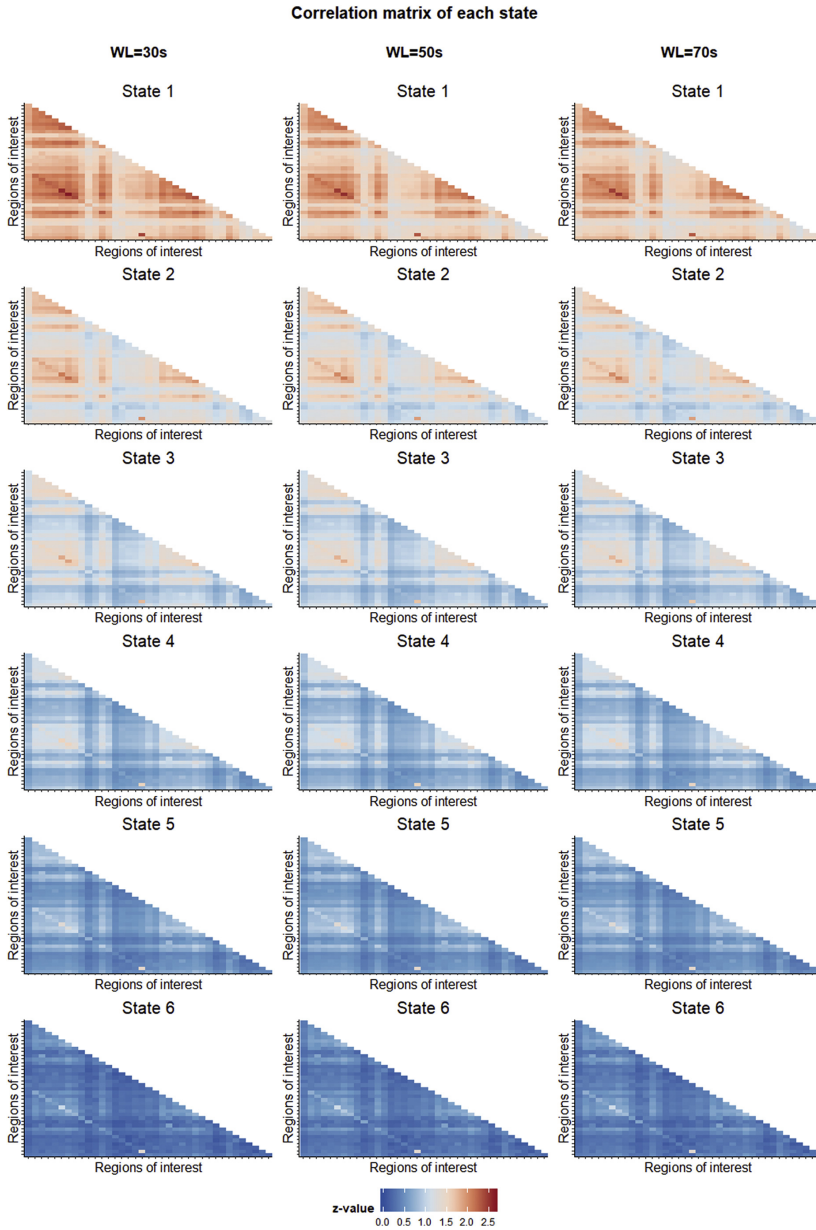


**Figure 7.12:** Correlation matrices (z-score) of 6 recurring states of functional connectivity, sorted from highest (State 1) to lowest (State 6) mean value for each window length.

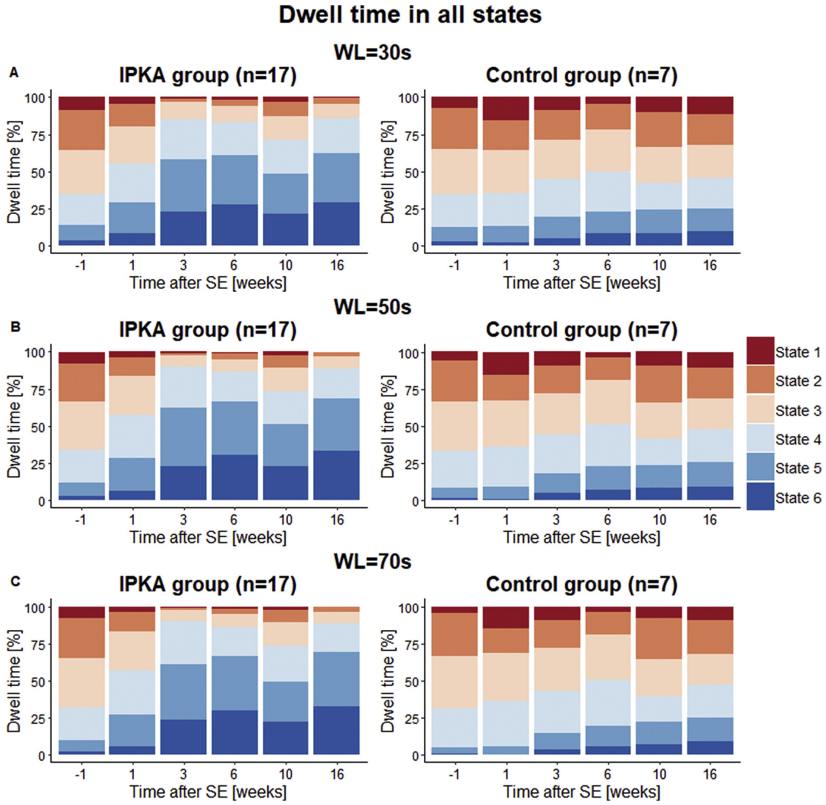


**Figure 7.13:** Percentage dwell time in each state for different window lengths. Data are visualized as a stacked bar graph with mean values.

## Bibliography

- [1] P. M. Matthews and P. Jezzard, “Functional magnetic resonance imaging,” *Journal of Neurology, Neurosurgery & Psychiatry*, vol. 75, no. 1, pp. 6–12, 2004.
- [2] J. Wang, X. Zuo, and Y. He, “Graph-based network analysis of resting-state functional mri,” *Frontiers in systems neuroscience*, vol. 4, p. 16, 2010.
- [3] K. Smitha, K. Akhil Raja, K. Arun, P. Rajesh, B. Thomas, T. Kapilamoorthy, and C. Kesavadas, “Resting state fmri: A review on methods in resting state connectivity analysis and resting state networks,” *The neuroradiology journal*, vol. 30, no. 4, pp. 305–317, 2017.
- [4] M. D. Fox and M. Greicius, “Clinical applications of resting state functional connectivity,” *Frontiers in systems neuroscience*, vol. 4, p. 19, 2010.
- [5] M. G. Preti, T. A. Bolton, and D. Van De Ville, “The dynamic functional connectome: State-of-the-art and perspectives,” *Neuroimage*, vol. 160, pp. 41–54, 2017.
- [6] C. Chang and G. H. Glover, “Time–frequency dynamics of resting-state brain connectivity measured with fmri,” *Neuroimage*, vol. 50, no. 1, pp. 81–98, 2010.
- [7] J. Grandjean, M. G. Preti, T. A. Bolton, M. Buerge, E. Seifritz, C. R. Pryce, D. Van De Ville, and M. Rudin, “Dynamic reorganization of intrinsic functional networks in the mouse brain,” *Neuroimage*, vol. 152, pp. 497–508, 2017.
- [8] R. M. Hutchison, T. Womelsdorf, E. A. Allen, P. A. Bandettini, V. D. Calhoun, M. Corbetta, S. Della Penna, J. H. Duyn, G. H. Glover, J. Gonzalez-Castillo *et al.*, “Dynamic functional connectivity: promise, issues, and interpretations,” *Neuroimage*, vol. 80, pp. 360–378, 2013.

- [9] B. Klugah-Brown, C. Luo, H. He, S. Jiang, G. K. Armah, Y. Wu, J. Li, W. Yin, and D. Yao, “Altered dynamic functional network connectivity in frontal lobe epilepsy,” *Brain topography*, vol. 32, no. 3, pp. 394–404, 2019.
- [10] R. Li, W. Liao, Y. Yu, H. Chen, X. Guo, Y.-L. Tang, and H. Chen, “Differential patterns of dynamic functional connectivity variability of striato–cortical circuitry in children with benign epilepsy with centrotemporal spikes,” *Human brain mapping*, vol. 39, no. 3, pp. 1207–1217, 2018.
- [11] R. Li, L. Wang, H. Chen, X. Guo, W. Liao, Y.-L. Tang, and H. Chen, “Abnormal dynamics of functional connectivity density in children with benign epilepsy with centrotemporal spikes,” *Brain imaging and behavior*, vol. 13, no. 4, pp. 985–994, 2019.
- [12] F. Liu, Y. Wang, M. Li, W. Wang, R. Li, Z. Zhang, G. Lu, and H. Chen, “Dynamic functional network connectivity in idiopathic generalized epilepsy with generalized tonic–clonic seizure,” *Human brain mapping*, vol. 38, no. 2, pp. 957–973, 2017.
- [13] M. Pedersen, A. Omidvarnia, E. K. Curwood, J. M. Walz, G. Rayner, and G. D. Jackson, “The dynamics of functional connectivity in neocortical focal epilepsy,” *NeuroImage: Clinical*, vol. 15, pp. 209–214, 2017.
- [14] Y. Wang, I. S. Berglund, M. Uppman, and T.-Q. Li, “Juvenile myoclonic epilepsy has hyper dynamic functional connectivity in the dorsolateral frontal cortex,” *NeuroImage: Clinical*, vol. 21, p. 101604, 2019.
- [15] R. S. Fisher, W. V. E. Boas, W. Blume, C. Elger, P. Genton, P. Lee, and J. Engel Jr, “Epileptic seizures and epilepsy: definitions proposed by the international league against epilepsy (ILAE) and the international bureau for epilepsy (IBE),” *Epilepsia*, vol. 46, no. 4, pp. 470–472, 2005.
- [16] J. Engel Jr, “Approaches to refractory epilepsy,” *Annals of Indian Academy of Neurology*, vol. 17, no. Suppl 1, p. S12, 2014.

- [17] H. Laufs, R. Rodionov, R. Thornton, J. S. Duncan, L. Lemieux, and E. Tagliazucchi, “Altered fmri connectivity dynamics in temporal lobe epilepsy might explain seizure semiology,” *Frontiers in neurology*, vol. 5, p. 175, 2014.
- [18] S. Chiang, E. R. Vankov, H. J. Yeh, M. Guindani, M. Vannucci, Z. Haneef, and J. M. Stern, “Temporal and spectral characteristics of dynamic functional connectivity between resting-state networks reveal information beyond static connectivity,” *PloS one*, vol. 13, no. 1, p. e0190220, 2018.
- [19] S. Chiang, A. Cassese, M. Guindani, M. Vannucci, H. J. Yeh, Z. Haneef, and J. M. Stern, “Time-dependence of graph theory metrics in functional connectivity analysis,” *NeuroImage*, vol. 125, pp. 601–615, 2016.
- [20] V. L. Morgan, B. Abou-Khalil, and B. P. Rogers, “Evolution of functional connectivity of brain networks and their dynamic interaction in temporal lobe epilepsy,” *Brain connectivity*, vol. 5, no. 1, pp. 35–44, 2015.
- [21] E. M. Goldberg and D. A. Coulter, “Mechanisms of epileptogenesis: a convergence on neural circuit dysfunction,” *Nature Reviews Neuroscience*, vol. 14, no. 5, pp. 337–349, 2013.
- [22] J. L. Hellier, P. R. Patrylo, P. S. Buckmaster, and F. E. Dudek, “Recurrent spontaneous motor seizures after repeated low-dose systemic treatment with kainate: assessment of a rat model of temporal lobe epilepsy,” *Epilepsy research*, vol. 31, no. 1, pp. 73–84, 1998.
- [23] R. Weber, P. Ramos-Cabrera, D. Wiedermann, N. Van Camp, and M. Hoehn, “A fully noninvasive and robust experimental protocol for longitudinal fmri studies in the rat,” *Neuroimage*, vol. 29, no. 4, pp. 1303–1310, 2006.
- [24] G. Paxinos and C. Watson, *The Rat Brain in Stereotaxic Coordinates*, 7th ed. Elsevier Science, 2013.

- [25] J. Wang, X. Wang, M. Xia, X. Liao, A. Evans, and Y. He, “Gretna: a graph theoretical network analysis toolbox for imaging connectomics,” *Frontiers in human neuroscience*, vol. 9, p. 386, 2015.
- [26] M. Rubinov and O. Sporns, “Complex network measures of brain connectivity: uses and interpretations,” *Neuroimage*, vol. 52, no. 3, pp. 1059–1069, 2010.
- [27] D. J. Ketchen and C. L. Shook, “The application of cluster analysis in strategic management research: an analysis and critique,” *Strategic management journal*, vol. 17, no. 6, pp. 441–458, 1996.
- [28] F. Battiston, J. Guillon, M. Chavez, V. Latora, and F. de Vico Falani, “Multiplex core–periphery organization of the human connectome,” *Journal of the Royal Society Interface*, vol. 15, no. 146, p. 20180514, 2018.
- [29] D. Bertoglio, H. Amhaoul, A. Van Eetveldt, R. Houbrechts, S. Van De Vijver, I. Ali, and S. Dedeurwaerdere, “Kainic acid-induced post-status epilepticus models of temporal lobe epilepsy with diverging seizure phenotype and neuropathology,” *Frontiers in neurology*, vol. 8, p. 588, 2017.
- [30] A. K. Sharma, W. H. Jordan, R. Y. Reams, D. G. Hall, and P. W. Snyder, “Temporal profile of clinical signs and histopathologic changes in an f-344 rat model of kainic acid-induced mesial temporal lobe epilepsy,” *Toxicologic pathology*, vol. 36, no. 7, pp. 932–943, 2008.
- [31] E. Christiaen, M.-G. Goossens, R. Raedt, B. Descamps, L. E. Larsen, E. Craey, E. Carrette, K. Vonck, P. Boon, and C. Vanhove, “Alterations in the functional brain network in a rat model of epileptogenesis: A longitudinal resting state fmri study,” *Neuroimage*, vol. 202, p. 116144, 2019.
- [32] T. Pirttimäki, R. A. Salo, A. Shatillo, M. I. Kettunen, J. Paasonen, A. Sierra, K. Jokivarsi, V. Leinonen, P. Andrade, S. Quittek *et al.*, “Implantable rf-coil with multiple electrodes for long-term eeg-fmri

- monitoring in rodents,” *Journal of neuroscience methods*, vol. 274, pp. 154–163, 2016.
- [33] D. Bertoglio, E. Jonckers, I. Ali, M. Verhoye, A. Van der Linden, and S. Dedeurwaerdere, “In vivo measurement of brain network connectivity reflects progression and intrinsic disease severity in a model of temporal lobe epilepsy,” *Neurobiology of disease*, vol. 127, pp. 45–52, 2019.
- [34] R. S. Gill, S. M. Mirsattari, and L. S. Leung, “Resting state functional network disruptions in a kainic acid model of temporal lobe epilepsy,” *NeuroImage: Clinical*, vol. 13, pp. 70–81, 2017.
- [35] Y. Jiang, C.-L. Han, H.-G. Liu, X. Wang, X. Zhang, F.-G. Meng, and J.-G. Zhang, “Abnormal hippocampal functional network and related memory impairment in pilocarpine-treated rats,” *Epilepsia*, vol. 59, no. 9, pp. 1785–1795, 2018.
- [36] L. Becerra, G. Pendse, P.-C. Chang, J. Bishop, and D. Borsook, “Robust reproducible resting state networks in the awake rodent brain,” *PloS one*, vol. 6, no. 10, p. e25701, 2011.
- [37] H. Lu, Q. Zou, H. Gu, M. E. Raichle, E. A. Stein, and Y. Yang, “Rat brains also have a default mode network,” *Proceedings of the National Academy of Sciences*, vol. 109, no. 10, pp. 3979–3984, 2012.
- [38] L. Douw, C. L. Leveroni, N. Tanaka, B. C. Emerton, A. C. Cole, C. Reinsberger, and S. M. Stuffelbeem, “Loss of resting-state posterior cingulate flexibility is associated with memory disturbance in left temporal lobe epilepsy,” *PLoS One*, vol. 10, no. 6, p. e0131209, 2015.
- [39] D. J. Englot, H. Birk, and E. F. Chang, “Seizure outcomes in nonresective epilepsy surgery: an update,” *Neurosurgical review*, vol. 40, no. 2, pp. 181–194, 2017.

## 8 | General discussion and conclusions

The main aim of this dissertation was to gain more insight into the mechanisms of epileptogenesis, with the ultimate goal of finding a biomarker to predict which patients will develop epilepsy after an initial precipitating injury. To this end, alterations in structural and functional brain networks during epileptogenesis were investigated in a rat model of temporal lobe epilepsy (TLE) using advanced magnetic resonance imaging (MRI).

### 8.1 Structural brain network changes during epileptogenesis

Diffusion-weighted MRI (dMRI) studies in patients with TLE have reported widespread changes in white matter integrity. In Chapter 5, these changes were investigated using more advanced analysis methods in a longitudinal multi-shell dMRI study in a rat model of TLE. In addition, the effect of these changes on structural network topology was assessed. The most commonly used model to analyze dMRI is diffusion tensor imaging (DTI). However, DTI metrics are not specific to microstructure or pathology, and the DTI model does not take into account crossing fibers, which may lead to erroneous results. To overcome these limitations, a more advanced model based on multi-shell multi-tissue constrained spherical deconvolution was used to perform tractography and tractometry with more precise fiber orientation estimates, and to assess changes in intra-axonal volume using fixel-based analysis. Diffusion-weighted MR images were acquired before and at several time points (1, 3, 11 and 16 weeks) after induction of status epilepticus in the intraperi-

toneal kainic acid (IPKA) rat model of TLE and age-matched controls. Tractography was performed and fixel metrics were calculated in several white matter tracts. The tractogram was analyzed using graph theory. In graph theory, the brain is represented as a network consisting of nodes, usually brain regions, and edges that show the relationship between the nodes. Several graph theoretical measures can be calculated to describe and quantify the network.

The objectives of this study were twofold: 1) to investigate how the structural brain network changes during epileptogenesis in the IPKA rat model, and which brain areas are most affected, and 2) to evaluate whether the changes in network topology were related to changes in the integrity of white matter tracts assessed using fixel-based analysis.

### **8.1.1 Decreased structural network connectivity and efficiency during epileptogenesis**

We found that global degree and local efficiency, measures of structural connectivity and segregation or local interconnectivity, respectively, significantly decreased in the IPKA group during epileptogenesis. In addition, global efficiency decreased and characteristic path length increased, which pointed to a decrease in integration or overall communication efficiency. Nodal degree decreased significantly during early epileptogenesis in hippocampus, subiculum, thalamus, septum, dorsolateral orbitofrontal cortex, globus pallidus, and nucleus accumbens. In cingulate cortex, caudate putamen, and somatosensory cortex, nodal degree decreased during early epileptogenesis and remained decreased during late epileptogenesis. Many of these are regions of the limbic system and/or part of the rat default-mode network (DMN). This indicates that primarily regions of the limbic system and the DMN are affected during epileptogenesis. Our findings are in line with studies investigating structural connectivity in patients with TLE where structural connectivity, global efficiency or integration, and local efficiency or segregation, are decreased in TLE patients, and mainly regions of the DMN and the limbic network are affected [1–5].

### 8.1.2 Structural network changes are related to decreased intra-axonal volume fraction in white matter

The analysis of white matter integrity using fixel-based analysis revealed that fiber density (FD) was decreased during early and late epileptogenesis in the IPKA group in several white matter tracts, including corpus callosum, internal capsule, and fimbria. Fiber-density-and-cross-section (FDC) was decreased during early epileptogenesis in anterior commissure, corpus callosum and fimbria, and in corpus callosum and cingulum during late epileptogenesis. These findings indicate that there is a decrease in intra-axonal volume fraction. This is in line with the neuropathological changes that are known to occur after status epilepticus in the IPKA model. Following the initial insult, it has been shown that neuronal loss occurs in hippocampus, entorhinal cortex, subiculum, and amygdala, but also in some extratemporal regions including thalamus, caudate putamen, and cerebral cortex, and especially piriform cortex. During this early phase, gliosis also takes place in hippocampus, piriform cortex, entorhinal cortex, olfactory bulb, substantia nigra, thalamus, and mesencephalon [6–8]. Both neuronal loss and gliosis will be reflected as a decrease in intra-axonal volume fraction. During late epileptogenesis, there is less (micro)gliosis compared to the early phase [6, 7]. The increase in FDC in fimbria, and to a lesser extent in corpus callosum, during late epileptogenesis may be related to reduced gliosis. On the other hand, it could also be associated with the occurrence of spontaneous seizures during this stage. During the periictal period, cerebral edema and cell swelling can cause a temporary decrease in diffusivity [9, 10], which may be reflected in an increase in FDC. The findings of reduced FD and FDC are in line with those of Vaughan et al. [11] and Feshki et al. [12], who reported decreased FD and FDC in white matter tracts in patients with TLE. Moreover, we also found that global degree, and global and local efficiency in the structural brain network, were positively correlated with FC and FDC in IPKA animals. This further indicates that decreased degree, integration, and segregation post-SE are likely related to decreased axonal density or decreased white matter integrity in the main white matter tracts in the rat brain.

## 8.2 Functional brain network changes during epileptogenesis

Changes in white matter integrity can also affect functional brain connectivity. In Chapter 6, functional network topology in a rat model of TLE was evaluated in a longitudinal resting state functional MRI (rsfMRI) study. Furthermore, the potential of functional network topology to predict seizure occurrence after an injury was investigated. RsfMRI is an imaging technique that allows visualisation of whole-brain activity, and can be used to identify and investigate functional brain networks. The topology of these networks can be assessed using graph theory. Using a 7T MRI system, rsfMRI images were acquired under medetomidine anesthesia before and 1, 3, 6, 10, and 16 weeks after status epilepticus (SE) induction in 20 IPKA animals and 7 healthy control animals. To obtain a functional network, the correlation between fMRI time series of 38 regions of interest (ROIs) was calculated. Then, graph theoretical network measures were calculated to assess changes in network topology. At least 17 weeks post-SE, IPKA animals were implanted with electrodes in the left and right dorsal hippocampus, electroencephalography (EEG) was measured for 7 consecutive days, and spontaneous seizures were counted.

The aim of this study was threefold: 1) to characterize how the functional organization of the rat brain changes after SE and during the development of TLE; 2) to identify brain regions with the highest degree of connectivity changes; 3) to evaluate whether connectivity changes are associated with the occurrence of spontaneous seizures.

### 8.2.1 Decreased functional connectivity and network efficiency during epileptogenesis

Analysis of the functional brain network revealed that clustering coefficient and local efficiency decreased during epileptogenesis, indicating a decrease in segregation or local interconnectivity. Characteristic path length increased and global efficiency decreased, indicating a decrease in integration or overall communication efficiency. Nodal degree decreased significantly in the most highly connected brain regions in the baseline

network, indicating a loss in connection strength. Most of these regions are part of the rat DMN, including cingulate cortex, retrosplenial cortex, visual cortex, auditory cortex, hippocampus, thalamus, motor cortex, and somatosensory cortex [13, 14]. Functional connectivity, segregation, and integration decreased most significantly between 1 and 3 weeks post-SE. Beyond this time point, the network topology remained unchanged. Although there is a large variability in changes in functional connectivity and network topology during epileptogenesis between studies and animal models, most studies agree that functional connectivity is decreased in several brain regions, including hippocampus and thalamus, which corresponds with our results [15–19]. Our findings are generally in line with most studies investigating functional connectivity and network topology in patients with TLE as well. Most studies agree that segregation is decreased in patients with TLE [20–22]. Integration has been found to be increased [20, 21] as well as decreased [22].

### 8.2.2 Decrease in connectivity of the retrosplenial cortex

The brain region that changed most profoundly in functional connectivity during epileptogenesis was the retrosplenial cortex, one of the most important nodes of the rat DMN [13, 14]. This finding is in line with a study in TLE patients that demonstrated a decrease in functional connectivity between the temporal lobe and the posterior cingulate cortex, the human equivalent of the rat retrosplenial cortex [5]. It is rather surprising that the retrosplenial cortex appears to be more affected than regions of the mesial temporal lobe (hippocampus, entorhinal and piriform cortices, and amygdala) that display most extensive cell loss [8, 23]. However, since the retrosplenial cortex plays a role in spatial navigation and episodic memory [24], the lower functional connectivity of this brain region could be a cause of the memory impairment seen in rats with TLE [17]. In addition to the retrosplenial cortex, the cingulum and parietal association cortex are affected during epileptogenesis as well. These brain regions have a high structural connectivity with other cortical regions, such as hippocampus and thalamus. Together, these regions form a connection between the primary sensory cortices [14, 25]. This could

explain why the decrease in functional connectivity in the brain network is so extensive, rather than limited to structurally lesioned brain regions.

### **8.2.3 Chronic seizure frequency is related to altered network topology during early epileptogenesis**

We also investigated whether the changes in network measures occurring during the development of epilepsy were associated with the occurrence of spontaneous epileptic seizures in the chronic epilepsy phase. Seizure frequency in the chronic epilepsy phase was positively correlated with functional connectivity, integration, and segregation 1 week post-SE, and with functional integration and segregation 16 weeks post-SE. In addition, seizure frequency was positively correlated with the degree of several brain regions, determined 1 week after SE. These regions included the hippocampus and thalamus, two regions heavily affected by neurodegeneration and gliosis in response to SE. In other words, the more functionally disconnected these brain regions are upon KA-induced SE, the less likely it is for seizures to occur in the chronic phase. These associations between seizure frequency and functional connectivity measures all point out a quite unexpected finding, namely that the more profound the brain network is affected by the KA-induced SE, the less likely it is that spontaneous epileptic seizures are generated. As such, it seems that the brain network needs to keep a minimal degree of organization to enable the emergence of seizures. This is in line with the potent therapeutic effects of resective/disconnective surgery as a treatment for epilepsy. Our findings correspond with those of [15], who also found that functional connectivity is correlated with seizure frequency. In addition, we found that those animals with the largest hippocampal volume loss displayed the lowest number of seizures. This could indicate that a sufficient amount of hippocampal tissue needs to be preserved as substrate for seizure generation. The correlation between network measures and seizure frequency 1 week after SE is very interesting, since we never recorded spontaneous epileptic seizures at that time point in the IPKA model for TLE. This indicates that network reorganisation upon an initial precipitating injury might have a predictive value and could

potentially be used as a biomarker for the development and progression of epilepsy.

### 8.3 Dynamic functional network topology during epileptogenesis

In most rsfMRI studies, functional connectivity is assumed to be stationary during the scanning session. However, in reality, it varies on a much shorter time scale. In Chapter 7, dynamic changes in functional network topology during the development of epilepsy were investigated using rsfMRI data acquired in the IPKA rat model of TLE. Dynamic functional connectivity was assessed by calculating the correlation matrices between fMRI time series of predefined regions of interest within a sliding window of 50 seconds using a step length of 2 seconds. The matrices were classified into 6 states of functional connectivity using k-means clustering, each characterized by a correlation matrix. In addition, several time-variable graph theoretical network metrics were calculated from the time-varying correlation matrices, and classified into 6 states of functional network topology, each characterized by a combination of network metrics.

The aim of this study was twofold: 1) to characterize how dynamic functional connectivity and network topology of the rat brain change after SE and during the development of TLE, and 2) to evaluate whether these changes are associated with the occurrence of spontaneous seizures.

#### 8.3.1 Dwelling in states with a lower mean functional connectivity, segregation and integration

Using dynamic functional connectivity analysis, 6 recurring states of functional connectivity could be distinguished in IPKA and control animals. Percentage dwell time (i.e., how often a state occurs) in the states with the highest mean functional connectivity was lower in the IPKA group compared to the control group, while dwell time was higher in the states with the lowest mean functional connectivity. In states with a higher mean functional connectivity, clustering coefficient and local

efficiency were higher as well, indicating a high segregation or local interconnectivity. In these states, characteristic path length was lower and local efficiency higher, indicating a high integration or overall communication efficiency. Similarly, segregation and integration were lower in states with a lower mean functional connectivity. The decomposition of time-varying global graph theoretical network metrics into states of functional network topology led to similar results. Dwell time was lower in states with a higher functional connectivity, segregation, and integration in the IPKA animals. Our results indicate that the epileptic rat brain is characterized by states with a lower overall functional connectivity, segregation, and integration, which is in line with studies investigating static functional connectivity in rat model of TLE, most of which found a decreased static functional connectivity in rat models of TLE [15–17, 19, 26].

### **8.3.2 Chronic seizure frequency is related to dwelling in states with high functional connectivity, segregation and integration**

Interestingly, average daily seizure frequency was positively correlated with percentage dwell time in states with a high mean functional connectivity, and high segregation and integration, and negatively with dwell time in states with a low mean functional connectivity, and low segregation and integration, 1 and 16 weeks post-SE. Accordingly, our findings indicate that animals that dwell in states with high functional connectivity, segregation, and integration have more chronic seizures. This is in line with the findings of [15], who reported a positive correlation between functional brain connectivity and seizure frequency in the IPKA model for TLE. On the other hand, residing in states of low functional connectivity, associated with lower seizure frequencies, may reflect the protective effect and effectiveness of the treatment of epilepsy by means of resective/disconnective surgery [27]. Since functional connectivity is more restricted to the states with the lowest functional connectivity, integration, and segregation in animals that have fewer seizures, it is conceivable that temporary increases in functional connectivity might

be necessary for seizures to be generated.

## 8.4 Limitations

### 8.4.1 Controlling resting state fMRI data for nuisance signals

The measured rsfMRI signal contains nuisance signals, i.e., signals unrelated to neural activity, such as signals related to respiration and the cardiac cycle, motion, arterial CO<sub>2</sub> concentration, blood pressure, vasomotion, or scanner-related artifacts. It is important to remove these signals, since they can cause spurious correlations in the data and affect the results [28, 29]. A common way to remove nuisance signals is using regression methods. The confounding signals that need to be regressed out can be recorded during the scanning session, such as cardiac or respiratory rate [28, 29]. They can also be derived from the rsfMRI data itself, such as motion signals or white matter, CSF, or global signals. In rats, motions signals in fMRI are typically related to respiratory rate. They can be derived from white matter or CSF signals. It is difficult to perform white matter or CSF signal regression, since these regions are very small. Global signal regression can be used, however this method is quite controversial [28, 29]. Another approach to remove nuisance signals from the fMRI signal is an ICA-based approach, such as Multivariate Exploratory Linear Optimised Decomposition of Independent Components (MELODIC). Using this approach, the fMRI signal is decomposed into signal components and artifact components. The nuisance signals can then be removed from the fMRI signal by subtracting the artifact components [29].

In this dissertation, we did not control for nuisance signals, mainly because the common regression methods are quite controversial. This may lead to spurious correlations in our data. However, we did filter our data using a classical band pass filter of 0.01 to 0.1 Hz to reduce physiological noise. To limit the effect of nuisance signals in future experiments, the use of a novel approach, such as MELODIC, could be an added value to further clean up the rsfMRI signal.

### **8.4.2 Histological analysis**

Another limitation of this dissertation is the lack of post-mortem histological analysis. Taking into consideration the 3R principle in animal research (Replacement, Reduction and Refinement), the animals used in this dissertation were also used in another experiment, during which the effect of chemogenetic inhibition of the hippocampus on seizure frequency was investigated. Therefore, histological analysis was not an option. However, it would have been very interesting to assess correlations between histopathological changes during epileptogenesis and altered structural and functional network topology. The main histopathological changes in the IPKA model are neuronal degeneration, gliosis and mossy fiber sprouting. To assess neuronal degeneration, a Nissl staining can be performed to detect the cytoarchitectonic boundaries of brain regions and to visualize the extent and severity of tissue damage. Another possibility is a Fluoro-Jade stain, which can be used to label degenerating neurons. Gliosis can be assessed using a stain for glial cells with anti-glial fibrillary acidic protein (GFAP). This stain visualizes astrocytes. To evaluate mossy fiber sprouting, a Timm's silver sulfide staining can be performed. These types of histological analyses could help to elucidate pathological processes during epileptogenesis.

## **8.5 Beyond epilepsy: functional brain network dysfunction in anxiety disorder**

Analysis of structural and functional brain networks is not limited to the application of epilepsy. Changes in functional network topology have been reported in several neurological and psychiatric network disorders, such as Alzheimer's disease, schizophrenia, attention-deficit hyperactivity disorder, and traumatic brain injury [30]. Another network disorder in which abnormal functional brain networks play a role is anxiety disorder [31]. Anxiety disorders are a group of disorders that are characterized by anxiety, i.e., a feeling of inner turmoil, often in combination with nervous behaviour, somatic symptoms, and obsessive thinking. They are the most prevalent psychiatric disorders and cause a significant burden of ill-

ness [32]. Gaining more insight into the aberrant brain networks that are involved in anxiety disorders could lead to a better understanding of the disease and help to find targets for new treatment options, such as transcranial magnetic stimulation [31]. Anxiety disorders are also common in dogs, and the neurobiological base is similar to its human counterpart, making dogs an excellent translational model [33]. To investigate brain network topology in dogs with anxiety, rsfMRI images were acquired in 13 dogs with anxiety and 25 healthy controls. In addition, symptoms of anxiety were evaluated using a canine behavioral questionnaire. Functional brain networks were constructed and analyzed using graph theory.

The aim of this study was threefold: 1) to evaluate differences in brain network topology between healthy dogs and dogs with anxiety; 2) to identify differences in functional connectivity in regions of the anxiety circuit; and 3) to assess whether different symptoms of anxiety are related to specific functional network changes.

No significant differences in global network topology between groups were observed. However, when focusing on the anxiety circuit, nodal degree and global efficiency were found to be significantly higher, and characteristic path length significantly lower in amygdala and mesencephalon in the anxiety group, compared to the healthy group (Figure 8.1). This indicates that functional connectivity, and integration or communication efficiency, were increased between these regions and the rest of the functional network. In amygdala, clustering coefficient and local efficiency were significantly higher in the anxiety group as well, indicating an increase in local interconnectivity in this region (Figure 8.1). Moreover, correlations between network metrics and anxiety symptoms in the canine behavioral assessment and research questionnaire were found. Altered network metrics in amygdala were correlated with stranger-directed fear and excitability, altered degree in hippocampus was related to attachment/attention seeking, trainability, and touch sensitivity, and abnormal clustering in the frontal lobe was related to chasing (Figure 8.2). This indicates that rsfMRI could be used as biomarker for anxiety, although further research is still required. The findings of this study shed light on the aberrant topological organization of the functional brain

network in dogs with anxiety, which can provide novel insights into the pathophysiological mechanisms and course of illness of anxiety in dogs, and humans, and may lead to more personalized and effective therapies. The results of this study are described in the manuscript 'Network analysis reveals abnormal functional brain circuitry in anxious dogs' by Yangfeng Xu, Emma Christiaen, Qinyuan Chen, Sara De Witte, Kathelijne Peremans, Robrecht Dockx, Jimmy Saunders, Christian Vanhove and Chris Baeken, which is in preparation.

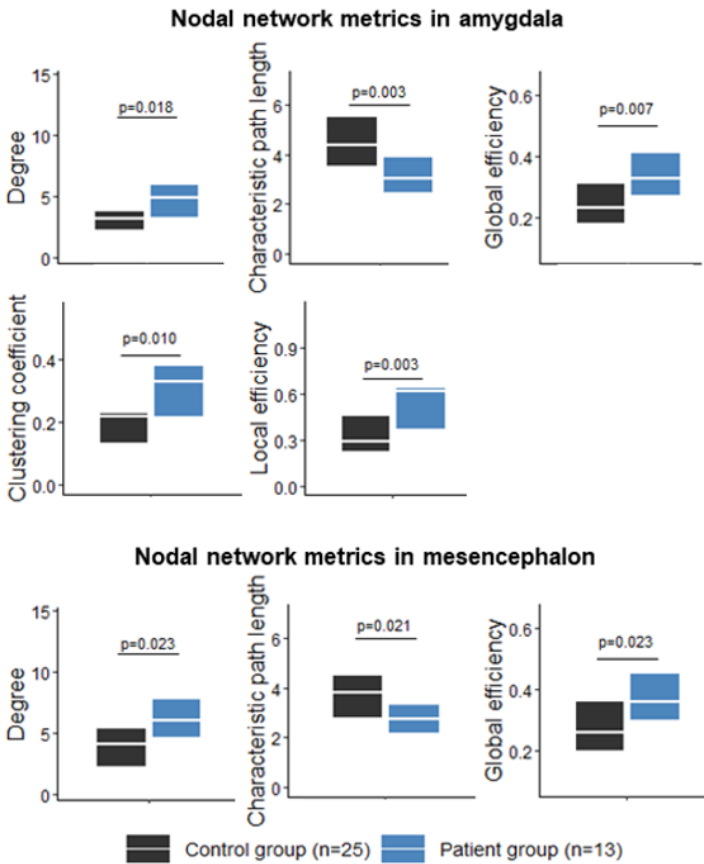


**Figure 8.1:** Nodal network metrics in amygdala and mesencephalon, two regions of the anxiety circuit. Data are visualized as a boxplot with median and interquartile range. Significant differences between patient group and control group, assessed using the non-parametric Mann-Whitney U test, are indicated in the graphs.

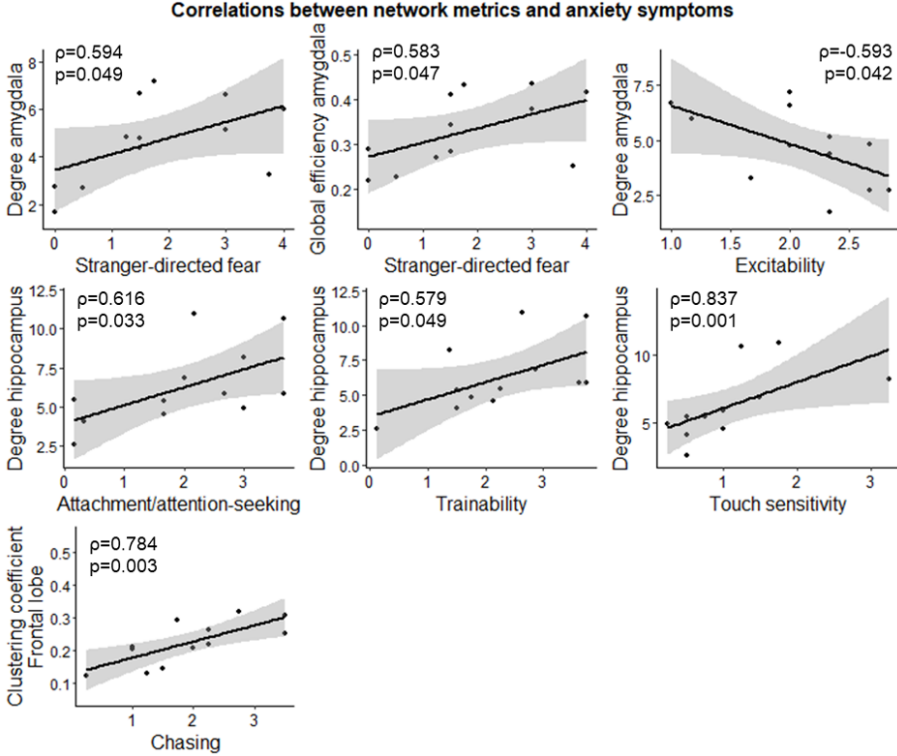


**Figure 8.2:** Correlations between nodal network metrics and anxiety symptoms. Data are visualized as a scatter plot with regression line and 95% confidence interval.

## 8.6 Future perspectives

### 8.6.1 Multilayer networks

Brain networks are a combination of structural and functional networks. Structural networks can be considered the ‘hardware’ of the brain, and functional networks the ‘software’, that uses the hardware to execute specific tasks. Structural and functional networks are usually investigated separately. However, by integrating information from both networks, more insights can be obtained about the relationship between structural and functional networks, and how a more static structural network is related to the more variable functional network [34]. Structural and functional information can be studied simultaneously using a multilayer

network approach. A multilayer, or multiplex, network consists of several distinct networks that each contain a different type of information. A multilayer network combining structural and functional information, consists of two layers. The nodes in the network represent brain regions, and have a replica in each layer. The edges represent the relationship between the nodes. In one layer, they reflect structural connectivity or anatomical information, obtained using diffusion-weighted MRI, and in the other layer they represent functional connectivity, obtained using resting state functional MRI. There are no connections across the two layers, except for links between replicas of a node [35, 36]. Both layers can contribute equally to the multilayer network, but it is also possible to give more importance to one of the layers [37]. During epileptogenesis, both structural and functional network topology are altered. It would be very interesting to investigate multilayer networks in epilepsy and during epileptogenesis, to obtain a more accurate estimate of the brain regions that are involved in the pathophysiology of epilepsy.

### 8.6.2 Biomarkers for epileptogenesis

In this dissertation, we found that changes in functional network topology during the latent phase of epileptogenesis were related to chronic seizure frequency. This indicates that functional network topology might have the potential to be used as a biomarker for epileptogenesis or disease prognosis in the future. However, further research is required to validate this finding.

In adults, epilepsy is often caused by an initial precipitating injury, such as head trauma, stroke or infection. At present, it is not possible to stop or alleviate the development of epilepsy after such an injury. Therefore, developing new treatment options to prevent epileptogenesis is a research priority. However, this research is progressing slowly, partly because of the lack of diagnostic biomarkers for epileptogenesis. This type of biomarkers could help to select the right patient populations for clinical trials, which would make them more cost effective. In addition, there is a need for response biomarkers to evaluate antiepileptogenic treatment quickly, instead of waiting anywhere from months up to years, to see

whether or not a patient develops epilepsy [38]. Two reasons why it is difficult to find biomarkers in humans are because of the heterogeneity of the initial precipitating injury and because of patient-specific factors. To overcome these limitations, rodent models of epileptogenesis can be used [39].

Several studies have used diffusion-weighted or resting state functional MRI to investigate structural and functional brain networks in patients with, and animal models of, epilepsy. The findings of these studies are quite variable. At least in part, this may be due to a lack of standardized procedures in clinical and preclinical studies. Therefore, it is very important to harmonize image acquisition and analysis in future studies [39]. This should reduce the variability in results and improve test-retest reliability, which in turn should make it possible to detect smaller effect sizes, and lead to better and more reliable identification of potential biomarkers for epileptogenesis.

## 8.7 Conclusion

Longitudinal diffusion-weighted and resting state functional MRI, in combination with graph theory, revealed dynamic changes in structural and functional network topology during epileptogenesis in a rat model of temporal lobe epilepsy. More specifically, structural and functional connectivity, integration, and segregation decreased during epileptogenesis. These changes were not limited to the epileptogenic focus, but were widespread, and mainly affected regions of the limbic system and the default-mode network. Structural and functional network topology changed most during early epileptogenesis, and the changes were related to reduced intra-axonal water fraction in white matter tracts. This indicates that these changes may be related to neurodegeneration and gliosis, which are known histopathological features of early epileptogenesis. Altered functional connectivity, integration, and segregation during the latent phase of epileptogenesis were related to chronic seizure frequency. This hints at the potential of functional network topology as a biomarker for disease prognosis after an initial precipitating injury. Further research is required to validate these promising findings.

## Bibliography

- [1] B. C. Bernhardt, F. Fadaie, M. Liu, B. Caldairou, S. Gu, E. Jefferies, J. Smallwood, D. S. Bassett, A. Bernasconi, and N. Bernasconi, “Temporal lobe epilepsy: Hippocampal pathology modulates connectome topology and controllability,” *Neurology*, vol. 92, no. 19, pp. E2209–E2220, may 2019. [Online]. Available: <https://n.neurology.org/content/92/19/e2209><https://n.neurology.org/content/92/19/e2209.abstract>
- [2] P. Besson, V. Dinkelacker, R. Valabregue, L. Thivard, X. Leclerc, M. Baulac, D. Sammler, O. Colliot, S. Lehéricy, S. Samson, and S. Dupont, “Structural connectivity differences in left and right temporal lobe epilepsy,” *NeuroImage*, vol. 100, pp. 135–144, oct 2014.
- [3] L. Bonilha, T. Nesland, G. U. Martz, J. E. Joseph, M. V. Spampinato, J. C. Edwards, and A. Tabesh, “Medial temporal lobe epilepsy is associated with neuronal fibre loss and paradoxical increase in structural connectivity of limbic structures,” *Journal of Neurology, Neurosurgery and Psychiatry*, vol. 83, no. 9, pp. 903–909, sep 2012. [Online]. Available: <http://www.fmrib.ox.ac.uk/fsl>
- [4] K. Kamiya, S. Amemiya, Y. Suzuki, N. Kunii, K. Kawai, H. MORI, A. Kunimatsu, N. Saito, S. Aoki, and K. Ohtomo, “Machine Learning of DTI Structural Brain Connectomes for Lateralization of Temporal Lobe Epilepsy,” *Magnetic Resonance in Medical Sciences*, vol. 15, no. 1, pp. 121–129, 2016. [Online]. Available: <https://www.jstage.jst.go.jp/article/mrms/15/1/15{ }2015-0027/{ }article>
- [5] W. Liao, Z. Zhang, Z. Pan, D. Mantini, J. Ding, X. Duan, C. Luo, Z. Wang, Q. Tan, G. Lu *et al.*, “Default mode network abnormalities in mesial temporal lobe epilepsy: a study combining fmri and dti,” *Human brain mapping*, vol. 32, no. 6, pp. 883–895, 2011.
- [6] D. Bertoglio, H. Amhaoul, A. Van Eetveldt, R. Houbrechts, S. Van De Vijver, I. Ali, and S. Dedeurwaerdere, “Kainic acid-induced post-status epilepticus models of temporal lobe epilepsy with diverg-

- ing seizure phenotype and neuropathology,” *Frontiers in neurology*, vol. 8, p. 588, 2017.
- [7] M. Drexel, A. P. Preidt, and G. Sperk, “Sequel of spontaneous seizures after kainic acid-induced status epilepticus and associated neuropathological changes in the subiculum and entorhinal cortex,” *Neuropharmacology*, vol. 63, no. 5, pp. 806–817, oct 2012.
- [8] M. Lévesque and M. Avoli, “The kainic acid model of temporal lobe epilepsy,” *Neuroscience & Biobehavioral Reviews*, vol. 37, no. 10, pp. 2887–2899, 2013.
- [9] J.-A. Kim, J. I. Chung, P. H. Yoon, D. I. Kim, T.-S. Chung, E.-J. Kim, and E.-K. Jeong, “Transient mr signal changes in patients with generalized tonicoclonic seizure or status epilepticus: periictal diffusion-weighted imaging,” *American journal of neuroradiology*, vol. 22, no. 6, pp. 1149–1160, 2001.
- [10] M. Yogarajah and J. S. Duncan, “Diffusion-based magnetic resonance imaging and tractography in epilepsy,” *Epilepsia*, vol. 49, no. 2, pp. 189–200, 2008.
- [11] D. N. Vaughan, D. Raffelt, E. Curwood, M.-H. Tsai, J.-D. Tournier, A. Connelly, and G. D. Jackson, “Tract-specific atrophy in focal epilepsy: Disease, genetics, or seizures?” *Annals of Neurology*, vol. 81, no. 2, pp. 240–250, feb 2017. [Online]. Available: <http://doi.wiley.com/10.1002/ana.24848>
- [12] M. Feshki, E. Parham, and H. Soltanin-Zadeh, “Fixel-Based Analysis of White Matter in Temporal Lobe Epilepsy,” in *2018 25th Iranian Conference on Biomedical Engineering and 2018 3rd International Iranian Conference on Biomedical Engineering, ICBME 2018*. Institute of Electrical and Electronics Engineers Inc., jul 2018.
- [13] L. Becerra, G. Pendse, P.-C. Chang, J. Bishop, and D. Borsook, “Robust reproducible resting state networks in the awake rodent brain,” *PloS one*, vol. 6, no. 10, p. e25701, 2011.

- [14] H. Lu, Q. Zou, H. Gu, M. E. Raichle, E. A. Stein, and Y. Yang, "Rat brains also have a default mode network," *Proceedings of the National Academy of Sciences*, vol. 109, no. 10, pp. 3979–3984, 2012.
- [15] D. Bertoglio, E. Jonckers, I. Ali, M. Verhoye, A. Van der Linden, and S. Dedeurwaerdere, "In vivo measurement of brain network connectivity reflects progression and intrinsic disease severity in a model of temporal lobe epilepsy," *Neurobiology of disease*, vol. 127, pp. 45–52, 2019.
- [16] R. S. Gill, S. M. Mirsattari, and L. S. Leung, "Resting state functional network disruptions in a kainic acid model of temporal lobe epilepsy," *NeuroImage: Clinical*, vol. 13, pp. 70–81, 2017.
- [17] Y. Jiang, C.-L. Han, H.-G. Liu, X. Wang, X. Zhang, F.-G. Meng, and J.-G. Zhang, "Abnormal hippocampal functional network and related memory impairment in pilocarpine-treated rats," *Epilepsia*, vol. 59, no. 9, pp. 1785–1795, 2018.
- [18] A. M. Mishra, X. Bai, B. G. Sanganahalli, S. G. Waxman, O. Shatillo, O. Grohn, F. Hyder, A. Pitkänen, and H. Blumenfeld, "Decreased resting functional connectivity after traumatic brain injury in the rat," *PloS one*, vol. 9, no. 4, p. e95280, 2014.
- [19] T. Pirttimäki, R. A. Salo, A. Shatillo, M. I. Kettunen, J. Paasonen, A. Sierra, K. Jokivarsi, V. Leinonen, P. Andrade, S. Quittek *et al.*, "Implantable rf-coil with multiple electrodes for long-term eeg-fmri monitoring in rodents," *Journal of neuroscience methods*, vol. 274, pp. 154–163, 2016.
- [20] W. Liao, Z. Zhang, Z. Pan, D. Mantini, J. Ding, X. Duan, C. Luo, G. Lu, and H. Chen, "Altered functional connectivity and small-world in mesial temporal lobe epilepsy," *PloS one*, vol. 5, no. 1, p. e8525, 2010.
- [21] J. Song, V. A. Nair, W. Gaggl, and V. Prabhakaran, "Disrupted brain functional organization in epilepsy revealed by graph theory analysis," *Brain connectivity*, vol. 5, no. 5, pp. 276–283, 2015.

- [22] M. Vlooswijk, M. Vaessen, J. Jansen, M. De Krom, H. Majoie, P. Hofman, A. Aldenkamp, and W. Backes, “Loss of network efficiency associated with cognitive decline in chronic epilepsy,” *Neurology*, vol. 77, no. 10, pp. 938–944, 2011.
- [23] A. K. Sharma, W. H. Jordan, R. Y. Reams, D. G. Hall, and P. W. Snyder, “Temporal profile of clinical signs and histopathologic changes in an f-344 rat model of kainic acid-induced mesial temporal lobe epilepsy,” *Toxicologic pathology*, vol. 36, no. 7, pp. 932–943, 2008.
- [24] S. D. Vann, J. P. Aggleton, and E. A. Maguire, “What does the retrosplenial cortex do?” *Nature reviews neuroscience*, vol. 10, no. 11, pp. 792–802, 2009.
- [25] L.-M. Hsu, X. Liang, H. Gu, J. K. Brynildsen, J. A. Stark, J. A. Ash, C.-P. Lin, H. Lu, P. R. Rapp, E. A. Stein *et al.*, “Constituents and functional implications of the rat default mode network,” *Proceedings of the National Academy of Sciences*, vol. 113, no. 31, pp. E4541–E4547, 2016.
- [26] E. Christiaen, M.-G. Goossens, R. Raedt, B. Descamps, L. E. Larsen, E. Craey, E. Carrette, K. Vonck, P. Boon, and C. Vanhove, “Alterations in the functional brain network in a rat model of epileptogenesis: A longitudinal resting state fmri study,” *Neuroimage*, vol. 202, p. 116144, 2019.
- [27] D. J. Englot, H. Birk, and E. F. Chang, “Seizure outcomes in nonresective epilepsy surgery: an update,” *Neurosurgical review*, vol. 40, no. 2, pp. 181–194, 2017.
- [28] W.-J. Pan, J. C. Billings, J. K. Grooms, S. Shakil, and S. D. Keilholz, “Considerations for resting state functional mri and functional connectivity studies in rodents,” *Frontiers in neuroscience*, vol. 9, p. 269, 2015.
- [29] V. Zerbi, J. Grandjean, M. Rudin, and N. Wenderoth, “Mapping the mouse brain with rs-fmri: An optimized pipeline for functional network identification,” *Neuroimage*, vol. 123, pp. 11–21, 2015.

- [30] J. Wang, X. Zuo, and Y. He, “Graph-based network analysis of resting-state functional mri,” *Frontiers in systems neuroscience*, vol. 4, p. 16, 2010.
- [31] C. M. Sylvester, M. Corbetta, M. Raichle, T. Rodebaugh, B. Schlaggar, Y. Sheline, C. Zorumski, and E. Lenze, “Functional network dysfunction in anxiety and anxiety disorders,” *Trends in neurosciences*, vol. 35, no. 9, pp. 527–535, 2012.
- [32] B. Bandelow, S. Michaelis, and D. Wedekind, “Treatment of anxiety disorders,” *Dialogues in Clinical Neuroscience*, vol. 19, no. 2, pp. 93–107, jun 2017. [Online]. Available: <https://pubmed.ncbi.nlm.nih.gov/28867934/>
- [33] K. L. Overall, “Natural animal models of human psychiatric conditions: Assessment of mechanism and validity,” *Progress in Neuro-Psychopharmacology and Biological Psychiatry*, vol. 24, no. 5, pp. 727–776, jul 2000.
- [34] J. J. Crofts, M. Forrester, and R. D. O’Dea, “Structure-function clustering in multiplex brain networks,” *EPL*, vol. 116, no. 1, p. 18003, oct 2016. [Online]. Available: [www.epljournal.org](http://www.epljournal.org)
- [35] F. Battiston, V. Nicosia, M. Chavez, and V. Latora, “Multilayer motif analysis of brain networks,” *Chaos*, vol. 27, no. 4, apr 2017.
- [36] M. De Domenico, “Multilayer modeling and analysis of human brain networks,” *Giga Science*, vol. 6, no. 5, p. gix004, 2017.
- [37] F. Battiston, J. Guillon, M. Chavez, V. Latora, and F. de Vico Fal-lani, “Multiplex core–periphery organization of the human connectome,” *Journal of the Royal Society Interface*, vol. 15, no. 146, p. 20180514, 2018.
- [38] A. Pitkänen, X. E. Nnode-Ekane, N. Lapinlampi, and N. Puhakka, “Epilepsy biomarkers—toward etiology and pathology specificity,” *Neurobiology of disease*, vol. 123, pp. 42–58, 2019.

- [39] R. Immonen, G. Smith, R. D. Brady, D. Wright, L. Johnston, N. G. Harris, E. Manninen, R. Salo, C. Branch, D. Duncan, R. Cabeen, X. E. Ndode-Ekane, C. S. Gomez, P. M. Casillas-Espinosa, I. Ali, S. R. Shultz, P. Andrade, N. Puhakka, R. J. Staba, T. J. O'Brien, A. W. Toga, A. Pitkänen, and O. Gröhn, "Harmonization of pipeline for preclinical multicenter MRI biomarker discovery in a rat model of post-traumatic epileptogenesis," *Epilepsy Research*, vol. 150, pp. 46–57, feb 2019.